REMOTE SENSING OF IMPERVIOUS SURFACE AREA AND ITS INTERACTION WITH LAND SURFACE TEMPERATURE VARIABILITY IN PRETORIA, SOUTH AFRICA

by

ADENIYI ADEDAYO ADEYEMI

submitted in accordance with the requirements for the degree of

DOCTOR OF PHILOSOPHY

in the subject of

ENVIRONMENTAL SCIENCES

at the

UNIVERSITY OF SOUTH AFRICA

SUPERVISOR: Professor Abel Ramoelo

CO-SUPERVISOR: Professor Moses Azong Cho

Date: December 2021

Declaration

Name:	Adeniyi Adedayo Adeyemi
Student number:	58547096
Degree:	Doctor of Philosophy Environmental Science

REMOTE SENSING OF IMPERVIOUS SURFACE AREA AND ITS INTERACTION WITH LAND SURFACE TEMPERATURE VARIABILITY IN PRETORIA, SOUTH AFRICA

I declare that the above dissertation is my own work and that all the sources that I have used or quoted have been indicated and acknowledged by means of complete references.

I further declare that I submitted the dissertation to originality checking software and that it falls within the accepted requirements for originality.

I further declare that I have not previously submitted this work, or part of it, for examination at UNISA for another qualification or at any other higher education institution.

	01 December, 2021
SIGNATURE	DATE

Abstract

Pretoria, City of Tshwane (COT), Gauteng Province, South Africa is one of the cities that continues to experience rapid urban sprawl as a result of population growth and various land use, leading to the change of natural vegetation lands into impervious surface area (ISA). These are associated with transportation (paved roads, streets, highways, parking lots and sidewalks) and cemented buildings and rooftops, made of completely or partly impermeable artificial materials (e.g., asphalt, concrete, and brick). These landscapes influence the micro-climate (e.g., land surface temperature, LST) of Pretoria City as evidenced by the recent heat waves characterized by high temperature. Therefore, understanding ISA changes will provide information for city planning and environmental management. Conventionally, deriving ISA information has been dependent on field surveys and manual digitizing from hard copy maps, which is laborious and time-consuming. Remote sensing provides an avenue for deriving spatially explicit and timely ISA information. Numerous methods have been developed to estimate and retrieve ISA and LST from satellite imagery. There are limited studies focusing on the extraction of ISA and its relationship with LST variability across major cities in Africa. The objectives of the study were: (i) to explore suitable spectral indices to improve the delineation of built-up impervious surface areas from very high resolution multispectral data (e.g., WorldView-2), (ii) to examine exposed rooftop impervious surface area based on different colours, and their interplay with surface temperature variability, (iii) to determine if the spatio-temporal built-up ISA distribution pattern in relation to elevation influences urban heat island (UHI) extent using an optimal analytical scale and (iv) to assess the spatio-temporal change characteristics of ISA expansion using the corresponding surface temperature (LST) at selected administrative subplace units (i.e., local region scale). The study objectives were investigated using remote sensing data such as WorldView-2 (a very high-resolution multispectral sensor), medium resolution Landsat-5 Thematic Mapper (TM) and Landsat-8 OLI (Operational Land Imager) and TIRS (Thermal Infrared Sensor) at multiple scales. The ISA mapping methods used in this study can be grouped into two major categories: (i) the classification-based approach consisting of an object-based multi-class classification with overall accuracy ~90.4% and a multitemporal pixel-based binary classification. The latter yielded an area under the receiver operating characteristic curve (AUROC) = 0.8572 for 1995, AUROC = 0.8709 for 2005, AUROC = 0.8949 for 2015. (ii) the spectral index-based approach such as a new built-up extraction index (NBEI) derived in this study which yielded a high AUROC = ~0.82 compared to Built-up Area Index (BAI) (AUROC = ~0.73), Built-up spectral index (BSI) (AUROC = ~0.78), Red edge / Green Index

(RGI) (AUROC = ~0.71) and WorldView-Built-up Index (WV-BI) (AUROC = ~0.67). The multitemporal built-up Index (BUI) also estimated with AUROC = 0.8487 for 1993, AUROC = 0.8302 for 2003, AUROC = 0.8790 for 2013. This indicates that all these methods employed, mapped ISA with high predictive accuracy from remote sensing data. Furthermore, the single-channel algorithm (SCA) was employed to retrieve LST from the thermal infrared (TIR) band of the Landsat images. The LST overall retrieval error for the entire study generally was quite low (overall root mean square RMSE $\leq$ ~1.48^{O}C), which signifies that the Landsat TIR used provided good results for further analysis. In conclusion, the study showed the potential of multispectral remote sensing data to quantify ISA and evaluate its interaction with surface temperature variability despite the complex urban landscape in Pretoria. Also, using impervious surface LST as a complementary metric in this research helped to reveal urban heat island distribution and improve understanding of the spatio-temporal developing trend of urban expansion at a local spatial scale.

Keywords: WorldView-2 (WV-2); spectral indices; built-up; very high resolution (VHR); Rooftops; SCA, LST; Landsat, ISA, BUI; ISA, Random forest; TIRS.

Acknowledgements

I would like to express my indebtedness to GOD ALMIGHTY who was by my side through the years, months, days and nights; to my Lord JESUS CHRIST, for his mercy and kindness and to the HOLY SPIRIT, my source of inspiration. My deep and sincere appreciation goes to wife Prophetess (Mrs.) Tema Matilda -Yebga Adeyemi and my children Jedidiah and Jethro for their constant prayers and support to see this program come to a success.

It is with a deep sense of appreciation that I acknowledge Professor Abel Ramoelo and Professor Moses Azong Cho, my research supervisors, for their patient guidance, enthusiastic inspiration and useful critiques of this research work. Professor Abel Ramoelo did a remarkable job by mentoring and teaching me critical thinking, ability to identify research gaps, scientific analysis and writing. I would also like to thank him for encouraging my research and for allowing me to grow under his tutelage to be independent as a research scientist. Professor Moses Azong Cho, you have been a tremendous mentor for me and by guiding me to progress on schedule. I would like to thank you for your brilliant comments and suggestions. Your advice on both research as well as on my career, have been priceless.

Special mention goes to the University of South Africa Student Funding Directorate (UNISA, DSF) and GeoTerraImage (Pty) Ltd for their support with the research funding needed for the execution of the study. This research was implemented at the Department of Environmental Science, College of Agriculture & Environmental Sciences, University of South Africa (UNISA) and Council for Scientific and Industrial Research (CSIR), South Africa.

I would also like to extend thanks to Mr. Pieter Sevenhuysen, Mr. Fanie Ferreira, Mr. Mark Thompson and Mr. Jacobus Strydom of GeoTerraImage (Pty) Ltd and Ms. Minétte Teessen (Editor) for their support, cooperation and kind assistance.

Finally, I also wish to recognize the support and affections of my parents Mr and Mrs. Adeyemi who have always been there for me as well. THANK YOU ALL!

Table of Contents

List of Tables

List of Figures

List of Abbreviations

AE	Automatic Encoder
ANOVA	Analysis of variance
ASTER	Advance Space borne Thermal Emission And Reflection Radiometer
AVHRR	Advanced Very High Resolution Radiometer
AUROC	Area Under The Receiver Operating Characteristic Curve
BAEI	Advance Space borne Thermal Emission And Reflection Radiometer
BAI	Built-up Area Index
BBI	Built-up and Bare-land index
BCI	Biophysical Composition Index
BSI	Built up spectral index
BSTBI	Blue Steel Tile-Roofed Buildings Index
BUI	Built up Index
CART	Classification and Regression Tree
CBD	Central Business District
CBI	Combinational Build-up Index
CDNGI	Chief Directorate National Geo-Spatial Information
CNN	Convolutional |Neural Network
COT	City of Tshwane
DBN	Deep Belief Network
DEM	Digital Elevation Models
DFFE	Department of Forestry, Fisheries and the Environment
DMSP-OLS	Defense Meteorological Satellite Program's Operational Linescan System
DN	Digital Number
DT	Decision Tree
EBBI	Enhanced Built-up and Bareness Index
ENDISI	Enhanced Normalized Difference Impervious Surfaces index
ENVI	Environment For Visualizing Images
ESRI	Environmental Systems Research Institute
ETM+	Enhanced Thematic Mapper Plus
FLAASH	Fast Line-of-sight Atmospheric Analysis of Hypercubes

GLCM	Gray Level Co-Occurrence Matrix
GOES	Geodynamic Experimental Ocean Satellite
GPS	Global positioning system
GTI	Geoterraimage
HCMM	Heat Capacity Mapping Mission
IBI	Index-Based Built-up Index
IRT	Infra-red thermometers
ISA	Impervious surface area
KNN	K Nearest Neighbour
LiDAR	Light Detection and Ranging
LSMA	Linear Spectral Mixture Analysis
LST	Land Surface Temperature
LULC	Land use / cover
MASTER	Moderate Resolution Imaging Spectroradiometer/Advance Space borne Thermal Emission and Reflection Radiometer airborne simulator
MAE	Mean Absolute Error
MNDISI	Modified Normalized Difference Impervious Surface Index
MNDWI	Modified Normalized Difference Water Index
MODIS	Moderate Resolution Imaging Spectroradiometer
NBEI	New Built-up Extraction Index
NBUI	New Built-up Index
NDBI	Normalized Difference Built-up Index
NDII	Normalized Difference Impervious Index
NDISI	Normalized Difference Impervious Surface Index
NDSI	Normalized Difference Soil Index
NDVI	Normalized Difference Vegetation Index
NHM	Normalized Height Model
NIR	Near Infrared
NLC	National Land Cover
NOAA	National Oceanic and Atmospheric Administration
NSMA	Normalized Spectral Mixture Analysis
OLI	Operation Land Imager

PISA	Percent Impervious Surface Area
PISI	Perpendicular Impervious Surface Index
RNN	Recurrent Neural Network
RGI	Red edge / Green Index
RMSE	Root Mean Square Error
RISI	Ratio-based Impervious Surface Index
SAR	Synthetic Aperture Radar
SASMA	Spatially Adaptive Spectral Mixture Analysis
SAVI	Soil Adjusted Vegetation Index
SAWS	South African Weather Station
SCA	Single Channel Algorithm
SEVIRI	Spinning Enhanced Visible And Infrared Imager
SRTM	Shuttle Radar Topography Mission
SVM	Support Vector Machine
SWIR	Shortwave Infrared Red
TIMS	Tropospheric Infrared Mapping Spectrometers
TIR	Thermal Infrared
TM	Thematic Mapper
TMA	Temporal Mixture Analysis
TOA	Top of Atmosphere
UHI	Urban Heat Island
UI	Urban Index
UN	United Nation
UN-DESA	United Nations Department of Economic and Social Affairs
UNFCCC	United Nations framework Convention on Climate Change
UTM	Universal Transverse Mercator
VHR	Very High Resolution
WEKA	Waikato Environment for Knowledge Analysis
WV-BI	WorldView-Built-up Index

Chapter 1 General Introduction

1.1. Background and problem statement

Globally, urbanization has grown at an unprecedented rate over the past 50 years, with the population rate in cities increasing from 30% in the 1950s to 54% in 2014 (World Bank., 2015; Man et al., 2019). UN (2014) projected that the global urban population was with a higher urban population compared to the rural areas since 2007. As reported in the study of Sahana, Hong and Sajjad (2018), more of the future urban sprawl due to the rapid development of large urban agglomerations will be witnessed in the developing countries. Notwithstanding, Africa being the least developed, its urbanization is certainly one of the fastest in the world (Güneralp et al., 2018). Africa's urban population has been growing at a very high rate from an estimated 28% in 1980 (Roxburgh et al., 2010) to 43% in 2018 and projected to be about 60% by 2050 (UN-DESA, 2018).

One consequence of rapid, uncontrolled and unplanned urban sprawl is the replacement of natural vegetation coverage with impervious surfaces area (ISA) made of completely or partly impermeable artificial materials (e.g., asphalt, concrete, and brick) (Adeyemi *et al.*, 2015). Man et al. (2019) further explained that though ISA sprawl is related to the increase of economic activities, the diversification of a locality's economy attracts ISA rapid increase as the infrastructure necessary for that development is created (Man et al. 2019). ISA might be considered an important element of economic development (Elvidge et al., 2007). It has a close connection with important features of the physical and biological environment, thus affecting the quality and maintenance of life (Kawakubo et al., 2019). There are many undesirable impacts of ISA increase that have been documented over the years in various studies. Since water cannot infiltrate the soil through ISA, natural hydrological conditions are altered with increase in velocity and volume of runoff and decrease in groundwater recharge and baseflow which potentially increases the risk of flooding (Chormanski et al., 2008; Pappas et al., 2008; Man et al., 2019). Moreover, ISA is also the main cause of soil degradation which threatens biodiversity (reducing or affecting habitats), causing a loss of fertile agricultural land and natural and semi-natural areas (Prokop, Jobstmann and Schönbauer, 2011).

Urban landscapes are characterized by the highest degree of imperviousness and continuous built-up areas which have negatively influenced their microclimate i.e., altering the sensible and latent heat fluxes (Artmann, 2014; Man et al., 2019). According to Kawakubo et al.(2019), urban impervious surface materials, such as asphalt, concrete and asbestos, can absorb more solar energy, which is then released as heat. Morabito et al. (2018) further explained that the high thermal conductivity and the heat storage capacity, often coupled with low solar reflectivity of most artificial impervious surfaces, cause alterations to the energy budget of the surfaces, increasing the sensible heat instead of the latent heat, and producing a generalized rise in the urban temperature. This situation is linked to the urban heat island (UHI) phenomenon (Oke, 1973, 1982; Kim, 1992).This phenomenon is also associated with an exacerbation of thermal discomfort (Qaid et al., 2016) and the higher levels of heat-related-mortality and morbidity of vulnerable people (i.e., elderly, young children and low-income residents) living in densely built-up districts of urban areas due to a variety of physical, social and economic reasons (Zhao et al., 2015; Morabito et al., 2018).

Ground measurements or surveys with a global positioning system (GPS) have been the earliest methods used to provide reliable information on ISA but have also been observed to be time-consuming, expensive and with accessibility problems (Xu, Mountrakis and Quackenbush, 2017). Since the 1970s, airborne and satellite sensor imagery have been utilized for interpretive, spectral and modelling applications on impervious surfaces mapping (Slonecker, Jennings and Garofalo, 2001; Weng, 2012). Satellite remote sensing data have served as a useful source of built-up area information in previous studies due to large-area coverage and short revisit cycles (Varshney and Rajesh, 2014). Furthermore, satellite-based sensors with different spatial resolutions such as Landsat Thematic Mapper/Enhanced Thematic Mapper Plus (TM/ETM+) (Nie et al., 2016; Henits, Mucsi and Liska, 2017), Landsat 8 Operational Land Imager (OLI) (Adeyemi, Botai and Ramoelo, 2015), Moderate Resolution Imaging Spectroradiometer (MODIS) (Zhang et al., 2017), IKONOS (Lu, 2009), WorldView-2, WV-2 (Cai, Li and Jin, 2016; Sun et al., 2019), WorldView-3, WV-3 (Iabchoon, Wongsai and Chankon, 2017), QuickBird (Lu, Moran and Hetrick, 2011; Zhao et al., 2015), Advanced Spaceborne Thermal Emission and Reflection Radiometer (ASTER) (Mallick, Rahman and Singh, 2013), GaoFen-1 (GF-1) (Yao et al., 2017), Synthetic Aperture Radar (SAR) data (Zhang, Zhang and Lin, 2012; Zhang, 2016; Zhang, Lin and Wang, 2018), Sentinel-2 (Xu, Liu and Xu, 2018), nighttime light data (Liu et al., 2013) and fused multi-source remote sensing imageries such as SAR/InSAR and optical data (Zhang, Zhang and Lin, 2014), Defense Meteorological Satellite Program's Operational Linescan System (DMSP-OLS) data and MODIS NDVI data (Guo, Lu and Kuang, 2017), WorldView-2 and LiDAR Data (Sun et al., 2018), WorldView-3, Sentinel-2, and Landsat 8 (Xian et al., 2019), have been assessed and applied to estimate ISA.

Previous studies in ISA mapping have employed various satellite data with different spatial resolutions and temporal frequencies. Medium and low spatial resolution images such as Landsat, MODIS data, have rich spectral information, high temporal resolution and covers large geographical extents which is suitable for large-scale impervious surface mapping (Xu et al., 2018). However, challenges associated with ISA mapping from medium and low spatial resolution satellite images especially in areas that have low ISA intensity and where urban lands are mixed with nonurban lands (Xian et al., 2019). Mixed pixels usually dominate most urban areas with complicated landscapes (Sun et al., 2018; Zhang and Huang, 2018) in many medium resolution images. For instance, ISA and other areas such as concrete roads and some natural rocks may have similar reflectance features and thus are difficult to separate. Therefore, the derive ISA from medium and low resolution images are usually underestimated (Weng, 2012; Cai, Li and Jin, 2016; Yu et al., 2018).

The availability of multispectral high-resolution imagery in recent years as provided by different satellite sensors such as QuickBird, IKONOS, and WorldView has offered a new opportunity for detailed impervious surface trajectory monitoring within urban areas (Iabchoon, Wongsai and Chankon, 2017; Zhang and Huang, 2018). Although these images support a more in-depth understanding of urban development patterns according to Feng et al. (2017), there are still challenges associated with ISA mapping from high spatial resolution satellite images. Zhang and Huang (2018) reported that few studies have focused on the monitoring of impervious surfaces using time series of high resolution images to depict the change profiles of ISA within urban landscapes. Also, most of these high resolution images have not been extensively used for mapping impervious surfaces in large areas (Xian et al., 2019). Both cases are attributed to lack of data availability, cost, processing time as well as large spatial heterogeneity in multitemporal high-resolution images (e.g., different viewing angles, illumination conditions, spatial registration errors, and different shadow sizes and shapes). Guo et al. (2014) also pointed out that spectral similarity of different objects and shadows of tall buildings or large trees limit the impervious surface extraction from high-resolution imagery. Alternatively, Tang and Xu (2017) study indicated that the spectral confusion problem among the impervious surface, soil, and vegetation shadow can be improved with the help of hyperspectral remote sensing images.

Xia et al. (2011) earlier study indicated that the hyperspectral remote sensing images can not only provide a broad variety of spectral features concerning visible light, near-infrared and short-wave infrared ranges but coupled with mixed pixels decomposition algorithms enables the extraction of urban impervious surfaces. Weber et al. (2018) also asserted that though hyperspectral images might be able to solve, the problem of spectral similarity of different land cover and spectral heterogeneity of the same land cover type, it is limited to small map coverage (Xu and Wang, 2016) and high price hinder the application. SAR images help extract impervious surfaces under the large tree crowns (Guo et al., 2014). Nonetheless, the coherent noise of SAR images is a significant problem for impervious surface extraction. The single-source imagery has various restrictions on urban impervious surface mapping according to (Sun et al., 2019).

Xu, Mountrakis and Quackenbush (2017) elucidated that the incorporation of multiple datasets from different satellite image sensors has been considered promising to address the uncertainties related to ISA extraction from low-medium and high- spatial-resolution images, optical images and SAR images, high-spatial-resolution images and light detection and ranging (LiDAR) data. Im et al. (2012) in an earlier study pointed out that LiDAR data height information that significantly distinguishes between urban land cover types with similar spectral signatures (e.g., buildings, roads, and bare) can help improve ISA extraction. Sun et al. (2019) and Xian et al. (2019) in their studies likewise pointed out that with the combination of available multiple spectral and spatial resolution data for satellites imagery from different sensors can offer the possibility of deriving information about the nature and properties of different materials on the urban ground at sub-pixel level.

Numerous methodologies have been developed to extract ISA from satellite images with various spatial scales and evaluate their dynamics (Sun et al., 2017; Xu et al., 2018). Basically, the methods for ISA mapping can be grouped into four major categories: classification-based (i.e., pixel or object-based), mixture analysis (i.e., sub-pixel-based), spectral index-based and deep learning-based segmentation (Weng, 2012; Sun et al., 2017, 2018; Yu et al., 2017; Tian et al., 2018; Wei and Blaschke, 2018; Zhang and Huang, 2018; Hua et al., 2020). Most classification-based methods (i.e., supervised classifiers) require training samples e.g., maximum likelihood classifier (Masek, Lindsay and Goward, 2000), machine learning classifiers such as artificial neural networks (ANN) (Hu, 2009; van de Voorde, de Roeck and Canters, 2009), decision tree (DT) (Xian and Crane, 2006; Lu, Moran and Hetrick, 2011; Xu, 2013), classification and regression tree (CART) (Xian and Crane, 2006; Xu and Wang, 2016), random forest (RF) (Zhang, Zhang and Lin, 2014; Adeyemi, Adeniyi; Botai, Joel; Ramoelo, 2015; Z. Xu *et al.*, 2018), support vector machine (Sun, 2011; Okujeni, van der Linden and Hostert, 2015; Shi et al., 2017; Xu, Mountrakis and

Quackenbush, 2017) and regression modelling (Okujeni et al., 2018; Yu et al., 2018). Some sub-pixel based methods that have been used for ISA mapping are spectral mixture analysis (SMA) e.g., normalized spectral mixture analysis (NSMA) (Henits, Mucsi and Liska, 2017), linear spectral mixture analysis (LSMA) (Ma, Kuang and Huang, 2010; Li et al., 2011; Wang et al., 2018), spatially adaptive SMA (SASMA) (Deng and Wu, 2013), modified Linear Spectral Mixture Analysis (Xu, Liu and Xu, 2018), multiple endmember spectral mixture analysis (MESMA) (Tan et al., 2014; Shahtahmassebi et al., 2016) and temporal mixture analysis(TMA) (Yang et al., 2012; Pok, Matsushita and Fukushima, 2017; Lilian et al., 2018).

The typical spectral index-based segmentation specified for built up ISA mapping are: normalized difference built-up index (NDBI) (Zha, Gao and Ni, 2003), modified normalized difference impervious surface index (MNDISI) (Sun et al., 2017), biophysical composition index (BCI) (Deng and Wu, 2012), perpendicular impervious surface index (PISI) (Tian et al., 2018), urban index (UI) (Kawamura, Jayamanna and Tsujiko, 1997), impervious surface area index (Carlson and Arthur, 2000), index-based built-up index (IBI) (Xu, 2008), exponential enhancing impervious surface method (P index) (Ma, Kuang and Huang, 2010), normalized difference impervious surface index (NDISI) (Xu and Du, 2010), enhanced built-up and bareness index (EBBI) (As-syakur et al., 2012), built-up and bare-land index (BBI) (Zhou et al., 2014), normalized difference impervious index (NDII) (Wang et al., 2015), combinational build-up index (CBI) (Sun et al., 2016), Visible Infrared Imaging Radiometer Suite with Day or Night Band (VIIRS-DNB) (Ma and Li, 2018), blue steel tile-roofed buildings index (BSTBI)(Guo et al., 2018), Enhanced Normalized Difference Impervious Surfaces index (ENDISI)(Chen et al., 2019) and ratio-based impervious surface index (RISI) (Fang, Wei and Dai, 2019).

More recently, deep learning-based method is topical in many research areas, including urban remote sensing., its unique ability in automatic feature learning and the remarkable strength in representation and fitting for non-linear complicated functions (LeCun, Bengio and Hinton, 2015; Zhang, Zhang and Du, 2016; Ma et al., 2019). According to the study of (Huang, Yu and Feng, 2019), the deep learning-based frameworks mainly include four prevalent algorithms which are: deep belief network (DBN) - semi-supervised learning, convolutional neural network (CNN) - supervised learning, automatic encoder (AE) - unsupervised learning and recurrent neural network (RNN) - regression analysis or object classification. Some examples of the most commonly used such as convolutional neural network (CNN) are: one-dimensional (1D) or two-dimensional (2D) CNNs (Maggiori et al., 2016; Marmanis et al., 2016; Kussul et al., 2017); deep convolutional neural networks (DCNNs) (Scott *et al.*, 2017; Zhu *et al.*, 2017), three-dimensional convolutional neural networks (3D CNNs) (Sun et al., 2018); fully convolutional network (FCN) (He et al., 2018), automatically extract impervious surfaces based on deep learning and multi-source remote sensing data (AEIDLMRS) (Huang, Yu and Feng, 2019), gated graph convolutional network (GCN) (Shi, Li and Zhu, 2020) etc.

Although these ISA extraction methods have been widely applied, there are some merits and demerits associated with some of these techniques based on data analysis (Table 1.1).

Table 1.1 Synoptic of some impervious surface area mapping techniques.

Categories	**Merits and Demerits**	**Reference**
Classification-based	They support the use of numerous training samples.	(Tian et al., 2018)
	It is difficult to resolve mixed-pixel problems in pixel-based classification i.e., with the spectral and textural complexity of ISA, there is mixed-pixel with combination of ISA and other land cover types that results in unsatisfactory results.	(Sun, 2011) (Zhang and Du, 2015)
	Optimizing the segmentation parameters limits the use of object-based classification in large study area.	(Yu et al., 2017)
	Regression models are though effective in ISA distribution mapping nationally and globally, their challenges are to select suitable dependent variables from low resolution images and independent variables from high quality ISA reference data.	(Lu et al., 2014)
	Decision tree can be effectively in large area ISA mapping from large, high dimensional and nonlinear data but it's also sensitive to noises as it, relies heavily on the quality of sample data	(Sun, 2011)
Sub-pixel based	This method has proven effective in handling mixed-pixel problem e.g., SMA is able to identify endmember proportion and their corresponding spectral signatures for a geographical scene in remote sensing image. TMA uses the endmember temporal spectral rather than electromagnetic spectral.	(Sun et al., 2017) (Tian et al., 2018)
	It is not suitable for large area mapping due to dependence on well selected representative endmembers (e.g., material difference),inter-class variability quantification, collinearity of endmembers and complicated implementation process.	(Somers et al., 2011) (Lu et al., 2014)
	ISA are normally overestimated in areas with low-density urban features and underestimated in high-density urban areas when using a sub-pixel-based method.	(Sun, 2011)
	Random forest is insensitive to noise in the training dataset, does not suffer from over-fitting ability to determine variable importance and handle unbalanced datasets.	(Watts and Lawrence, 2008;Watts et al., 2009;Loosvelt et al., 2012;Rodriguez-Galiano et al., 2012)

(continued overleaf)

Table 1.1 (continued)

spectral index-based	They are easy to implement in practical application, with no need of training sample and endmembers selection. i.e., characterized by simplicity and flexibility.	Tian et al. (2018)
	Before extraction of ISA spectral indices such as NDBI, BCI and CBI requires masking of water bodies and bare land or soil due to spectral similarity with built-up materials.	Deng and Wu (2012) (Xu and Wang, 2016)
	It is difficult to select an optimal threshold to segment ISA from background surfaces in these indices.	(Lu et al., 2014)
	NDISI takes the advantage of the thermal infrared (TIR) bands coupled with distinctively different emissivity of ISA during urban mapping. The low resolution of TIR bands of multispectral sensor (Landsat) also limits their identification of ISA with varying surface properties. Though MNDISI is with the advantage of night time light luminosity and a soil-adjusted vegetation index to enhance the ISA features, nevertheless, it is difficult to use due to lack of data sources. Subsequently, PISI has a significant positive correlation with ISA percentage, the threshold can be adjusted according to actual needs with higher ISA extraction precision and better separability from soil and vegetation.	(Xu, 2010) (Liu et al., 2013) (Sun et al., 2017) (Tian et al., 2018)
	RISI effectively distinguishes impervious surfaces distribution from other ground objects, especially bare soil in Landsat imagery. This spectral index requires the use of the coastal band after a 0-1 transformation to further increase the difference between impervious surfaces and bare soil.	(Fang, Wei and Dai, 2019)
Deep learning-based	It has a unique ability in automatic feature learning and the remarkable strength in representation and fitting for non-linear complicated functions	(Zhang, Zhang and Lin, 2014) (Yin, Wang and Wang, 2015)
	FCN can accommodate the integration of multi-source remotely sensed data and combination of features at multiple scales (i.e., transmitting information between multiple convolutional layers, pooling layers, activation layers and concatenation layers) which improves algorithm accuracy. FCN have the ability to transfer learning, which enables the extraction of dynamic information (e.g., urban land detection at different scales) using parameters obtained from training samples in a single period.	(He et al., 2018) (Yang et al., 2017) (Chen et al., 2016) (Maggiori et al., 2016) (Fu et al., 2017)
	DNN fails to fine local detail without the consideration of the interactions between pixels i.e., coarse segmentation outputs such as non-sharp boundaries and blob-like shapes caused by convolution filters with large receptive fields and pooling layers.	(X. Zhu *et al.*, 2017)
	GCN can be generally applied to other binary or multi-label segmentation tasks, such as road extraction, settlement layer extraction, or semantic segmentation of very high-resolution data in general. It can also work directly with unstructured data, such as point clouds.	(Shi, Li and Zhu, 2020)
	3D CNN method can automatically extract spectral, spatial, textural, and elevation features via multi-step convolutional, ReLU, and pooling operators, which result in better extraction performance of impervious surfaces (especially for building roofs and roads).	(Sun et al., 2018)

Despite the significance of ISAs studies, most of the satellite data and methods for estimating or mapping ISA data have not been sufficiently explored in major cities in Africa.

Environmental and urban climate studies used land surface temperature (LST) and emissivity data for numerous purposes but mainly to analyse LST patterns and how they contribute to urban heat island predictions, surface characteristics and surface energy fluxes so that landscape properties, and patterns can be characterized (Ibrahim, 2017). Awareness of LST provides information on spatio-temporal variations on the state of surface stability which is essential in many applications (Leprieur et al., 2000). Although in urban thermal environment studies, traditional methods such as *in-situ* land surface temperature (LST) measured by meteorological station were used, but it hardly reflect the spatial air-temperature variation based on different surfaces that characterize the heterogeneous urban landscape (Weng, 2009; Morabito et al., 2015). The development of thermal infrared bands of remote sensing data of space-borne sensors over the years has offered considerable measurement possibilities (e.g. spectral, spatial and temporal) combined with timely data acquisition and wide area coverage i.e., regional to global scale (Li *et al.*, 2013; Yu and Lu, 2014). However, the spatial resolution of the commonly used thermal remote sensed data is medium or low, which limits the extracted information needed for a fine investigation of the urban environment (Xiao et al., 2018).

Some of these wide varieties of infrared thermal sensors are: National Oceanic And Atmospheric Administration - Advanced Very High Resolution Radiometer (NOAA–AVHRR), Moderate Resolution Imaging Spectroradiometer (MODIS), Geodynamic Experimental Ocean Satellite (GOES), Heat Capacity Mapping Mission (HCMM), infra-red thermometers (IRT), Thermal Infrared Sensor (TIRS), Spinning Enhanced Visible and Infrared Imager (SEVIRI), Tropospheric Infrared Mapping Spectrometers (TIMS), Advance Spaceborne Thermal Emission And Reflection Radiometer (ASTER), Moderate Resolution Imaging Spectroradiometer/Advance Spaceborne Thermal Emission And Reflection Radiometer airborne simulator (MASTER), and Landsat (Voogt and Oke, 2003; Olarewaju Oluseyi, Fanan and Magaji, 2009; Weng, 2009; Tomlinson et al., 2011; Abutaleb et al., 2015; Adeyemi et al., 2015; Zhao and Wentz, 2016; Tran et al., 2017). The retrieval of the LST from thermal infrared bands of remote sensing data of space-borne sensors has attracted much attention, and its history dates back to the 1970s (McMillin, 1975). Li et al. (2013) elucidated for accurate direct estimation of LST from the radiation emitted in the TIR spectral region, radiometric calibration, cloud screening, atmospheric correction and emissivity are necessary parameters.

Consequently, there have been several algorithms and methods used for land surface temperature (LST) retrieval from remote sensing data. Previous studies have used spectral radiance model to assess LST from data (Sobrino, Jiménez-Muñoz and Paolini, 2004; Weng, Dengsheng and Jacquelyn, 2004). Although LST has also been directly linked to satellite based thermal infrared (TIR) data through the radiative transfer equation, the disadvantage is that it requires an *in-situ* atmospheric profile which must be launched simultaneously with the satellite passes which is very difficult to achieve (Alipour, Sarajian and Esmaeily, 2011). Qin, Karnieli and Berliner (2001) in an earlier study developed the split window and mono window algorithm and demonstrated their effectiveness of using Landsat data. Some scholars further used single band of Landsat data for retrieving LST by applying mono-window algorithm (Li et al., 2013; Ning et al., 2018) while others used two thermal bands applying split-window algorithm (Rozenstein et al., 2014). Sahana, Hong and Sajjad (2018) asserted that the mono window algorithm had an advantage over split window algorithm based on the comparative study because the creation of the algorithms was initially based on single thermal band. Jiménez-Munoz and Sobrino (2003) and Jiménez-Muñoz and Sobrino (2010) also developed the single-channel algorithm for land surface temperature retrieval from Landsat and Advanced Spaceborne Thermal Emission and Reflection Radiometer (ASTER) data respectively. Alipour, Sarajian and Esmaeily (2011) pointed out that the single-channel algorithm has an advantage as it can be used when the ground truth data is not available.

The degree of urban sprawl has been measured by the increase of ISA (Hereher, 2016). With increasing concern in many African cities, examining the interaction between the LST and ISA in an urbanized environment is key to understanding components of urban climate e.g., urban heat island (UHI) extent. In the past, many researchers have explored this relationship as a key environmental indicator mostly in the developed countries (Zhang, Odeh and Han, 2009; Deng and Wu, 2013). Some of the studies that have also investigated this relationship were based on the several methods that have been developed to extract ISA from satellite images at different spatial scales (Yu and Lu, 2014; Nie and Xu, 2015; Morabito *et al.*, 2016, 2018; Henits, Mucsi and Liska, 2017; Wei and Blaschke, 2018).

In major cities in Africa, very few studies have been conducted by scholars regarding the examination of the interplay between land surface temperature variation and the spatial and temporal patterns of built-up impervious surfaces. Kamdoum, Adepoju and Akinyede (2014) investigated the relationship between SUHI and the percent impervious surface area (%ISA) in Ibadan, south-west Nigeria between 1984 and 2006. They used Landsat 5 TM (1984) and the Landsat 7 ETM+ to characterize the %ISA and vegetation with Linear Mixture Spectral Analysis (LMSA) and NDVI respectively. Their results indicated a positive correlation between LST and %ISA suggesting that percentage ISA accounts for a large share of SUHI problem in the study area. Adeyemi et al. (2015) describes the effect of impervious surface area and vegetation changes on mean surface temperature using thematic spectral indices and mean surface temperatures derived from the thermal bands of Landsat 7 ETM+ and Landsat 8 LCDM respectively in Tshwane Metropolis, Gauteng Province, South Africa. Simwanda et al. (2019) conducted a comparative analysis to examine the relationship between LST and the spatial patterns, composition and configuration of impervious surfaces and green spaces in four representative African cities, Lagos (Nigeria), Nairobi (Kenya), Addis Ababa (Ethiopia) and Lusaka (Zambia) using Landsat OLI/TIRS data.

In general, despite the above mentioned, most of the studies conducted on ISA mapping and the relationship with LST i.e., quantitatively (comparison based on spatial distribution; statistical analysis based on sampling methods; scale effects of their relationship) and spatial pattern-wise have been in developed cities across the globe (e.g., Europe, Asia and America) with few have been done in major cities in Africa. As a pilot area of comprehensive innovation modification in the City of Tshwane (COT), Gauteng, South Africa, Pretoria has experienced population growth coupled with rapid socio-economic development (i.e., uncontrolled and unplanned urbanization and industrialization) over the years, which have given rise to increase in impervious surface area. Thus, the question posed asked is whether ISA is distinguishable from non-ISA using satellite remote sensing data (e.g., multispectral low or medium or high resolution imagery) using various methods (e.g., classification-based or sub-pixel-based or spectral index-based etc.) in a complex urban landscape in South Africa? ISA emerging not only as a feature of urbanization but also a major index of environmental quality. Therefore, its sprawl experienced over the years in relation to surface temperature variability may provide more insight that is key to understanding other components of urban climate in Pretoria, South Africa.

1.2. Significance of the research

The result from this study will presents methodologies that can be incorporated in frameworks significant in addressing existing uncertainties of urbanization (i.e., ISA mapping) and its impact on climate change (i.e., LST variability) in major cities in South Africa (e.g., Pretoria). Therefore, the consistent results derived from this research will also provide vital information on the degree of urban sprawl and influence on urban heat island extent to a multitude of social, economic, and environmental policies, city planners, sustainable developers, ecological assessment, regulations, and decision-makers across the country.

1.3. Research Aim

The main aim of this study is to explore built-up ISA mapping and investigate its influence on land surface temperature variability using remote sensing and ancillary data in Pretoria, City of Tshwane, Gauteng Province, South Africa.

1.4. Research Objectives

The specific objectives were to:

1. explore spectral index to improve built-up impervious surface area delineation from very high-resolution multispectral data (e.g., WorldView-2).
2. examine exposed rooftop impervious surface area based on different colours (properties) their interplay with surface temperature variability
3. determine if the spatio-temporal built-up ISA distribution pattern in relation to elevation and its influences urban heat island (UHI) extent using an optimal analytical scale, across Pretoria, South Africa.
4. assess the spatio-temporal change characteristics of ISA expansion using its retrieved surface temperature at selected administrative subplace units (i.e., local region scale).

1.5. Research hypothesis

1. Improved spectral index-based segmentation method will be able to delineate ISA from a high resolution multispectral imagery.
2. ISA properties (e.g., colour of rooftop impervious surface area) could influence LST variations.
3. Spatio-temporal distribution of built-up ISA in relation to elevation and its interplay with LST can help detect UHI magnitude.

4. ISA surface temperature weighted SDE method could reveal the principle direction of ISA expansion at local region level.

1.6. General methodology of the study

The first technical chapter (i.e., chapter 2) uses the spectral reflectance from a very high resolution pan-sharpened (~0.5m) WorldView-2 (WV-2) imagery. The second chapter (i.e., chapter 3) employed pan-sharpened (~0.5m) WorldView-2 (WV-2) imagery, LIDAR-derived normalized height model and bare earth model or DEM (2m) and Landsat 8 TIRS (pan-sharpened 15m). Both chapters 2 and 3 were conducted in an urban residential area of Pretoria, Lynnwood Ridge, Gauteng Province, South Africa. Chapter 4 and Chapter 5 study analysis employed medium resolution multispectral Landsat (30m) imager data respectively. These studies were conducted in Pretoria, Gauteng Province, South Africa.

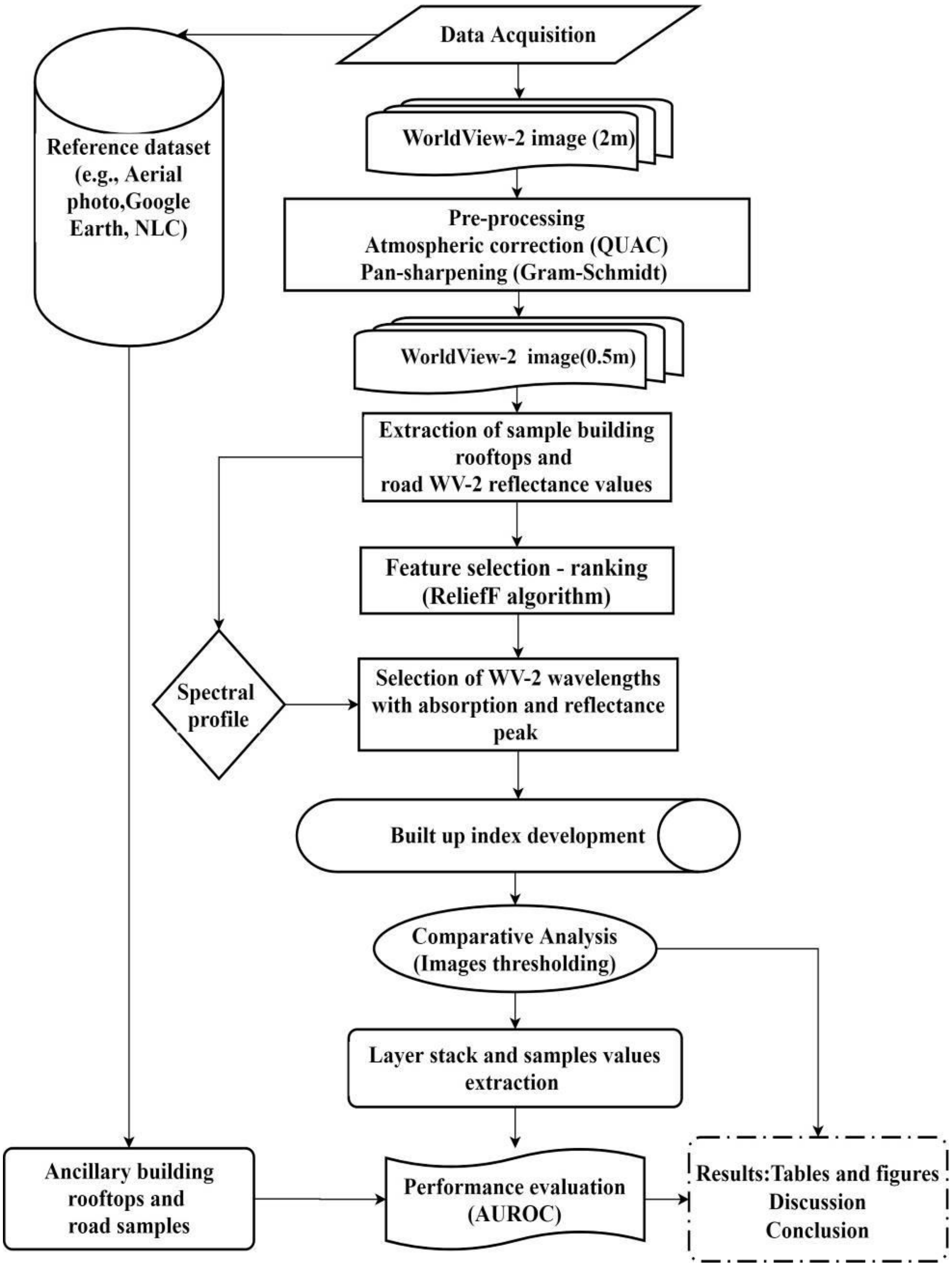

Figure 1.1 Flowchart showing the methodology for the NBEI for WV-2.

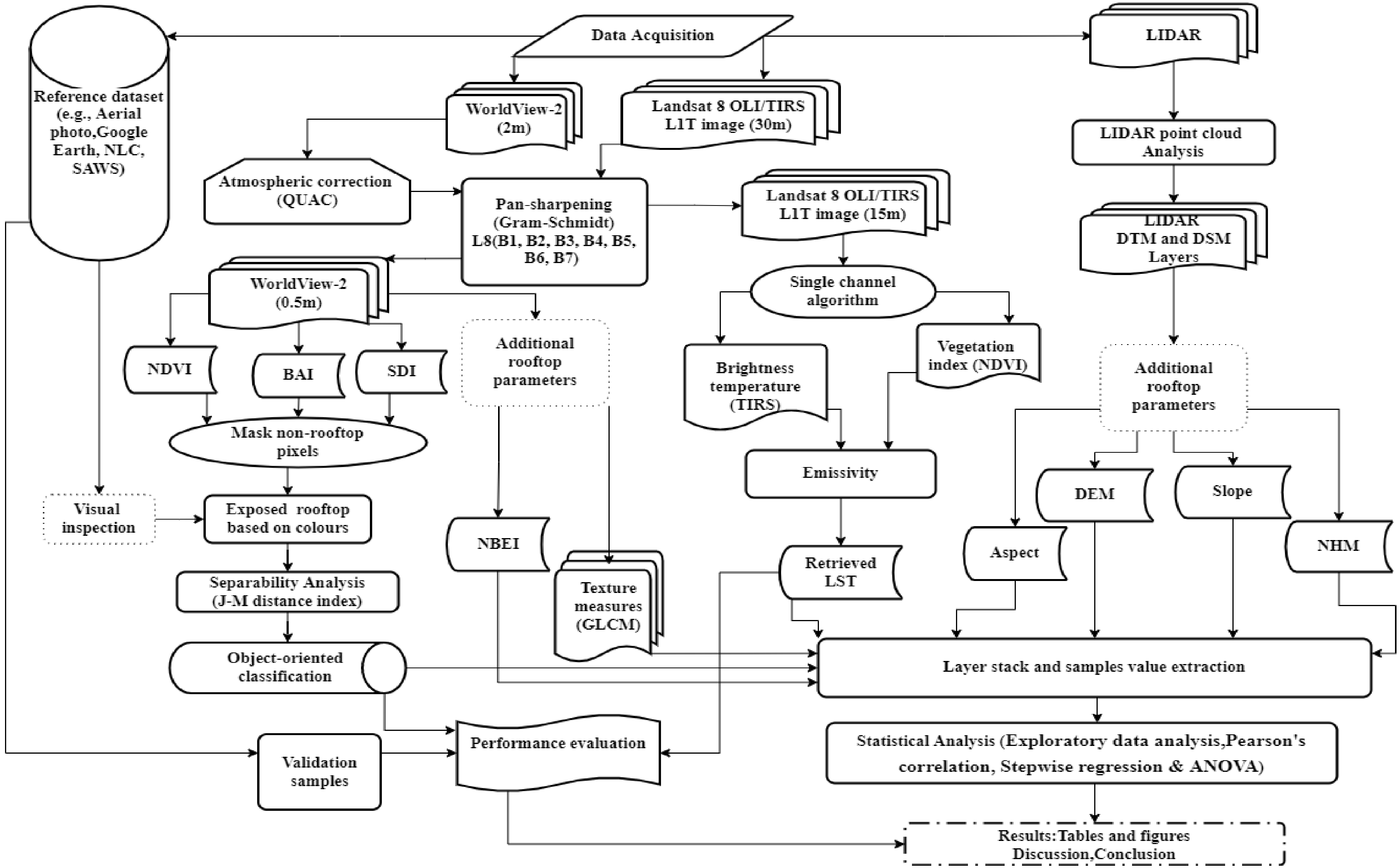

Figure 1.2 Flowchart showing the methodology to analyse rooftop impervious surfaces impact on surface temperature (LST)variability.

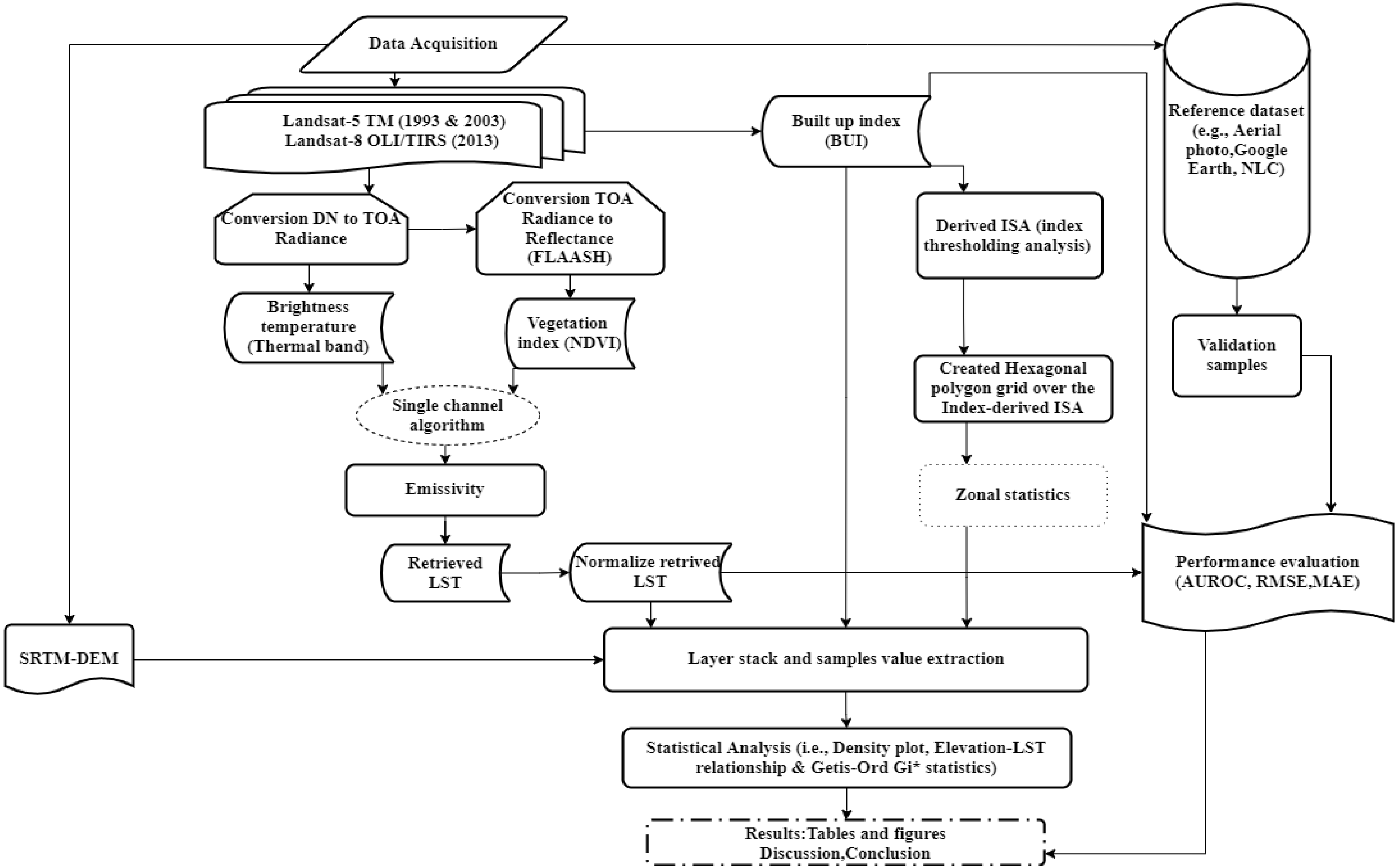

Figure 1.3 Flowchart showing the methodology to analyse of ISA-elevation and surface temperature distribution.

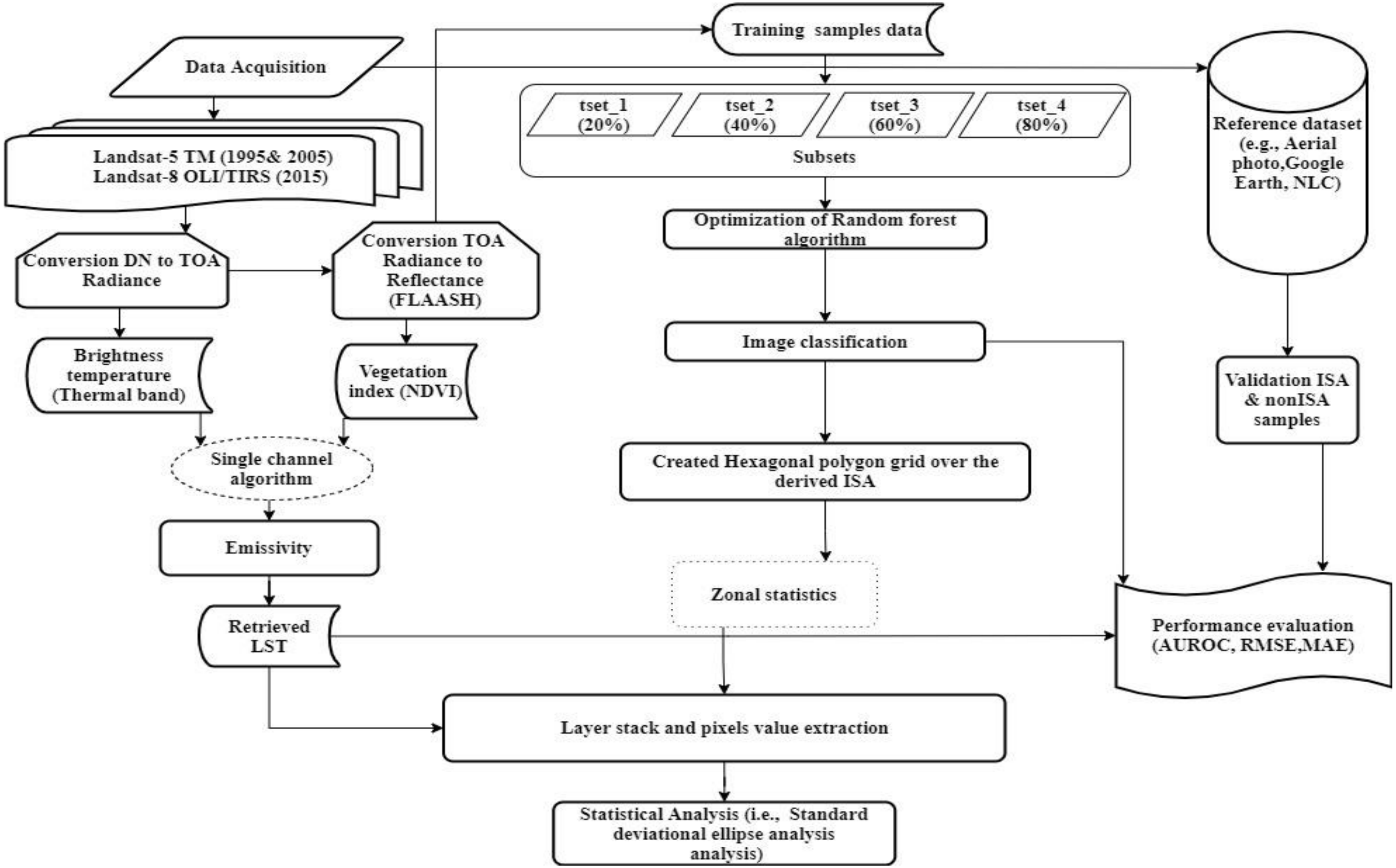

Figure 1.4 Flowchart showing the methodology to assess spatio-temporal urban expansion trend analysis.

1.7. Study area

The study covers Pretoria (Figure 1.5) which is a city in the north-northeast of Johannesburg in the northeast of South Africa. It is located at Longitude 25044’46’’S and Latitude 28011’17’’E of which is the central part of the City of Tshwane Metropolitan Municipality. According to Raper (1987), Pretoria is named after the Voortrekker leader Andries Pretorius. It is also popularly known as the Jacaranda City due to the thousands of Jacaranda trees planted in its streets, parks, and gardens. According to South African Weather Service, (2011), the Province was estimated to have a population of 12.2 million people which is 25% of South Africa total population and indicating it is the fastest-growing Province that has witnessed a population growth of over 33% between 1996 and 2011. The geographical distributions of the major languages in Pretoria are Afrikaans, English, Ndebele, Zulu, Northern Sotho, Tswana, and Tsonga.

The climate is influenced by altitude and it experiences hot and rainy summer and also winter (crispy and dry with frost occurring in the southern areas) in the major cities i.e., Pretoria on the other hand with a topography 1330m above sea level has an average temperature ranging from 29 °C max to 18 °C min in January; 19 °C max to 5 °C in June and precipitation of 674mm (Climate data for Pretoria, 2011). Also, South African Weather Services, (2013) reported that during a nationwide heat wave in November 2011, Pretoria experienced temperatures that reached 39 °C which was unusual for that time of the year. Similar record-breaking extreme heat events were observed in January 2013, when Pretoria experienced temperatures exceeding 37 °C (99 °F) on several days. The all-time high recorded in Pretoria was 42 °C (108 °F) on 25 January 2013 South African Weather Services (2013). The year 2014 saw one of the wettest years on record for the city with precipitation of 914 mm experienced to the end of December.

Because of its status as the economic hub of South Africa and a large influx of people into the city and her sub-urban population is expected to increase drastically in coming years coupled with different levels of urban development according to Statistic South Africa report in the year 2011. In this research we selected as pilot study areas an urban residential area of Lynnwood Ridge (Figure 1.6), Pretoria subplace units (Figure 1.7) and Pretoria (Figure 1.5), Gauteng Province, South Africa.

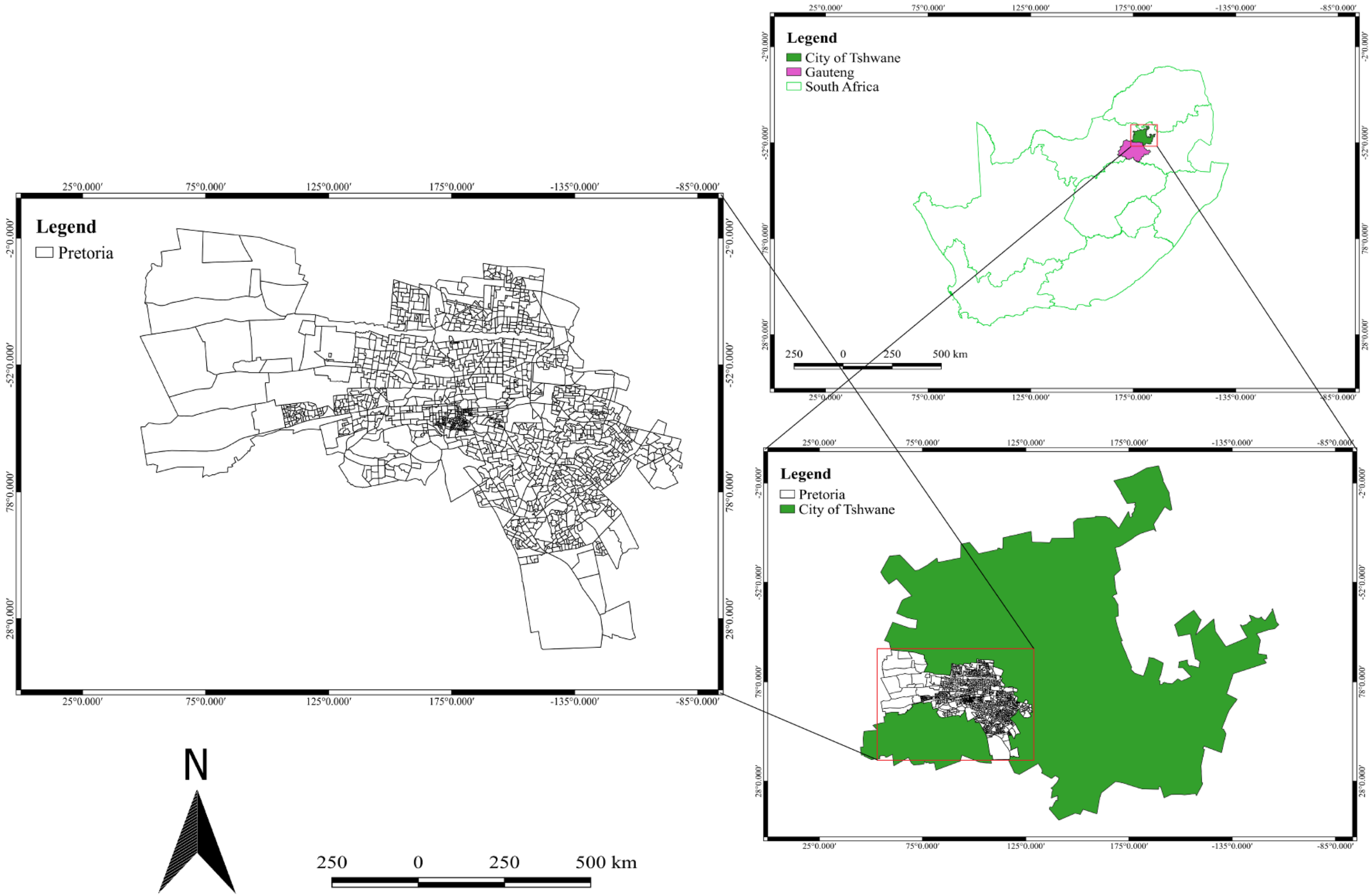

Figure 1.5 The location of the study area relative to Pretoria, South Africa.

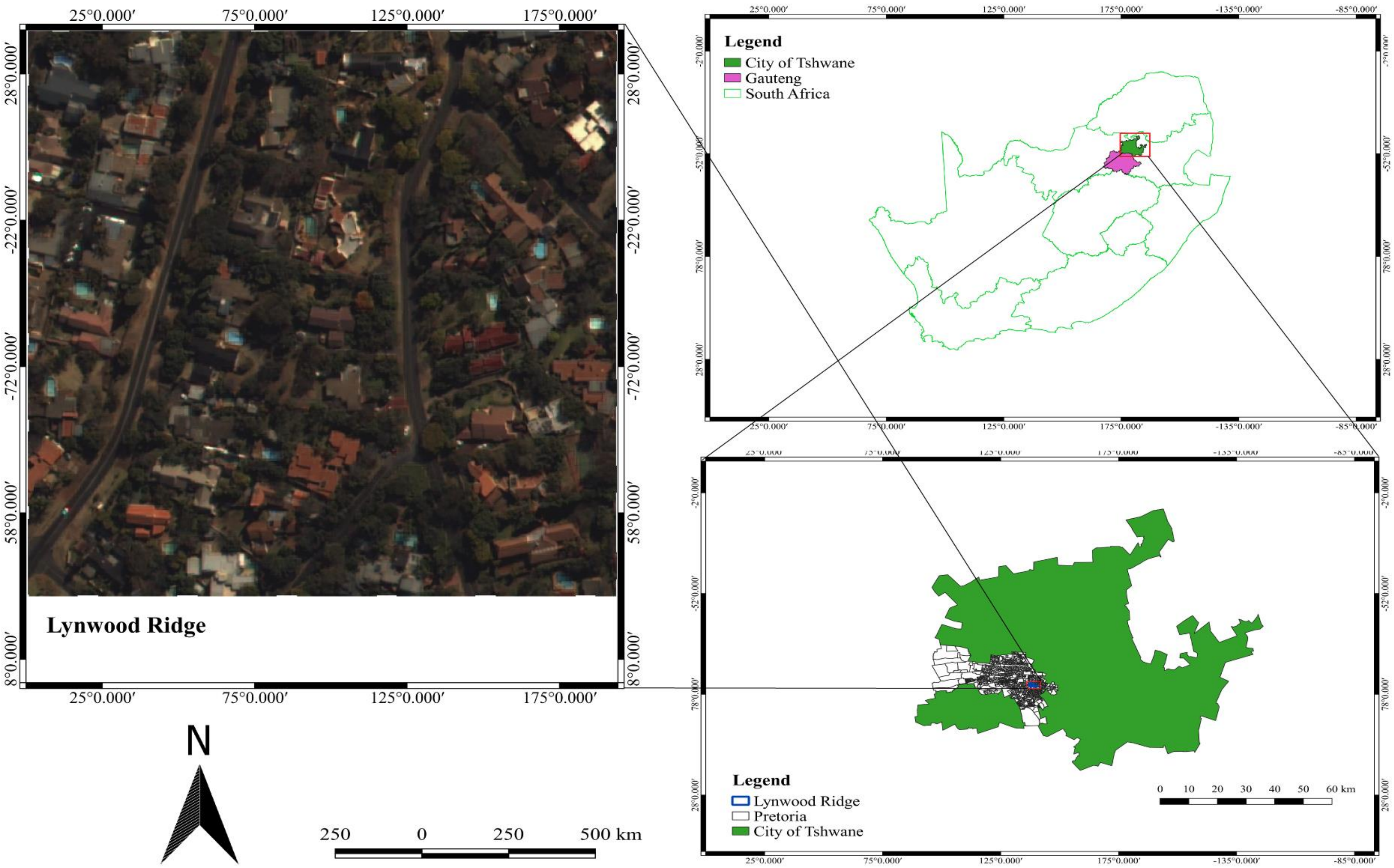

Figure 1.6 The location of the study area relative to Lynnwood Ridge, Pretoria, South Africa.

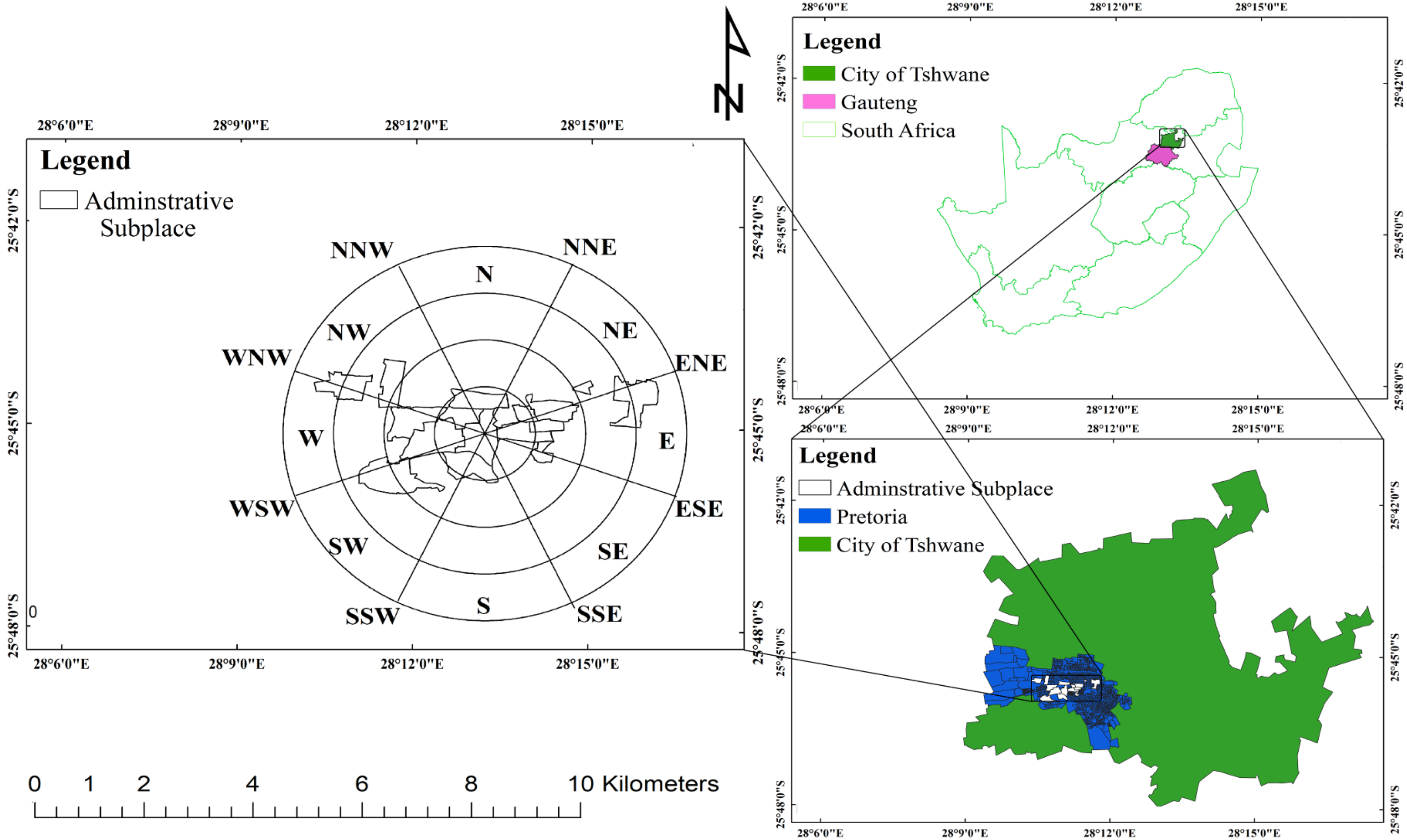

Figure 1.7 The location of the study area relative to Pretoria administrative subplace, South Africa.

1.8. Structure of the thesis

This study will be organized into the following chapters:

Chapter 1. The first chapter presents the overall background and research problem areas, research aim and objectives of the dissertation and hypothesis. This chapter also shows the significance of the research, general methodology of the study and structure of the thesis.

Chapter 2. we proposed a New Built-up Extraction Index (NBEI) based on WorldView-2 (WV-2) imagery. The chapter further explored the feature selection (ranking) ReliefF algorithm to selected important bands that show the spectral variability of the types of the built-up materials, age, colour, etc. We further performed a comparative examination with previous built up spectral indices and threshold analysis to eliminated non-built-up interference.

Chapter 3. we determined the delineate rooftop impervious surface area using WV-2 (pan sharpened ~0.5m) imagery, derived texture measures and LIDAR-derived normalized height model and bare earth model or DEM (2m) in the urban residential area Lynnwood Ridge, Pretoria, Gauteng Province, South Africa. We assessed the utility of Landsat 8 TIRS (pan sharpened 15m) to retrieve LST.

Chapter 4. we tested the methodology for multi-temporal evaluation of ISA distribution in relation to elevation and its influence on daytime surface temperature variability using Landsat 8 OLI TIRS data acquired over across Pretoria, South Africa. Moreover, we assessed the use of Getis-Ord Gi* statistics to identifying clusters of ISA surface temperature (hotspot regions) to reveal the urban heat island (UHI) extent.

Chapter 5. we tested the methodology to understand the spatio-temporal characteristics of ISA expansion with surface temperature based on Landsat-5 Thematic Mapper (TM) and Landsat-8 OLI (Operational Land Imager) and TIRS (Thermal Infrared Sensor) at selected administrative subplace units (i.e., local region level) in Pretoria, South Africa. Additionally, we assessed the use of the weighted standard deviational ellipse to reveal the principle direction of ISA expansion at local region level.

Chapter 6. Synthesis - Conclusion, Limitation, Recommendation and Future Research.

Chapter 7. References

Chapter 2 Spectral index to improve the extraction of built-up impervious surface area from WorldView-2 imagery

Satellite level (high resolution)

This chapter is based on Adeniyi Adeyemi, Abel Ramoelo, Moses Cho, Cecilia R. Masemola (2021) - Spectral index to improve the extraction of built-up area from WorldView-2 imagery, Journal of Applied Remote Sensing 15(2) 024510 (26 April 2021), https://doi.org/10.1117/1.JRS.15.024510

Abstract

Globally, the unprecedented increase in population in many cities has led to rapid changes in urban landscape, which requires timely assessments and monitoring. Accurate determination of built-up information is vital for urban planning and environmental management. Often, the determination of the built-up area information has been dependent on field surveys, which is laborious and time-consuming. Remote sensing data is the only option for deriving spatially explicit and timely built-up area information. There are few spectral indices for built-up areas and often not accurate as they are specific to impervious material, age, colour, and thickness, especially using higher resolution images. The objective of this study is to test the utility of a new built-up extraction index (NBEI) using WorldView-2 to improve built-up material mapping irrespective of material type, age and colour. The new index was derived from spectral bands such as Green, Red edge, NIR1 and NIR2 bands that profoundly explain the variation in built-up areas on WorldView-2 image (WV-2). The result showed that NBEI improves the extraction of built-up areas with high accuracy (area under the receiver operating characteristic curve, AUROC = ~0.82) compared to the existing indices such as Built-up Area Index (BAI) (AUROC = ~0.73), Built-up spectral index (BSI) (AUROC = ~0.78), Red edge / Green Index (RGI) (AUROC = ~0.71) and WorldView-Built-up Index (WV-BI) (AUROC = ~0.67). The study demonstrated that the new built-up index could extract built-up areas using high-resolution images. The performance of NBEI could be attributed to the fact that it is not material specific, and would be necessary for urban area mapping.

2.1. Introduction

The global urban population proliferated from 220 million to 2.8 billion over the twentieth century (Xu, 2010). This unprecedented increase in population concentration in cities led to rapid urban landscape changes (Odindi, Mhangara and Kakembo, 2012; UNDP, 2012). The highest rate of urbanization and associated land use or cover changes have been observed in developing countries (Montgomery and Hewett, 2005). Over the last decades, Southern Africa has been facing significant land use and land cover changes, such as loss of natural land, i.e., forest or plantations, agricultural lands and grasslands coupled with growing built-up impervious surfaces which are developed and constructed artificial surfaces that water cannot infiltrate to reach the soil, such as buildings or rooftops, paved roads, driveways, roads sidewalks, parking lots and so on (Adeyemi *et al.*, 2015). The dynamic nature of land use or cover is associated with economic benefits and improved life. The latter effect has been associated with a series of ecological, environmental and climatic issues (Jennings and Jarnagin, 2000; Xu, 2010; Deng *et al.*, 2015). Therefore, in recent years, detecting these human-made features has attracted increasing interest especially for understanding their adverse impact in the context of planning and improvement of the environment. Often, the determination of the built-up area information has been dependent on field data collection, which is tedious and time-consuming.

Satellite remote sensing data have served as a useful source of built-up area information in previous studies due to large-area coverage and short revisit cycles (Varshney and Rajesh, 2014). Among these studies, Landsat imagery is the most commonly used because the satellite series provide nearly 45-year data records with wide-swath coverage, free availability and relatively medium spatial resolution (Yu *et al.*, 2017). However, confusion among various urban land features based on factors such as the spectral and spatial resolution of the data and technique employed has made it impossible to yield desirable results (Waqar *et al.*, 2012). Weber (2001) earlier pointed out that due to the complexity of the urban landscape, classification from satellite images is a difficult task because these images do not exhibit a unique and distinguishable spectral response. On the other hand, high spatial resolution images (e.g., IKONOS, Quickbird, WorldView-2/3) have provided new research opportunities especially with the growing demands for monitoring most exceptional urban objects such as building or rooftop footprints and road which were difficult to identify in medium resolution images such as Landsat (Bouziani, Goïta and He, 2007; Bouzekri, Lasbet and Lachehab, 2015). The primary challenge with using high-resolution images is cost, but when available it provides useful information for urban assessment and monitoring as compared to moderate resolution satellite images.

According to Sun *et al.*(2017), the numerous ways to estimate the extent and quantities of built-up areas from medium resolution imagery (e.g., Landsat) in the previous studies can be grouped into five categories: pixel/object-based classification; spectral mixture analysis (SMA); regression model, decision tree and spectral index-based segmentation. They further asserted that though these classification methods have been widely used, there are challenges and limitations for applying at regional and global scales e.g., subjective scene-to-scene data analysis, time-consuming and complicated computing (Deng *et al.*, 2015). The limitation of pixel-based approach which is commonly used but does not account for the spatial pattern (i.e., image texture, pixel proximity, feature size and shape) and mixed-pixel problems in the classification (Sun, 2011). The object-oriented approach treats an image as a set of significant objects, which requires spatial, spectral and texture characteristics (Yan *et al.*, 2006; Qian, Zhou and Hou, 2007a). These requirements create difficulty in optimizing segmentation parameters that hinders the application of object-oriented classification to a large area (Yu *et al.*, 2017). Although, SMA-based methods have proven useful for handling the mixed-pixel problems in medium resolution imagery, built-up or impervious surface area, are commonly overestimated in areas with low-density urban features and underestimated in high-density urban areas (Sun, 2011; Weng, 2012). SMA-based methods are also not suitable for large-area mapping due to difficulties in end-members related to inter-class variability quantification, and complicated implementation process (Yang, Matsushita and Fukushima, 2010; Lu *et al.*, 2014). Also, the regression models (e.g., decision tree) limitations are associated with model calibration and validation from medium resolution images and high-quality impervious surface area (ISA) reference data and extrapolation of the models in other study areas(Weng, 2012). Although decision tree is a rule-based method that can effectively process large, high dimensional and nonlinear data, which is suitable for large-area built-up mapping, it is more sensitive to noise and depends significantly on the quality of sample data (Sun, 2011). Thus, all of the above mentioned are semi-automated and involves human intervention such as a manual selection of representative samples required by the classifiers and incorporates urban morphology information (Waser *et al.*, 2014; Wei and Blaschke, 2018).

Thematic-oriented spectral indices have proven to be of good potential in large-area built-up automated mapping due to their easy implementation, parameter-free and convenience in practical applications (Sun *et al.*, 2016). Most of the built-up indices for rapid mapping of built-up areas have been developed for medium resolution imagery (Kaimaris and Patias, 2016). Table 2.1 lists built-up indices developed from medium resolution multispectral Landsat with their merits and demerits. Sameen and Pradhan (2016) reported that most of the studies only developed spectral indices for the rapid extraction of built-up areas from medium resolution satellite images (e.g., Landsat).

Therefore, with the growing demands to observe, assess and monitor land change processes and biophysical characteristics of urban environments more accurately, it is necessary to develop new built-up indices for recently available multispectral high spatial resolution satellite imagery such as IKONOS, Quickbird, and WorldView-2/3 (Myint *et al.*, 2010). Based on the problems mentioned above- in index-based built-up area mapping, there is a need to develop new indices that are accurate and able to accommodate the spectral variability of the built-up materials. The objective of the study is to propose and test the utility of a NBEI based on WV-2 imagery. The key research questions are:

1. Which WV-2 spectral bands are essential in characterizing built-up areas i.e., consider the spectral variability of the built-up materials (e,g., types, age, colour, etc)?
2. Could NBEI threshold analysis eliminate non built-up interference to ensure high accuracy for build-up ISA extraction?
3. In a comparative analysis with previous spectral indices, will NBEI perform better?

2.2. Material and Methods

The methodological workflow is briefly summarized in the flowchart of Figure 1.1.

2.2.1. Study Data

One cloud-free WV-2 multispectral image of the study area was obtained from Digital Globe in October 2015. WV-2 was launched in October 2009 as the first commercial multispectral satellite that comprises 2 m eight multispectral bands and 0.5 m panchromatic bands(Wolf, 2010). The satellite has a swath width of 16.4 km, an average revisits time of 1.1 days and is capable of collecting up to 9.75×105 km2 per day. Therefore, the satellite has the spectral and spatial resolutions that meet a variety of remote sensing applications such as mapping rooftops (Nasarudin and Shafri, 2011; Taherzadeh and Shafri, 2013). the Department of Forestry, Fisheries and the Environment (DFFE), South Africa (https://www.environment.gov.za) subcontracted National Land Cover (NLC) classification dataset of 2013-2014 completed by a consulting company GeoterraImage (Pty) ltd in 2015, 1:10,000 aerial photography at 0.5m spatial resolution (November 2015) from CDNGI together with Google Earth search engine were used for validation purpose to verify the rooftop colours in the study site. Software to be used for desktop analysis were; ESRI (ArcGIS), EXELIS Environment for Visualizing Images (ENVI) IDL version 5.2, QGIS, Microsoft office, WEKA, R statistical software environment (RStudio, Inc., Boston, MA, USA, Version 1.1.463) software.

Table 2.1 List of built-up indices

Formula	Imagery	Merits and Demerits	References
NDBI = ((SWIR1-NIR)/(SWIR1+NIR))	Landsat	Ineffective in differentiating built-up area from bare land areas and requires modification to enhance its accuracy.	(Zha, Ni and Yang, 2003)
NB1 = (RED*SWIR1)/NIR	Landsat	Higher positive values of NBI indicated a greater possibility of bare ground areas.	(Chen *et al.*, 2006)
IBI = (NDBI-(NDVI+MNDWI)/2)/(NDBI+(NDVI+MNDWI))	Landsat	Detect asphalt and concrete surfaces and eliminate other land use or cover classes using the vegetation and water index values.	(Xu, 2008)
Improved NDBI = NDBI -NDVI	Landsat	High subtracted values between the continuous images of NDBI and NDVI coupled with thresholding technique indicates more probability of having built-up regions	(Chunyang *et al.*, 2010)
NBI = (SWIR1*RED)/NIR	Landsat	Red band spectral response was used to enhance the extraction of the built-up region	(Chen *et al.*, 2010)
NDISI=(T_b-(MNDWI+NIR+SWIR1)/3)/T_b+ (MNDWI+NIR+SWIR1)/3)	Landsat	It can represent the real percentage of the impervious surface but sensitive to seasonality.	(Xu, 2010)
EBBI = (SWIR1-NIR)/10*√(SWIR1+TIR)	Landsat	It is terrific in distinguishing between built-up and bare land due to the use of TIR band. It detects mixed regions as built-up in bare land areas in regions with a highly heterogeneous landscape, which exhibit high values in NIR and SWIR because of the drier vegetation.	(As-syakur *et al.*, 2012)
BAEI = (RED + L)/(GREEN + SWIR1)	Landsat	Excellent in detecting built-up regions, it also has some portion of confusion between built-up and rock due to similar spectral response. Masking of vegetation was required because of its enhancement with built-up regions due to the Red band.	(Bouzekri, Lasbet and Lachehab, 2015)

(continued overleaf)

Table 2.1 (continued)

Formula	Imagery	Merits and Demerits	References
BUI=(2*((RED*SWIR2)-(SWIR1*SWIR1))/((RED+SWIR1)+(SWIR1+SWIR2))	Landsat	It reveals high positive values for water, high negative values for bare soil and vegetation, and minor negative values for the built-up area. The main focus is on the last finding, i.e. in values ranging around 0.0. Although, it does not follow the logical boundary of the built-up area values adopted in previously developed indices but allows for the best distinction of constructions.	(Kaimaris and Patias, 2016)
NBUI = EBBI - (SAVI + ((GREEN-SWIR1)/(GREEN+SWIR1))	Landsat	It highlights the contrast reflection range and absorption in built-up and bare land areas	(Sinha, Verma and Ayele, 2016)
MNDISI=(T_S-(MNDWI+NIR+SWIR1)/3)/T_S+(MNDWI+NIR+SWIR1)/3)	Landsat	It suggests that built-up indices are sensitive to image seasonality, and summer is the best time phase for ISA mapping	(Sun *et al.*, 2017)
BSTBI = (W_1BLUE+W_2NIR-GREEN) * SWIR2 Where, W_1 = (λGREEN – λBLUE) / (λNIR -λ BLUE); W_2 = (λNIR – λGREEN) / (λNIR –λ BLUE)	Landsat	It cannot represent the totality of the industrial zone, i.e. underestimation. Age and covering of dust could also suppress the performance of the index.	(Guo *et al.*, 2018)
ENDISI = BLUE – α * [(SWIR1/SWIR2) + (MNDWI)^2] / BLUE + α * [(SWIR1/SWIR2) + (MNDWI)^2] α = 2 * $(BLUE)_{Mean}$/ [$(SWIR1/SWIR2)_{Mean}$ + $((MNDWI)^2)_{Mean}$] MNDWI = (Green – SWIR1)/(Green + SWIR1)	Landsat	It reduce the impacts of arid land, bare rock, and bare soil on IS extraction effectively (i.e., higher separability degree). It presented high values in some grassland areas i.e. making impervious surface pixels covered with pervious surface pixels	(Chen *et al.*, 2019)
L represents an arithmetic constant equal to 0.3, *NDBI* = "Normalized difference built-up index name", *NBI* = "New Built-up Index", *IBI* = "Index-based Built-Up Index", *NBI* = "New Built-up Index", *EBBI* = "Enhanced Built-Up and Bareness Index", *BAEI* = "Built-up area extraction index", *BUI* = "Built-up index", *NBUI* = "New Built-up Index", *Ts* = "retrieved surface temperature", T_b = " brightness temperature of the thermal band", *MNDWI* = " modified normalized difference water index", *NDISI* = " normalized difference impervious surface index", *MNDISI* = " Modified Normalized Difference Impervious Surface Index". *SAVI* = "Soil-adjusted Vegetation Index ", *BSTBI* = "blue steel tile-roofed buildings index", *ENDISI*=" Enhanced Normalized Difference Impervious Surfaces index",$(.)_{Mean}$ = "image mean value, *RED, BLUE, GREEN, NIR, SWIR1* and *SWIR2* = " wavelength of surface reflectance bands".			

2.2.2. Image acquisition and pre-processing

The WV-2 scene used in this study was orthorectified and geometrically corrected by Digital Globe (Mutanga *et al.*, 2015; Gairola *et al.*, 2016; Madonsela *et al.*, 2017). The WV-2 bands (Table 2.2) were then atmospherically corrected and transformed into canopy reflectance using the Quick Atmospheric Correction (QUAC) extension in Environment for Visualizing Images (ENVI) software (ENVI, 2015). After the radiometric calibration, the WV-2 multispectral bands pan-sharpening was performed using the ENVI Gram-Schmidt Spectral Sharpening algorithm that improved the visualisation of rooftop material (Laben and Brower, 2000). Finally, the WV-2 image was then referenced to the Universal Transverse Mercator (UTM zone 35 South) projection using WGS-84 Geodetic datum (Omer *et al.*, 2015).

Table 2.2 WorldView-2 imagery characteristics

Spectral bands	**Wavelength (nm)**	**Spatial resolution (m)**
Coastal blue	400-450	2
Blue	450-510	2
Green	510-580	2
Yellow	585-625	2
Red	630-690	2
Red-edge	705-745	2
NIR1	770-895	2
NIR2	860-1040	2
Pan	450-800	0.5

2.3. Feature selection using ReliefF Algorithm

2.3.1. Feature selection

Feature selection is an important pre-processing step in pattern recognition and machine learning, artificial intelligence and data mining communities. It helps us to focus the attention of a classification algorithm on those features or bands that are the most relevant to predict the classes (i.e., built-up) (Durgabai and Ravi Bhushan, 2014). Based on statistical distribution using a large number of features as the inputs of initiating algorithms have the disadvantage (e.g., inefficient as it consumes memory and time, irrelevant features may confuse classification algorithms) and advantages (e.g., improving understandability and lowering the cost of data acquisition and handling). Feature selection methods can be grouped into two categories, which are ranking features according to the same evaluation criterion and choosing a minimum set of features that satisfies an evaluation criterion. In this work, we implemented the ReliefF algorithm for feature ranking in the WEKA software to identify the significant wavelengths sensitive to the built-up areas (e.g., road and rooftops).

2.3.2. Algorithm implementation

In this study, we employed the use of the robust ReliefF algorithm because of its ability to handle both a binary and multiclass problems and accommodate an incomplete and noisy data(Robnik and Konenko, 2003). Based on the generated training or stratified random sample points (n=130) on built-up areas (e.g., roads and rooftops), we first extracted from the eight WV-2 bands (i.e., features) reflectance values using the "Extraction" module of the spatial analyst tool of ArcGIS software. Before this step, the validity of all these sample points selected was carefully checked through visual inspection of both aerial photography (November 2015) as well as Google Earth engine to avoid mislabelling problems. Subsequently, the ReliefF algorithm was implemented in the WEKA software using the k nearest neighbours (KNN). The ReliefF algorithm randomly selects from the training a sample n_i, and then performs searches for k nearest neighbors in two ways i.e., from the same class (nearest hits h_j) and a different class, called nearest misses $m_j(C)$ (see Equation 2.1). It updates the quality estimation $W[A]$ for all attributes *"A"* depending on the WV-2 reflectance values associated with the training sample (n_i) hits and misses. The contribution for each class of the misses is weighted with the prior probability of that class $p(C)$ (estimated from the sample points). Since we want the contributions of hits and misses in each step to be in 0 to 1 symmetric, we ensured that misses probability weights sum to 1. As the class of hits is missing in the sum, we divided each probability weight with factor 1 - p (class (n_i)) (which represents the sum of probabilities for the misses). The process is repeated for t times. Selection of k hits misses and ensured greater robustness of the ReliefF algorithm about the noise. k parameter that controls the locality of the estimates was set to 10 (Robnik and Konenko, 2003; Durgabai and Ravi Bhushan, 2014). Finally, the ReliefF algorithm ranked the WV-2 bands sensitiveness to the built-up areas based on the estimated weight ranging from 0 to 1 with large weights assigned to important WV-2 bands. ReliefF algorithm was used successfully for feature extraction (Durgabai and Ravi Bhushan, 2014; Wieland and Pittore, 2014; Anusha and Sathiyamoorthy, 2016).

2.3.3. Algorithm representation

The input: for each training instance a vector or point of the attribute (i.e., either road or rooftop)

Output: the vector w of estimations of the qualities of attributes.

1. set all weights $w[A]$:=0.0;

2. for i:=1 to t do begin

3. randomly select an instance n_i;

4. find k-nearest hits h_j ;

5. for each class $C \neq$class (n_i) do

6. from class C find k nearest misses m_j (c);

7. for A: =1 to a do

8. $$w[A] = w[A] - \sum_{j=1}^{k} \frac{diff\,(\mathrm{A,ni,hj})}{(m,k)} + \sum_{C \neq class\ n_i} \frac{[\frac{p(\mathrm{c})}{1-p(\mathrm{class(n_i)})} \sum_{j=1}^{k} diff\,(\mathrm{a,n_ih_j})]}{(\mathrm{m,k})}$$ Equation 2.1

9. End

2.4. Built-up spectral Index creation

2.4.1. Spectral index creation

Spectral indices are part of processing methods called multi-spectral transformations (Bouzekri, Lasbet and Lachehab, 2015). Caloz and Collet (2001) earlier defined an index as a variable synthetic, digital characterizing the intensity or the extension of an overly complex phenomenon to be broken down into a manageable number of parameters. The stratified random sampling technique was used to develop an empirical method to formulate the built-up index. Deng *et al.* (2015) asserted that the selection of stratified random samples is vital for the construction of the spectral index. Gao and Mas (2008) pointed out that in the selection of samples, the large number represents the reliability of specific land cover spectral signature much better than small numbers. Therefore, in this study as a compromise of efficiency and reliability, the generated stratified random sample points or pixels on built-up materials used in the above feature ranking were comprehensively used to examine their spectral pattern. In the development of the NBEI we employed the following steps:

1. Evaluating the spectral pattern to identify significant WV-2 wavelengths that are sensitive to dissimilarities in a target’s spectral response, which represent the built-up areas as compared to other land features (Samsudin, Shafri and Hamedianfar, 2016).

2. We postulate that the significant WV-2 bands obtained from the feature ranking using the ReliefF algorithm will be the same spectral bands that show the absorption and reflectance regions of the spectral pattern.
3. Since built-up samples may exhibit a high spectral variability due to their complex materials, we hypothesize that an effective spectral index will be developed based on the ratios (i.e. band combinations) between the sum of spectral bands that signifies the absorption and reflectance regions of the spectral pattern.

2.4.2. Comparative Analysis

To better examine the performance of NBEI in creating a distinction between built-up and non built-up features in WV-2 imagery, we also conducted a comparative analysis. In this study, five related spectral indices: built-up area index (BAI) (Mhangara *et al.*, 2011), built-up the spectral index (BSI) (Sameen and Pradhan, 2016), red edge/green Index (RGI) (Belgiu, Drăguţ and Strobl, 2014) and Worldview built-up index (WV-BI) (Environment for Visualizing Images ENVI, 2014) were implemented for the comparative analysis since they could enhance built-up features information with a degree of vagueness. The empirical formulas of these indices are expressed in Table 2.3 below. Finally, the threshold technique employed in the study for the separation of built-up and non built-up areas i.e., to determine the optimal threshold value follows the same steps employed in the study of (Xu, 2008; Chen *et al.*, 2010).

Table 2.3 List of compared WV- 2 images built-up indices.

Name	**Formula**	**Reference**
Built-up area index (BAI)	((Blue - NIR1))/ ((Blue + NIR1))	(Mhangara *et al.*, 2011)
Built-up spectral index (BSI)	((Yellow - 2*NIR1)/ (Yellow + 2*NIR1))	(Sameen and Pradhan, 2016)
Red edge/Green Index (RGI)	((Red edge - Green)/ (Red edge +Green))	(Belgiu, Drăguţ and Strobl, 2014)
Worldview built-up index (WV-BI)	((Coastal blue - Red edge)/ (Coastal blue + Red edge))	(Wolf, 2010; Environment for Visualizing Images ENVI, 2014)
New built-up extraction index	((NIR2 +NIR1) - (Green + Red edge))/ ((NIR2 +NIR1) + (Green + Red edge))	(Adeyemi *et al.*, 2021a)

2.4.3. Precision Evaluation

In this study, the accuracy of the five built-up spectral indices was assessed based on un-stratified random evenly distributed samples (n=244) obtained from reference data (aerial photo at 0.5m spatial resolution and visual inspection on Google Earth) to validate the index derived image. 10-fold cross-validation was used to rearrange the samples to ensure that each fold is a good representation of the whole datasets i.e., with a lower sample distribution variance compared to the hold-out cross-validation (Danjuma,2015). Finally, we implemented the performance evaluation metrics using the area under the receiver operating characteristic curve (AUROC) which is a graph that summarizes the performance of the indices (classifier) over all possible thresholds. It is generated by plotting the true positive rate (y-axis) against the false positive rate (x-axis). Wieland and Pittore (2014) further explained that the true positive rate is the proportion of actual positives that are classified as positives, while true negative rate, is the proportion of actual negatives, which are classified as negatives. It was computed using InformationValue and plotROC package in the R statistical software environment (RStudio, 2018; Prabhakaran, 2016; Sameen and Pradhan, 2016).

2.5. Results

2.5.1. An empirical analysis of ReliefF algorithm

Figure 2.1 gives an overview of the WV-2 bands importance for delineating built-up using the ReliefF algorithm. As shown in Figure 2.1, *NIR2* is ranked the highest with weight of 0.017. Amongst the eight spectral band features, the most important features that can be used for the formulation of the new normalized band ratio for built-up area delineation were *NIR2, NIR1*, *Red edge* and *Green* or *Yellow.*

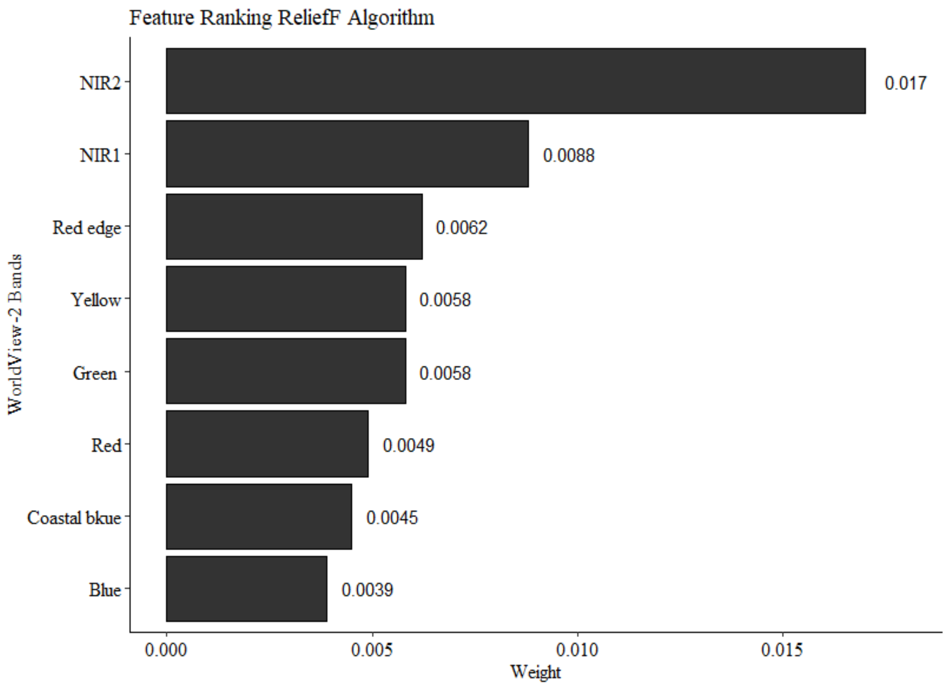

Figure 2.1 WV-2 spectral bands features ranked by their importance for identifying built-up areas.

2.5.2. Reflectance profile of built-up surfaces and spectral index creation

The concept for developing spectral indices is to identify the weakest and strongest reflectance band from multi-spectral data (Wu, 2004). Figure 2.2 shows that the built-up (i.e., rooftop and roads) reflectance is distinct. As indicated in Figure 2.2, the spectral profiles of rooftop and road exhibit a similar reflectance pattern of shape, but differ largely in the magnitude particularly in the *Red edge* to *NIR* spectrum. The built-up surfaces indicated reflection highly in the *NIR* (centered between 833nm and 950nm) regions and absorption at the *Green* (545nm) and *Red edge* (725nm) regions of the WV-2.

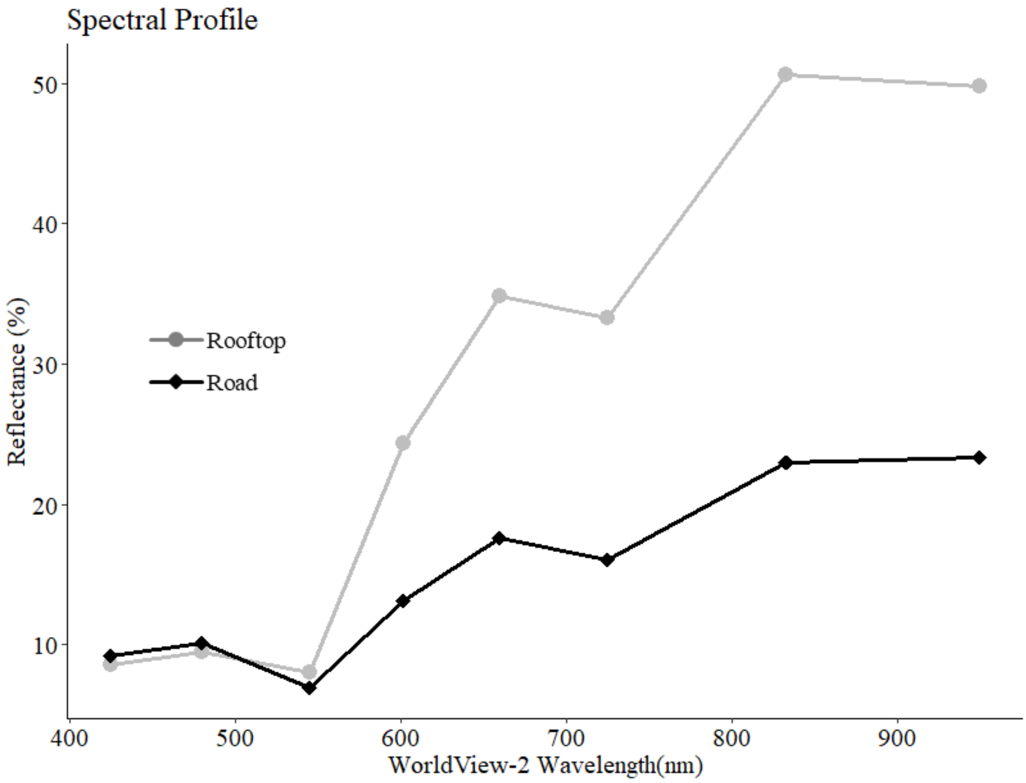

Figure 2.2 WV-2 mean spectral profiles of built-up areas extracted.

2.5.3. Spectral index creation and Threshold Selection for built-up mapping

Based on the identified weakest and strongest bands coupled with conventional approaches, Waqar *et al.*(2012) explained that spectral indices are formed to enhance required land cover over wide range of wavelength values and suppress others. To develop the NBEI, the WV-2 bands *NIR2, NIR1*, *Red edge* and *Green* were used respectively. NBEI was developed using normalized ratio of the addition of *NIRs* and *Green* and *Red edge* spectral regions which is mathematically expressed in Equation 2.2 as:

$$NBEI = \frac{\left(\left(NIR2 + NIR1\right) - \left(Green + Red\ edge\right)\right)}{\left(\left(NIR2 + NIR1\right) + \left(Green + Red\ edge\right)\right)}$$

Equation 2.2

The NBEI can enhance the built-up land feature easily because the subtraction of the *Green* and *Red edge* bands from the *NIR* bands will result in positive values for built-up land pixels only i.e., the index takes advantage of the condition where the features with higher *NIR2* and *NIR1* values but lower *Green* and *Red edge* values. Likewise, the subtraction of the *Green* and *Red edge* bands from the *NIR* bands in the band combination helped enhance the depiction of built-up area while suppressing other non-built-up areas (Xian *et al.*, 2019). Evidently, the NBEI is a normalized difference index with features such as: (1) a ratio-based index, (2) values ranging between -1 to + 1 and (3) enhanced built-up information has positive values, while the suppressed land covers (e.g., vegetation, base land or soil etc.) has zero to negative values.

Furthermore, based on threshold analysis of binary images (Figure 2.4) derived from previously developed built-up indices, the results of the comparative study in Figure 2.3 indicate the following threshold values in Table 2.4 respectively.

Table 2.4 Dynamic ranges of previous WV-2 built-up indices.

Index	**Threshold**
BAI	-0.09≥ built-up ≥-0.81
BSI	-0.390≥ built-up ≥-0.894
NBEI	0.03 ≥ built-up ≥ 0.509
RGI	0.085 ≥ built-up ≥0.69
WV-BI	-0.009 ≥ built-up ≥-0.689

In comparison, our developed index (i.e. NBEI) demonstrated its potential to map built-up rooftops and asphaltic roads based on the produced index threshold values in Table 2.4 and Figure 2.3. The stratified 10-fold cross-validation indicate the AUROC of NBEI improved the detection of built-up (AUROC = ~0.82) as compared to the existing ones such as BSI (AUROC = ~ 0.78), BAI (AUROC = ~0.73), RGI (AUROC = ~0.71) and WVBI (AUROC = ~0.67) respectively (Figure 2.6). The threshold values indicate built-up or impervious surfaces (i.e., n=130 stratified random samples of built-up pixels). Threshold values within the range of 0.03 to 0.509 (see Table 2.4), are primarily clustered values with histogram frequencies of 5 to 20. Threshold values within ranges of <0.03 and >0.509 are mostly frequency that optimizes non-built-up areas. Overall, our results shows that NBEI has successfully separated built-up areas from other land cover types with relatively high precision.

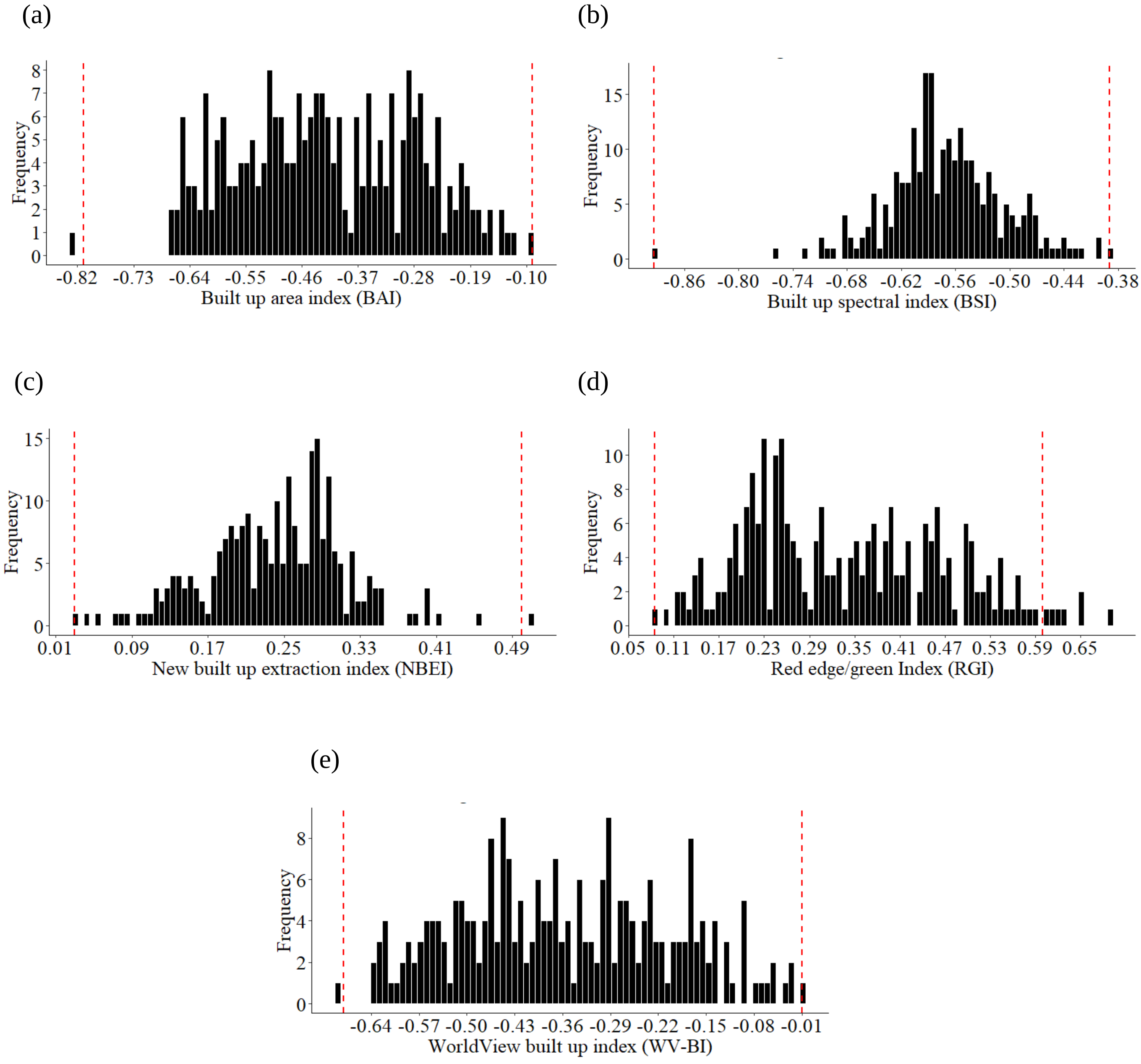

Figure 2.3 Threshold histograms showing the range of the threshold pixel values depicting built-up areas in (a) BAI, (b) BSI, (c) Proposed (NBEI), (d) RGI (e)WV-BI.

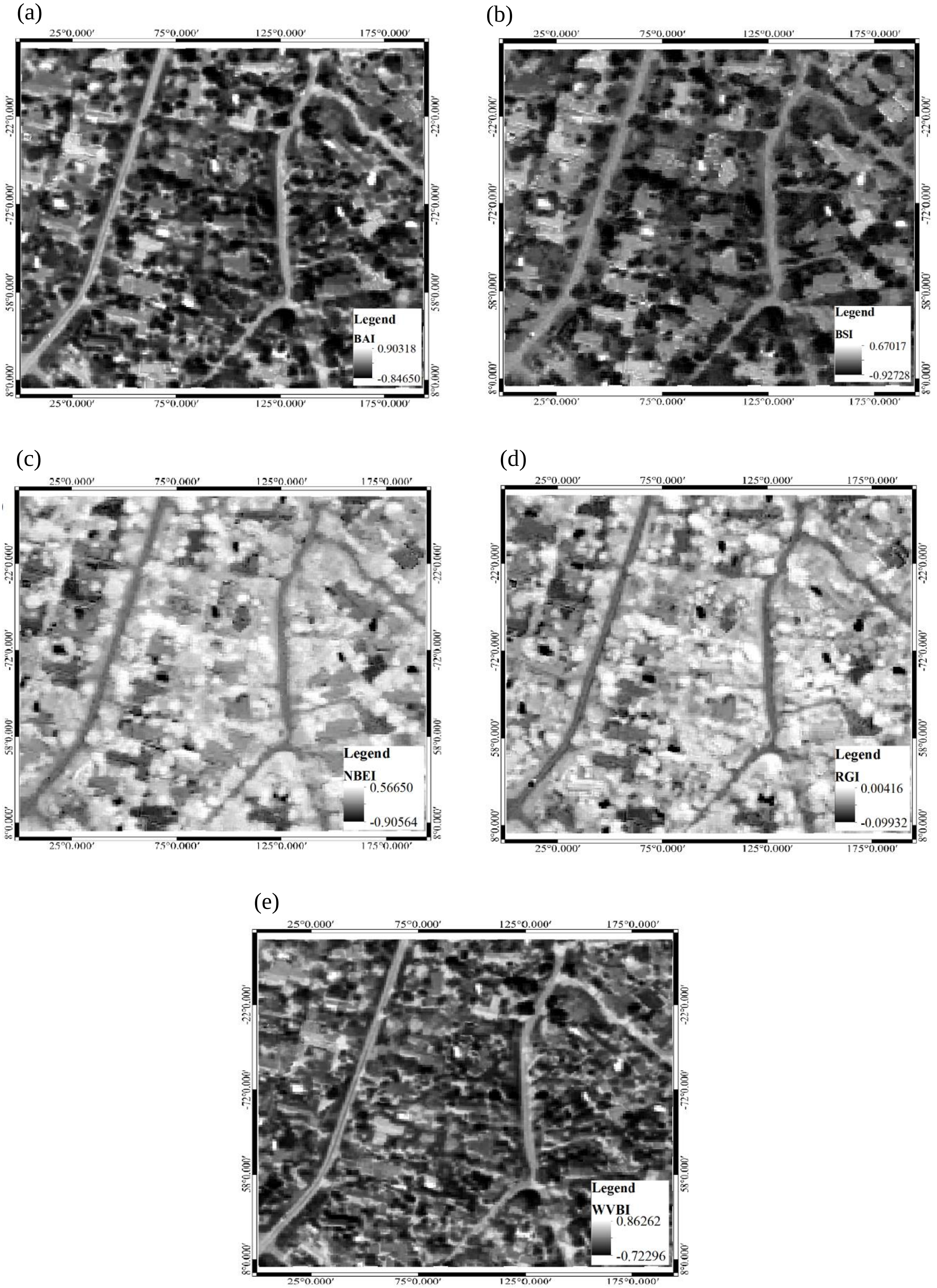

Figure 2.4 Result of compared spectral indices images (a) BAI, (b) BSI, (c) Proposed (NBEI), (d) RGI, (e) WV-BI.

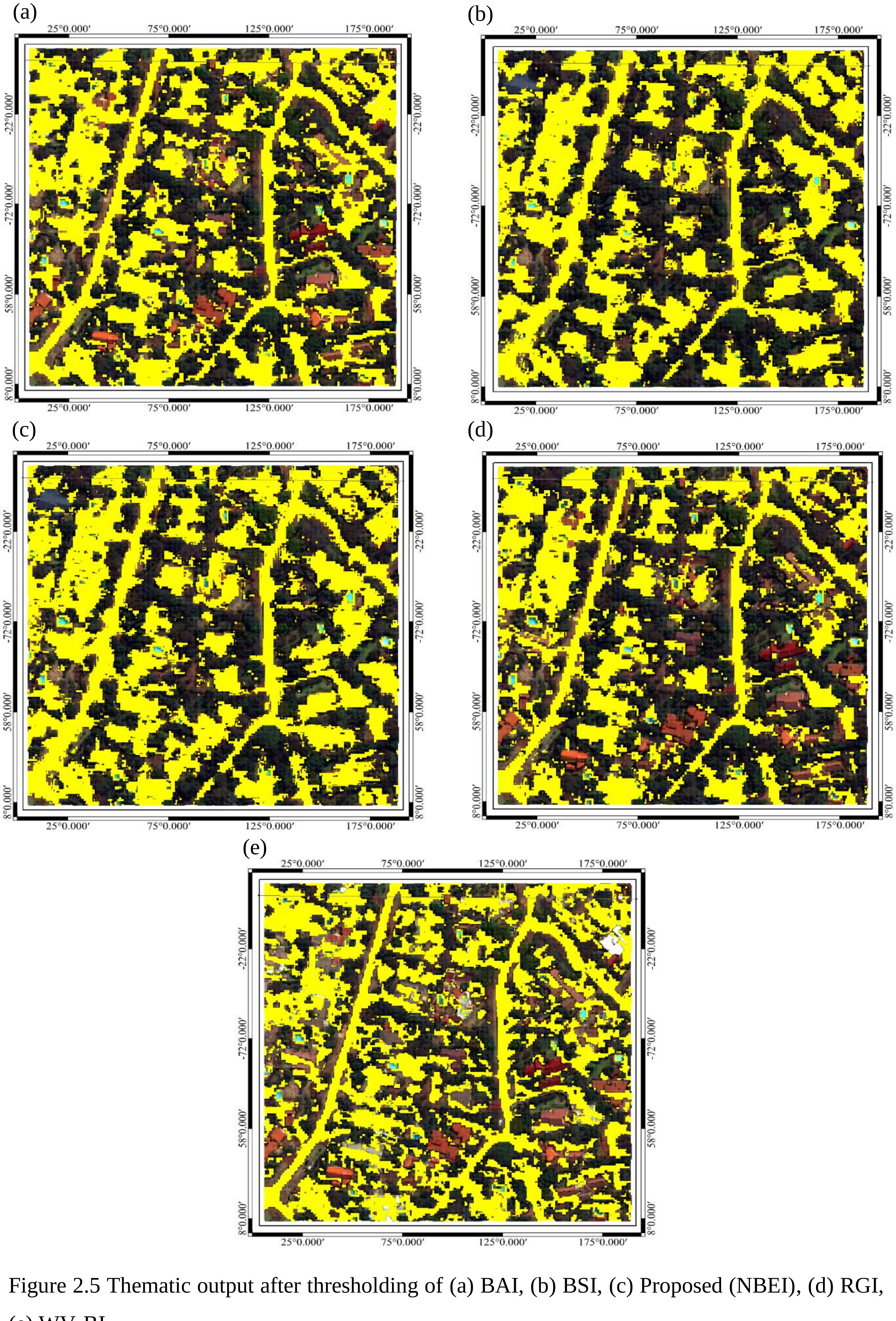

Figure 2.5 Thematic output after thresholding of (a) BAI, (b) BSI, (c) Proposed (NBEI), (d) RGI, (e) WV-BI.

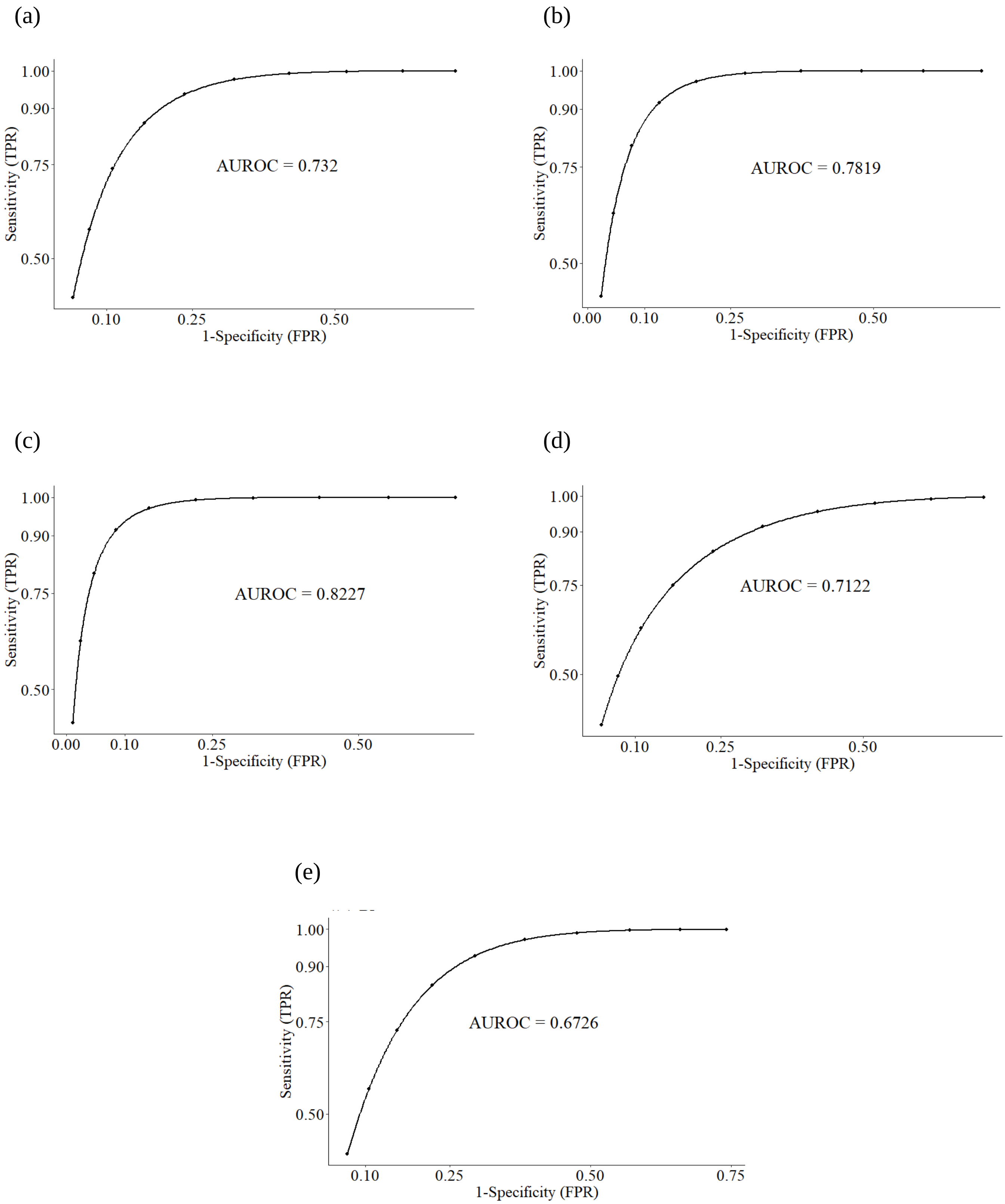

Figure 2.6 AUROC curve showing the 10-fold cross-validation performance evaluation of all the built-up indices of WV-2, (a) BAI, (b) BSI, (c) Proposed NBEI, (e) RGI, (d) WV-BI.

2.6. Discussion

According to Varshney and Rajesh (2014), index-based algorithms it is possible to classify built-up areas such as roads and rooftops and so on automatically at the minimal time when compared to the conventional image classification process. Due to the convenience of spectral indices in detecting specific land cover, a large number of indices have been developed in the past decade (Deng *et al.*, 2015). However, few spectral indices are available to enhance built information directly from the VHR image (e.g., WV-2). This study proposed NBEI for built-up extraction based on WV-2 bands. Accuracy assessment results show that overall extraction accuracy for built-up areas using NBEI is greater than that of previously developed indices. This shows that our proposed NBEI can be used to achieve much better results for extraction and better delineating of built-up areas in our study area.

In this study, we examined the capability of NBEI to identify different roads and to build rooftops materials. Amongst, the eight WV-2 spectral bands, the significant bands used for the formulation of the new index for built-up area detection were *NIR2, NIR1, Red edge* and *Green*. These significant wavelengths were able to depict a significant difference in the shape of spectral signature (Shahi *et al.*, 2015). The *NIR1* and *NIR2* bands located at the reflectance region and the *Green* band at the absorption region helped to enhance built-up areas (Samsudin, Shafri and Hamedianfar, 2016) while the *Red edge* band suppresses the vegetation (Pu and Landry, 2012; Y. Zhu *et al.*, 2017). Although previous worldview-2 built-up indices employed for comparison were based on various bands (i.e., Coastal Blue, Blue, Green, Yellow, Red edge and NIR1), the ReliefF algorithm employed in our approach, found that *Green*, *Red edge*, *NIR1* and *NIR2* are the most suitable bands to extract the built-up areas from the worldview-2 image. Also, the visual examination of these spectral indices performance presented in Figure 2.5, further explains the superior performance obtained of NBEI. For instance, the low accuracy of BAI, RGI and WV-BI (AUROC $\leq$ 0.73) could be attributed to the fact that many rooftops (e.g., red and brown) were not detected accurately. This might be because of the absence of *NIR2* in these indices that can comprehend the different rooftops surface illumination. Also, the subtraction of the *Green* and *Red edge bands* from the *NIR* bands in the band combination was helpful in enhancing the depiction of built-up area while suppressing other non-built-up areas (Xian *et al.*, 2019) i.e., vegetation and bare land or soil. BSI performed reasonably well with negative threshold values when compared to NBEI which had good coverage of built-up areas with positive threshold values. Even though the study area comprises a heterogeneous natural (e.g., vegetation, bare land or soil) and artificial land cover, NBEI developed in this study provides the advantage of independence from making a mask for non-built-up to focus only on built-up areas.

2.7. Conclusion

The new spectral index (NBEI) proposed in this study improves the extraction of built-up areas automatically from WV-2 imagery. The evaluation of the NBEI compared with four other spectral built-up indices developed for WV-2 imagery in the previous study showed a better result for the detection and extraction of built-up areas with less time and pre-processing. Since the performance of the spectral index depends on the spectral response of land cover characteristics that vary from one region to another due to climatic, topographic and socio-economic changes, the effectiveness of the new built-up extraction index for WV-2 still needs to be tested at different study sites within the urban settings (e.g., commercial, industrial etc.), provided there is the availability of this commercial satellite imagery.

Chapter 3 Exposed rooftop impervious surface analysis using satellite data in an urban residential environment.

Satellite level (high resolution and medium resolution)

Abstract

Rapid urbanization because of population growth has led to the conversion of natural lands into large man-made landscapes which affects the micro-climate. Rooftop reflectivity, material, colour, slope, height, aspect, elevation are factors that potentially contribute to temperature variability. Therefore, strategically designed rooftop impervious surfaces have the potential to translate into significant energy, long-term cost savings, and health benefits. In this experimental study, we used the semi-automated Environment for Visualizing Images (ENVI) Feature Extraction that uses an object-based image analysis approach to classify rooftop based on colours from WorldView-2 (WV-2) image with overall accuracy ~90.4% and kappa coefficient ~0.87 respectively. The daytime retrieved surface temperatures were derived from 15m pan-sharpened Landsat 8 TIRS with a range of ~14.6^{O}C to ~65^{O}C (retrieval error = 0.38^{O}C) for the same month covering Lynwood Ridge a residential area in Pretoria. Thereafter, the relationship between the rooftops and surface temperature (LST) were examined using multivariate statistical analysis. The results of this research reveal that the interaction between the applicable rooftop explanatory features (i.e., reflectance, texture measures and topographical properties) can explain over 22.10% of the variation in daytime rooftop surface temperatures. Furthermore, analysis of spatial distribution between mean daytime surface temperature and the residential rooftop indicated that the red, brown and green roof surfaces show lower LST values due to high reflectivity, high emissivity and low heat capacity during the daytime. The study concludes that in any study related to the spatial distribution of rooftop impervious surface area surface temperature, effect of various explanatory variables must be considered. The results of this experimental study serve as a useful approach for further application in urban planning and sustainable development.

3.1. Introduction

Generally, there has been an unprecedented increase in population concentration in cities which have led to rapid urban landscape changes (UNDP, 2012). Parece and Campbell (2013) reflected that over 50% of the global population lives in urban settlements and the United Nations Population Division (2009) estimate that it will increase to 69% by 2050. One of the most important environmental impacts of urban land modification is land surface temperature (LST) and atmospheric temperature variability which affects urban microclimate and heat stress (Voogt and Oke, 2003). Chudnovsky, Ben-Dor and Saaroni (2004) also pointed out that physical properties of urban landscape (i.e. ISA) such as colour, street geometry, sky view and other man-made activities influence surface temperature. LST variability has likewise been seen as the main indicator of surface urban heat island when observed at a large geographical scale i.e., urban-rural surface temperature difference (Yuan and Bauer, 2007; Rajasekar and Weng, 2009; Hu and Jia, 2010; Rinner and Hussain, 2011; Ahmed et al., 2013; Deng and Wu, 2013) to mention a few. Based on the studies of Zhao et al. (2015), asserted that urban heat island aggravates heat waves, increases energy consumption and elevates the risk of heat-related morbidity and mortality due to heat stress. Due to the above mentioned concerned, urban heat island has continuously gained increasing attention from ecologist, environmentalist, urban planners and policymakers in developed counties. This has led to the suggestion of several mitigation strategies such as: increasing the number parks and green spaces, use of green or high albedo cooling rooftops, cold pavement materials and better urban design for airflow (Javed Mallick and Bharath, 2008; Chen, Wei and Wu, 2009; Susca, Gaffin and Dell'Osso, 2011; Ng et al., 2012; Doick, Peace and Hutchings, 2014; Gao et al., 2014).

Over the last decades, Southern Africa has been facing major unplanned land transformation such as loss of vegetation cover (e.g., cultivated lands and grasslands) coupled with increasing impervious surfaces areas (i.e., rooftops, cemented areas and asphaltic roads) and bare lands due to continuous increase in population and socio-economic activities (Adeyemi et al., 2015). Therefore, understanding the dynamic nature of land use or cover can enable us to further understand the direct impact of anthropogenic activities on the environment. The main aim of this experimental study is to assess the impact of rooftop impervious surface based on a property (colours) on surface temperature variability through WV-2 (pan-sharpened ~0.5m), Landsat 8 TIRS (pan-sharpened 15m) and LIDAR-derived normalized height model and bare earth model (2m). In particular, we conducted the study in an urban residential area Lynnwood Ridge, Pretoria, Gauteng Province, South Africa (Figure 1.6).

3.2. Background

Growth is sometimes reflected by the chaotic expansion of urban sprawl and the spontaneous appearance of urban buildings in rural areas or on the peripheries of cities (Bouzekri, Lasbet and Lachehab, 2015). This rapid urban landscape change as indicated by Odindi, Mhangara and Kakembo (2012) has been because of the exceptional increase in population concentration in cities. Deng and Wu (2013) also asserted that one of the most significant environmental impacts of land modification is land surface temperature (LST) and atmospheric temperature variability which affects surface energy exchange, anthropogenic heat discharge, building energy consumption, atmospheric pollution, urban microclimate and heat stress (Voogt and Oke, 2003; Weng, 2009). As a result, the research on LST variability is crucial in the development of sustainable urban policy (Ahmed et al., 2013).

3.2.1. Brief assessment satellite measurement of surface temperature

LST had been previously acquired by in-situ measurements i.e., ground-based observation from fixed thermometer networks at meteorological or weather stations or by mounted thermometer on vehicles traversing the study areas (Voogt and Oke, 2003; Weng, Dengsheng and Jacquelyn, 2004). Consequently, improved satellite data over the years have led to the use of a wide variety of infrared thermal sensors that gives a more synoptic coverage of LST at local and regional level (Yuan and Bauer, 2007). These satellite or airborne thermal sensors are AVHRR, MODIS, ASTER, Landsat TM/ETM+/LDCM, GOES, HCMM, IRT, TIRS, SEVERI, TIMS, MODIS/ASTER Airborne Simulator (MASTER) etc. (Voogt and Oke, 2003; Olarewaju Oluseyi, Fanan and Magaji, 2009; Weng, 2009; Tomlinson et al., 2011; Abutaleb et al., 2015; Zhao and Wentz, 2016).

Based on the thermal infrared bands of remote sensing data of space-borne sensors, three recommended methods have been used to retrieve LST. These three methods are: (1) the radiative transfer equation, (2) Qin, Karnieli and Berliner (2001) mono-window and split window algorithm, and (3) Single-Channel Algorithm (Jiménez-Munoz and Sobrino, 2003; Sobrino, Jiménez-Muñoz and Paolini, 2004; Jiménez-Muñoz and Sobrino, 2010). The disadvantage of the first method is that it requires in situ atmospheric profile launched simultaneously with the satellite passes which makes it very difficult to achieve. Usually, the second and third methods are used when the ground truth data is not available (Alipour, Sarajian and Esmaeily, 2011). The disadvantage of the first method is that it requires in-situ atmospheric profile launched simultaneously with the satellite passes which makes it very difficult to achieve. Usually, the second and third methods are used when the ground truth data is not available.

Quantitative studies on land use or cover change associated with urbanization impact on LST distribution have also been a source of vital information for urban planners (Zhang, Odeh and Han, 2009; Liu and Zhang, 2011; Xie and Zhou, 2015). The degree of urban sprawl has been measured by the increase of impervious surface area (Civco et al., 2002; Yang et al., 2003). These impervious surfaces are associated with transportation (asphaltic roads and streets, highways, parking lots and sidewalks) and cemented buildings and rooftops (Adeyemi, Botai, Ramoelo, 2015). Since impervious surface area is more stable and less affected by seasonal changes unlike vegetation, it provides a good metric for analysis of urban thermal patterns (Yuan and Bauer, 2007; Zhang, Odeh and Han, 2009; Xie and Zhou, 2015).

Even though remote sensing data continues to contribute to the detection and understanding of the interplay between man-made land features and surface temperature in most studies performed in the developed countries, very little research has been done on rooftop properties impacts. Zhao et al. (2015) pointed out that rooftops are the major impervious surfaces in the urban environment and it is important to evaluate their surface property (colours) interaction with land surface temperature. Thus in Pretoria, South Africa (i.e., a developing country), much work is needed to promote such an approach.

3.2.2. ISA semi-automatic detection using high-resolution imagery

Though recent studies have indicated that automatic detection and assessment of the percentage of impervious surface areas such as building rooftop types or materials in heterogeneous urban areas has been challenging but also an important task in remote sensing of urban landscape (Ghaffarian and Ghaffarian, 2014). Detection of rooftop type according to Taherzadeh and Shafri (2013) studies pointed out its importance in disaster awareness, solar photovoltaic energy modelling, urban heat island assessment, and runoff quality (Szykier, 2008; Rajasekar and Weng, 2009). Li, Zhang and Davey (2015) also explicated that rooftop information plays a prominent role in widespread applications such as urban planning, 3D city modelling and flight simulation. Even though advantages of having rooftop information have been indicated in previous studies, accurate extraction of the rooftop appearance (colour) remains a challenge with existing and traditional image classification methods due to many factors (Ok, 2013).

The need for new satellite sensors coupled with new classification methods in recent years has been used to meet up the requirements of urban sprawl. This is because traditional classification methods are time-consuming, laborious and expensive (Han, 2010). For instance, the study of Zhou and Troy (2008), indicated that supervised classification of rooftop impervious surfaces in a complex urban landscape at parcel level does not only require very high resolution (VHR) imagery but also adequate training data due to lack of physical accessibility to the rooftops that requires permission. Also, many studies around the world have been done to depict complex urban landscape using discriminant capabilities of available hyperspectral data which is better than the traditional multispectral imagery that only used a few wide-bands spectral channels (Heiden et al., 2007; He Yang; Ben Ma; Qian Du; Chenghai Yang, 2010; Taherzadeh and Shafri, 2011). Even though, Kaszta et al. (2016) suggested that combined airborne LiDAR and hyperspectral survey as one of the several remote sensing solutions useful for differentiation of land cover components in heterogeneous urban landscape, it is very expensive and limited in Africa. Other high spatial resolution satellites such as IKONOS and Quickbird though have been used, Herold et al. (2002) revealed that they have relatedly low spectral resolution which limits their ability to separate impervious and non-impervious materials. New satellite sensors such as WorldView-2 (WV-2), which are readily available, not only offers a very high spatial resolution but also extended and innovative spectral bands when compared with other multispectral sensors like Landsat and SPOT (i.e., medium spatial resolution) which are not recommended for urban studies (Taherzadeh and Shafri, 2013; Belgiu, Drăguţ and Strobl, 2014).

Furthermore, studies have shown that the traditional pixel-oriented approach has been used for classifying urban landscapes using high spatial resolution multispectral imagery (Chen, Stow and Gong, 2004; Wang et al., 2007). Adam, Csaplovics and Elhaja (2016) explained that the pixel-oriented approach utilizes spectral information (digital numbers, DN) stored in the image i.e., classifies images by considering only the spectral similarities with the pre-defined land cover classes. This spectral information has also been asserted in earlier studies to be insufficient in classifying urban impervious surfaces (rooftops) in detail due to the spectral similarities between materials leading to misclassified pixels (Van der Linden, 2007). In contrast to the pixel-oriented approach are the image objects and segments which are the basic units used in object-oriented classification (Ishimwe, Abutaleb, Ahmed and Ngie, 2014). Each image object is composed of spatially adjacent pixels clustered based on homogeneity criteria used in image segmentation procedure (i.e., partitioning of an image into non-intersecting regions) (Blaschke, 2005). Object-oriented approach does not only use the image spectral and spatial information like the pixel-oriented approach but has the advantage of other information such as texture, shape and contextual relationship which improves the classification accuracy (Juniati and Arrofiqoh, 2017). Several comparative investigations have also been conducted that examines the relative performance of the pixel-oriented against the objected-oriented approach using different classification algorithms on high spatial resolution imagery (Blaschke, 2008; Ouyang et al., 2011; Makinde et al., 2016). Although many authors claimed that object-oriented classification performs better on a high spatial multispectral resolution imagery in depicting impervious surface areas in a complex urban landscape, very few studies have been carried out in Africa.

Aldred and Wang (2007) earlier revealed that rooftops are prominent features of buildings as seen from above by satellite sensors and can be considered as useful surrogates for building footprints that are essential to mapping urban landscapes. As separate land cover class as indicated in impervious studies, the large variability in material composition, colour, shape, size and orientation of buildings in complex urban areas means that rooftops are distinguishable from other impervious surfaces more by properties (Herold et al., 2002). Even though previous studies asserted that high spatial resolution multispectral imagery created the possibility to delineate rooftops (Liu, Wang and Liu, 2005; Aldred and Wang, 2007; Taherzadeh and Shafri, 2013; Zhao et al., 2015), there is no extensive study exploring this method in major cities in Africa.

3.3. Materials and Methods

3.3.1. Data and Material Acquisition

One cloud-free WorldView-2 (WV-2) multispectral high-resolution image of the study area was obtained from Digital Globe in October 2015. WV-2 was launched in October 2009 as the first commercial multispectral satellite that comprises 2m eight multispectral bands and 0.5 m panchromatic bands (Wolf, 2010). The satellite has a swath width of 16.4 km, an average revisits time of 1.1 days and is capable of collecting up to 975,000 square kilometres per day. Therefore, the satellite has spectral and spatial resolutions that meet a variety of remote sensing applications such as mapping rooftops (Nasarudin and Shafri, 2011; Taherzadeh and Shafri, 2013). The spectral ranges of the eight bands in nanometres are described in Table 3.1.

Table 3.1 WorldView-2 imagery characteristics

Band Number	**Spectral Range (nm)**	**Band Name**	**Spatial resolution (m)**	**Year**
1	400-450	Coastal blue	2	2015
2	450-510	Blue	2	
3	510-580	Green	2	
4	585-625	Yellow	2	
5	630-690	Red	2	
6	705-745	Red-edge	2	
7	770-895	NIR1	2	
8	860-1040	NIR2	2	

Pan	450-800	Pan	0.5	

One cloud-free spring time Level 1 Terrain Corrected (L1T) medium-resolution image recorded by Landsat-8 OLI (Operational Land Imager) and TIRS (Thermal Infrared Sensor) on 16th September 2015 at 08:02h local time (Path =170, Row = 078) were obtained from the US Geological Survey (USGS) Global Visualization Viewer (United States Geological Survey, 2013). The spectral ranges of the eleven bands in micrometres are described in Table 3.2.

Table 3.2 Details of Landsat-8 OLI and TIRS image used for the study.

Band Number	**Spectral Range (μm)**	**Spatial Resolution (m)**	**Band Name**	**Path/Row**	**Year**
1	0.435–0.451	30	Coastal/Aerosol	170/078	2015
2	0.452–0.512	30	Blue		
3	0.533–0.590	30	Green		
4	0.636–0.673	30	Red		
5	0.851–0.879	30	NIR		
6	1.566–1.651	30	SWIR 1		
7	2.107–2.294	30	SWIR-2		
8	0.503–0.676	15	Pan		
9	1.363–1.384	30	Cirrus		
10	10.60–11.19	100	TIR-1		
11	11.50–12.51	100	TIR-2		

Furthermore, the already pre-processed Airborne LiDAR (light detection and ranging) point clouds data for 2013 by the Natural Resources and Environment (NRE) Council for Scientific and Industrial Research (CSIR), South Africa was acquired from using the Carnegie Airborne Observatory (CAO) Alpha system (Cho et al., 2012; Naidoo et al., 2015). The processing of the raw LiDAR cloud data points is detailed in Asner and Levick (2012). The LIDAR data provided highly accurate building height information need for detailed rooftop temperature analysis based on rooftop configuration and properties feasible and executable (Awrangjeb, Zhang and Fraser, 2013; Zhao et al., 2015). Likewise in this study, ancillary data such as temperature data from the South African Weather Station (SAWS), the Department of Environmental Affairs (DEA), the Department of Forestry, Fisheries and the Environment (DFFE), South Africa (https://www.environment.gov.za) subcontracted National Land Cover (NLC) classification dataset of 2013-2014 (https://egis.environment.gov.za/sa_national_land_cover_datasets) completed in 2015; Pretoria administrative shapefile boundary source from Statistics South Africa 2011 (http://www.statssa.gov.za); 1:10,000 aerial photography 0.5m (2012-2015) from the Chief Directorate National Geo-spatial Information (CDNGI) (http://www.cdngiportal.co.zatogether with

Google Earth search engine were used for validation purpose to verify the rooftop colours in the study site. Software used for desktop analysis will be; ESRI (ArcGIS), ENVI - Environment for Visualizing Images (image processing software; Research Systems, Inc. Version 5.3), QGIS (version 3.8.0), Microsoft office, and Matlab version 8.5 software.

3.3.2. Satellite image pre-processing

The WV-2 scene used in this study (acquired in October 2015) was orthorectified and geometrically corrected by Digital Globe (Mutanga et al., 2015; Gairola et al., 2016; Madonsela et al., 2017). The WV-2 was then atmospherically corrected and transformed to canopy reflectance using the Quick Atmospheric Correction (QUAC) extension in Environment for Visualizing Images (ENVI) software (Environment for Visualizing Images ENVI, 2014). After the radiometric calibration, the WV-2 multispectral bands pan-sharpening to 0.5m was performed using the ENVI Gram-Schmidt Spectral Sharpening algorithm which improved the visualization of roofing materials (Laben and Brower, 2000). Also, the obtained Landsat-8 OLI and TIRS Level 1 Terrain Corrected (L1T) was pan-sharpening to 15m was performed using the ENVI Gram-Schmidt to have the highest possible resolution comparable to the above high resolution imagery for further analysis. Finally, all the resultant images were referenced to the Universal Transverse Mercator (UTM zone 35 South) projection using WGS-84 Geodetic datum (Omer et al., 2015).

3.4. Methodology

3.4.1. Masking non-rooftop impervious surfaces

The environment of the study area (Figure 1.6) comprises a heterogeneous natural and artificial land cover. Preliminary mask was implemented on the WV-2 image to exclude the non-rooftop impervious surfaces with the aid of threshold analysis of spectral indices (Table 3.4) and other ancillary data (Kaszta et al., 2016). As observed from the study area, the non-rooftop impervious surfaces were vegetation Normalized Difference Index by Rouse et al. (1973); Wolf (2010), asphaltic road; Built up Area Index by Mhangara et al. (2011) and shadow detection index (SDI) by Shahi et al. (2014). The generated thematic outputs from each index representing the above non-rooftop impervious surface areas were polygonized and merged. The resultant vector was used to build a mask that was applied to exclude non-rooftop pixels from the subsequent classification process.

3.4.2. Creation of rooftop samples

Training datasets is significant to understanding the features in the real world and to map a mental picture of the land use or cover type while the validation samples were used for independent validation of the obtained land cover maps (Bhaskaran, Paramananda and Ramnarayan, 2010; Aguilar et al., 2014; Ishimwe, Abutaleb, Ahmed and Ngie, 2014). Lynwood Ridge is a residential area with privately owned properties, so we couldn’t use a handheld GPS receiver to collect rooftop footprint samples. As a result, X and Y coordinates of these rooftops were manually digitized based on six colours observed from the WV-2 imagery (0.5m) and reference data such as 1:10,000 aerial photography (0.5m) and Google Earth Engine (Digital Globe). The rooftop polygons were uploaded using the ESRI ArcGIS and ENVI software (Table 3.3). These exposed building rooftops created were used as both training objects (58 polygons) and validation objects (58 polygons) for classification and accuracy assessment (Figure 3.1).

Table 3.3 Summary of the rooftop colour classes assigned to training and validation dataset.

Rooftops colours	Assigned Training Objects	Assigned Validation Objects	Total ∑
Blue	2	2	4
Brown	29	29	58
Dark	7	7	14
Green	4	4	8
Red	6	6	12
White	10	10	20
			116

Figure 3.1 WV-2 (0.5m pan-sharpened) exposed building footprints used for classification.

3.4.3. Separability analysis of samples

Spectral separability analysis test is a measure of how similar the distribution of the groups of pixels are (i.e., which configuration can be correctly associated with these classes) using statistical pattern classification (Richards and Jia, 2006). In comparison to previous studies of (Jia and Richards, 1999; Flasse, 2001; Yeom, Han and Kim, 2013) to mention a few, separability of the training objects for the rooftops footprints based on six colours observed in the study areas was assessed using the Jeffries-Matusita (*J-M*) distance index using ENVI software. The *J-M* distance is mathematically described in Equation 3.1 and 3.2. Where, *a* and *b* = the two region classes, *Ca* is the covariance matrix of *a, δa* is the mean vector of *a*, *T* is the transposition function. Yeom, Han and Kim (2013) pointed out that the value range commonly used in remote sensing practice is from 0 to 2.0 to indicate how statistically separable the selected pairs. In this study, we used a *J-M* distance of ≥ 1.90 as a threshold of spectral separability between different rooftop footprints based on colour group pair.

$$J-M_{ab}=\sqrt{2(1-e^{-\alpha})}$$ Equation 3.1

$$\alpha=\frac{1}{8}(\delta_a-\delta_b)^T\left(\frac{C_a+C_b}{2}\right)^{-1}(\delta_a-\delta_b)+\frac{1}{2}\ln\left[\frac{\frac{1}{2}\left|C_a+C_b\right|}{\sqrt{\left|C_a\right|\times\left|C_b\right|}}\right]$$ Equation 3.2

3.4.4. Additional rooftop parameters

Apart from the WV-2 eight spectral bands earlier used to classify the rooftops, additional features or bands selected to further explore its relationship with the derived surface temperature are described in Table and Figures below. A self-developed band ratio named built up extraction index (NBEI) for WV-2 image which effectively detects built-up materials was used as one of the explanatory features for the rooftops (Figure 3.3). Furthermore, Waser et al. (2014) explicated that the Principal Component Analysis (PCA) involves a mathematical procedure that transforms a number of (possibly) correlated variables into a (smaller) number of uncorrelated variables called principal components. In this study, after performing the PCA transformation on the WV-2 image using ENVI software to reducing the redundancy and intercorrelation among the original spectral bands, the first principal component accounted for as much of the variability in the data as possible, and each succeeding component accounts for as much of the remaining variability as possible (Swan and Sandilands, 1995). Since the first principal component explain >95% of the variance (i.e., cumulative proportion of all components), we used it to extract information on spatial variability (Pacifici, Chini and Emery, 2009; Gong, Liu and Huang, 2019). Similar to the report of Madonsela et al. (2017), information on spatial variability was extracted in the form of texture using Gray Level Co-occurrence Matrix (GLCM) in ENVI software (Haralick, Dinstein and Shanmugam, 1973). In this study, we adopted second-order co-occurrence texture measures (Table 3.4) on the first principal component simply because they account for spatial relations amongst neighbouring pixels using a co-occurrence matrix (Zhang, Zhang and Lin, 2014; Salas, Boykin and Valdez, 2016) based on a 3x3 window size to detect fine-scale variability according to Kelsey and Neff (2014).

Subsequently, Salas, Boykin and Valdez (2016) asserted that the incorporation of some topographic features such as which describe terrain component is an important part of spectral response (Strahler, Logan and Bryant, 1978; Janssen, Jaarsma and Van Der Linden, 1990). According to previous studies, the first and last vertical returns are derived from the LIDAR point clouds (Asner and Levick, 2012; Cho et al., 2012; Naidoo et al., 2015; Zhao et al., 2015). The digital terrain model (DTM) or bare earth model was constructed from ground points (last return) with all the anthropogenic features removed while the digital surface model (DSM) representing all the above-ground features such as buildings and vegetation was computed from non-ground points (first return). The normalized height model (NHM) with a pixel size of 0.5m was computed by subtracting the DTM from DSM (Awrangjeb, Zhang and Fraser, 2013). Rooftop height was easily derived by extracting pixel values of intersecting exposed rooftops from the NHM (Figure 3.4 a-d). Furthermore, the slope and aspect raster layers were computed from the DTM using the ENVI-LiDAR software extension (Environment for Visualizing Images ENVI, 2014). Few studies have investigated whether these additional rooftop parameters can influence daytime rooftop surface temperature except for the study of Zhao et al. (2015).

Table 3.4 List of spectral dataset and texture features.

Name	**Formula**	**Reference**
Normalized Difference vegetation Index (NDVI)	((Red - NIR2)/(Red + NIR2))	(Wolf, 2010)
Built up area index (BAI)	((Blue - NIR1))/((Blue + NIR1))	(Mhangara et al., 2011)
Shadow detection index (SDI)	(((NIR2 - Blue)/(NIR2 + Blue)) - NIR1)	(Shahi et al., 2014)
New built up extraction index (NBEI)	((NIR2 +NIR1) - (Green + Red edge))/ ((NIR2 +NIR1) + (Green + Red edge))	(Adeyemi *et al.*, 2021)
GLCM Contrast	$\sum_{i=1}^{Ng}\sum_{j=1}^{Ng} P(i,j)(i-j)^2$	(Haralick, Dinstein and Shanmugam,1973; Zhang, Zhang and Lin, 2014; Salas, Boykin and Valdez, 2016).
GLCM Correlation	$\frac{\sum_i \sum_j (i,j)P(i,j)-\mu_x\mu_y}{\sigma_x\sigma_y}$	
GLCM Dissimilarity	$\sum_{i=1}^{Ng}\sum_{j=1}^{Ng} P(i,j)\lvert i-j\rvert$	
GLCM Entropy	$\sum_{i=1}^{Ng}\sum_{j=1}^{Ng} P(i,j)\log(P(i,j))$	
GLCM Homogeneity	$\sum_{i=1}^{Ng}\sum_{j=1}^{Ng} \frac{1}{1+(i-j)^2}P(i,j)$	
GLCM Mean	$\sum_{i=1}^{Ng}\sum_{j=1}^{Ng} i*P(i,j)$	
GLCM Second moment	$\sum_{i=1}^{Ng}\sum_{j=1}^{Ng} \{P(i,j)\}^2$	

GLCM Variance	$\sum_{i=1}^{Ng}\sum_{j=1}^{Ng}(i-\mu)^2 P(i,j)$	

N represents the number of distinct gray levels in the quantized image, μ represents the mean value of P, $P(i, j)$represent $(i, j)th$ entry in normalized gray-tone spatial-dependence matrix, = $P(i, j)/R$, R represents a normalizing factor.

3.5. Image classification

Image classification refers to the extraction of differentiated classes or themes (land use or cover categories) based on spatial, spectral and temporal patterns from remote sensing data (Qian, Zhou and Hou, 2007b). A wide range of classification methods has been developed to derive land cover information from remote sensing images. Pixel-oriented approach (supervised or unsupervised classification) has been the conventional method of land cover mapping. Even though it is a widely used technique, it has been reported that it suffers from ignoring the spatial pattern (i.e., image texture, pixel proximity, feature size and shape) in classification (Qian, Zhou and Hou, 2007b). Maximum likelihood classifier has been the most widely used pixel-oriented algorithm that only utilizes the spectral information (i.e., brightness and colour) without considering texture and contextual information (Zhou and Robson, 2001). Object-oriented approach, on the other hand, treats an image as a set of significant objects, making use of spatial, spectral and or texture characteristics (Yan et al., 2006).

3.6. Object-oriented classification

Object-oriented classification have to do with the understanding of image objects (i.e., region of interest) rather than pixels (Bhaskaran, Paramananda and Ramnarayan, 2010). This classification method does not operate directly on a single pixel or region of pixels, but objects which are regions of pixels, but objects which are regions of interest with similar spectral (brightness and colour), spatial and texture characteristics (Ishimwe, Abutaleb, Ahmed, and Ngie, 2014). Due to the emergence of high-resolution multispectral imagery (e.g., Quickbird, IKONOS, WV-2) commercial software, object-oriented classification has increasingly been used to improve accuracy and better discriminate urban land cover are spectrally similar (Wang et al., 2007). The advent of this commercial software such as ENVI Feature Extraction module an image processing software package from ITT Visual Information Solution (formerly Research Systems, Inc.), implements a standard object-based approach consisting of segmentation, segment-classification and generalization, based on attributes of spatial, spectral (brightness and colour), and texture characteristics (Environment for Visualizing Images ENVI, 2014). Similar to the study of Tsai, Stow and Weeks (2011), we employed the ENVI Feature Extraction to segment WV-2 image into regions of pixels that is partitioning a raster image into objects (real-world features) by grouping neighbouring pixels with common values and location (Blaschke, 2004; Wang et al., 2007). During the segmentation phase, the edge detection algorithm was used to detect edges of features were objects of interest (rooftops) coupled with an appropriate Scale Level of 90. Merging segments is a step used to aggregate small segments within larger ones where over-segmentation may be a problem. The Merge Level that delineates the boundaries of features as well as possible was iteratively chosen to be 30 (i.e., the lowest 30% of gradient magnitude values are discarded from the gradient image). The Full Lambda- Schedule algorithm created by Robinson, Redding and Crisp (2002) was employed. The algorithm iteratively merges adjacent segments based on a combination of spectral and spatial information. Merging segments is a step used to aggregate small segments within larger ones where over-segmentation may be a problem. The Merge Level that delineates the boundaries of features as well as possible was iteratively chosen to be 27. Texture Kernel Size value, which is the size of a moving box centred over each pixel in the image was set to 3 because we were segmenting smaller areas with higher variance such as urban residential environment. Furthermore, the rooftop footprint delineations (polygons) from the aerial images were rarely similar to the automatically generated segments of the WV-2 image, the corresponding image segments had to be selected manually based on their positions by visually checking. From Table 3.1, a total of 116 evenly distributed rooftop footprints selected based on the six colours classes observed, were used both for training and validation purposes (Waser et al., 2014). Feature attributes are necessary to compensate for some common problems associated with high-resolution image data such as the spectral variability within the same land-cover class (Lu and Weng, 2007). According to Hirose et al. (2004), coupled with spectral information, texture and shape information of image objects provide useful information for detailed object-based classification. Therefore, in this research, feature attribute selection for predefined segments was based on several trials from past reported studies that pointed out their contribution to improving the object based classification results (Myint et al., 2011; Salah, 2014; Kaszta et al., 2016).

Finally, the semi-automated object-based classification (Feature Extraction) was based on a K-nearest neighbour classifier (KNN) that classifies segments based on their proximity to neighbouring training regions was used to perform the classification. The KNN is identified by a distance measure that compares the feature vectors of the unlabelled instance and the set of training instances provided to the classifier. Wieland and Pittore (2014) asserted that once a list of nearest neighbours is obtained (e.g., 1, 3, 5 etc., odd value less than or equal to the total number of training regions for all classes), the prediction is based on voting (majority or distance-weighted). KNN algorithm as indicated in previous object-oriented classification studies is applied in this study because of its simplicity and flexibility (Waser et al., 2014).

3.7. Performance evaluation of object-oriented classification

In this study, the accuracy of the object-oriented KNN classifier was assessed based on validation objects or samples obtained from the reference data described above. To determine the accuracy of the generated classification maps, a confusion matrix according to the works of (Congalton, 1991) was employed. For the classification map, the Overall Accuracy (OA) and kappa coefficient parameters were computed. The kappa (also known as KHAT in Equation 3.3) variance is the most commonly used measure to assess the correlation between the reference and validation datasets (Fan, Weng and Wang, 2007). Its values have been categorized into three possible ranges: values greater than 0.80 (i.e., > 80%) signifies strong agreement; values between 0.40 and 0.80 (i.e., 40-80) signifies moderate agreement and values below 0.40 (i.e., <40) signifies poor agreement (Congalton and Green, 2009). The ground truth training samples (i.e., reference) were acquired from high spatial resolution data (Google earth imagery) coupled with reference data such as the National Land Cover datasets (2000 - 2014). Therefore, the sample variance of the kappa is computed using Delta method (Congalton and Green, 2009):

$$K = \frac{N\sum_{i=1}^{r} X_{ii} - \sum_{i=1}^{r} X_{i+} \times X_{+i}}{\mathrm{N}^2 - \sum_{i=1}^{r} (X_{i+} \times X_{+i})}$$

Equation 3.3

Where, r = the number of rows in the error matrix, Xii = the number of observations in row i column i(along the diagonal),$Xi+$ = is the marginal total of row i (right of the matrix), $X+i$ = the marginal total of column i (bottom of the matrix), N = the total number of observations included in the matrix., kappa value of 0.80 (i.e., >80%) signifies strong agreement; 0.40 and 0.80 (i.e., 40-80) signifies moderate agreement; below 0.40 (i.e., <40%) signifies poor agreement.

3.8. Land surface temperature (LST) retrieval from Landsat 8 TIRS bands

The single-channel algorithm (SCA) developed by Jiménez-Munoz and Sobrino (2003) was employed to retrieve LST from the ENVI pan-sharpened (15m) and geometrically corrected TIRS bands from Landsat 8 (10.6 – 11.19 µm).

3.8.1. Conversion to at-satellite brightness temperature

The thermal band's digital numbers were first calibrated to minimize the noise caused by aerosols, water vapour etc. before being converted to top-of-the-atmosphere (TOA) radiance. The following formulas are used to perform this process Equation 3.4):

For Landsat 8:

$$R = M_L * Band10_{DN} + A_L$$ Equation 3.4

Where, R is TOA radiance (watts/ (meter squared * ster * μm), M_L and A_L were also obtained from the header file of the Landsat 8 image (Survey, 2013). Thereafter, the radiance (R) images of the two Landsat sensors were converted to at-satellite brightness temperature, T_b i.e., blackbody temperature under the assumption of a uniform emissivity in Equation 3.5:

$$T_b = \frac{K_2}{\ln\left(K_1/R\right)+1}$$ Equation 3.5

Where, T_b is at-satellite brightness temperature, R is radiance while K_1 (WATTS/METER SQUARED * STER * MM) and K2 (KELVIN) are constants which are 774.89 and 1321.08 respectively. The K_1 and K_2 constant for Landsat sensors are provided in the image header file. As indicated by many authors, T_b is not the true surface temperature due to atmospheric interference and variations in land cover (Weng and Lu, 2008; Hu and Jia, 2010). In this study, the (Sobrino, Jiménez-Muñoz and Paolini, 2004) single-channel atmospheric correction method was used to remove the noise.

3.8.2. Determination of emissivity (ε)

Firstly we derived the surface emissivity (ε) which is commonly carried out by differentiation of NDVI which has an advantage when the researcher has no detailed information on derived land cover in the study area (Carlson and Ripley, 1997; Sobrino, Raissouni and Li, 2001). The Normalized Difference Vegetation Index (NDVI) was now used to estimate the Proportion of vegetation (Pv) which is to assess the role of vegetation in each pixel of the satellite images (Gutman and Ignatov, 1998). The formula in Equation 3.6 below was designed for calculating the vegetation proportion:

$$Pv = \left(\frac{NDVI - NDVI_{min}}{NDVI_{max} - NDVI_{min}}\right)^2$$ Equation 3.6

Where the $NDVI_{min}$ and $NDVI_{max}$ were the maximum and minimum values obtained from the derived vegetation index image. The emissivity was then calculated by from (Sobrino, Jiménez-Muñoz and Paolini, 2004) established formula (Equation 3.7):

$$\varepsilon = 0.004Pv + 0.986$$ Equation 3.7

Where ε is the surface emissivity image.

3.8.3. Conversion of at-satellite brightness temperature to LST

Finally, the calculated land surface emissivity for each Landsat image was used to convert the brightness temperature image to Land Surface Temperature (LST) using the Planks equation described in Equation 3.8 (Weng, Dengsheng and Jacquelyn, 2004) ;

$$LST_{(\text{KELVIN})} = \frac{T_b}{1 + (\lambda + T_b / \rho) * \ln \varepsilon}$$ Equation 3.8

To convert the LST image to Celsius image using the Equation 3.9

$$LST_{(\text{CELSIUS})} = LST_{(\text{KELVIN})} - 273.15$$ Equation 3.9

Where λ is the wavelength of radiation emitted in Landsat 5 TM (11.5µm) (Markham and Barker, 1985)(Markham and Baker, 1985) and Landsat 8 LCDM (10.8 µm) (Survey, 2013). ρ= h * c/σ, σ = Stefan Boltzmann’s constant, *h* = Plank’s constant, *C* = velocity of light, ε = surface emissivity image, LST = surface temperature image. The daytime time Landsat 8 TIR retrieved mean surface temperature imagery is shown in Figure 3.2. Also, the Landsat 8 TIRS retrieved mean surface temperature of 27.6^{O}C was compared with the ground observation mean temperature from the South African Weather Station (SAWS) for the same day which was 27.218^{O}C. Thus, the LST retrieval error was 0.38^{O}C. Therefore, the retrieved surface temperature from the Landsat 8 TIR employed for this study provided good results and can be used for further analysis.

3.9. Statistical analysis

Exploratory data analysis was further applied to understand the relationship among the above-listed rooftop explanatory features (independent variables) and satellite-derived surface temperature (dependent variable). Based on the stratified random rooftop samples (n = 116), a descriptive statistic of the dependent and independent variables was first performed. Pearson's correlation was subsequently used to examine the dependence between the multiple variables (i.e., spectral and texture variables) at the same time to generate a resultant table containing the correlation coefficients between each variable and the others i.e., (1) WV-2 spectral bands (2) among the texture measures. Afterwards, the stepwise regression method (i.e., Automated forward and backward stepwise selection using Matlab software – trial version) was used to determine the best regression model to predict the temperature (Zhao et al., 2015). The One-way analysis of variance (ANOVA) was implemented to test if there is a significant difference in retrieved daytime rooftop surface temperature based on the six rooftop colours (with stratified random sample n = 116) at a confidence level of 95%, $p<0.05$ (Adeyemi et al., 2015). The above statistical analysis was implemented using Matlab software. Finally, the methodological workflow is briefly summarized in the flowchart of Figure 1.2.

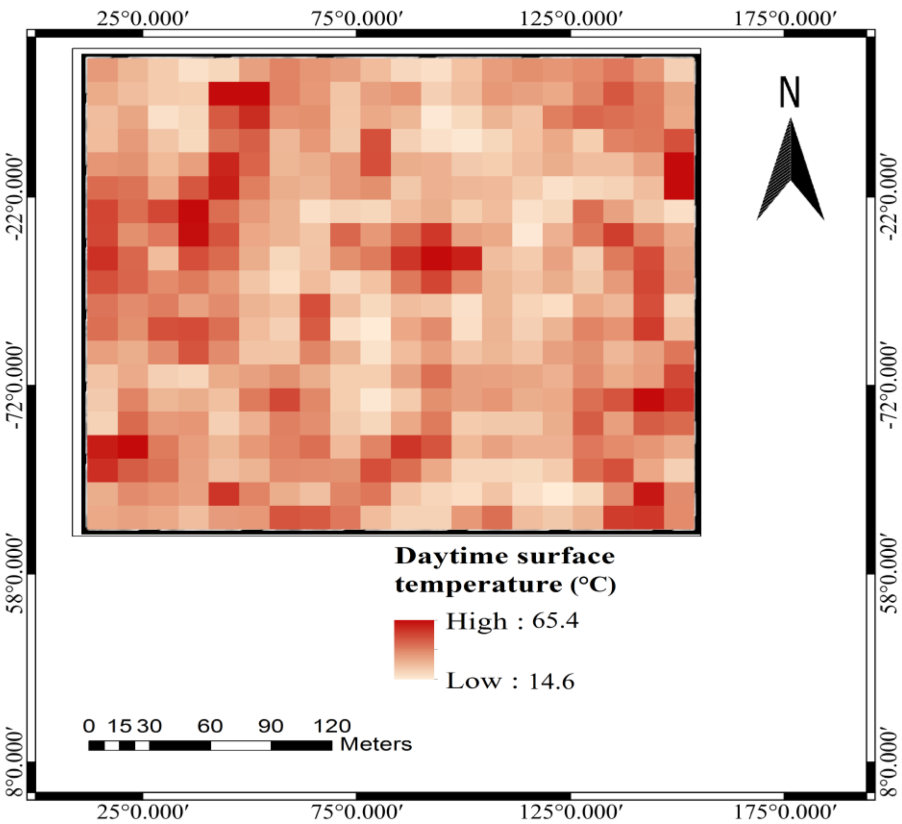

Figure 3.2 Daytime surface temperature derived from Landsat 8 TIRS (15m pan-sharpened).

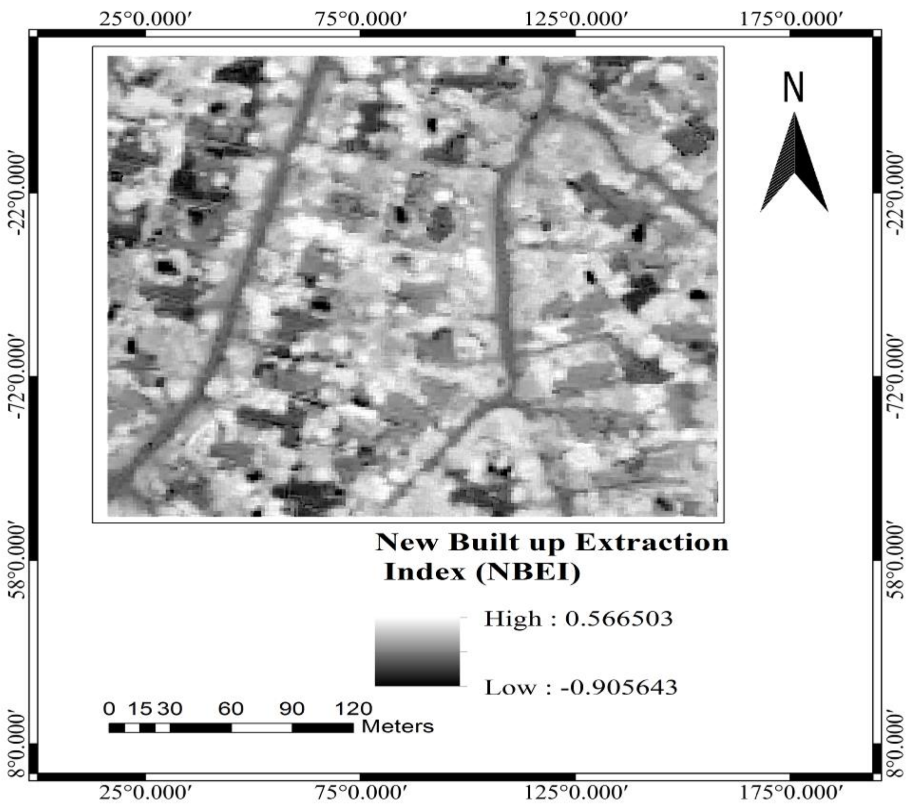

Figure 3.3 New built up extraction index (NBEI) for WV-2.

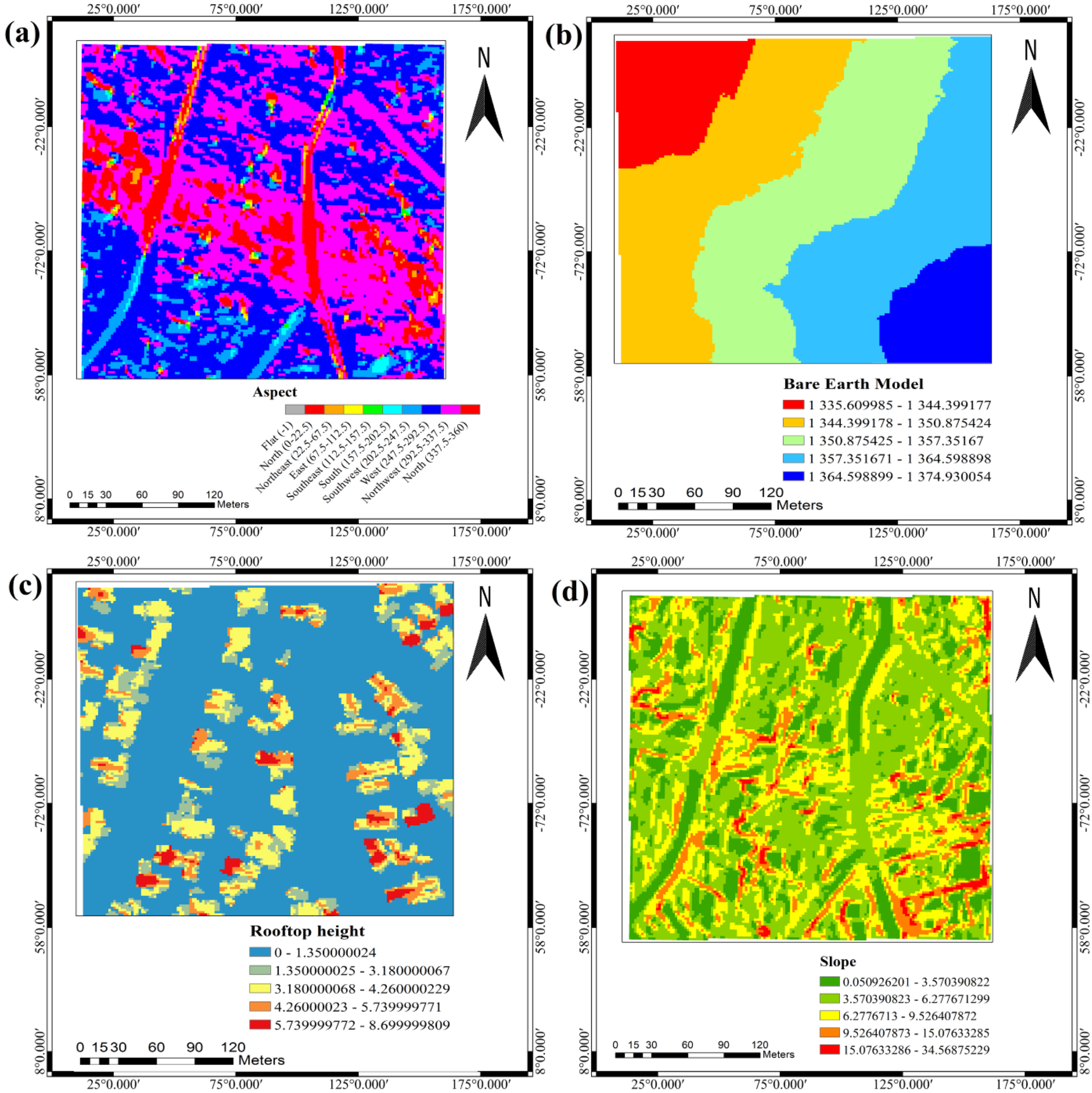

Figure 3.4 Topographic features (a) Aspect (b) Bare Earth Model BEM/DEM (c) Normalized height model, NHM (d) Slope.

3.10. Results and discussion

3.10.1. Reflectance profile for representative rooftop colours in WV-2 image

Figure 3.5 depicts the mean spectral profile for the six dominant rooftop colours observed on the WV-2 images covering the study area. As noticed in Figure 3.5, though the profile exhibits a similar reflectance pattern, the difference in peak reflectance values at the NIR1 for the identified rooftop colours samples (Figure 3.5) shows that they have different reflectivity. The white and brown rooftop exhibited the highest reflectance peak (i.e., 0.326µm and 0.305µm), followed by the red and green rooftop reflectance peak (0.286µm and 0.273µm) while the blue and dark rooftop have the lowest reflectance peak (0.171µm and 0.133µm) respectively. Therefore, the spectral signatures of white, brown, red and green rooftop have a high surface reflectivity i.e., more of the incoming solar energy is reflected to space even though they absorb at the visible region when compared with the study of Adeyemi et al., 2015). The low reflectivity of the surface can be attributed to blue and dark rooftops spectral signature because they tend to absorb more of the visible. To further know how separable and representative the rooftop colour samples are for subsequent classification, a separability test was also performed.

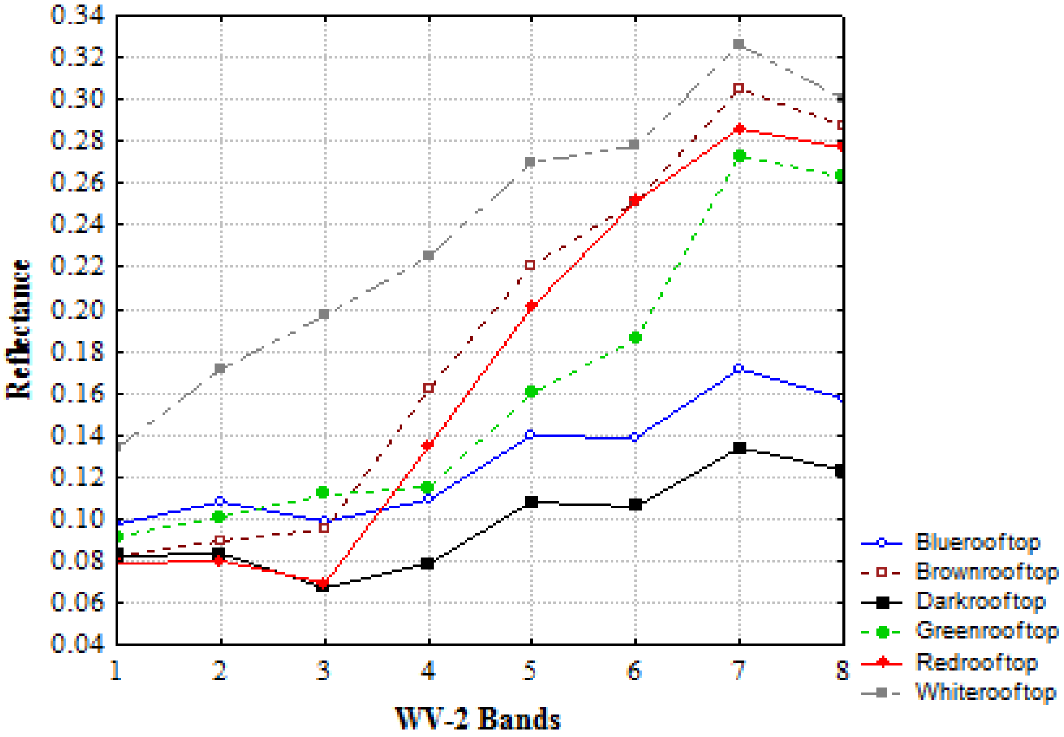

Figure 3.5 WV-2 mean spectral profiles of the actual rooftop colours extracted.

3.10.2. Separability Analysis

Table 3.5 shows the result of the spectral separability algorithms (i.e., Jeffries-Matusita distance) using ENVI software. J-M separability analysis result of the representative rooftop (n=116) colour classes in ascending order. Table 3.5 Jeffries-Matusita separability algorithm report of the representative rooftop colour classes in ascending order. The J-M distance show dependency upon the rooftop classes considered using all the WV-2 spectral bands. High J-M distance between the rooftop colours classes indicates a significant spectral separability as seen between the following groups such as Blue-Dark, Green-Red, Blue-Brown, Blue-Green, Blue-white, Red-white, Blue-Red pairs with values close to the upper bound (~ 1.866 - 1.978). Moderate separability with J-M distances of ~1.641 - 1.855 was detected for Brown-Red, Dark-white, Brown-white, Dark-Red pairs.

Table 3.5 J–M distance between the representative rooftop colours in the WV-2 spectral spaces.

Rooftop colour pair	**J-M Distance**
Green - white	1.38617024
Dark - Green	1.52418354
Brown - Green	1.55813549
Brown - Dark	1.56200107
Brown - Red	1.64132219
Dark - white	1.70556618
Brown - white	1.71307072
Dark - Red	1.85500190
Blue - Dark	1.86611820
Green - Red	1.86728293
Blue - Brown	1.91279785
Blue - Green	1.92979360
Blue - white	1.94408315
Red - white	1.94669041
Blue -Red	1.97819866

A low J-M distance value between ~1.386-1.562 indicated a possible overlap (low separability) between the rooftop colours classes such as Green-white, Dark-Green, Brown-Green, Brown-Dark pairs since the maximum value is 2.0. From the observed J-M distance values, it could be deduced that the representative rooftop colour classes accounted for a good spectral separability using the WV-2 bands. Therefore, remote detection of rooftop colours using the above colour samples in the study may not require subclasses of spectral confusion is minimal across the WV-2 bands.

3.10.3. Performance evaluation report

The performance evaluation was achieved in ENVI software was based on the set of independently derived reference polygons (ground truth ROI). The actual ROIs were used to test the semi-automated object-based classification of the rooftop colours from the WV-2 image using the KNN. The confusion matrix result presented in Table 3.6 shows that the KNN classifier exhibited the lowest CE i.e., below 5% in the Blue, Green and Red rooftops relative to the other classes.

Similarly, the KNN classifier had a CE ≤ 10% particularly in the Brown (~9%) rooftop, whereas, the highest CE was observed in white (~12%) and Dark (~17%) rooftops.

Table 3.6 Confusion matrix for rooftop colour classification on a WV-2 image using KNN (%).

Object-Based classification (KNN)										
	Actual									
	Rooftop colours	Blue	Brown	Dark	Green	Red	White	**Row Total**	**UA (%)**	**CE (%)**
Predicted	Blue	67.26	0	0	0	0	0	3.08	100	0
	Brown	0	96.69	2.39	30.95	3.95	2.53	47.13	90.94	9.06
	Dark	32.74	3.16	95.40	0	0.10	0.16	17.47	83.19	16.81
	Green	0	0	0	49.07	0	0.02	5.01	99.93	0.07
	Red	0	0.15	0	0	95.95	0	6.61	98.98	1.02
	White	0	0	2.21	19.99	0	97.29	20.64	88.49	11.51
	Column Total	100	100	100	100	100	100	100		
	PA (%)	67.26	96.69	95.40	49.07	95.95	97.29			
	OE (%)	32.74	3.31	4.60	50.93	4.05	2.71			
	Overall Accuracy	90.35								
	kappa Coefficient	0.865								

Based on the spectral separability of image objects, Green rooftop was mostly confused with Brown (~31%) and white (~20%) rooftops. Though, < 35% of blue rooftops were misclassified as dark (~33%), the confusion matrix result shows that other rooftops had <5% misclassification. The improved classification accuracy in the confusion matrix described above for the KNN classifier can be attributed to the fact that the object-based classification is conducted on image objects (multi-pixel segments) rather than on individual pixel. Therefore, the chances of misclassification are minimized since the image objects used to share similar spectral characteristics. Overall results shows, the object-based classification (KNN) based on the rooftop colours presented in Figure 3.6 produced an overall accuracy of ~90.4% and a kappa coefficient of ~0.87 respectively on the WV-2 image.

3.10.4. Descriptive statistics

Table 3.7 reports descriptive statistics of selected dependent and independent variables generated from WEKA. The dependent variable was the rooftop surface temperature (LST) derived from the pan-sharpened (15m X 15m pixels) Landsat 8 TIRS sensor on daytime time with a standard deviation of 6.54^{O}C. Also, the independent variables were rooftop configuration variables, which are grouped into spectral reflectance (WV-2 bands), spectral index (NBEI), texture (second-order co-occurrence measures) and topography (slope, height, aspect, elevation). Correspondingly, spectral reflectance, spectral index, and texture measures all have low standard deviations. These low standard deviation values illustrate the similarity of rooftops in this residential neighbourhood. Although the topographical variables such as elevation (DEM/BEM), slope, height (NHM) all have a low standard deviation, aspect indicates a higher standard deviation which signifies that the positioning or directions of these rooftops are not the same.

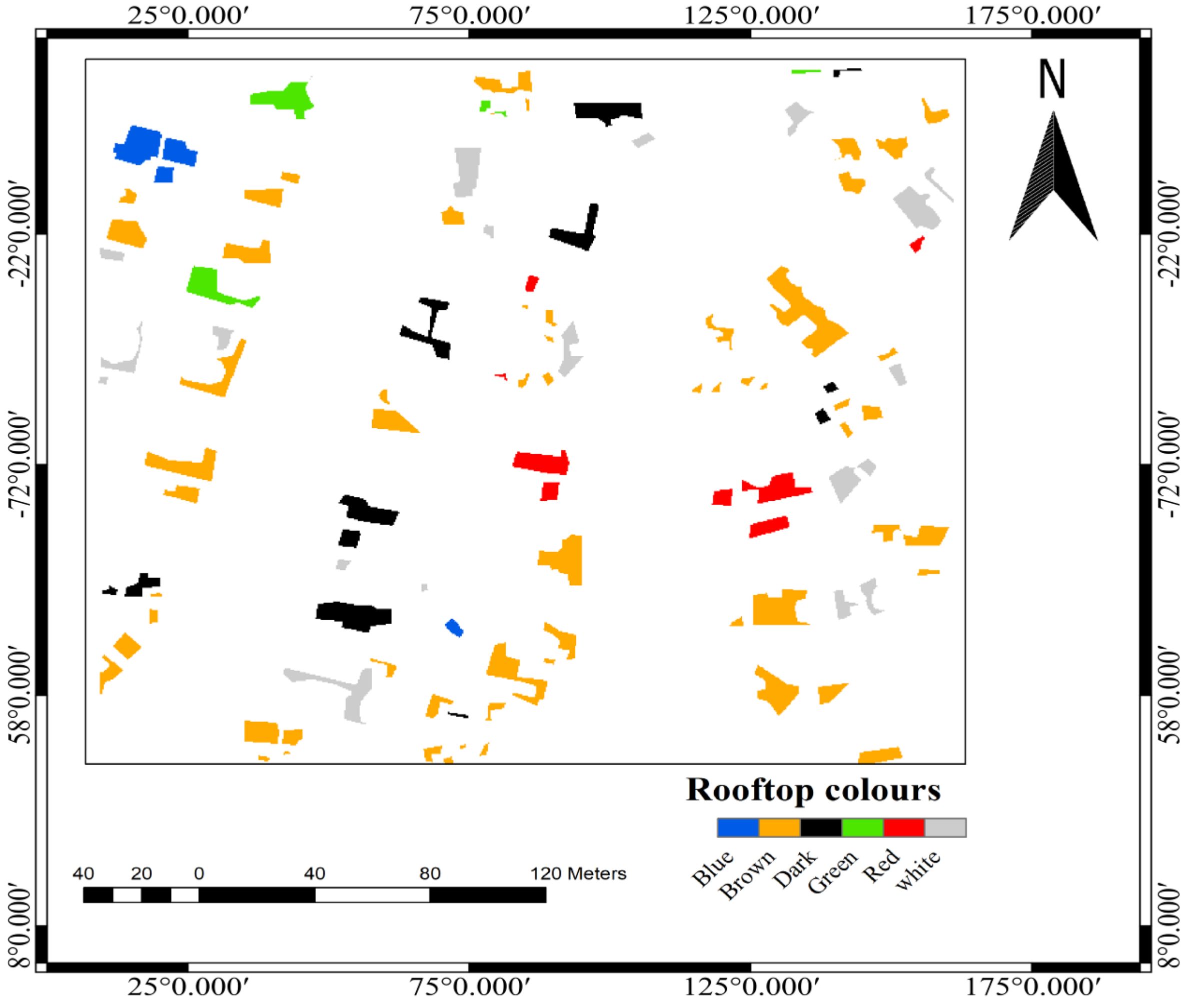

Figure 3.6 Object-based classification result for exposed rooftop colours using K Nearest Neighbour (KNN) algorithm.

Table 3.7 Descriptive statistics of the rooftops selected dependent variable and independent variables (n=114rooftop samples).

Features(Daytime analysis)	**Minimum**	**Maximum**	**Mean**	**Standard deviation**
LST (Degree Celsius)	15.82	64.01	25.58	6.54
Coastal Blue reflectance	0.061	0.115	0.092	0.018
Blue reflectance	0.058	0.222	0.102	0.028
Green reflectance	0.050	0.295	0.103	0.037
Yellow reflectance	0.053	0.336	0.146	0.047
Red reflectance	0.080	0.400	0.190	0.056
Red edge reflectance	0.08	0.430	0.216	0.070
NIR1 reflectance	0.095	0.63	0.267	0.089
NIR2 reflectance	0.082	0.622	0.256	0.091
NBEI	0.024	0.484	0.233	0.081
Contrast	0	30.667	1.127	3.068
Correlation	-0.750	1	0.517	0.409
Dissimilarity	0	4.889	0.559	0.632
Entropy	0	2.197	1.030	0.592
Homogeneity	0.162	1	0.767	0.187
Mean	0.667	19.670	6.880	3.062
Second Moment	0.111	1	0.465	0.270
Variance	0	16.321	0.607	1.723
Aspect	2.582	359.14	268.37	69.26
DEM	1337.95	1370.64	1353.76	7.172
Normalized Height Model (NHM)	0	7.750	3.737	1.251
Slope	0.661	12.539	4.960	2.442

Pearson's correlation among eight reflectance bands from WV-2 is shown in Table 3.8. With few variables having low correlation between (0.16 – 0.44) while many have a high correlation (≥ 0.51). This indicates that there is a more high correlation among all reflectance variables. Therefore, either of the eight WV-2 reflectance was entered into a regression model at any one time. Furthermore, Table 3.9 shows the correlation among the second-order co-occurrence texture measures. Although, both high and low, positive and negative correlation was observed among the texture measures, in this study we considered the texture measure that only indicates low positive and low negative correlation with other variables. In this case, the GLCM mean and correlation features were the only texture measure that satisfies this benchmark.

Since each model has the same parameters, we can compare these results and decide which WV-2 spectral bands contribute most to understanding rooftop surface temperature. From the R-square adjusted value (p-value < 0.05) in Table 3.10, Green reflectance represent good spectral parameters that explain variations in rooftop surface temperature. Detailed regression analysis results by using Green reflectance band as spectral information will be discussed next.

Table 3.8 Pearson correlation of WV-2 reflectance bands.

		CB	**B**	**G**	**Y**	**R**	**RE**	**NIR1**	**NIR2**
CB		1							
B		0.97	1						
G		0.87	0.94	1					
Y		0.51	0.57	0.76	1				
R		0.35	0.44	0.66	0.96	1			
RE		0.17	0.23	0.46	0.86	0.90	1		
NIR1		0.17	0.21	0.42	0.72	0.77	0.93	1	
NIR2		0.16	0.18	0.36	0.63	0.67	0.86	0.97	1

Table 3.9 Pearson correlation of texture measures.

	Contrast	**Correlation**	**Dissimilarity**	**Entropy**	**Homogeneity**	**Mean**	**Second moment**	**Variance**
Contrast	1							
Correlation	-0.04	1						
Dissimilarity	0.89	-0.14	1					
Entropy	0.43	-0.32	0.69	1				
Homogeneity	-0.64	0.25	-0.91	-0.83	1			
Mean	0.31	-0.14	0.33	0.19	-0.28	1		
Second moment	-0.34	0.39	-0.61	-0.97	0.78	-0.13	1	
Variance	0.93	0.07	0.82	0.44	-0.58	0.25	-0.35	1

Table 3.10 Regression Comparison.

	CB	**B**	**G**	**Y**	**R**	**RE**	**NIR1**	**NIR2**
R^2 (%)	28.3	27.6	29.7	17.3	28.8	27.3	21.8	23.7
R^2 (Adj) (%)	19	19.8	22.1	13.5	17.1	17.8	16.6	16.3

All the p-value < 0.05.

3.10.5. Regression Analysis Results for the Daytime Rooftop Temperature

Table 3.11 Stepwise regression models.

Model Summary				
df	**R^2**	**R^2(Adj)**	**p-value**	**RMSE**
102	29.7%	22.1%	9.87e-05	5.78
Coefficients				
Variables	**Estimates**	**SE Coefficient**	**t-Statistic**	**p-value**
Correlation	-29.87	11.62	-2.57	0.011
Mean	1.87	0.62	2.99	0.003
NHM	6.89	2.63	2.62	0.010
Green*Correlation	242.22	83.71	3.38	0.001
Green*NHM	-50.71	16.30	-3.11	0.002
NBEI*NHM	-18.22	6.74	-2.70	0.008
Correlation*Mean	-3.36	0.88	-3.83	0.000
Correlation*NHM	3.19	1.35	2.36	0.020
95% statistically significant				

The stepwise regression employed minimizes within-class variance while maximizing the between-class variance at 5% significance level (Montgomery, Peck and Vining, 2012). In this case, the dependence of some of the covariates on each other and how it affects the model was observed i.e., the combination of backward elimination (starting with all candidate variables and deleting all non-significant variables by testing them one by one) and forward selection (all variables are tested one by one if their contribution is significant after a new variable has been added). Table 3.11 reports on stepwise regression models based on different WV-2 spectral bands coupled with the relevant texture measures (i.e., GLCM mean and correlation), proposed spectral index (NBEI) and topographic features (slope, height/NHM, aspect, and elevation/BEM/DEM).

Regression equation:

LST = -29.87Correlation +1.87Mean + 6.89NHM + 242.22Green*Correlation – 50.71Green*NHM – 18.22NBEI*NHM – 3.36Correlation*Mean + 3.19Correlation *NHM

Table 3.11 describes the automated stepwise regression analysis results between the variables (mean daytime rooftop surface temperature, LST) and independent variables or explanatory features such as *Green reflectance* from the WV-2 image, *NBEI*, *GLCM Mean*, *GLCM Correlation* coupled with topography. By using all of these selected variables in the detailed stepwise regression analysis, we successfully explain 22.10% of the daytime rooftop temperature. In daytime temperature analysis, the *Green* reflectance from WV-2 imagery coupled with the *normalised height model* (*NHM*) of each building negatively and strongly contributes to the daytime rooftop surface temperature i.e., in this study the reflectance interactions with a height of rooftops result in low daytime temperature. For rooftop texture measures, correlation negatively contributes to the rooftop surface temperature but mean positively contributes to the rooftop surface temperature. Also, the self-developed *New built up extraction index* (*NBEI*) interaction with *NHM* negatively contribute to the daytime rooftop surface temperature.

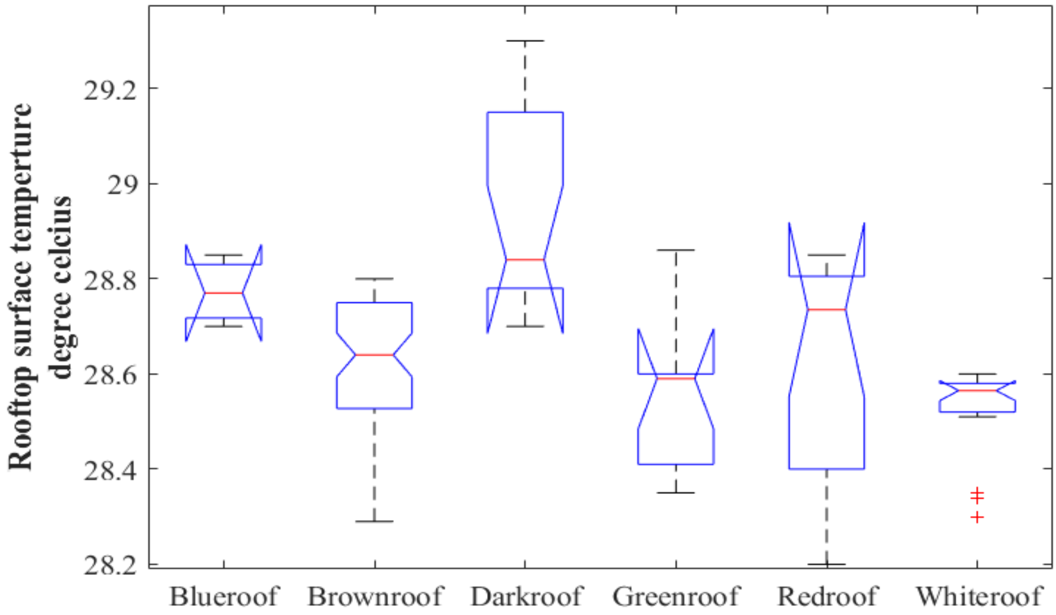

Figure 3.7 Boxplot of rooftop surface temperature variability based on colours.

3.10.6. Effects of rooftop colours on LST

Spatial distribution between mean daytime surface temperature and the residential rooftop colours were analysed to investigate their degree of correspondence. Based on the stratified random samples (n=116), the mean LST of each rooftop colours were summarized using boxplots analysis (Figure 3.7). Rooftop colour types such as dark and blue roof tend to have higher surface temperatures ranging from 28.7^{O}C – 29.3 ^{O}C and 28.7^{O}C – 28.85^{O}C followed by green, red and brown roof with temperature values ranging from 28.35^{O}C – 28.86^{O}C, 28.2 ^{O}C – 28.85^{O}C, 27.8^{O}C – 28.8^{O}C. A similar pattern appears for white roof where the temperature values are lower i.e., 28.16^{O}C – 28.60^{O}C. Meanwhile, the dark roof shows the highest value (i.e., 28.84 ^{O}C) among the rooftop colours during the daytime. The result also showed that some rooftop colours have a homogenous surface temperature (e.g., white roof) while some have a heterogeneous temperature such as blue roof i.e., depending on the size of the rooftop whether the pixel is boundary pixel. Based on these findings, it can be said that these rooftop types of the urban residential environment impact the daytime surface temperature differently not only due to the surface material but also surface reflectivity and emissivity of the rooftop colours.

Table 3.12 Analysis of Variance of rooftop surface temperature variability based on colour.

Source	**SS**	**Df**	**MS**	**F**	**Prob>F**
Groups	1.05197	5	0.37039	9.77	1.01159e-07
Error	4.09469	108	0.03791		
Total	5.94666	113			

At 95% significant level (α =0.05)

Furthermore, the analysis of variance was conducted to see how statistically significant the influence of each rooftop colour was on the mean daytime surface temperature pattern. The hypothesis for this analysis is that at 95% confidence interval, H_o: Null hypothesis specifies there is no significant difference in the LST values of these rooftops based on colour, while the H_1: Alternative hypothesis indicates there is a difference in their LST values. To test the hypothesis that the rooftop colour type has a significant effect on the LST value, a one way ANOVA was performed. From the result in Table 3.12, the small p-value of about 1.01159e-07 indicates that the rooftop means surface temperatures are not the same. Since the p-value is < 0.05 (p-value =1.01159e-07) when comparing mean LST values of these rooftops mean surface temperatures, we reject Ho null hypothesis and accept H1 the alternative hypothesis (i.e., blue roof ≠ brown roof≠ dark roof ≠ green roof ≠ red roof ≠ white roof). Also, this implies that there is a significant difference between the rooftop colours spectrally derived from WV-2 image using the supervised semi-automated feature extraction or object-based classification.

3.11. Discussion

The urban expansion experienced across Pretoria over the years is observed as a sign of growth and prosperity but has continuously brought about expanded infrastructure that makes use of more rooftop impervious surfaces (Adeyemi, Botai, and Ramoelo, 2015). An increase in rooftop which is the major ISA in the urban residential environment according to Zhao et al. (2015) has brought about a series of adverse impacts on the environment of which surface temperature variation resulting in urban heat islands is one of the major effects. In this study, we focused on assessing the impact of rooftop impervious surface based different colours on surface temperature variability in a residential area Lynnwood Ridge in Pretoria, Gauteng Province, South Africa. We first analysed the factors (i.e. explanatory variables such as texture measures, topography) that influence both daytime rooftop surface temperatures to understand this relationship at a comprehensive level.

From the processed satellite images, the result clearly shows that the interaction between the applicable rooftop explanatory features (i.e., reflectance, texture features and topographical properties) can explain over 22.10% of the variation in daytime rooftop surface temperatures (Table 3.11). This adjusted R^2 value with these significant explanatory variables suggests that most of the rooftops exhibited fewer heat retentions as observed in the daytime temperature variations. In addition, the low feature explainability can be attributed to the study of Zhao *et al.* (2015) that asserted that the main challenge in using remotely sensed data for structure-based analysis (e.g., rooftop size) is that most freely available thermal imagery (e.g., ASTER and Landsat imagery) fail to offer fine-resolution spatial details at the structure level.

Furthermore, analysis of spatial distribution between mean daytime surface temperature and the residential rooftop indicated that dark and blue roof surface exhibited a high LST value (i.e., 28.84^{O}C and 28.78^{O}C) due to the low reflectivity, low emissivity and high heat capacity while the red, brown and green roof surface show lower LST values (i.e., 28.77^{O}C, 28.65^{O}C and 28.58^{O}C) due to high reflectivity, high emissivity and low heat capacity during the daytime (Figure 3.7). Similarly, our findings partly confirm what has already been highlighted in the few previous studies (Myint et al., 2013; Zheng, Myint and Fan, 2014; Zhao et al., 2015; Morabito et al., 2016) to mention a few that have dealt with similar issues but not in the African context. Based on the findings of this experimental study we propose that remotely sensed imagery and processing can be used potentially to evaluate the contribution of residential rooftop properties (i.e., colour) in understanding urban heat island in South Africa. Future research should focus on obtaining other related rooftop ancillary features by fieldwork or survey and use of fine resolution surface temperature from thermal infrared images such as MASTER (7m MODIS/ASTER airborne simulator) (Zhao and Wentz, 2016)for a better understanding of microclimate patterns at the urban level to provide sustainable approaches to ameliorate urban heat island effect.

3.12. Conclusion

This study investigates the relationship between rooftop surface temperature, rooftop reflectance, texture measures and topographical properties based on rooftop colours in an urban residential environment. Very high-resolution (VHR) multispectral imagery (WorldView-2) enables detailed analysis of urban residential rooftop spectral characteristics and texture measures while the medium resolution multispectral imagery (Landsat 8 TIR) facilitates the retrieved rooftop surface temperature. Also, the LiDAR point clouds make it possible to obtain rooftop topographical properties such as rooftop aspect, slope, building height and elevation when integrated into the statistical regression analysis. The results of the regression analysis explained around 22.10% of the daytime rooftop temperature. The interaction between the rooftop spectral properties and normalized height for the buildings were the major factors influencing rooftop surface temperatures. Further statistical analysis also revealed a clear, statistically significant difference in emissivity and heat capacity rooftops with different colour during the daytime. Even though, our study confirms the dominance of some installed rooftop colours with high reflectivity, high emissivity and low heat capacity (i.e., red, brown and green roof) visually the presence of urban residential tree canopy also might have contributed to heat mitigation as pointed out in previous studies of (Rinner and Hussain, 2011; Susca, Gaffin and Dell'Osso, 2011; Ng et al., 2012; Doick, Peace and Hutchings, 2014; Zhao et al., 2015) to mention a few. Finally, findings from this study are not generalizable and are only valid for formal residential areas i.e., with similar climate, socio-economic activities and urban characteristics (e.g., rooftop properties) and comparable imperviousness densities. Therefore, this experimental research provides relevant information and methodology that will not only helps to understand the impact of rooftop properties (e.g., colour) on surface temperature but also encourage sustainable rooftop designs to mitigate urban heat island effects in residential environment.

Chapter 4 Spatio-temporal analysis of built-up impervious surface area and interplay with land surface temperature in Pretoria, South Africa.

Satellite level (medium resolution)

Adeniyi Adeyemi, Abel Ramoelo, Moses Cho, Jacobus Strydom (2021) - Spatio-temporal analysis of built-up impervious surface area and interplay with land surface temperature in Pretoria, South Africa., Geocarto International, (13 September 2021), https://doi.org/10.1080/10106049.2021.1980617

Abstract

Evaluating changes in built-up impervious surface area (ISA) to understand the urban heat island (UHI) extent is valuable for governments in major cities in developing countries experiencing rapid urbanization and industrialization. This work aims at assessing built-up ISA spatio-temporal and influence on land surface temperature (LST) variability in the context of urban sprawl. Landsat-5 Thematic Mapper (TM) and Landsat-8 OLI (Operational Land Imager) and TIRS (Thermal Infrared Sensor) were used to quantify ISA using built-up Index (BUI) and spatio-temporal dynamics from 1993-2013. Thereafter using a suitable analytical sampling scale that represents the estimated ISA-LST, we examined its distribution in relation to elevation using the Shuttle Radar Topography Mission (SRTM) and also create Getis-Ord Gi* statistics hotspot maps to display the UHI extent. The BUI ISA extraction results show a high predictive accuracy with area under the receiver operating characteristic curve, AUROC = 0.8487 for 1993, AUROC = 0.8302 for 2003, AUROC = 0.8790 for 2013. The ISA spatio-temporal changes within ten years interval time frame results revealed a 14% total growth rate during the study year. Based on a suitable analytical scale (90x90) for the hexagon polygon grid, the majority of ISA distribution across the years was at an elevation range of between >1200m – 1600m. Also, Getis-Ord Gi* statistics hotspot maps revealed that hotspot regions expanded through time with a total growth rate of 19% and coldspot regions decreased by 3%. Our findings can represent useful information for policymakers by providing a scientific basis for sustainable urban planning and management.

4.1. Introduction

Growth is sometimes reflected by an expansion of urban sprawl and the spontaneous appearance of urban buildings in rural areas or on the peripheries of cities (Bouzekri et al. 2015). These rapid urban landscape changes as indicated by Odindi et al. (2012) have been because of the exceptional increase in population concentration in cities. According to Demographia (2017) and Sahana et al. (2018) 53% of the global population lives in urban settlements and by 2030 this number is expected to have increased more than 60%. Developing countries are more likely to experience the highest rate of urbanization and industrialization in the near future i.e., conversion of vegetation areas to impervious surface materials (Sahana et al. 2018). Over the last decades, Pretoria, South Africa has been facing major land use or cover changes, such as loss of natural land, i.e. forest or plantations, agricultural lands and grasslands coupled with growing ISA such as roads, sidewalks, parking lots, rooftops and bare lands due to a continuous increase in the population (Schoeman et al. 2013; Adeyemi et al. 2015). Though the loss of vegetation (i.e., ISA increase) may have increased surface temperature due to change in surface component distinctive radiative, thermal, moisture and aerodynamic properties (Owen et al. 1998), there is still limited spatially explicit information on how ISA surface temperature is affecting the city (e.g., urban heat island extent).

With the development of satellite thermal infrared remote sensing data, considerable LST measurements can be retrieved (Nie and Xu 2015). Consequently, there have been several algorithms and methods used for LST retrieval from remote sensing data. Qin et al.(2001) in an earlier study developed the split window and mono window algorithm and demonstrated their effectiveness of using Landsat data. Jiménez-Munoz and Sobrino (2003) and Jiménez-Muñoz and Sobrino (2010) also developed the single-channel algorithm for LST retrieval from Landsat and ASTER data respectively. In this study, the single-channel algorithm was employed due to its advantage of been used when the ground truth data is not available (Alipour et al. 2011). Oke (1982) in an earlier study revealed that latent heat exchange was observed in vegetation areas while impervious surface and low vegetated areas exhibited sensible heat exchange. Since then, much emphasis was first placed on using the normalized difference vegetation index (NDVI) as the major land cover indicator of urban microclimate (Gallo et al. 1993; Lo et al. 1997; Owen et al. 1998). Nevertheless, successive studies have indicated the subjectiveness of NDVI (vegetation) seasonal variations (Zhang et al. 2009) and the presence of bare soil which displays a wider variation in surface radiant temperature due to soil moisture variations, land surface emissivity, albedo (Carlson and Traci Arthur 2000; Chen et al. 2006; Huang et al. 2008; Jiang and Tian 2010). This inconsistency suggests that NDVI alone may not be a sufficient metric to quantify surface urban heat island (Yuan and Bauer 2007).

The degree of urbanization has been measured by an increase of ISA (Civco et al. 2002; Yang et al. 2003; Bauer et al. 2004). With increasing environmental concerns, examining the relationship between the ISA and LST provided an alternative for studies of urban expansion and related urban heat island (UHI) phenomena. In previous studies, Yuan and Bauer (2007) found that a strong positive linear relationship exists between LST and %ISA for different study seasons. Likewise, a strong positive correlation of LST with normalized difference built-up index (NDBI) suggested that the index ISA can quantitatively describe the spatial distribution and temporal variation of urban thermal patterns (Zhang et al. 2009). Although many recent studies in developed nations have examined urban imperviousness effects on LST (e.g., Nie and Xu 2015; Henits et al. 2017; Morabito et al. 2018; Wei and Blaschke 2018 etc.), very few studies have looked into how the expansion of urban built-up ISA in major cities in Africa have intensified UHI (Kamdoum et al. 2014; Adeyemi et al. 2015; Dissanayake et al. 2019 etc.). Since built-up impervious surface areas are more stable and less affected by seasonal changes, it may provide a complementary metric for spatio-temporal analysis of land surface temperature variability and pattern in major cities in developing countries (e.g., South Africa). Therefore, the aim of this study is to assess built-up ISA spatio-temporal distribution and influence on LST variability using a optimal spatial analytical scale across Pretoria, Gauteng Province, South Africa (Figure 1.5). The key research questions are:

1. Can the built-up Index (BUI) reveal the spatio-temporal changes of ISA within ten years interval time frame?
2. With a suitable analytical scale, is it possible to describe the distribution of ISA-LST in relation to elevation?
3. Could the Getis-Ord Gi* statistics hotspot maps display the UHI extent based on the distribution of estimated ISA-LST?

4.2. Materials and Methods

4.2.1. Data Collection and Pre-processing

Remote sensing data used in this research was mainly from the Landsat 5-TM (Thematic Mapper) recorded on 19th September 1993 at 07:24 h local time, 18th November 2003 at 07:40 h local time and Landsat-8 OLI (Operational Land Imager) and TIRS (Thermal Infrared Sensor) on 13th November 2013 at 08:04 h local time (Path: 170, Row: 78)

Table 4.1). The Landsat images were pre-processed using two important steps: (1) converting digital numbers (DNs) to top-of-atmosphere (TOA) radiance and then to TOA reflectance; and (2) conversion of the TOA reflectance to surface reflectance using the Fast Line-of-sight Atmospheric Analysis of Hypercubes (FLAASH) in ENVI software (Liang et al. 2003; Krause 2005; Environment for Visualizing Images, 2014). The digital elevation model (DEM) data came from the Shuttle Radar Topography Mission (SRTM) for September 2014. It was employed to obtain the elevation pixels for this study area due to its unique combination of worldwide coverage and void-filled high spatial resolution (30m). The above image data were acquired from the United States Geological Survey Global Visualization Viewer (https://glovis.usgs.gov) and reprojected to the UTM Zone 35S projection system with WGS84 datum. Also, ancillary data such as the Department of Forestry, Fisheries and the Environment (DFFE), South Africa (https://www.environment.gov.za) subcontracted National Land Cover (NLC) classification dataset of 2013-2014 (https://egis.environment.gov.za/sa_national_land_cover_datasets) completed in 2015; Pretoria administrative shapefile boundary source from Statistics South Africa 2011 (http://www.statssa.gov.za); 1:10,000 aerial photography 0.5m (2012-2015) from the Chief Directorate National Geo-spatial Information (CDNGI) (http://www.cdngiportal.co.za), together with Google Earth Images were also used. Software used for desktop analysis include: ESRI (ArcGIS), QGIS (v3.8.0), Microsoft office and R statistical software environment (RStudio, Inc., Boston, MA, USA, Version 1.1.463).

Table 4.1 Summary of data used in research.

Data Types		Datasets	
	Date	**Image type**	**Path/Row**
	1993-09-19	Landsat 5-TM	170/78
Remote Sensing data	2003-11-18	Landsat 5-TM	170/78
	2013-11-13	Landsat-8 OLI/TIRS	170/78
DEM data	2014-09-25	Shuttle Radar Topography Mission (SRTM) with 30m spatial resolution	
Boundary file	2011	Pretoria Administrative boundary shape data	
Ancillary data	2012-2015	1:10,000 aerial photography from 2012-2015 with spatial resolution of 0.5m and	
	2015	Google Earth Images	
	2015	NLC classification dataset of 2013-2014	

4.3. Methodology

The methodological workflow is briefly summarized in the flowchart of Figure 1.3.

4.3.1. Spectral index derived impervious surface area

The ISA was retrieved using the Kaimaris and Patia, (2016) built up index (BUI) using *Red* bands, *SWIR1* and *SWIR2* of the Landsat imagery. Their combination leads to a new optimal construction index. They indicated that the manual thresholding of the built up index (BUI), the focus is on the last finding which happens to be built up areas i.e. in values ranging around 0.0, isolating the irrelevant information for green vegetation, bare soil and water to high positive or negative values. Although this spectral index may not follow the logical boundary of the built-up or ISA area values adopted in indexes that have been developed in the past for multispectral images (Jayamanna, Kawamura and Tsujiko, 1996; Zha, Ni and Yang, 2003; Xu, 2007, 2008; As-syakur *et al.*, 2012 etc.), but allows for the best distinction of ISA. The new index, BUI, is calculated according to the formula in Equation 4.1:

$$BUI = \frac{2*[(\mathrm{Red}*SWIR2)-(\mathrm{SWIR1}*\mathrm{SWIR1})]}{[(\mathrm{Red}+\mathrm{SWIR1})*(\mathrm{SWIR1}+\mathrm{SWIR2})]} \qquad \text{Equation4.1}$$

4.3.2. Performance evaluation of spectral indices

In this study, the accuracy of the built up spectral index (BUI) for the three years was assessed based on well distributed ancillary samples (n=200) obtained from reference datasets (e.g., aerial photo and Google Earth images) to validate each derived thematic output. Based on 10-fold cross-validation (Danjuma, 2015; Adeyemi *et al.*, 2021a), we implemented the accuracy assessment of BUI by computing area under the receiver operating characteristic curve (AUROC) using Information Value package in the R statistical software environment (RStudio; Prabhakaran, 2016). The AUROC is a graph that summarizes the performance of the spectral index (classifier) over all possible thresholds. It is generated by plotting the true positive rate or sensitivity (y-axis) against the false positive rate or specificity (x-axis). Wieland and Pittore (2014) further explained that the true positive rate is the proportion of actual positives that are classified as positives, while true negative rate, is the proportion of actual negatives, which are classified as negatives. It measured how the indices BUI performed in identifying impervious surfaces or built-up areas in this research.

4.3.3. Land Surface Temperature (LST) Retrieval

The single-channel algorithm (SCA) developed by Jiménez-Munoz and Sobrino (2003) was employed to retrieve LST from the geometrically corrected TIR band 6 from Landsat 5-TM (10.44 - 12.42µm) and mean of band 10 and 11 from Landsat-8 TIRS (10.6 – 11.19 µm) and (11.50–12.51 µm) respectively.

4.3.3.1. Conversion to at-satellite Brightness Temperature (Tb)

The thermal band's digital numbers were first calibrated to minimize the noise caused by aerosols, water vapour etc. before being converted to top-of-the-atmosphere (TOA) radiance. The following formulas are used to perform this process (Equation 4.2):

For Landsat 5TM:

$$R = \left(\frac{L_{\max} - L_{\min}}{Q_{cal\max} - Q_{cal\min}} \right) \left(Band6_{DN} - Q_{cal\min} \right) + L_{\min}$$

Equation 4.2

Where R is TOA radiance (watts/ (meter squared * ster * µm), Q_{calmax} = 255, Q_{calmin} = 0 while L_{max} and L_{min} can be obtained from the header file of the Landsat 5TM imagery (Markham and Barker, 1985) in Equation 4.3:

For Landsat 8:

$$R = M_L * Band10_{DN} + A_L$$ Equation 4.3

Where R is TOA radiance (watts/ (meter squared * ster * µm), M_L and A_L were also obtained from the header file of the Landsat 8 image (United States Geological Survey, 2013). Thereafter, the radiance (R) images of the two Landsat sensors were converted to at-satellite brightness temperature, T_b i.e., blackbody temperature under the assumption of a uniform emissivity in Equation 4.4:

$$T_b = \frac{K_2}{\ln\left(K_1 / R\right) + 1}$$ Equation 4.4

Where T_b is at-satellite brightness temperature or black body temperature, R is radiance while K_1 (WATTS/METER SQUARED * STER * MM) and K_2 (KELVIN) are constants which are 774.89 and 1321.08 respectively. The K_1 and K_2 constant for Landsat sensors are provided in the image header file. As indicated by many authors, T_b is not the true surface temperature due to atmospheric interference and variations in land cover (Weng and Lu, 2008; Hu and Jia, 2010). In this study, the (Sobrino, Jiménez-Muñoz and Paolini, 2004) single-channel atmospheric correction method was used to remove the noise.

4.3.3.2. Determination of surface emissivity (ε)

Firstly we derived the surface emissivity (*ε*) which is commonly carried out by differentiation of NDVI which has an advantage when the researcher has no detailed information on derived land cover in the study area (Carlson and Ripley, 1997). Surface emissivity (ε) varies with land covers on ground surfaces (Sun *et al.*, 2017). In urban environments, vegetated surfaces have stronger thermal holding capacity and higher cooling effects than non-vegetated areas. The Normalized Difference Vegetation Index (NDVI) was now used to estimate the Proportion of vegetation (P_v) which is to assess the role of vegetation in each pixel of the satellite images (Gutman and Ignatov, 1998). The formula below was designed for calculating the NDVI and vegetation proportion (Equation 4.5 and Equation 4.6):

$$NDVI = \frac{NIR - \mathrm{Red}}{NIR + \mathrm{Red}}$$ Equation 4.5

$$Pv = \left(\frac{NDVI - NDVI_{min}}{NDVI_{max} - NDVI_{min}} \right)^2$$ Equation 4.6

Where the $NDVI_{min}$ and $NDVI_{max}$ were the maximum and minimum values obtained from the derived vegetation index image. (Sobrino *et al.*, 2008) measured the relationships between ε and proportion of vegetation (P_v) on a variety of ground surfaces based on the Landsat-extracted NDVI, at each 30m pixel with formula established according to (Sobrino, Jiménez-Muñoz and Paolini, 2004) in Equation 4.7:

$$\varepsilon = \begin{cases} 0.979 - 0.035\mathrm{Red} & NDVI < NDVI_{min} \\ 0.986 + 0.004P_v & NDVI_{min} \leq NDVI \leq NDVI_{max} \\ 0.99 & NDVI > NDVI_{max} \end{cases}$$ Equation 4.7

Where ε is the surface emissivity image and *Red* is the surface reflectance of the Red band.

4.3.3.3. Conversion of at-satellite brightness temperature to LST

Finally, the calculated land surface emissivity for each Landsat images was used to convert the brightness temperature image to Land Surface Temperature (LST) using the Planks equation described in Equation 4.8 (Weng, Dengsheng and Jacquelyn, 2004) ;

$$LST_{(\mathrm{KELVIN})} = \frac{T_b}{1 + (\lambda + T_b / \rho) * \ln \varepsilon}$$ Equation 4.8

To convert the LST image to Celsius image using the Equation 4.9:

$$LST_{(\mathrm{CELSIUS})} = LST_{(\mathrm{KELVIN})} - 273.15$$ Equation 4.9

Where λ is the wavelength of radiation emitted in Landsat 5 TM (11.5µm) (Markham and Barker, 1985) and Landsat 8 LCDM (10.8 µm) (United States Geological Survey, 2013). ρ= h * c/σ, σ = Stefan Boltzmann's constant, *h* = Plank's constant, *C* = velocity of light, ε = surface emissivity image, *LST* = surface temperature image. The rescaled to 30m spatial resolution daytime time retrieved surface temperature (LST) images were also normalized.

4.3.4. LST Level Distribution

Recent studies have pointed out that if thermal data were not recorded on the same date each year, a normalization method should be used to reclassify the LST results (Tang and Xu, 2010; Zhang *et al.*, 2017; Wei and Blaschke, 2018). Hence, the retrieved LST from the Landsat images thermal bands for the three years were normalized between maximum and minimum values to be able to conduct a comparative analysis (Amiri *et al.*, 2009; Song and Wu, 2016). The formula in Equation 4.10 for the Normalization of retrieved LST was expressed as:

$$N_{LST\,(Celsius)} = \frac{LST_{(Celsius)} - LST_{(Celsius)\ \min}}{LST_{(Celsius)\ \max} - LST_{(Celsius)\ \min}}$$

Equation 4.10

Where LST_i is the LST of the pixel for a particular image, LST_{max} is the maximum value of LST, LST_{min} is the minimum value of LST of the same image as that of the LST_i. Furthermore, based on stratified random samples (n=200) on land cover types generated on reference data (e.g., aerial photo and Google earth engine), we verified the overall metrics error for the normalized retrieved LST image for each year using the root mean square error (RMSE) and mean absolute error (MAE). Both RMSE and MAE are measures of precision used to quantify the relative estimation error at the pixel level (Ishola, Okogbue and Adeyeri, 2016). This was implemented using and mmetrics package in the R statistical software environment (RStudio; Cortez, 2015). These metrics can be expressed as follows in Equation 4.11 and Equation 4.12:

$$RMSE = \sqrt{\frac{1}{n}\sum_{j=1}^{n}(\mathrm{LST}_j - \overline{\mathrm{LST}}_j)^2}$$

Equation 4.11

$$MAE = \frac{1}{n}\sum_{j=1}^{n}\left|\mathrm{LST}_j - \overline{\mathrm{LST}}_j\right|$$

Equation 4.12

Where $\overline{LST}_j$ is the estimated LST for pixel *j*; LST_j is the actual LST of pixel *j* retrieved from the Landsat thermal images; *n* is the total number of pixel samples of the Landsat images.

4.3.5. Hexagon sampling grid

Grid analysis has been used to evaluate the composite effects due to its flexibility of analysis with scale variation, bounding of quantitative values and locations, and statistics of area proportions in these regular shapes (Xiao *et al.*, 2018). Regular rectangular or square grid and hexagonal grid have also been compared in some studies and their relative merit was also examined. Aiazzi *et al.* (2002) earlier study analyzed hexagonal sampling under general assumptions and compared with conventional rectangular sampling and found out that hexagonal sampling was attractive for remote sensing application where the acquisition process is crucial to preserve image quality without introducing data transmission overheads. He and Jia (2005) affirmed that hexagonal structure is considered to be preferable to the rectangular structure due to its higher sampling efficiency, consistent connectivity and higher angular resolution and is even proved to be superior to square structure in many applications. Birch, Oom and Beecham (2007) also investigated the use of rectangular and hexagonal grids application in ecological observation, experiment and simulation such as the role of nearest neighbourhood in experimental design, the representation of connectivity in maps, and a new method for performing field surveys. They establish that a hexagonal grid is simpler and less ambiguous than a rectangular grid. Furthermore, studies have shown that quantifying the indeterminacy and complexity of the LST response to urban land cover requires a flexible and effective method of examination since suitable scales must also be selected to evaluate the composite effects (Liu and Weng, 2009; Schwarz, Lautenbach and Seppelt, 2011; Zhou *et al.*, 2016; Zhou, Wang and Cadenasso, 2017; Xiao *et al.*, 2018). Therefore, we created a hexagonal polygon grid with a size 90 X 90 grid over the spectral index derived ISA extent for each year (i.e., 1993, 2003 and 2013) within the study area with the origin coordinate system. The decision to use the grid size of 90 is similar to the study of Xiao *et al.* (2018) after empirically testing various grid sizes. At the 90 X 90grid scale, we observed that the hexagon grid size is much smaller than the impervious surface patches, thereby preserving useful interpretation of variables such as LST and elevation pixels i.e., ensure that an adequate number of pixels is considered. Afterward, the mean LST and elevation pixels values intersecting with each grid were aggregated with the spatial statistics tool "zonal statistics module" of ArcGIS software.

4.3.6. Statistical Analysis

We ensure that all the ISA elevation pixels value for each year is delineated based on the hexagonal polygon grid at 90x90 scale covering the spectral index estimated ISA, to calculate the ISA change at each meter increment in elevation by their mean LST and for further statistical analysis in this study. Also based on the sampling grid, we computed a density plot to describe the distribution of ISA-elevation for each year using the acquired value of each grid. To further investigate the relationship between the ISA-LST with elevation, the correlation analysis was used to show a consistent linear trend at the 95% confidence level ($p<0.05$) for each year using the scatterplot. Finally, the optimized hot spot analysis (Getis-Ord Gi*) tool in the ArcGIS software, developed by Environmental Systems Research Institute (Mitchell, 1999; Environment for Visualizing Images, 2016) was applied to explore the spatial cluster of ISA surface temperature arrangements appearing in Pretoria based on the hexagonal polygon grid covering the spectral index estimated ISA. This technique characterizes the presence of hot spots (high clustered values) and cold spots (low clustered values) over an entire area by looking at ISA-LST value within the context of its neighbouring features (Getis and Ord, 1992; Ord and Getis, 1995). To be a statistically significant hot spot, a feature must have a high value and should also be surrounded by other features with high values and vice versa (Tran *et al.*, 2017; Kang, Cho and Son, 2018).

The Getis-Ord Gi* statistical formula used for the hotspot analysis is mathematically expressed as follows in Equation 4.13, Equation 4.14 and Equation 4.15 (Environment for Visualizing Images, 2016; Kim and Choi, 2017; Tran *et al.*, 2017):

$$G_i^* = \frac{\sum_{j=1}^{n} w_{i,j} x_j - \bar{X} \sum_{j=1}^{n} w_{i,j}}{S \sqrt{\frac{\left[n \sum_{j=1}^{n} w^2_{i,j} - \left(\sum_{j=1}^{n} w_{i,j} \right)^2 \right]}{n-1}}}$$

Equation 4.13

where x_j is the attribute value for feature j, $w_{i,j}$ is the spatial weight between feature i and j n is equal to the total number of features and:

$$\bar{X} = \frac{\sum_{j=1}^{n} x_j}{n}$$

Equation 4.14

and

$$S = \sqrt{\frac{\sum_{j=1}^{n} x_j^2}{n} - \left(\bar{X} \right)^2}$$

Equation 4.15

The resultant Getis-Ord Gi* statistic generates z-scores that identifies hexagon bin having spatially clustered high or low ISA-LST values across the city for each of the study years (Harris *et al.*, 2017). For positive and larger z-scores indicated the more intense the clustering of high values (hot spot), negative and the smaller the z-score signified the more intense the clustering of low values (cold spot) and z-score near zero indicates no apparent spatial clustering (Jana and Sar, 2016; Tran *et al.*, 2017). The z-score represents the statistical significance of clustering for a specified distance (i.e., 90% significant: >1.65 or < -1.65;

95% significant: >1.96 or <-1.96; 99% significant: >2.58 or <-2.58). From the final resultant Getis-Ord Gi* statistic map, the ISA-LST pattern will be divided into seven categories: very hot spot, hot spot, warm spot, not statistically significant, cool spot, cold spot, and very cold spot. This method will give a better display of the UHI extent through the study years. The above list of statistical analysis was implemented using both R statistical software environment and ESRI (ArcGIS).

4.4. Results

4.4.1. Spectral index derived impervious surface features

The derived BUI images for the three selected years (i.e., 1993, 2003, 2013) shows ranges from -0.499 to 0.688, -0.527 to 0.610 and -0.229 to 0.616 respectively (Table 4.2). After thresholding analysis of the built up spectral index (BUI) for the three years, Figure 4.1(a-c) shows thematic images each indicating built-up ISA i.e., asphaltic roads, cemented floors and buildings etc., in Pretoria. The resultant threshold values derived from the BUI images (1993, 2003 and 2013) are shown in Table 4.2 for the identification of ISA respectively.

Table 4.2 Dynamic ranges of BUI index derived ISA or built-up from the Landsat images.

BUI index	Minimum	Maximum	Threshold
1993	-0.499	0.688	-0.131≥ISA≥0.195
2003	-0.527	0.610	-0.166≥ISA≥0.006
2013	-0.229	0.616	0.06≥ISA≥0.616

Moreover, the extracted ISA thematic images were quantitatively assessed for their accuracy. The area under the receiver operating characteristic curve (AUROC) shows that the performance of each of the BUI threshold values in detecting the impervious surface or built-up areas across the study area over the 30year period. As shown in Figure 4.1(d-f), the AUROC values calculated were: BUI (AUROC = 0.85) for 1993, BUI (AUROC = 0.83) for 2003, BUI (AUROC = 0.88) for 2013 respectively. Therefore, based on the stratified 10-fold cross-validation the results indicate that the BUI threshold values successfully identified built-up with relatively high precision.

4.4.2. Dynamics of impervious surface area with elevation

In this study, the percent ISA was used to indicate the extent of the urban development. Impervious surface, as an important urban land cover feature, not only indicates the degree of urbanization, but is also a major contributor to the environmental impacts of urbanization

(Arnold and Gibbons, 1996). Figure 4.1(a-c) shows the ISA changes and persistence across Pretoria. After, the ISA of the study area was mapped from the Landsat images spanning a total time frame of 30 years: 1993, 2003, and 2013, the change detection was based on impervious surface coverage in Hectares (ha.) for each year i.e., Total Area = 68722.76ha;1ha = pixel count X 900m^2 X 0.0001.

Table 4.3 Spatio-temporal analysis of the impervious surfaces across the study years.

1993	**2003**	**2013**	**1993-2003**	**2003-2013**	**1993-2013**
Area(Ha)	**Area(Ha)**	**Area(Ha)**	**Growth rate (%)**	**Growth rate (%)**	**Growth rate (%)**
12111	16466	21646	5	9	14

Table 4.3 reveals the spatial and temporal changes of the impervious surfaces during the 30 study years. The result shows that the ISA increased dramatically from 12111ha in 1993 to ~16466ha in 2003 and further to 21646ha in 2013, a net increase of 9535ha during the study period. Therefore, temporally the ISA growth rate of 5% was observed between the years 1993 and 2003, while a significant growth rate of 9% was recorded between the years 2003 and 2013. Hence, the total ISA growth rate during the 30 study years is 14%. Subsequently, the DEM image is at a spatial resolution of approximately 30m same as BUI and LST images, therefore it is possible to aggregate (i.e., zonal statistics) their corresponding ISA pixel values for further analysis. In our study, based on the hexagon polygon grid (90 x 90) covering thematic ISA output, sample pixels of approximately 135,000, 183,000 and 240,000 were selected for 1993, 2003 and 2013 thematic images respectively. These ISA pixels for each year formed 8%, 11% and 15% of the total number of pixels in the study areas which was used to plot their elevation distribution histogram (i.e., fitted normal distribution). Figure 4.2(a-c) density plot illustrates the distribution of the ISA over the years over different elevation levels with a mean and standard deviation of 1342.72m and 75.64m (1993), 1587.25m and 83.58m (2003) and 1357.58m and 84.04m (2013) respectively. The count and histogram peaks enabled us to depicts the elevation range with the majority of ISA across the years i.e., most of the ISA spread were concentrated between an elevation of between > 1200m-1600m.

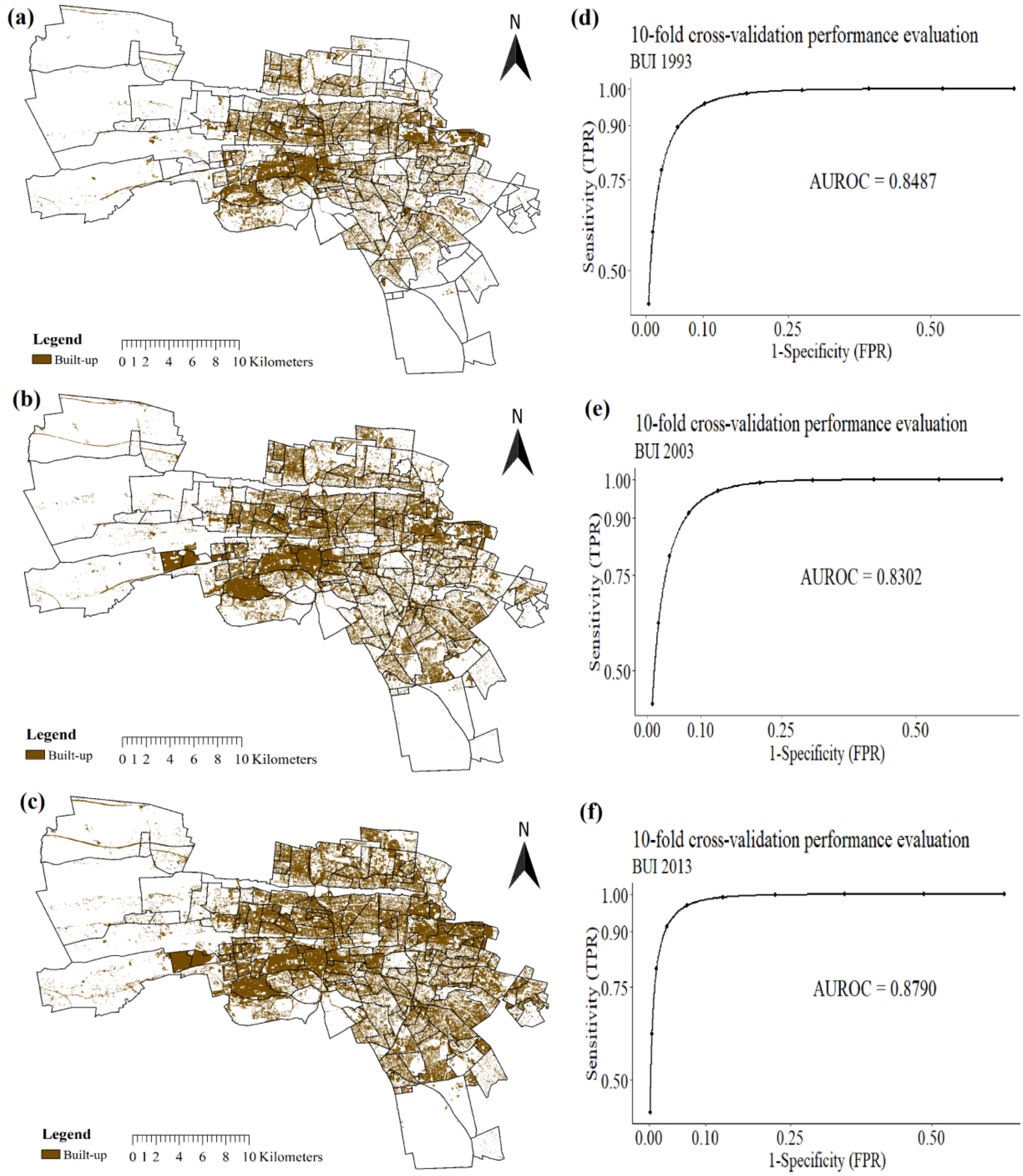

Figure 4.1 (a)-(c) shows the thematic output after thresholding of BUI index image and (d)-(f) illustrates AUROC curve showing the performance of spectral index in delineating built-up ISA for 1993,2003 and 2013.

4.4.3. Land Surface Temperature Retrieval (LST) for ISA

Over the years, the urban expansion experienced in the selected administrative subplaces for this study in Pretoria is not only seen as a sign of growth and prosperity but has continuously brought about expanded infrastructure which are impervious surfaces (Adeyemi *et al.*, 2015). These increase in man-made features (i.e., ISA) and their sequential relationship with climatic variables such as surface temperature (e.g., LST) are crucial to understanding urban sprawl (Tian *et al.*, 2018). In this study, the ISA data extracted with multispectral Landsat-5 TM and Landsat 8 with six bands (VIS-SWIR) images, were used to investigate the spatio-temporal dynamics and the expansion direction of urban sprawl at local administrative subplace units in Pretoria from 1995 to 2015. The first results in Figure 5.1 highlight the potential use of random forest classifier with different sample sizes to estimate ISA from Landsat image for the entire study years. Based on the four sub-datasets with corresponding sizes 20%, 40%, 60% and 80% of the total training data for each year, two different trends were clear: when the training sample size was large enough (80%), the highest accuracy for the RF model was observed for 1995 and 2015 i.e., ~97% and ~98% respectively. Whereas highest accuracy for rf model for 2005 occurred with 20% of the training samples i.e., ~95%. The high accuracies associated with the training samples sizes which were large enough for each of the years, shows that the RF model was less sensitive to the imbalanced training data. Though this might be contradictory to many past studies on different satellite images such as Jin et al. (2014), Colditz (2015) and Mellor et al. (2015) to mention a few that asserted that the greater the land cover class area is, the more training samples that are needed to produce the best classification accuracy. The use of RF model in our study reveals similarity to the studies of Shrestha, et al. (2021) and Thanh Noi and Kappas (2017) that asserted that the RF classifier is less sensitive to the imbalanced training data as long as the training sample size is representative enough i.e. either large or small. After the visual examination of the random forest classifier thematic ISA outputs for the study years presented in Figure 5.2, their quantitative assessment based on 10-fold cross-validation, the AUROC was used to assess the unbiased predictive accuracy. Although the random forest classifier overall predictive accuracy was fairly high (i.e., AUROC = 0.8572 for 1995, AUROC = 0.8709 for 2005, AUROC = 0.8949 for 2015) because of the selection of representative training samples or pixels (Maxwell, Warner and Fang, 2018), there were still errors observed in the final thematic outputs due to mixed pixels i.e., ISA and vegetation (Xu et al. 2018) associated with the use of medium resolution multispectral satellite imagery. Secondly, we examined the ISA spatio-temporal dynamics within ten years interval time frame (i.e., 1995 -2015) at local region level. Results in Table 5.3 and Figure 5.4 above reveals while more than 70 % of the selected administrative subplaces (i.e., Arcadia, Capital Park, Eastwood 2, Loftus Stadium, Koedoespoort Industrial, Pretoria Central, Pretoria Industrial, Pretoria West, Riviera) in this study experienced dramatically increase in ISA growth rate. Generally, the ISA spatio-temporal dynamics in the study area could be attributed to the incessant urban sprawl resulting in many places across Pretoria. Since Pretoria is one of the three capital cities in South Africa, the remarkable ISA growth over the years could also be due to political and socio-economic factors.

Finally in our study, guided by the previous study of Xiao et al. (2018) on an optimal analytical scale, we used the hexagon sampling grid covering and aggregating the depicted ISA surface temperature pixels to examine the spatio-temporal developing trends of ISA expansion with the aid of weighted standard deviational ellipse (SDE) method. Similar to the recent studies of Xu et al., 2018; Man et al., 2019 and Hua et al., 2020), our results indicated that the ISA exhibited an expansion trend generally in the east-south-east, east, north-north-east, east-north-east and south-east directions. This can be attributed to the change ISA growth rate coupled with population and various land use activities at the local administrative subplace units. In this study, it can therefore be asserted that the spatio-temporal pattern of ISA surface temperature is an important metric in understanding the principle direction of ISA expansion.

(a-c) illustrates the spatial pattern of absolute normalized LST retrieved for the study. The computed LST map for the entire study area shows that for 1993, 2003 and 2013, LST values range between 13.42 ^{O}C - 42.12 ^{O}C, 16.72 ^{O}C - 48.23 ^{O}C and 18.99 ^{O}C - 53.26 ^{O}C respectively. This study revealed that the maximum LST for the whole area went up by 11 ^{O}C from 1993, 2003 and 2015, which were 42.12 ^{O}C, 48.23 ^{O}C and 53.26 ^{O}C; the minimum temperature increased by 5 ^{O}C from 13.42 ^{O}C, 16.72 ^{O}C and 18.99 ^{O}C, during the same season with ten-year interval. This result indicates that the changes in land cover types thermal emittance have resulted in changes in temperature as reported by the South African Weather Service (SAWS) in recent years. Adeyemi *et al.* (2015) point out in an earlier study that ISA can be used as a complementary metric for surface urban heat island studies. Consequently, the hexagon polygon grid earlier created covering more than 15,000 of the spectral index estimated ISA pixel, was used to performed zonal analysis on the retrieved LST images (i.e., aggregate mean of the ISA-LST pixel values) for the 30 study years in Pretoria. Based on the spatial distribution of ISA surface temperature, the results show that the mean ISA-LST of 1993 was 29.08 ^{O}C (standard deviation of 1.89 ^{O}C), followed by 2003 with a mean ISA-LST of 31.14 ^{O}C (standard deviation of 2.44 ^{O}C) and the highest mean ISA LST of 37.07 ^{O}C (standard deviation of 1.20) in 2013. Also, we verified the overall metrics error between the predicted and actual LST to assess the accuracy of the retrieved normalized LST image for the study area. The result indicates that the overall error for the study area is quite low: ~1.48

^{O}C for RMSE and ~1.07 ^{O}C for MAE (1993), ~1.43 ^{O}C for RMSE and ~1.10 ^{O}C for MAE (2003) and ~0.84 ^{O}C for RMSE and ~0.54 ^{O}C for MAE (2013) respectively. Thus, the thermal bands of Landsat 5TM and Landsat 8 TIRS data employed for this study provided good retrieved surface temperature results and were further used to describe the distribution of ISA (urban expansion) in relation to elevation and hotspot analysis in subsequent sections.

4.4.4. Relationship between ISA surface temperature and elevation

The DEM image was also snapped with LST images so that pixels of different images represent same area on ground, we performed the zonal statistics on them using the hexagon polygon grid to evaluate the distribution of ISA-LST in relation to elevation. Figure 4.2(d-f) scatter plots show a consistent linear pattern between ISA-LST and elevation for all three years. The result does not only show the equation of the linear relationship between ISA-LST and elevation but also indicated negative correlation coefficient values i.e., r = -0.184, -0309 and -0.298 for the three years respectively. The slope of the trend line specifies the change in ISA-LST distribution with elevation change. It can be seen that the mean ISA-LST has a falling trend with elevation, with the steepest slope found in the 2003 image (Figure 4.2e), indicating that the magnitude of UHI reaches the highest while the lowest level of magnitude of UHI was found in the 1993 image (Figure 4.2d).

4.4.5. Hotspot analysis

Based on the hexagon polygon grid (90 x 90) covering ISA pixel samples, we were able to also identify the location and degree of spatial clustering of ISA-LST for the study years with the aid of Getis-Ord Gi* statistics hotspot maps. The spatial distribution of the Getis-Ord Gi* critical value (*z*-scores) and significant level (*p*-values) was derived from the hot spot analysis. The statistical results for the ISA-LST pattern were divided into seven categories: very hot spot, hot spot, warm spot, not statistically significant, cool spot, cold spot, and very cold spot (Kim and Choi, 2017; Tran *et al.*, 2017; Kang, Cho and Son, 2018). The resultant maps for this study (Figure 4.3d-f) show that the spatial clustering of hot regions in red colours (significant level $0.10 \leq$p-value≤ 0.01) are places with high clusters of ISA with high LST values i.e. with critical value (z-score): 90% significant: 1.65-1.96, 95% significant: 1.96-2.58 and 99% significant: >2.58).On the other hand, the spatial clustering of cold regions in blue colours (significant level $0.01 \leq$p-value≤ 0.10) correspond to areas with high clusters of ISA but with low LST values i.e. with critical value (z-score): 90% significant: -1.96 - -1.65, 95% significant: -2.58 - -1.96 and 99% significant: <-2.58. Based on the spatial pattern of ISA-LST, significant hotspots regions increased by 13% between the years 1993 to 2003 and 6% between the years 2003 to 2013. Hence, the total hotspot region growth rate during the 30 study years is 19%. In contrast, significant coldspot regions decreased by 2% between the years 1993 to 2003 and 1% between the years 2003 to 2013. Also comparing the results of the hotspot analysis for the study years, there is clear spatial patterns of high ISA-LST that mostly spread north-northwest, north-west, west-northwest, west, west-southwest, south-west, south, north-northeast and north-east from the central part of Pretoria since 1993-2013. However, most of the cold spots were found in the east, east-southeast and south-east part of Pretoria.

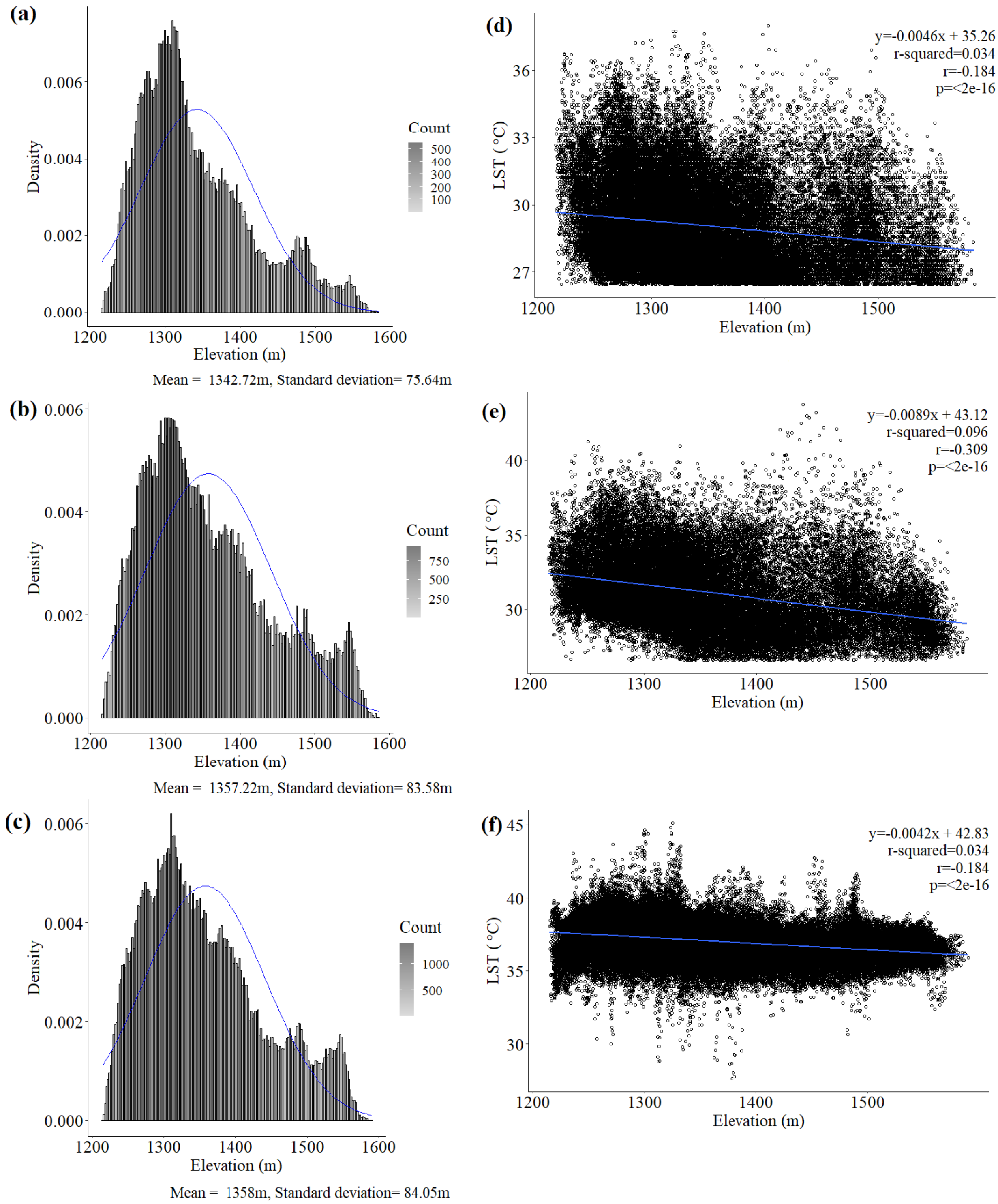

Figure 4.2 (a)-(c) Density plot showing the elevation range with majority of ISA and (d)-(c) Scatterplots explaining the relationship between ISA-elevation and ISA-LST for each year.

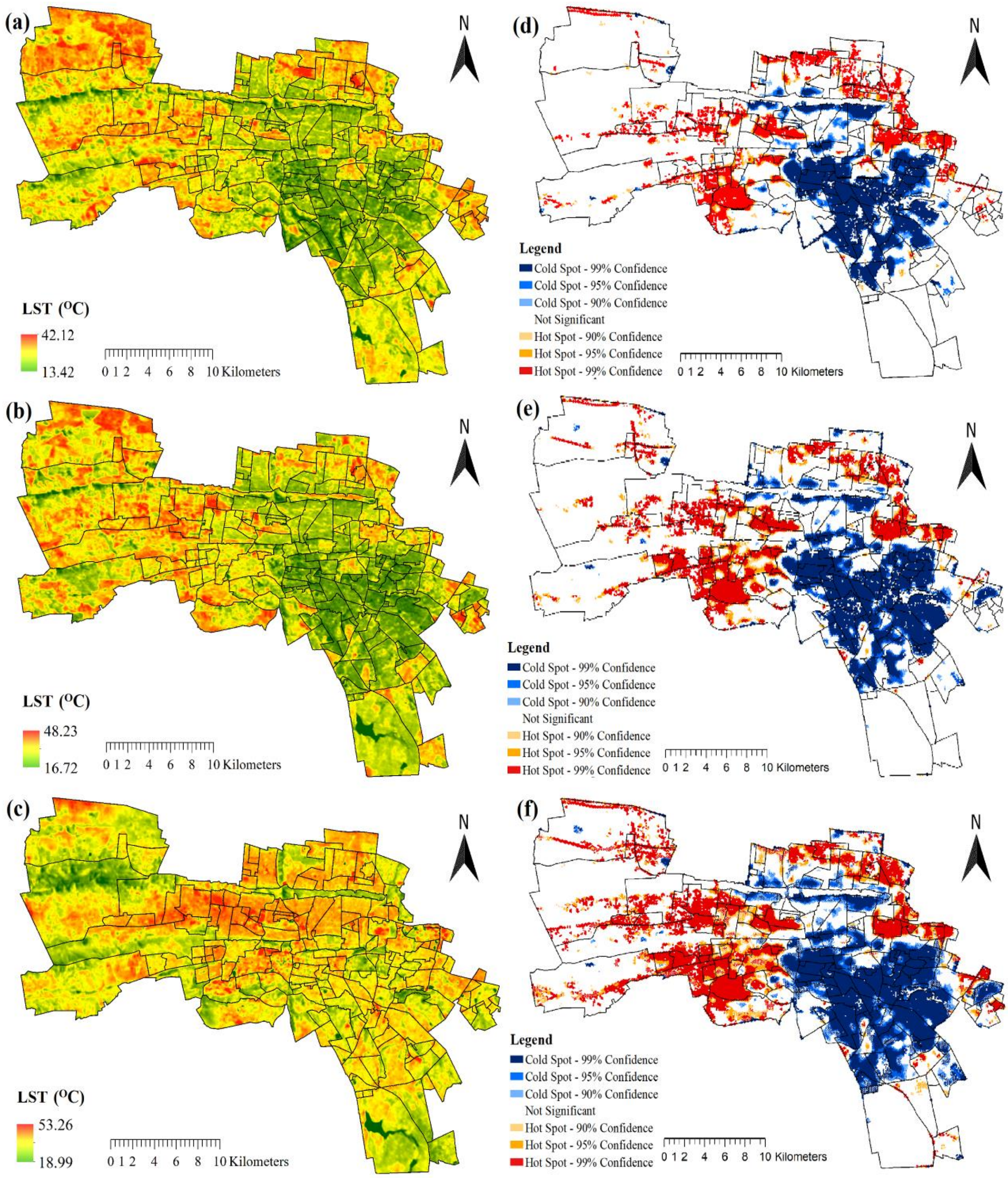

Figure 4.3 (a)-(c) Retrieved LST maps (^{O}C) and (d)-(e) hotspot analysis of Pretoria city based on ISA-LST for 1993, 2003 and 2013.

4.5. Discussion

The urban expansion experienced across the Pretoria perceived as a sign of growth and prosperity has continuously brought about expanded infrastructure that makes use of more ISA (Adeyemi et al., 2015). These increase in man-made features are crucial to understanding urbanization and its impact on urban heat islands, earth surface energy balance, hydrological cycles, and biodiversity (Tian *et al.*, 2018). In this study, we first performed the multi-temporal analysis of ISA across Pretoria from the Landsat images spanning a total time frame of 30 years: 1993, 2003, and 2013. The first results in Table 4.2 highlight the potential use of BUI to estimate built-up ISA from the medium resolution multispectral Landsat images using the threshold analysis. Although the threshold index value showed high positive values for water, high negative values for bare soil and vegetation, and minor negative values for the built-up area, similar to the study of Kaimaris and Patias (2016), we focused on the last finding, i.e. in values ranging around 0.0. Secondly, results in Table 4.3 above reveal that ISA growth rate of 5% was observed between the years 1993 and 2003, while a significant growth rate of 9% was recorded between the years 2003 and 2013. Hence, the total built-up ISA growth rate during the 30 study years is 14 %. Since Pretoria is one of the three capital cities in South Africa, the remarkable built-up ISA growth over the years could be attributed to political and socio-economic factors.

Guided by the previous study of Xiao et al. (2018) on a suitable analytical scale for the use of hexagon polygon grid (90m x 90m) covering thematic ISA output, sample pixels of approximately 135,000, 183,000 and 240,000 were selected for 1993, 2003 and 2013 thematic images respectively. These ISA pixels for each year formed 8%, 11% and 15% of the total number of pixels in the study areas which was used to plot their elevation distribution histogram (i.e., fitted normal distribution). Figure 4.2 density plot illustrates the distribution of the ISA over the years over different elevation levels with a mean and standard deviation of 1342.72m and 75.64m (1993), 1587.25m and 83.58m (2003) and 1357.58m and 84.04m (2013) respectively. The count and histogram peaks enabled us to depicts the elevation range of > 1200m – 1600m were with the majority of ISA distribution across the years i.e., areas suitable for constructions.

According to Mathew et al. (2016), the maximum and minimum temperatures for different periods of different years are highly variable due to the climatic unpredictability with the season which makes the UHI intensity at a particular location change significantly. Due to the above reasons, they asserted that retrieved LST values of all pixels of an image have to be normalized to make it possible to consolidate the UHI effect over the study area over a long period. In this study, Figure 4.3 illustrates the spatial pattern of absolute normalized LST images retrieved from 1993-2013. This study results revealed that the maximum LST for the whole area went up by 11^{O}C from 1993, 2003 and 2015, which were 42.12 ^{O}C, 48.23 ^{O}C and 53.26 ^{O}C; the minimum temperature increased by 5 ^{O}C from 13.42 ^{O}C, 16.72 ^{O}C and 18.99 ^{O}C, during the same season with ten-year interval. The red colour in Figure 4.3(a-c) indicates high temperature in central part of the city, and the light greenish colour shows low temperature at the periphery or outskirt of the study area which comes under new developed formal residential or rural areas. Temperature is low in new developed formal residential or rural areas because of vegetation while the central part of the city shows higher temperature pixels due to the presence of ISA. Additionally, Adeyemi et al. (2015) point out that ISA can be used as a complementary metric for surface urban heat island studies. Therefore, we sampled using the hexagon polygon grid the aggregated mean of the ISA-LST pixel values for each study year. Based on the spatio-temporal distribution of the satellite retrieve ISA-LST pixels their a mean of 29.08 ^{O}C (standard deviation of 1.89 ^{O}C) for 1993, followed by 2003 with a mean of 31.14 ^{O}C (standard deviation of 2.44 ^{O}C) and the highest mean ISA LST of 37.07 ^{O}C (standard deviation of 1.20) in 2013. This can be attributed to the changes in land cover types surface characteristics over the years i.e., loss of natural vegetation that produces a cooling effect surface temperature to being replaced by artificial impervious surface materials with high emissivity.

Furthermore, the scatter plots were used to evaluate the distribution of ISA-LST in relation to elevation as shown in Figure 4.2(d-f). The relationship between elevation and LST is similar for all three study years with a negative linear trend based on the slope that specifies the change in ISA-LST distribution with change in elevation in Figure 4.2(d-f). This signifies that the ISA-LST is having a falling trend with altitude, with the steepest slope found in the 2003 image (Figure 4.2e), indicating that the magnitude of UHI reaches the highest while the lowest level of magnitude of UHI was found in the 1993 image (Figure 4.2d). The above results could be attributed to the fact that ISA-LST for the different years is influenced by many parameters such as solar incident radiation, angle of incidence of solar radiation, surface properties such as surface roughness and most importantly extent of vegetation and air temperature that results in the different scattering (Abdullah 2012; Adeyemi, Botai and Ramoelo 2015; Mathew et al. 2016; Khandelwal et al. 2018). From the results in Figure 4.2(d-f), we could also assert that the falling ISA-LST trend with elevation observed for the study years is because the distribution of ISA is still mainly dominant in flat terrains or low altitudes, making elevation and slope an important constraint for the expansion of ISA in the study area (Qian and Wu, 2019).

Finally, based on the use of hexagon polygon grid covering the estimated ISA-LST pixel samples, we were also able to create Getis-Ord Gi* statistics hotspot maps on three different dates (Figure 4.3d-f) representing the total time frame of 30 years. According to (Shariati *et al.*, 2020), the stated that Hotspot analysis (Getis-Ord Gi*) is considered a helpful tool to recognize spatial clusters of both high and low values. The resultant maps for this study (Figure 4.3d-f) were divided into seven categories: very hot spot, hot spot, warm spot, not statistically significant, cool spot, cold spot, and very cold spot (Kim and Choi 2017; Tran et al. 2017; Kang et al. 2018). The result indicated a total hotspot region growth rate by 19% and total coldspot regions decreased by 3% during the study years i.e., in general, more hotspots were occupying larger areas than coldspots. Similar to the study of Tran et al. (2017), the resultant maps for this study (Figure 4.3d-f) indicates that the increased hot regions were highly clustered in the urban areas with main roads zones with predominant land use activities such as industrial, commercial, smallholdings and formal residential. The decreased cold regions correspond to areas with loss of natural land cover types (e.g., agriculture, vegetation and water bodies or wetlands etc.) in the rural areas or townships or city outskirts, with predominant land use activities such as formal residential, collective living quarters, parks and recreation. Also similar to the earlier study of Jana and Sar (2016), our results indicated a clear spatial pattern of the cluster of ISA-LST orientation and direction in the study area over the years. Likewise, our results also fulfil part of the request of the earlier study of Smith et al. (2014) as cited by (Shariati *et al.*, 2020) that pointing out the need to evaluate the influencing factors such as environmental, climatic, etc. components that have caused the formation of hot spot clusters. Based on our overall findings in this study, we could therefore conclude that the distribution and clustering of ISA-LST is an important metric in understanding UHI extent.

4.6. Conclusion

Remote sensing technology continues to provide an effective way to continuously monitor changing processes on the landscape. The main strengths of the current study were: (1)The use of built-up Index (BUI) the enable us to estimate and reveal the spatio-temporal changes of ISA within ten years interval time frame in Pretoria; (2) Based on the suitable analytical scale of hexagon polygon grid covering spectral index estimated ISA used to aggregate corresponding ISA-LST and elevation pixels samples (i.e. zonal statistics), we investigated the elevation range with the majority of ISA distribution using density plot, the relationship between ISA-LST and elevation with a scatterplot as well as Getis-Ord Gi* statistics hotspot maps that enable us to identify the clear spatial pattern of the cluster of ISA-LST orientation and UHI extent. The results of this study are important for land use planning and urban management.

Chapter 5 Assessment of spatio-temporal direction of impervious surface area surface temperature in Pretoria, South Africa.

Satellite level (medium resolution)

Adeniyi Adeyemi, Abel Ramoelo, Moses Cho, Jacobus Strydom (2021) - Assessment of spatio-temporal direction of impervious surface area surface temperature in Pretoria, South Africa, Geocarto International, (29 December 2021), https://doi.org/10.1080/10106049.2021.2022018

Abstract

Over the years, rapid urban growth has led to the conversion of natural lands into large man-made landscapes due to enhanced political and economic growth. This study assessed the spatio-temporal change characteristics of impervious surface area (ISA) expansion using its surface temperature (LST) at selected administrative subplace units (i.e., local region scale). ISA was estimated for 1995, 2005 and 2015 from Landsat-5 Thematic Mapper (TM) and Landsat-8 OLI (Operational Land Imager) and TIRS (Thermal Infrared Sensor) images using a Random Forest (RF) algorithm. The spatio-temporal trends of ISA were assessed using an optimal analytical scale to aggregate ISA LST coupled with weighted standard deviational ellipse (SDE) method. The ISA was quantified with high predictive accuracy (i.e., AUROC = 0.8572 for 1995, AUROC = 0.8709 for 2005, AUROC = 0.8949 for 2015) using RF classifier. More than 70% of the selected administrative subplaces in Pretoria experienced an increase in growth rate (415.59%) between 1995 and 2015. LST computations from the Landsat TIRS bands yielded good results (RMSE = ~1.44^{O}C, 1.40^{O}C, ~0.86^{O}C) for 1995, 2005 and 2015 respectively. Based on the hexagon polygon grid (90x90), the aggregated ISA surface temperature weighted SDE analysis results indicated ISA expansion in different directions at the selected administrative subplace units. Our findings can represent useful information for policymakers in evaluating urban development trends in Pretoria, City of Tshwane (COT).

5.1. Introduction

Development is sometimes reflected by the chaotic expansion of urban expansion and the spontaneous appearance of urban buildings in rural areas or on the peripheries of cities (Bouzekri, Lasbet and Lachehab, 2015). This rapid urban landscape change as indicated by Odindi et al. (2012) has been because of the exceptional increase in population concentration in cities. According to Demographia (2017) and Sahana et al. (2018) 53% of the global population lives in urban settlements and by 2030 this number is expected to have increased more than 60%. Developing countries are more likely to experience the highest rate of urbanization and industrialization in the near future i.e., conversion of vegetation areas to impervious surface materials (Sahana, Hong and Sajjad, 2018). Over the last decades, Pretoria, South Africa has been facing major land use or cover changes, such as loss of natural land, i.e. forest or plantations, agricultural lands and grasslands coupled with growing impervious surface areas (ISA) such as roads, sidewalks, parking lots, rooftops and bare lands due to a continuous increase in the population (Adeyemi et al., 2015).

In past decades, depending upon the research objectives, many methods have been proposed to extract impervious surfaces using satellite images. However, ISA mapping in major cities in Africa in the body of literature is still very few. An overview of the methods for ISA mapping can be grouped into four major categories: classification-based (i.e., pixel or object-based), mixture analysis (i.e., sub-pixel-based), spectral index-based and deep learning-based segmentation (Weng 2012; Yu et al. 2017; Tian et al. 2018; Wei and Blaschke 2018; Zhang and Huang 2018; Hua et al. 2020; Adeyemi, et al. 2021). Most classification-based methods (i.e., supervised classifiers) require training samples e.g., maximum likelihood classifier (Masek, Lindsay and Goward, 2000), machine learning classifiers such as artificial neural networks (ANN) (Hu, 2009; van de Voorde, de Roeck and Canters, 2009), decision tree (DT) (Xian and Crane, 2006; Lu, Moran and Hetrick, 2011; Xu, 2013), classification and regression tree (CART) (Xu and Wang, 2016), random forest (RF) (Zhang et al. 2014; Adeyemi et al. 2015; Xu et al. 2018), support vector machine (Sun, 2011; Okujeni, van der Linden and Hostert, 2015; Shi *et al.*, 2017; Xu, Mountrakis and Quackenbush, 2017) and regression modelling (Okujeni *et al.*, 2018; Yu *et al.*, 2018). Among the above-mentioned pixel-scale, classification-based methods on multispectral imagery, the non-parametric Random Forest (RF) algorithm has been reported to perform excellently in ISA estimation from multispectral imagery (Adeyemi, Botai and Ramoelo 2015). Nonetheless, the potential and effectiveness of random forest machine learning algorithms based on different training sample sizes in spatio-temporal analysis of urban impervious surfaces in major cities in Africa using remote sensing is still very little and needs to be explored.

Furthermore, the most significant environmental impact of the high degree of imperviousness as documented by many studies is land surface temperature (LST) and atmospheric temperature variability (Deng and Wu, 2013; Artmann, 2014; McGregor *et al.*, 2015; Morabito *et al.*, 2016; Ward *et al.*, 2016; Tian *et al.*, 2018). With the development of satellite thermal infrared remote sensing data, considerable LST measurements can be retrieved (Nie and Xu, 2015). Consequently, there have been several algorithms and methods used for LST retrieval from remote sensing data. Qin et al. (2001) developed the split window and mono window algorithm and demonstrated their effectiveness of using Landsat data. Jiménez-Munoz and Sobrino (2003) and Jiménez-Muñoz and Sobrino (2010) also developed the single-channel algorithm for LST retrieval from Landsat and ASTER data respectively. In this study, the single-channel algorithm was employed due to its advantage of being used when the ground truth data is not available Alipour et al. (2011). Even though, increase in ISA results in surface temperature rise due to change in land surface component distinctive radiative, thermal, moisture and aerodynamic properties according to Owen et al. (1998), there is still limited explicit information using surface temperature as a complementary metric for spatio-temporal urban expansion trend analysis.

An analytical method such as standard deviational ellipse (SDE) (Lefever, 1926) has been widely used in recent studies to evaluate the spatial distribution evolution and trends in various fields (Vanhulsel *et al.*, 2011; Al-Kindi *et al.*, 2017; Li *et al.*, 2017; Xu *et al.*, 2018), because it can reveal the spatial concentration of geographical phenomena and the change characteristics of the geospatial distribution. Recent studies in developed countries have used the SDE to examine the spatio-temporal dynamics of urban expansion over a long-time period by using the impervious surfaces estimated with remote-sensing data (Jian et al. 2016; Qiao et al. 2018; Xu et al. 2018; Man et al. 2019). Nevertheless, sufficient spatio-temporal details may still be required to understand the spatio-temporal urban expansion at different spatial scales coupled with the trends. Since none of this studies have been performed in major cities in Africa, we undertook a study using selected Pretoria administrative subplaces (Figure 1.7) as a pilot area of comprehensive innovation reform. The aim of this study was to improve understanding of the spatio-temporal developing trend of ISA expansion at a local spatial scale based on surface temperature (i.e., a complementary metric) in Pretoria, South Africa during the past 30 years. The key research questions are:

1) Can the random forest algorithm based on different training sample subsets influence the accuracy of estimated ISA from optical Landsat imagery?
2) At local spatial scale, can the spatio-temporal changes of the extracted ISA be revealed within ten years interval time frame?
3) With an optimal analytical scale, is it possible to reveal the principle direction of urban expansion at local region level using the weighted standard deviational ellipse (SDE) method?

5.2. Materials and Methods

The overall methodological workflow is summarized in the flowchart of Figure 1.4.

5.2.1. Data Collection and Pre-processing

In this study, three cloud-free springtime images (Table 5.1) recorded by Landsat 5-TM (Thematic Mapper) on 25th September 1995 at 07:03 h local time, 20th September 2005 at 07:50 h local time and Landsat-8 OLI (Operational Land Imager) and TIRS (Thermal Infrared Sensor) on 16th September 2015 at 08:02 h local time were obtained from the United States Geological Survey Global Visualization Viewer and reprojected to the UTM Zone 35S projection system with WGS84 datum. The Landsat images were pre-processed using two important steps: (1) converting digital numbers (DNs) to top-of-atmosphere (TOA) radiance and then to TOA reflectance; and (2) conversion of the TOA reflectance to surface reflectance using the Fast Line-of-sight Atmospheric Analysis of Hypercubes (FLAASH) a first principle atmospheric correction tool that incorporates the standard MODTRAN model in ENVI software (Felde *et al.*, 2003; Krause, 2005; Environment for Visualizing Images ENVI, 2014). Also, in this study, we used the Pretoria administrative shapefile boundary at Enumeration Area (EA) and subplace (SP) level source from Statistics South Africa (STATSSA).

The dominant land use per EA was extracted by analysing the building-based land use dataset and then rolled up to subplace level. As pilot areas(Figure 1.7), the following subplaces within Pretoria were selected based on the dominant land use (EA type) i.e., Formal residential (Arcadia, Capital Park, Claremont, Eastwood 2, Philip Nel Park, Riviera, Rietondale), Commercial (Loftus Stadium, Pretoria Central, Pretoria West), Industrial (Kirkney, Koedoespoort, Koedoespoort Industrial, Pretoria Industrial) and Collective living quarters (Salvokop). Other data used in this study are listed in Table 5.1.

Table 5.1. Summary of data used in research.

Data Types			**Datasets**	
	Date		Image type	Path/Row
	1995-09-25		Landsat 5-TM	170/78
Remote Sensing data	2005-09-20		Landsat 5-TM	170/78
	2015-09-16		Landsat-8 OLI/TIRS	170/78
Boundary file	2011		Pretoria Administrative boundary shape dataset based on Enumeration Area level (i.e., the smallest geographical unit, with typically 100 to 250 households, into which the country is divided for census or survey purposes) and subplace level (i.e., the second (lowest) level of the place name category, namely a suburb, section or zone of an (apartheid) township, smallholdings, village, sub-village, ward or informal settlement.	
Ancillary data	2012-2015		1:10,000 aerial photography from 2012-2015 with spatial resolution of 0.5m and	
	2015		Google Earth Images	
	2015		NLC classification dataset of 2013-2014	

5.3. Methodology

5.3.1. Land Surface Temperature (LST) Retrieval

The single-channel algorithm (SCA) developed by Jiménez-Munoz and Sobrino (2003) was employed to retrieve LST from the geometrically corrected TIR band 6 from Landsat 5-TM (10.44 - 12.42µm) and mean of band 10 and 11 from Landsat-8 TIRS (10.6 – 11.19 µm) and (11.50–12.51 µm) respectively.

5.3.1.1. Conversion to at-satellite Brightness Temperature (Tb)

The thermal band's digital numbers were first calibrated to minimize the noise caused by aerosols, water vapour etc. before being converted to top-of-the-atmosphere (TOA) radiance. The following formulas are used to perform this process (Equation 5.1):

For Landsat 5TM:

$$R=\left(\frac{L_{\max}-L_{\min}}{Q_{cal\max}-Q_{cal\min}}\right)\left(Band6_{DN}-Q_{cal\min}\right)+L_{\min}$$ Equation 5.1

Where R is TOA radiance (watts/ (meter squared * ster * μm), Q_{calmax} = 255, Q_{calmin} = 0 while L_{max} and L_{min} can be obtained from the header file of the Landsat 5TM imagery (Markham and Barker, 1985) :

For Landsat 8:

$$R=M_L*Band10_{DN}+A_L$$ Equation 5.2

Where R is TOA radiance (watts/ (meter squared * ster * μm), M_L and A_L were also obtained from the header file of the Landsat 8 image (United States Geological Survey, 2013). Thereafter, the radiance (R) images of the two Landsat sensors were converted to at-satellite brightness temperature, T_b i.e., blackbody temperature under the assumption of a uniform emissivity in Equation 5.3:

$$T_b=\frac{K_2}{\ln\left(K_1/R\right)+1}$$ Equation 5.3

Where T_b is at-satellite brightness temperature or black body temperature, R is radiance while K_1 (WATTS/METER SQUARED * STER * MM) and K_2 (KELVIN) are constants which are 774.89 and 1321.08 respectively. The K_1 and K_2 constant for Landsat sensors are provided in the image header file. As indicated by many authors, T_b is not the true surface temperature due to atmospheric interference and variations in land cover (Weng and Lu, 2008; Hu and Jia, 2010). In this study, the (Sobrino, Jiménez-Muñoz and Paolini, 2004) single channel atmospheric correction method was used to remove the noise.

5.3.1.2. Determination of surface emissivity (ε)

Firstly we derived the surface emissivity (ε) which is commonly carried out by differentiation of NDVI which has an advantage when the researcher has no detailed information on derived land cover in the study area (Carlson and Ripley, 1997). Surface emissivity (ε) varies with land covers on ground surfaces (Sun *et al.*, 2017). In urban environments, vegetated surfaces have stronger thermal holding capacity and higher cooling effects than non-vegetated areas. The Normalized Difference Vegetation Index (NDVI) was now used to estimate the Proportion of vegetation (P_v) which is to assess the role of vegetation in each pixel of the satellite images (Gutman and Ignatov, 1998). The formula below was designed for calculating the NDVI and vegetation proportion (Equation 5.4 and Equation 5.5):

$$NDVI = \frac{NIR - \text{Red}}{NIR + \text{Red}}$$ Equation 5.4

$$Pv = \left(\frac{NDVI - NDVI_{min}}{\text{NDVI}_{max} - NDVI_{min}} \right)^2$$ Equation 5.5

Where the $NDVI_{min}$ and $NDVI_{max}$ were the maximum and minimum values obtained from the derived vegetation index image. (Sobrino *et al.*, 2008) measured the relationships between ε and proportion of vegetation (P_v) on a variety of ground surfaces based on the Landsat-extracted NDVI, at each 30m pixel with the formula established according to (Sobrino, Jiménez-Muñoz and Paolini, 2004) in Equation 5.6:

$$\varepsilon = \begin{cases} 0.979 - 0.035\text{Red} & NDVI < NDVI_{min} \\ 0.986 + 0.004P_v & NDVI_{min} \le NDVI \le NDVI_{max} \\ 0.99 & NDVI > NDVI_{max} \end{cases}$$ Equation 5.6

Where ε is the surface emissivity image and *Red* is the surface reflectance of the red band

5.3.1.3. Conversion of at-satellite brightness temperature to LST

Finally, the calculated land surface emissivity for each Landsat image was used to convert the brightness temperature image to Land Surface Temperature (LST) using the Planks equation described below (Weng, Dengsheng and Jacquelyn, 2004):

$$LST_{(KELVIN)} = \frac{T_b}{1 + (\lambda + T_b / \rho) * \ln \varepsilon}$$ Equation 5.7

To convert the LST image to Celsius image using the Equation 5.8:

$$LST_{(\text{CELSIUS})} = LST_{(\text{KELVIN})} - 273.15$$ Equation 5.8

Where λ is the wavelength of radiation emitted in Landsat 5 TM (11.5µm) (Markham and Barker, 1985) and Landsat 8 LCDM (10.8 µm) (United States Geological Survey, 2013). ρ= h * c/σ, σ = Stefan Boltzmann's constant, h = Plank's constant, C = velocity of light, ε = surface emissivity image, LST = surface temperature image. The rescaled to 30m spatial resolution daytime time retrieved surface temperature (LST) images were also normalized.

5.3.2. Collection of Training and validation samples

Training datasets are significant to understanding the features in real-world and to map a mental picture of the land use or cover type while the validation samples were used for independent validation of the obtained land cover maps (Bhaskaran et al. 2010; Aguilar et al. 2014; Ishimwe, Abutaleb, Ahmed and Ngie 2014). Although the selected Pretoria subplaces comprises of the following dominant land use types formal residential, commercial, industrial and collective living quarters, unfortunately, we were unable to visually inspect with a handheld GPS receiver all ISA samples. As a result, the ISA used for validation samples were manually digitized from the reference data such as 1:10,000 aerial photography (0.5m), Google Earth Engine (DigitalGlobe) and OpenStreetMap. The ISA polygons were uploaded using the ESRI ArcGIS software (Table 5.2). These exposed ISA created on the multispectral images were used as training and validation samples (obtained from reference datasets) for classification and accuracy assessment. Furthermore, Ramezan et al. (2019) recently detailed that the size and quality of training sample data couple with sample selection method used can affect the classification and accuracy assessments.

Therefore, in this study, we similarly assess the effect of the training sample sizes and the machine learning algorithm performance based on the classification accuracies. We randomly divided the training sample dataset into 4 different imbalanced datasets (i.e., tset_1,tset_2,tset_3,tset_4) with corresponding sizes 20%, 40%, 60% and 80% of the total training data (Figure 1.4). The create Data Partition function in the caret package in the R statistical software environment (RStudio, Inc., Boston, MA, USA, Version 1.1.463) software was used to ensure that the number of pixels chosen in each class for every sub-dataset to keep the most consistent size in the imbalanced training sample size.

Table 5.2 Summary of the ISA and NonISA classes assigned as training and validation dataset.

Samples	**Training (ISA/NonISA)**	**Validation (ISA/NonISA)**	**Total (∑)**
1995	183(112/71)	315(163/152)	498
2005	164(88/76)	441(166/275)	605
2015	154(93/61)	273(144/129)	427
			1530

5.3.3. Random Forest Impervious Surface Area Extraction

Random Forests (RF) classifier, developed by Breiman (2001), is an ensemble algorithm developed in the field of machine learning that uses a similar but enhanced method of bagging (bootstrap aggregation) operation (Adelabu et al. 2013; Cracknell and Reading 2014; Adeyemi et al. 2015). After the assemblages of trees built by RF, the majority ‘vote’ is used to decide the class assignment for each given pixel (Berhane *et al.*, 2018; Maxwell, Warner and Fang, 2018; Guo *et al.*, 2020). RF classifies the data that is not in the trees as out-of-bag

(OOB) data, and the average OOB error rates from all trees give an error rate called the OOB classification error for each input variable i.e., an independent estimate of the overall accuracy of the RF classification (Breiman, 2001). Furthermore, to implement the RF according to Breiman (2001), two parameters need to be set up which are the number of trees (*ntree*) and the number of features in each split (*mtry*). Regarding the *mtry* parameter, many studies use the default value *mtry* such as the number of predictor variables or bands according to (Belgiu and Drăgu 2016; Shrestha, et al. 2021) while Feng et al. (2015) stated that with *ntree* >= 200, RF could achieve accurate results. Although some studies stated that satisfactory results could be achieved with the default parameters while others indicated that large number of trees will provide a stable result of variable importance (Thanh Noi and Kappas 2017; Shrestha, et al. 2021). In addition, RF classifier can determine the "best split" threshold of input values for given classes by implementing the Gini Index, which returns a measure of class heterogeneity within child nodes as compared to the parent node (Waske and Braun, 2009). RF classifier has some advantages which are: (1) easy to implement as only two parameters (*ntree* and *mtry*) need to be optimized (Özçift, 2011), (2) can be more reliable than other iterative techniques that do not always consider parameters as independent (Adelabu *et al.*, 2013), (3) insensitive to noise (Watts and Lawrence, 2008), does not suffer from over-fitting or a long training time (Loosvelt *et al.*, 2012), faster computation and (4) ability to determine input variable importance by comparing the OOB error rate (Rodriguez-Galiano et al. 2012) and can handle imbalanced data sets (Maxwell et al. 2018).

5.3.4. Optimization for Impervious Surface Area Extraction

Thanh Noi and Kappas (2017) asserted that parameter tuning plays an important role in producing high accuracy results when using machine learning algorithms. Therefore, in this study to find the optimal RF classifier parameters that could accurately depict ISA, we tested a series of values for the tuning process. From the Landsat 5TM and Landsat 8OLI, we used 6 bands (VIS-SWIR) equalling 6 input predictor variables for the parameter tuning of the RF classifier. Four different sub-datasets with corresponding sizes 20%, 40%, 60% and 80% of the total training data were used to train the model and the rest to test the model (Figure 1.4). Finally, a range of values was used for the parameterization of both: ntree = 500:3000 with a step size of 500.; *mtry* = 1:6 with a step size of 1. We implemented RF classification using Caret - RandomForest package in the R statistical software environment (RStudio, Inc., Boston, MA, USA, Version 1.1.463).

5.3.5. Model Performance Evaluation

In this study, the RF classifier performance evaluation was to assess the accuracy of the derived binary classification results for the three years based on samples obtained from reference data such as Google Earth images and aerial photo. We implemented the performance evaluation metrics based on 10-fold cross-validation using area under the receiver operating characteristic curve (AUROC)(Danjuma, 2015). The AUROC graph was generated by plotting the true positive rate (y-axis) against the false positive rate (x-axis) (Wieland and Pittore, 2014). The performance evaluation metric was computed using InformationValue, plotROC and ggplot2 packages in the R statistical software environment RStudio, Inc., Boston, MA, USA, Version 1.1.463 (Prabhakaran,2016; Sameen and Pradhan 2016).

5.3.6. Hexagon polygon grid to determine sampling scale

Grid analysis has been used to evaluate the composite effects due to its flexibility of analysis with scale variation, bounding of quantitative values and locations, and statistics of area proportions in these regular shapes (Xiao *et al.*, 2018). Regular rectangular or square grid and hexagonal grid have also been compared in some studies and their relative merit was also examined. Aiazzi et al. (2002) in earlier studies compared the hexagonal sampling polygon under with rectangular sampling polygon, and found out that the hexagonal was more suitable for remote sensing applications as it preserves image quality without introducing data transmission overheads. He and Jia (2005) confirmed that hexagonal structure is considered to be preferable to the rectangular structure because of its higher sampling efficiency, consistent connectivity and higher angular resolution. Birch et al. (2007) in earlier research also investigated the use of rectangular and hexagonal grids application in ecological observation, experiment and simulations e.g., application of nearest neighbourhood in experimental design and field surveys. Since hexagonal grid is simpler and less ambiguous than a rectangular grid, we used QGIS (version 3.8) software to create a hexagonal polygon grid with matching centroids covering the RF extracted ISA extent for each year (i.e., 1995, 2005 and 2015) within the study area with the origin coordinate system. The decision to use the grid size of 90mx90m is similar to the study of Xiao et al. (2018) after empirically testing various grid sizes. At the optimal 90m grid-scale, we observed that the hexagon grid size is much smaller than the impervious surface patches or thematic outputs, thereby preserving useful geometry for the interpretation of corresponding variables such as LST pixels i.e., ensure that an adequate number of pixels is considered. Afterwards, the hexagon grids were used to aggregate the LST raster layer over the grid cells (i.e., ISA surface temperature pixel values were averaged over the hexagon grid cells with the spatial analyst tool "zonal statistics module" of ArcGIS software) finally used to measure the geographical distribution (i.e., weighted standard deviational ellipse).

5.3.7. Spatial analytic method

5.3.7.1. Standard deviational ellipse analysis

The standard deviational ellipse (SDE) (Lefever, 1926) methods were widely used to assess the spatial distribution evolution and distributional trends in many fields, because they can reveal the spatial concentration of geographical phenomena and the change characteristics of the geospatial distribution (Al-Kindi *et al.*, 2017; Li *et al.*, 2017; J. Xu *et al.*, 2018; Qiao *et al.*, 2018). To measure at local region scale the spatio-temporal developing trends of urban expansion in Pretoria, the weighted standard deviational ellipse (SDE) (Lefever, 1926) method based on ISA surface temperature was used in this study. We also put into consideration the use of the Central Business District (CBD) as its reference point of expansion from the centre to suburbs in the form of concentric circles, Qian and Wu (2019). Based on sampling hexagon polygon grid centroids representing the ISA surface temperature, the calculated parameters of the weighted SDE representing the dispersion and directional trends of the ISA at local region scale (sub-place units) were the long axis, short axis, and rotation angle. The rotation angle of the weighted SDE is calculated as follows:

$$a = \left(\sum_{i=1}^{n} w_i^2 \tilde{X}_i^2 - \sum_{i=1}^{n} w_i^2 \tilde{Y}_i^2 \right)$$

Equation 5.9

$$b = \sqrt{\left(\left(\sum_{i=1}^{n} w_i^2 \tilde{X}_i^2 - \sum_{i=1}^{n} w_i^2 \tilde{Y}_i^2 \right) - 4 \left(\sum_{i=1}^{n} w_i^2 \tilde{X}_i \tilde{Y}_i \right) \right)}$$

Equation 5.10

$$\tan\theta = \frac{a+b}{2\left(\sum_{i=1}^{n} w_i^2 \tilde{X}_i \tilde{Y}_i\right)}$$ Equation 5.11

$$\begin{cases} \tilde{X} = X_i - \overline{X} \\ \tilde{Y} = Y_i - \overline{Y} \end{cases}$$ Equation 5.12

where θ is the rotation angle of the ellipse, indicating the angle measured clockwise from the North to the long axis of the ellipse (Equation 5.9, Equation 5.10 and Equation 5.11). The X and Y are the coordinates while $\bar{X}$ and $\bar{Y}$ are the mean X and Y coordinates (Equation 5.12). $\tilde{X}_i$ and $\tilde{Y}_i$ are the deviation between the *i-th* grid centre in the X and Y direction respectively and w_i is the weight. In this study, the weight w_i indicates the ISA surface temperature of the *i-th* grid. The standard deviations σ_x and σ_y of the ellipse in the X and Y directions (Equation 5.13) are calculated as follows:

$$\begin{cases} \sigma_x = \sqrt{\dfrac{\sum_{i=1}^{n}\left(w_i\tilde{X}_i\cos\theta - w_i\tilde{Y}_i\sin\theta\right)^2}{\sum_{i=1}^{n} w_i}} \\ \sigma_y = \sqrt{\dfrac{\sum_{i=1}^{n}\left(w_i\tilde{X}_i\sin\theta - w_i\tilde{Y}_i\cos\theta\right)^2}{\sum_{i=1}^{n} w_i}} \end{cases}$$ Equation 5.13

The long axis, short axis and rotational angle represent the dispersion and directional trends of the urban ISA i.e., as the rotation angle changes in the SDEs show the spatio-temporal changes in the local impervious surfaces in a particular spatial direction. Subsequently, ellipse centre was drawn from the above SDE parameters, allowing us to see the elongation of the spatial distribution of impervious surface and its particular orientation. Finally, we quantified the SDE using the spatial statistic “measuring geographical distribution” toolbox in ArcGIS.

5.4. Results

5.4.1. Random forest classifier

The success of the RF classifier depended on the optimization of key parameters i.e., *ntree* and *mtry*. In the grid search method, we used 5-fold cross-validation while optimizing the RF classifier. The idea behind the grid search technique was to examine different pairs of parameters and the one yielding the highest level of accuracy is selected (Kavzoglu and Colkesen, 2009). To find the optimal parameters for the RF classifier, several values (*mtry* = 1:6; *ntree* = 500:3000) were tested for all 4 sub-datasets. A sub-datasets of 80%, 20% and 80% respectively had the highest results for the Landsat-derived ISA obtained with mtry equal to 2 or 3 for 1995, 1 for 2005 and 1 or 2 for 2015 (Figure 5.1 (a-c)). Furthermore, Figure 5.1(d-f) show that out-of-bag (OOB) error decreased sharply when *ntree* increased. Increase in *ntree* to ≥2000, ≥1000 and ≥1500 respectively based on different sub-datasets for each year had slightly different trends as indicated in Figure 5.1(a-c), however, generally, the OOBs were slightly reduced at all sub-datasets (Figure 5.1(d-f)).

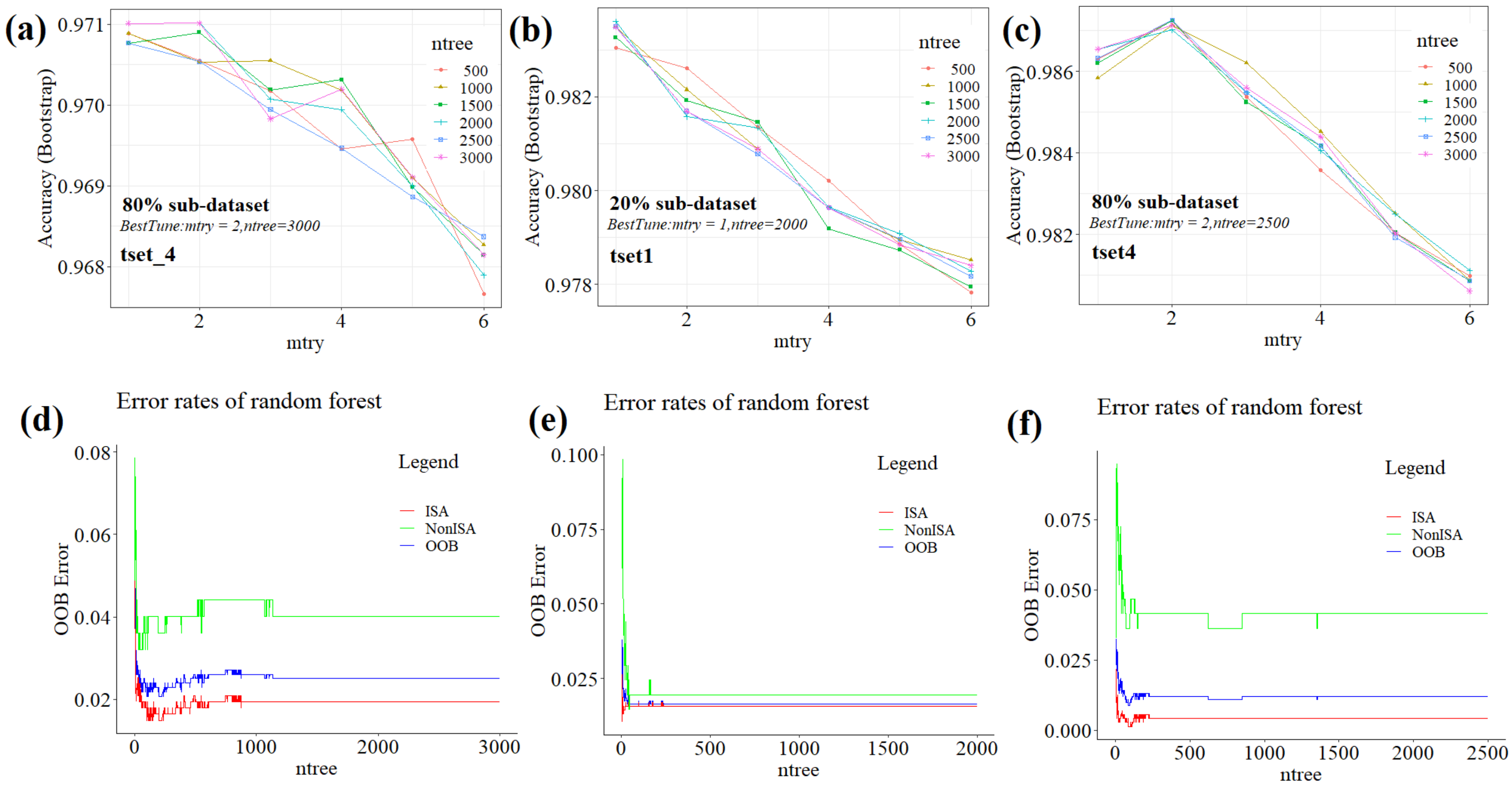

Figure 5.1 (a) – (c) Effect of the number of trees and the number of random split variables at each node (*mtry*) while (d) –(f) shows the relationship between OOB error (y-axis) and *ntree* parameter (x-axis) of the RF classifier based on the best sub-datasets of training sample data for 1995, 2005 and 2015.

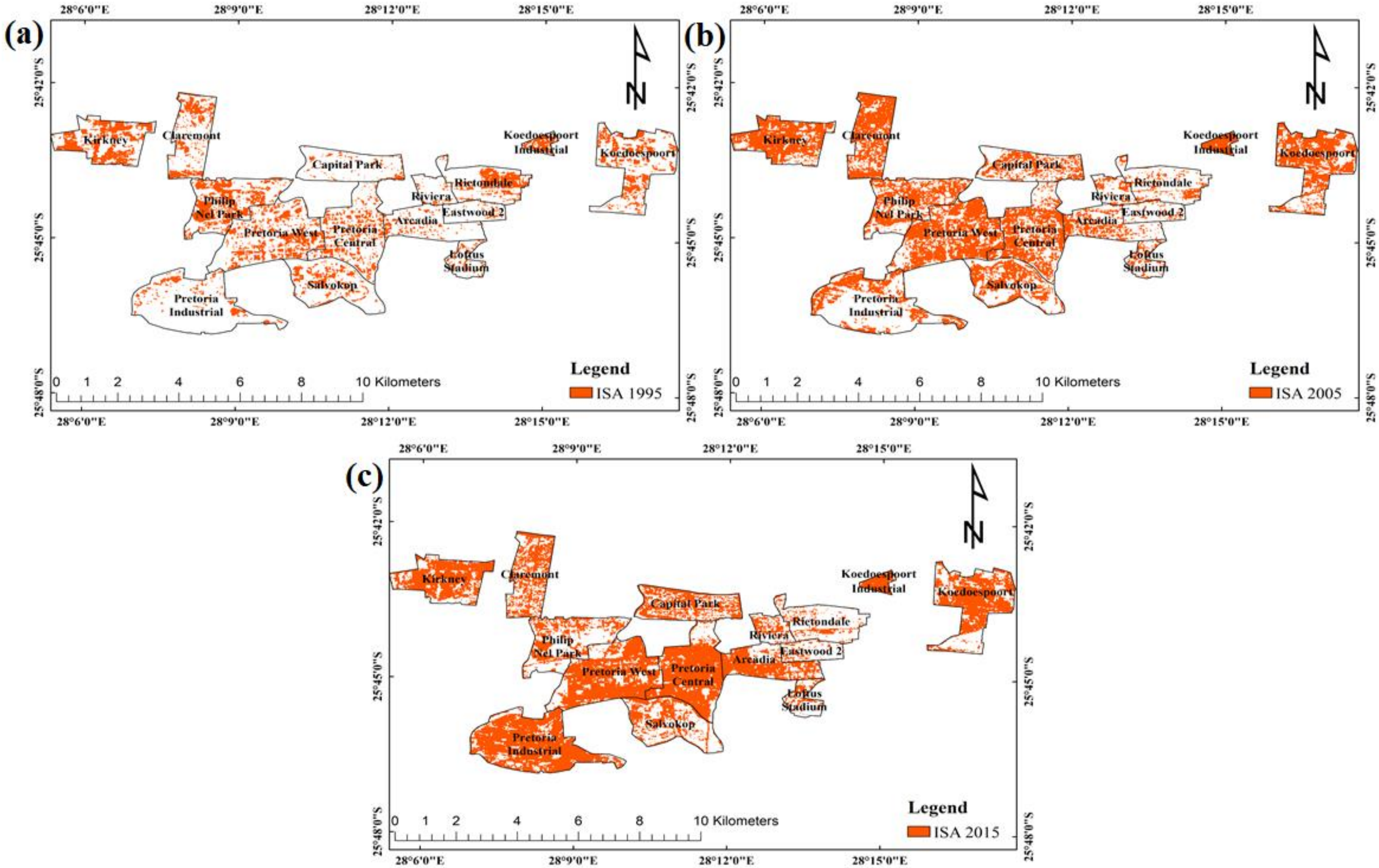

Figure 5.2 Random forest ISA classification maps of different periods (a)1995, (b) 2005 and (c) 2015.

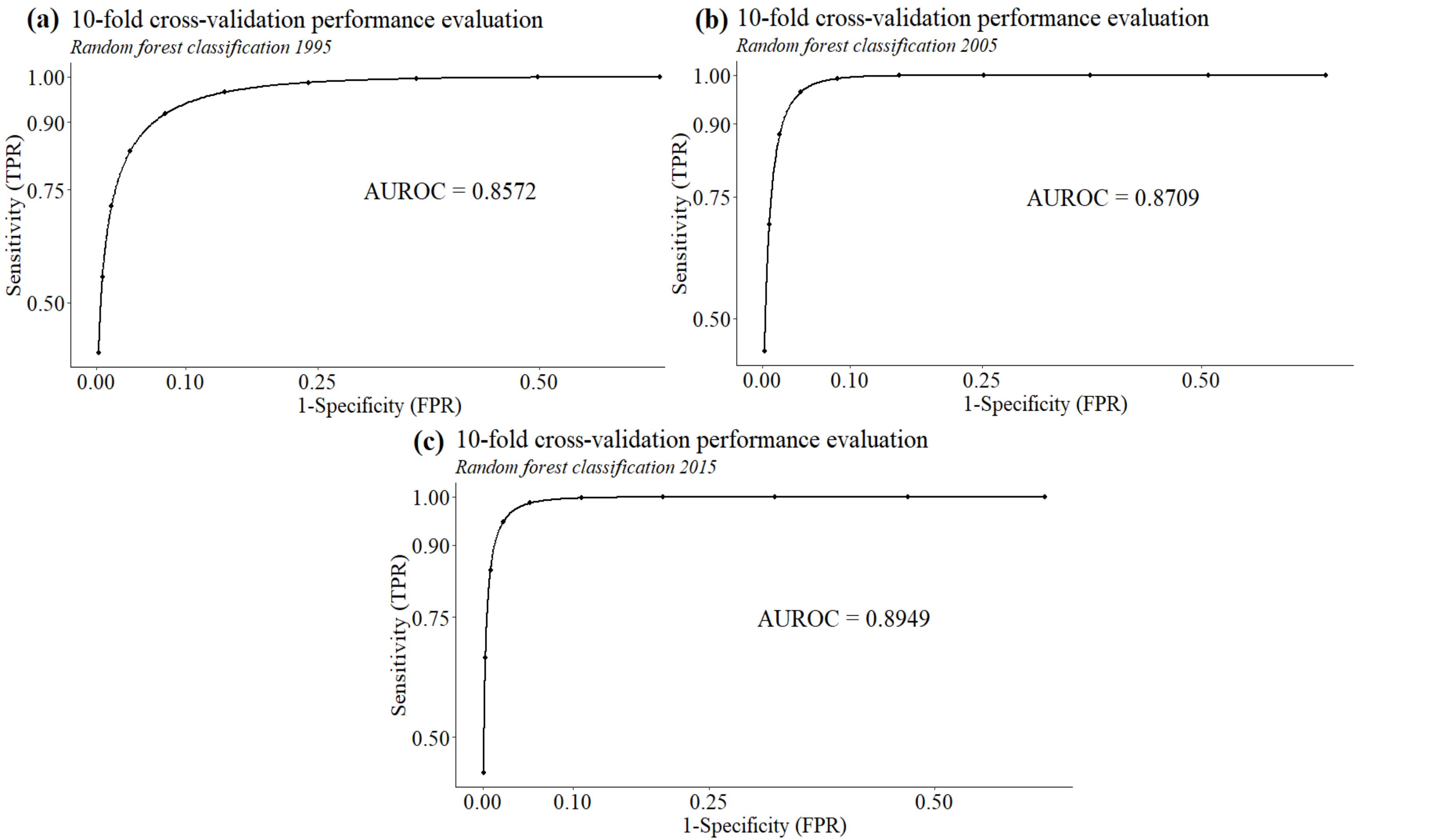

Figure 5.3 AUROC curve showing the performance evaluation of random forest ISA classification (a) 1995 (b) 2005 (c) 2015.

Also, all OOBs of all sub-datasets remain stable when ntree increase from 2000 to 3000, 1000 to 2000 and 1500 to 2500 respectively for each year used in this study (Figure 5.1(d-f)). Hence, *ntree* = 3000, 2000 and 2500 coupled with the highest results of *mtry* were the best parameters used.

5.4.2. The performance evaluation of random forest classifier on sub-datasets

As shown in Figure 5.1(a-c) with the best sub-datasets for each year, the three highest accuracies were considered for the random forest model. The highest accuracy for the random forest model for 1995 and 2015 was observed when the training sample size was large enough (80%) i.e., ~97% and ~98% accuracies respectively. Whereas the highest accuracy for random forest model for 2005 occurred with 20% of the training samples i.e., ~95% (Figure 5.1b). In addition to visual examination of all the thematic images outputs shown in Figure 5.2(a-c), the area under the receiver operating characteristic curve (AUROC) was used to evaluate the performance of the random forest classifier in extracting ISA or built-up areas across the study area over the 30year period. As shown in Figure 5.3(a-c), the computed AUROC values were: AUROC = 0.8572 for 1995, AUROC = 0.8709 for 2005, AUROC = 0.8949 for 2015 respectively. Therefore, based on the stratified 10-fold cross-validation, the results indicate that the random forest classifier effectively depicted ISA with relatively high precision.

5.4.3. Dynamic change in ISA in the administrative subplace Units

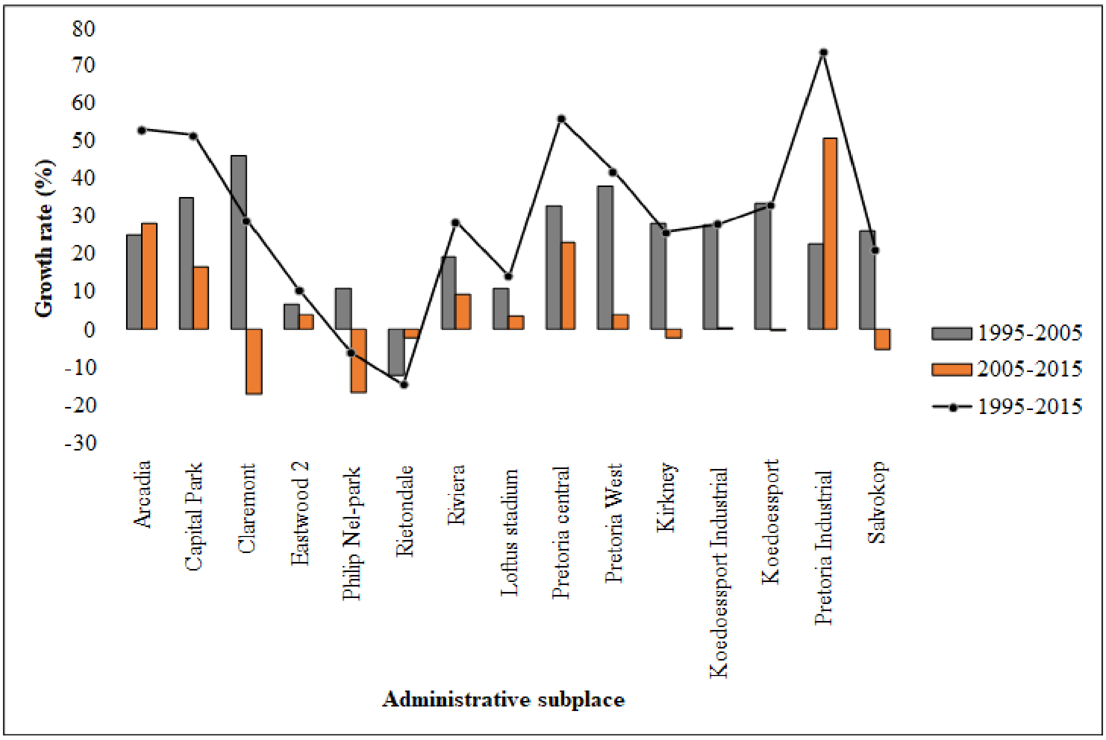

Figure 5.4 Variations in ISA growth rate for the selected administrative sub-places.

Table 5.3 and Figure 5.4 reveals the spatial and temporal changes of the impervious surfaces area during the 30 study years. Based on the selected dominant land use of the administrative sub places, the results show an increase from 1995 to 2015 in ISA (hectares, ha) and growth rate (%) respectively. For instance, formal residential: Arcadia(~41ha to ~197ha; 53%), Capital Park(~31ha to ~206ha; 51%), Eastwood 2(~13ha to ~28ha; 11%), Riviera(11ha to ~44ha; 29%); Commercial: Loftus Stadium(21ha to 37ha; 14%), Pretoria Central(~140ha to 419ha; 55%), Pretoria West(197ha to 454ha; 42%); Industrial: Kirkney(~178ha to ~277ha; ~26%), Koedoespoort Industrial(~38ha to 53ha; 28%), Pretoria Industrial(~59ha to 543ha; ~74%) and Collective living quarters: Salvokop(8ha to ~169ha; 21%). Although the ISA relatively decreased in other places during the same period (e.g., Formal residential: Claremont(~264ha to 204.03ha), Philip Nel Park(243ha to ~168ha), Rietondale(~66ha to 59%) and Industrial: Koedoespoort(323ha to 321ha), it is still observed that more than 70% of the selected administrative subplace units in this study experienced dramatic growth in impervious surfaces.

Table 5.3 Spatio-temporal analysis of the impervious surfaces area of selected sub-places in the study area.

Pretoria Administrative Subplace	Dominant land use type	ISA 1995 (ha)	ISA 2005 (ha)	ISA 2015 (ha)
Arcadia	Formal residential	40.77	115.02	197.01
Capital Park	Formal residential	30.51	149.76	206.10
Claremont	Formal residential	102.24	263.61	204.03
Eastwood 2	Formal residential	12.87	21.96	27.54
Philip Nel-park	Formal residential	195.12	243.27	167.67
Rietondale	Formal residential	104.85	65.88	59.04
Riviera	Formal residential	11.25	33.12	43.56
Loftus stadium	Commercial	21.15	33.39	37.44
Pretoria central	Commercial	135.99	302.04	418.86
Pretoria West	Commercial	197.10	432	454.05
Kirkney	Industrial	177.75	285.66	276.48
Koedoessport Industrial	Industrial	37.80	52.74	53
Koedoessport	Industrial	150.93	323.37	321.93
Pretoria Industrial	Industrial	58.77	208.08	543.33
Salvokop	Collective living quarters	82.44	189.63	168.75

Total Area selected subplaces in Pretoria = 5263ha; 1ha = pixel count X 900m^2 X 0.0001

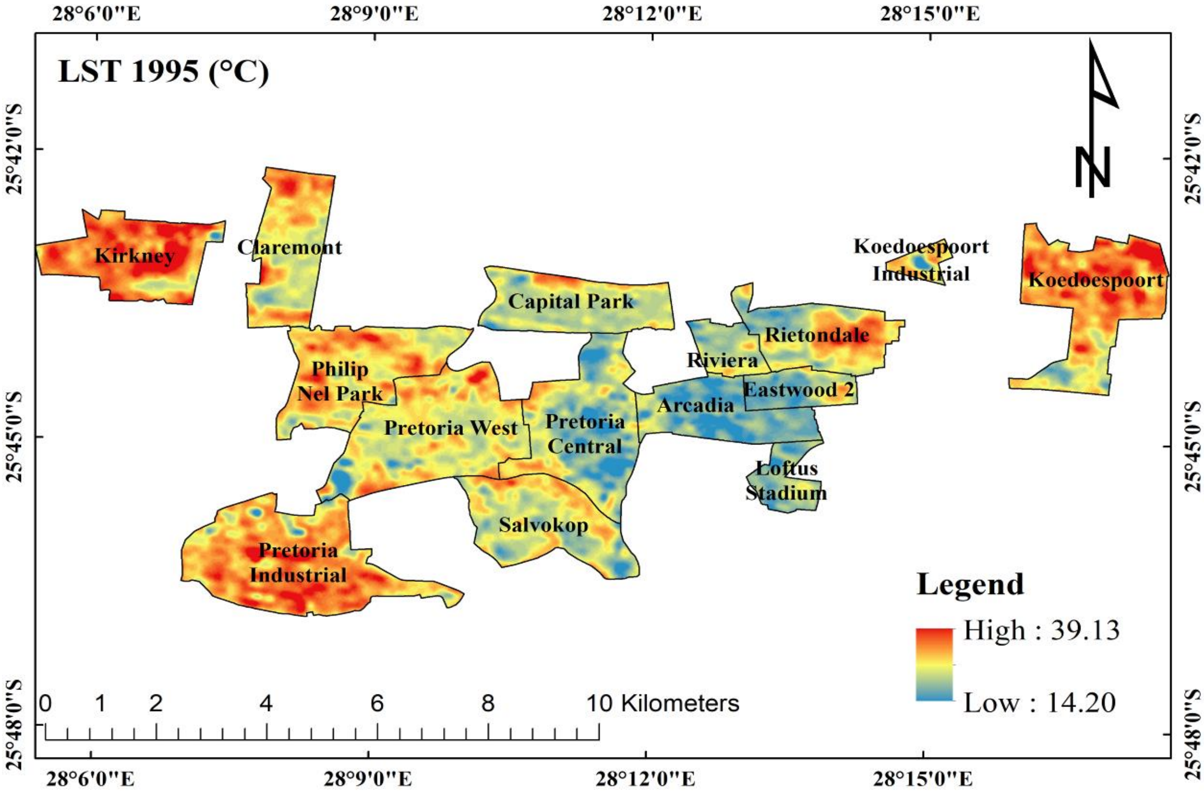

Figure 5.5 LST maps (^{O}C) of selected sub-place in Pretoria city in 1995.

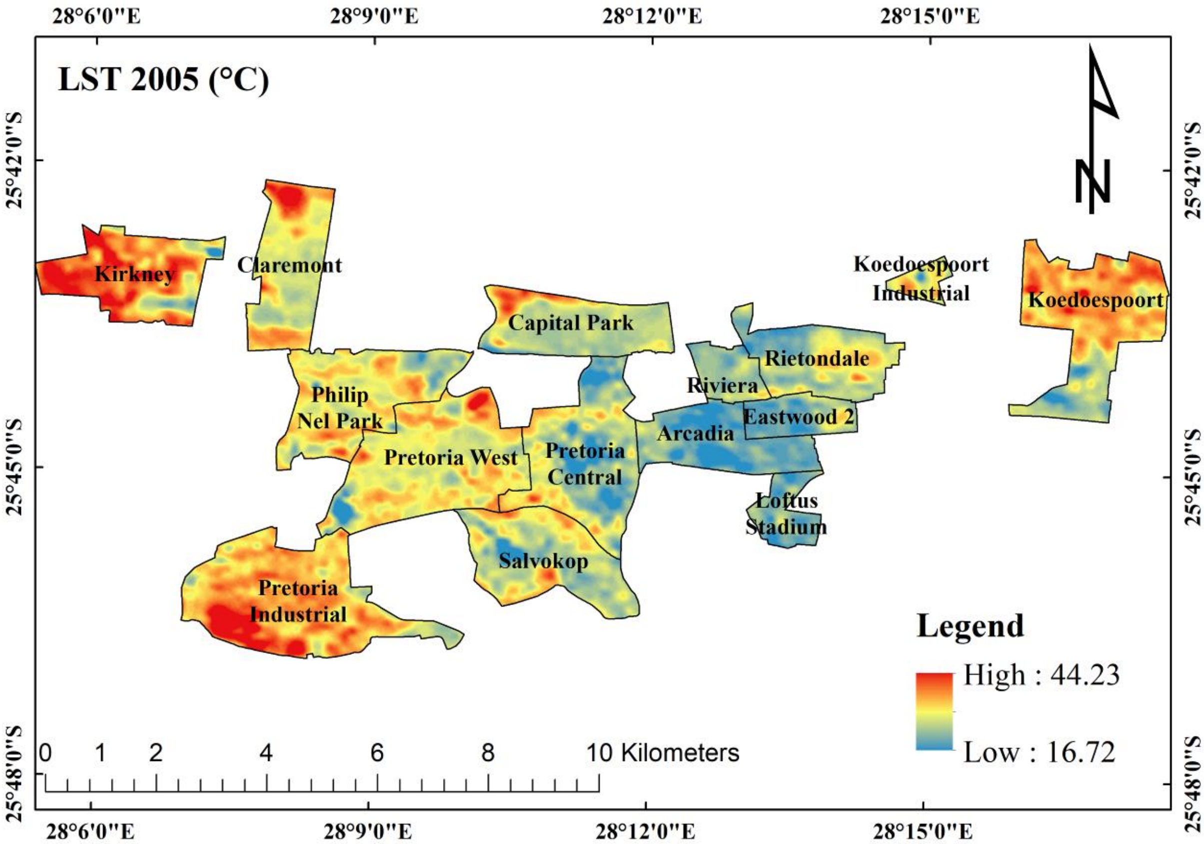

Figure 5.6 LST maps (^{O}C) of selected sub-place in Pretoria city in 2005.

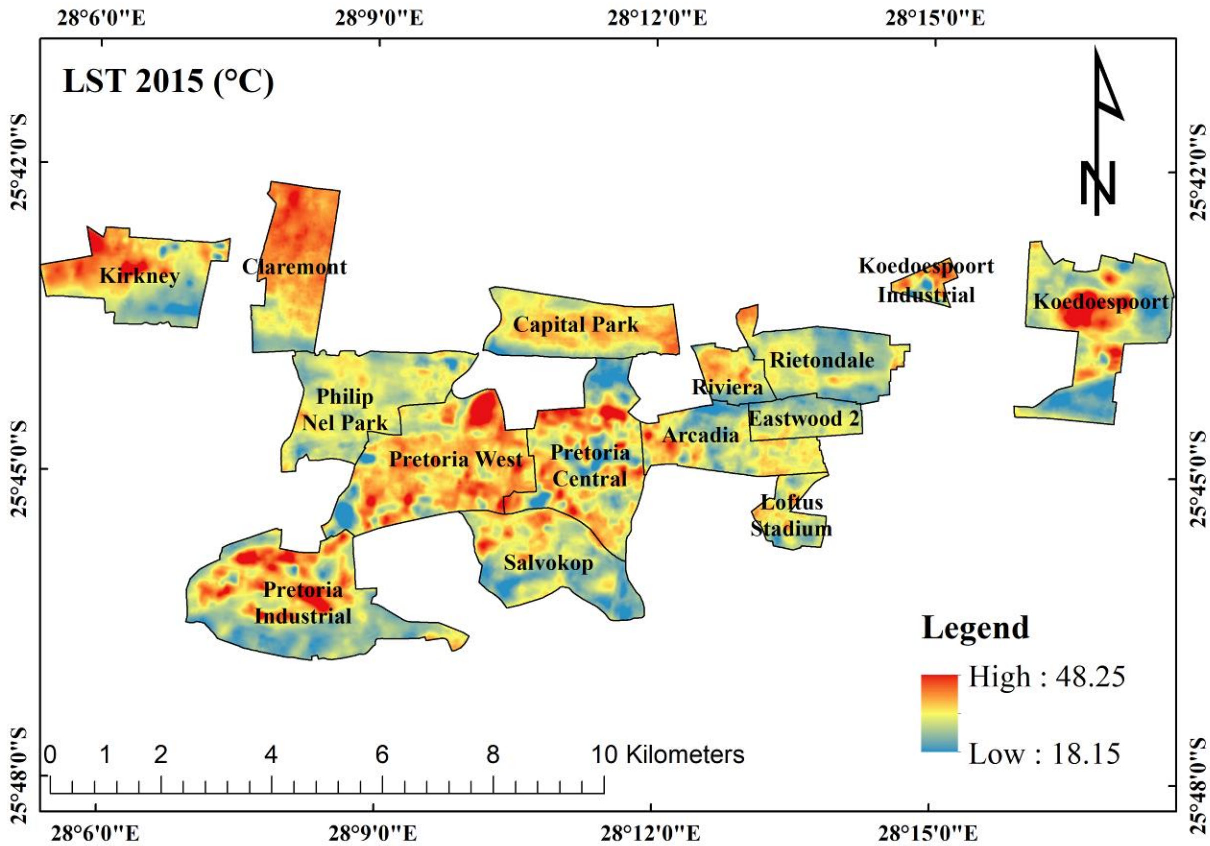

Figure 5.7 LST maps (^{O}C) of selected sub-place in Pretoria city in 2015.

5.4.4. Land Surface Temperature Retrieval (LST) for ISA

Figure 5.5, Figure 5.6 and Figure 5.7 illustrate the spatial pattern of absolute normalized LST retrieved for the study. The computed LST map for the entire study area shows that for 1995, 2005 and 2015, LST values range between 14.20 ^{O}C – 39.13 ^{O}C, 16.72 ^{O}C – 44.23 ^{O}C and 18.15 ^{O}C – 48.25 ^{O}C respectively. This study revealed that the maximum LST for the whole area went up by ~9 ^{O}C from 1995 to 2015, which were 42.12^{O}C to 53.26^{O}C; the minimum temperature increased by 3 ^{O}C from 14.20 ^{O}C to 18.15 ^{O}C, during the same season with the ten-year interval. This result indicates that the changes in land cover types thermal emittance have resulted in climate change as reported by the South African Weather Service (SAWS) in recent years. An earlier study by Adeyemi *et al.* (2015) revealed that ISA can be used as a complementary metric for surface urban heat island studies, in this study we also examined the variation in ISA thermal emittance for 1995, 2005 and 2015 based on the above pixel samples. Based on the spatial distribution of land surface temperatures of ISA derived from the Landsat images for the selected administrative subplace units study years in Pretoria, the mean ISA surface temperature for 1995 was 22.51^{O}C (standard deviation of 1.38 ^{O}C), followed by 2005 with a mean of 27.01 ^{O}C (standard deviation of 1.62 ^{O}C) and the highest mean ISA LST of 29.48 ^{O}C (standard deviation of 2.21) in 2015.

Also, we verified the overall metrics error between the predicted and actual LST to assess the accuracy of the retrieved LST image for the study area. The result indicates that the overall retrieval error for the study area is quite low: ~1.44^{O}C for RMSE and ~1.05 ^{O}C for MAE (1995), ~1.40 ^{O}C for RMSE and ~1.08 ^{O}C for MAE (2005) and ~0.86 ^{O}C for RMSE and ~0.59 ^{O}C for MAE (2015) respectively. Thus, the thermal bands of Landsat 5TM and Landsat 8 TIRS data employed for this study provided good results and can be used for further temperature variability analysis.

5.4.5. Spatio-temporal developing trends of ISA expansion

In this study, the ISA surface temperature weighted standard deviation ellipse (SDE) was used to further reveal the spatio-temporal developing trends of ISA expansion. We used the rotation angle of SDE to analyse the spatial direction of impervious surface expansion (Table 5.4 and Figure 5.8(a-o). It can be seen from Figure 5.8(a-o) that the SDEs of 15 administrative subplaces at the local region scale indicated significantly different ISA expansion directions. In Eastwood 2, with an approximated rotation angle of ~92^{O} the spatial direction of ISA expansion was eastern in 1995 and 2005 (Figure 5.8d). After that the rotation angle decreased by 3.4^{O} (Table 5.4), indicating a change in ISA distribution in an east-north-east in 2015. In Riviera, the rotation was maintained at an angle of ~114^{O} - ~116^{O} from 1995-2015 (Figure 5.8n). This implies that during the study period, the ISA mainly expanded towards the southeast. In Arcadia (Figure 5.8a), Pretoria Industrial (Figure 5.8k), Rietondale (Figure 5.8m) and Salvokop (Figure 5.8o) with rotation angles > 90^{O}, the ISA mainly expanded to the east-south-east from 1995 and 2005. Also, a north-north-east ISA expansion trend was observed from 1995-2015 in Claremont (Figure 5.8c), Koedoespoort (Figure 5.8f), Loftus Stadium (Figure 5.8h) and Pretoria Central (Figure 5.8j) with rotation angles < 45^{O}. In Capital Park (Figure 5.8b) and Kirkney (Figure 5.8e) with rotation angles slightly > 90^{O}, the ISA expanded to the east. In Koedoespoort Industrial (Figure 5.8g), Philip Nel Park (Figure 5.8i) and Pretoria West (Figure 5.8l), with rotation angle maintained < 90^{O}, the ISA significantly expanded towards the east-northeast in these subplaces during the study period.

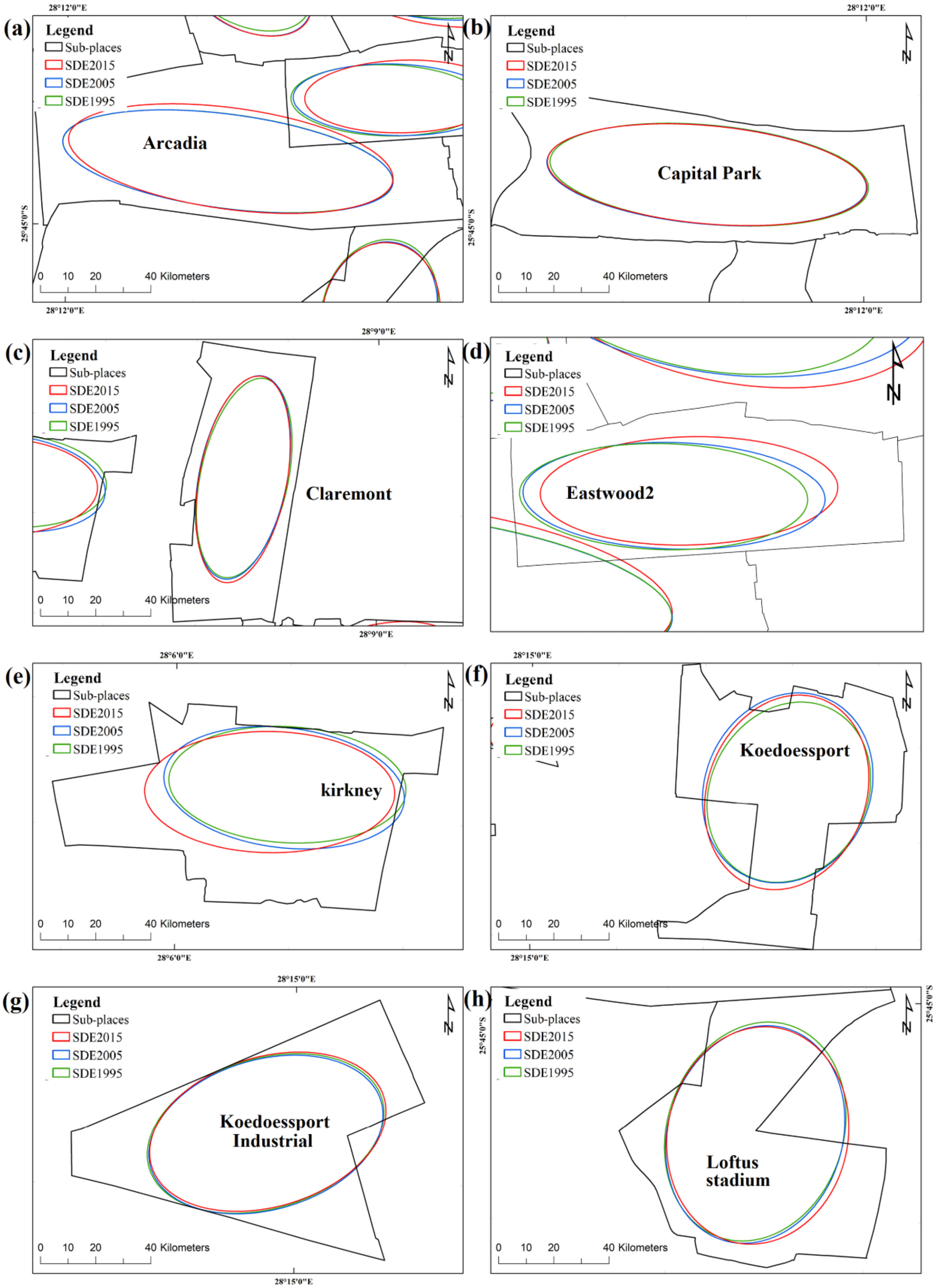

Figure 5.8 SDEs of ISA surface temperature for the selected administrative sub-places (i.e., local region scale) for different periods (continued overleaf).

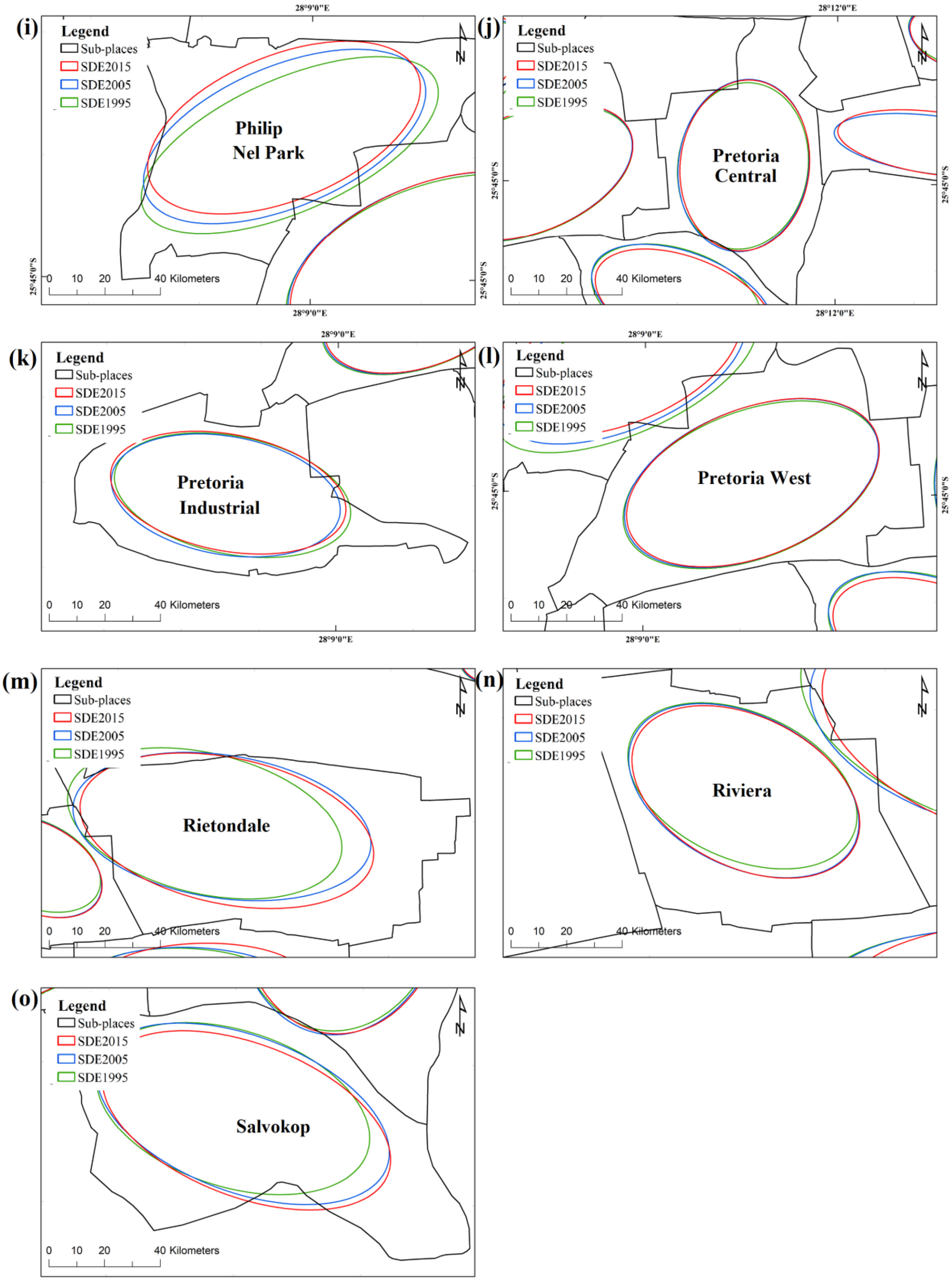

Figure 5.8. (continued)

Table 5.4 SDE parameters of impervious surface expansion from 1995 to 2015.

Subplace	Dominant land use type	Year	Rotation angle (^{O})	ISA Expansion Direction
Arcadia	Formal Residential	1995	97.433	ESE-ESE-ESE
		2005	97.532	
		2015	97.825	
Capital Park	Formal Residential	1995	95.234	E-E-E
		2005	94.998	
		2015	95.261	
Claremont	Formal Residential	1995	11.915	NNE-NNE-NNE
		2005	11.169	
		2015	10.763	
Philip Nel Park	Formal Residential	1995	66.276	ENE-ENE-ENE
		2005	67.229	
		2015	67.625	
Rietondale	Formal Residential	1995	103.429	ESE-ESE-ESE
		2005	98.664	
		2015	101.424	
Riviera	Formal Residential	1995	114.033	SE-SE-SE
		2005	116.313	
		2015	116.343	
Eastwood 2	Formal Residential	1995	91.457	E-E-ENE
		2005	91.588	
		2015	88.604	
Kirkney	Industrial	1995	93.274	E-E-E
		2005	96.762	
		2015	90.893	
Koedoespoort	Industrial	1995	28.309	NNE-NNE-NNE
		2005	24.712	
		2015	21.535	
Koedoespoort Industrial	Industrial	1995	73.335	ENE-ENE-ENE
		2005	73.995	
		2015	74.045	
Pretoria Industrial	Industrial	1995	101.356	ESE-ESE-ESE
		2005	99.848	
		2015	100.258	
Loftus Stadium	Commercial	1995	18.671	NNE-NNE-NNE
		2005	16.692	
		2015	11.769	

Pretoria Central	Commercial	1995	8.319	NNE-NNE-NNE
		2005	8.005	
		2015	6.561	
Pretoria West	Commercial	1995	68.786	ENE-ENE-ENE
		2005	68.396	
		2015	68.495	
Salvokop	Collective living quarters	1995	107.829	ESE-ESE-ESE
		2005	110.535	
		2015	110.813	

5.5. Discussion

Over the years, the urban expansion experienced in the selected administrative subplaces for this study in Pretoria is not only seen as a sign of growth and prosperity but has continuously brought about expanded infrastructure which are impervious surfaces (Adeyemi *et al.*, 2015). These increase in man-made features (i.e., ISA) and their sequential relationship with climatic variables such as surface temperature (e.g., LST) are crucial to understanding urban sprawl (Tian *et al.*, 2018). In this study, the ISA data extracted with multispectral Landsat-5 TM and Landsat 8 with six bands (VIS-SWIR) images, were used to investigate the spatio-temporal dynamics and the expansion direction of urban sprawl at local administrative subplace units in Pretoria from 1995 to 2015. The first results in Figure 5.1 highlight the potential use of random forest classifier with different sample sizes to estimate ISA from Landsat image for the entire study years. Based on the four sub-datasets with corresponding sizes 20%, 40%, 60% and 80% of the total training data for each year, two different trends were clear: when the training sample size was large enough (80%), the highest accuracy for the RF model was observed for 1995 and 2015 i.e., ~97% and ~98% respectively. Whereas highest accuracy for rf model for 2005 occurred with 20% of the training samples i.e., ~95%. The high accuracies associated with the training samples sizes which were large enough for each of the years, shows that the RF model was less sensitive to the imbalanced training data. Though this might be contradictory to many past studies on different satellite images such as Jin et al. (2014), Colditz (2015) and Mellor et al. (2015) to mention a few that asserted that the greater the land cover class area is, the more training samples that are needed to produce the best classification accuracy. The use of RF model in our study reveals similarity to the studies of Shrestha, et al. (2021) and Thanh Noi and Kappas (2017) that asserted that the RF classifier is less sensitive to the imbalanced training data as long as the training sample size is representative enough i.e. either large or small. After the visual examination of the random forest classifier thematic ISA outputs for the study years presented in Figure 5.2, their quantitative assessment based on 10-fold cross-validation, the AUROC was used to assess the unbiased predictive accuracy. Although the random forest classifier overall predictive accuracy was fairly high (i.e., AUROC = 0.8572 for 1995, AUROC = 0.8709 for 2005, AUROC = 0.8949 for 2015) because of the selection of representative training samples or pixels (Maxwell, Warner and Fang, 2018), there were still errors observed in the final thematic outputs due to mixed pixels i.e., ISA and vegetation (Xu et al. 2018) associated with the use of medium resolution multispectral satellite imagery. Secondly, we examined the ISA spatio-temporal dynamics within ten years interval time frame (i.e., 1995 -2015) at local region level. Results in Table 5.3 and Figure 5.4 above reveals while more than 70 % of the selected administrative subplaces (i.e., Arcadia, Capital Park, Eastwood 2, Loftus Stadium, Koedoespoort Industrial, Pretoria Central, Pretoria Industrial, Pretoria West, Riviera) in this study experienced dramatically increase in ISA growth rate. Generally, the ISA spatio-temporal dynamics in the study area could be attributed to the incessant urban sprawl resulting in many places across Pretoria. Since Pretoria is one of the three capital cities in South Africa, the remarkable ISA growth over the years could also be due to political and socio-economic factors.

Finally in our study, guided by the previous study of Xiao et al. (2018) on an optimal analytical scale, we used the hexagon sampling grid covering and aggregating the depicted ISA surface temperature pixels to examine the spatio-temporal developing trends of ISA expansion with the aid of weighted standard deviational ellipse (SDE) method. Similar to the recent studies of Xu et al., 2018; Man et al., 2019 and Hua et al., 2020), our results indicated that the ISA exhibited an expansion trend generally in the east-south-east, east, north-north-east, east-north-east and south-east directions. This can be attributed to the change ISA growth rate coupled with population and various land use activities at the local administrative subplace units. In this study, it can therefore be asserted that the spatio-temporal pattern of ISA surface temperature is an important metric in understanding the principle direction of ISA expansion.

5.6. Conclusion

Satellite imagery that measures spatio-temporal dynamics of impervious surface areas (ISA) in the context of rapid development, is key to understanding the process of urban expansion.

The information obtained this way can serve as valuable input when dealing with challenges related to the environment, climate (for example shifts in land surface temperature (LST)), population health, natural resources etc.). Using a combination of quantitative remote sensing images such as Landsat 5 Thematic Mapper (TM), Landsat 8 Thermal Infrared Sensor (TIRS) and Operational Land Imager (OLI), and spatial statistical methods, the study investigated the spatio-temporal direction of ISA expansion at a local spatial scale, based on its surface temperature and within a time frame interval of ten years. The study displayed two main strengths. Firstly, the use of random forest algorithm (RF) based on different training sample subsets, enabled the researchers to accurately estimate and reveal the spatio-temporal dynamics of ISA in selected administrative sub place levels in Pretoria. Secondly, the researchers were able to identify the principal direction of urban expansion at a local spatial scale in Pretoria by combining zonal statistics with weighted SDE spatial statistical method. The findings of this study could be used by policymakers and urban planners as a key measure to detect places where urbanization is rapid, and prioritize areas of immediate attention and development of smart growth strategies. Future studies should focus on spatio-temporal urban expansion at different spatial scales (e.g., local and regional), depending on the coverage and commercial availability of fine resolution multispectral satellite imagery. Population, gross domestic product (GDP), topography, hydrology, socio-economic settings etc. may also be considered as drivers when modelling spatio-temporal urban dynamics.

Chapter 6 Synthesis – Conclusion, Limitations, Recommendations And Future Research

This chapter presents the conclusion of this study which includes a summary of results, discussion and deduction for each technical chapter followed by limitations encountered in the entire study and at the end we provided recommendations and further considerations for future studies.

6.1. Conclusion

The overall aim of this study was to explore built-up ISA mapping and investigate its interaction with land surface temperature variability using remote sensing and ancillary data in Pretoria, City of Tshwane, Gauteng Province, South Africa. This was investigated at high and medium resolution multispectral levels. Overall, we revealed that the information contained in high resolution (WorldView-2) and medium resolution (Landsat) multispectral data could accomplish the task of mapping the ISA and assessing its interaction with retrieved surface temperature.

This conclusion was based on the following observations made at experimental levels.

6.1.1. Spectral index to improve built-up impervious surface area delineation

The first objective explored the utility of a new spectral index (NBEI) to improve the delineation of built-up impervious surface area from very high-resolution multispectral data (e.g., WorldView-2) i.e., the capability of NBEI to accurately extract built-up ISA (e.g., roads and building rooftops materials). Since the challenge in built-up ISA extraction in any satellite imagery is the confusion with other non-built-up land covers, we first analysed the spectral profiles of sample pixels for built-up ISA. The significant WV-2 bands or wavelengths selected for the formulation of the new index (NBEI) for built-up area detection were NIR2 (860-1040nm) , NIR1 (770-895nm), Red edge(705-745nm) and Green(510-580nm) (Table 2.2) as they were able to depict a significant difference in the shape of spectral signature. Also, the feature selection and ranking reliefF algorithm employed, found that Green, Red edge, NIR1 and NIR2 are the most suitable bands to extract the built-up ISA pixels from the WV-2 image (Figure 2.1).

After the threshold and comparative analysis with other existing built-up spectral indices in the study area (Figure 2.5), the precision evaluation results in Figure 2.6 showed that NBEI improves the extraction of built-up areas with high accuracy (area under the receiver operating characteristic curve, AUROC = ~0.82) compared to the existing indices such as Built-up Area Index (BAI) (AUROC = ~0.73), Built-up spectral index (BSI) (AUROC =

~0.78), Red edge / Green Index (RGI) (AUROC = ~0.71) and WorldView-Built-up Index (WV-BI) (AUROC = ~0.67). This implies that NBEI exhibited optimal separability from non-ISA and better performance in built-up ISA extraction in high resolution multispectral imagery. In contrast to other methods of built-up ISA extraction from VHR multispectral imagery. NBEI is very easy to implement and more reliable. Since the performance of the spectral index depends on the spectral response of land cover characteristics (i.e., age, colour, material, texture etc.) which varies from one region to another due to climate and topography coupled with socio-economic activities, the effectiveness of the new built up extraction index for WV-2 still needs to be tested at different study sites within the urban setting.

6.1.2. Investigating exposed rooftop impervious surface area interplay with surface temperature variability

The second objective was set to examine exposed rooftop impervious surface area based on different colours and its impact on surface temperature variation. We first analysed the factors (i.e. explanatory variables such as texture measures, topography) that influence both daytime rooftop surface temperatures to understand this relationship at a comprehensive level. From the satellite images, the result clearly shows that the interaction between the applicable rooftop explanatory features (i.e., reflectance, texture features and topographical properties) can explain over 22.10% of the variation in daytime rooftop surface temperatures (Table 3.11). This adjusted R^2 value with these significant explanatory variables suggests that most of the rooftops exhibited fewer heat retentions as observed in the daytime temperature variations.

Moreover, analysis of spatial distribution between mean daytime surface temperature and the residential rooftop indicated that dark and blue roof surface exhibited a high LST value (i.e., 28.84 ^{O}C and 28.78 ^{O}C) due to the low reflectivity, low emissivity and high heat capacity while the red, brown and green roof surface show lower LST values (i.e., 28.77 ^{O}C, 28.65 ^{O}C and 28.58 ^{O}C) due to high reflectivity, high emissivity and low heat capacity during the daytime (Figure 3.7). Similarly, our findings partly confirm what has already been highlighted in the few previous studies of (Huang, Zhou and Cadenasso, 2011; Myint *et al.*, 2013; Zheng, Myint and Fan, 2014; Zhao *et al.*, 2015; Morabito *et al.*, 2018) to mention a few that have dealt with similar issues but not in an African context. Therefore, this experimental study confirms the possibility of remote sensing data not only to understand the spatial distribution of building rooftop appearances but also how it influences microclimate patterns (i.e., rooftop heat insulation or retention properties) at the urban level, providing useful information for local authorities, land-use decision-makers, and urban planners.

6.1.3. Spatio-temporal distribution pattern of built-up ISA and its influence on UHI magnitude

The third objective was set to determine if the spatio-temporal built-up ISA distribution pattern in relation to elevation influences urban heat island (UHI) extent using an optimal analytical scale, across Pretoria, South Africa. Tian *et al.* (2018) pointed out that ISA distribution in recent years has emerged not only as a feature of urbanization but also as a major index of environmental quality. Therefore, accurate extraction of built-up ISA is crucial to ecological assessment. In this study, we first performed the multi-temporal analysis of built-up ISA across Pretoria from the Landsat (TM, OLI and TIRS) images spanning a total time frame of 30 years: 1993, 2003, and 2013 using built-up index (BUI). The computed indices provided empirical insight into a realistic multi-temporal built-up ISA situation and its spatial expansion change rates in the study timeframe.

Results from Table 4.3 above reveal that ISA growth rate of 5% was observed between the years 1993 and 2003, while a significant growth rate of 9% was recorded between the years 2003 and 2013. Hence, the total built-up ISA growth rate during the 30 study years is 14 %. Spatially, the increased built-up ISA in the study area could be attributed to the incessant urbanization that has resulted in many fold increase in Pretoria as it is one of the three capital cities in South Africa. The remarkable built-up ISA growth over the years is also due to political and socio-economic activities. The distribution of built-up ISA spatio-temporally over different elevation levels was also assessed using the density plot. The count and histogram peak enabled us to depicts that most of the built-up ISA increase occurred between >1200m – 1600m. Since, built-up ISA can be used as a complementary metric for surface urban heat island (i.e., LST variability) studies, we examined the variation in built-up ISA-related LST over the years.

Furthermore, based on an optimal analytical scale we used the hexagon polygon grid to establish the match between the index derived built-up ISA, LST and elevation pixel values to examine: Firstly their relationship using correlation analysis to identify spatio-temporal ly the direction of significant built-up ISA growth. Secondly, to understand the UHI extent using the Getis-Ord Gi* statistics (hotspot and cold spot maps) to identify the location and degree of spatial clustering of built-up ISA surface temperature pixel values. In conclusion, this study indicates built-up ISA growth pattern affects the magnitude of UHIs. The useful information and methodology presented in this study will be helpful in sustainable planning of urban areas and for the mitigation of effects of UHI especially in the African context where very little has been done in this regard.

6.1.4. Spatio-temporal direction of impervious surface area surface temperature at local region scale

Finally, the fouth objective was set to assess the spatio-temporal change characteristics of ISA expansion using its surface temperature (LST) at selected administrative subplace units (i.e., local region scale). Xu et al. (2018) asserted that impervious surfaces can absorb heat from sunshine during the daytime which leads to higher LSTs in urban areas than rural counterparts, making this concept a key factor in studying urban development and the related environmental issues (Shahtahmassebi *et al.*, 2016; Zhang and Shao, 2017). Thus, accurate time-series impervious surface extraction and mapping are relevant to the research of urban expansion and development. In this study, we first performed the multi-temporal analysis of ISA extraction from the multispectral Landsat-5 TM and Landsat 8 images at ten years intervals with a spanning total time frame of 30 years: 1995, 2005, and 2015 using random forest classifier.

The results in Figure 5.3 indicated ISA estimation with high predictive accuracy (i.e., area under the receiver operating characteristic curve AUROC = 0.8572 for 1995, AUROC = 0.8709 for 2005, AUROC = 0.8949 for 2015) using RF classifier. This highlight the potential use of random forest classifier with different sample sizes to estimate ISA from the Landsat images for the entire study years. The use of RF model in our study reveals similarity to the study of Thanh Noi and Kappas (2017) that hypothesis that the classifier is less sensitive to the imbalanced training data if the training sample size is large enough. After the visual examination and predictive accuracy assessment, thematic ISA outputs provided practical insight into a realistic ISA situation and its spatial expansion change rates at each selected administrative subplace in the study timeframe.

In addition, guided by the previous study of Xiao et al. (2018) on an optimal analytical scale, we used the hexagon polygon grid covering the ISA to aggregate its surface temperature pixels to examine the spatio-temporal characteristics of ISA expansion with the aid of weighted standard deviational ellipse (SDE) method. Also, the results indicated that the ISA exhibited an expansion trend generally in the east-south-east, east, north-north-east, east-north-east and south-east directions, similar to the recent studies of Xu et al. (2018), Man et al. (2019) and Hua et al. (2020). This study affirms that ISA surface temperature weighted SDE method could reveal the principle direction of ISA expansion at local region level. The useful information and methodology presented in this study will be helpful in better identifies areas with urban sprawl with no implementation of proper planning and control policies in Pretoria, City of Tshwane (COT), Gauteng, South Africa.

6.2. Limitations

1. The research conducted involved various desktop analysis and few field verification due to limited resources.
2. Several spectral signatures could not be obtained during the field verification because many private properties were restricted areas and it would have taken months to sort out the necessary documentation to gain access into this premise.
3. Similarly, few multispectral medium and high satellite images were used for the research.
4. The thermal infrared images selected were considered as key limitations in this research. Apart from them being a medium resolution, the selection also depends on the existence of cloud cover. Since the thermal images do not offer a comprehensive LST pattern in the study area, it was difficult to identify precise LST tend since the temperature of a specific day might not be representative of the general trend during the study period.
5. When mapping ISA in a large area using very high resolution imagery (e.g., WV-2), we encountered limitations with the hardware system used i.e., requires high computation. Therefore, we could not implement our ISA mapping method on the entire study area but obtained a subset.

6.3. Recommendations

Some recommendations are highlighted below:

1. Additional information can also be acquired through comprehensive field observations to address issues of mapping reliability of the various ISA associated with different land use types.
2. Direct measurement of thermal response and emissivity of ISA can also be of great advantage in understanding of UHI pattern and thermal properties of urban landscape.

3. Also, policymakers must focus on strategies to modify urban geometry, for example, use of vegetation as a replacement for unnecessary impervious surface area can help minimize UHI effects.
4. Urban planners can also improve air quality in urban landscapes by including vegetation (e.g. trees, grasses) especially in major Africa cities e.g., Pretoria.

6.4. Future research

1. Different remote sensing data that may be explored to extract the ISA in future studies include very high spatial resolution WorldView-3, WorldView-4, hyperspectral data, DMSP-OLS Night-time Light etc.

2. Extraction of ISA from multi-source datasets such as very high spatial resolution multispectral imagery and airborne LIDAR data using various Convolutional Neural Networks should also be explored.

3. Fine resolution surface temperature commercial satellite data such as MASTER (7m MODIS/ASTER airborne simulator) depending on its coverage, may be employed to retrieve more accurate surface temperature variability in future studies.

4. Future studies may be conducted taking into consideration the influence of other metrics such as population, government policy, Gross Domestic Product (GDP), land availability, topography, hydrology, socio-economic settings etc. in the modeling of spatio-temporal dynamic patterns of ISA.

6.5. Conflicts of Interest

The authors declare no conflict of interest.

Acknowledgements

The author would like to thank the University of South Africa Student Funding Directorate (UNISA, DSF) and GeoTerraImage (Pty) Ltd for providing the research bursary to conduct this study. We acknowledge the United States Geological Survey Global Visualization Viewer (https://glovis.usgs.gov) due to their freely accessible Landsat and Shuttle Radar Topography Mission (SRTM) digital elevation model (DEM) data and the Natural Resources and the Environment, NRE, Council for Scientific and Industrial Research, CSIR for the WorldView-2 imagery and LiDAR dataset.

REFERENCES

Abdullah, H. (2012) *The use of Landsat 5 TM imagery to detect urban expansion and its impact on land surface temperatures in the city of Erbil, Iraqi Kurdistan, MSc diploma work, University of Leicester*. Leicester University.

Abutaleb, K. *et al.* (2015) 'Assessment of Urban Heat Island Using Remotely Sensed Imagery over Greater Cairo, Egypt', *Advances in Remote Sensing*, 04(01), pp. 35–47. doi: 10.4236/ars.2015.41004.

Adam, H. E., Csaplovics, E. and Elhaja, M. E. (2016) 'A comparison of pixel-based and object-based approaches for land use land cover classification in semi-arid areas, Sudan', in *IOP Conference Series: Earth and Environmental Science*. doi: 10.1088/1755-1315/37/1/012061.

Adelabu, S. *et al.* (2013) 'Exploiting machine learning algorithms for tree species classification in a semiarid woodland using RapidEye image', *Journal of Applied Remote Sensing*, 7(1), p. 073480. doi: 10.1117/1.jrs.7.073480.

Adeyemi, Adeniyi; Botai, Joel; Ramoelo, A. (2015) *Analysis of impervious surfaces and surface temperature over Tshwane metropolitan using in-situ and remotely sensed data*. University of Pretoria. Available at: https://repository.up.ac.za/handle/2263/50884.

Adeyemi, A. *et al.* (2015) 'Effect of impervious surface area and vegetation changes on mean surface temperature over Tshwane metropolis, Gauteng Province, South Africa', *South African Journal of Geomatics*, 4(4). doi: 10.4314/sajg.v4i4.1.

Adeyemi, A. *et al.* (2021a) 'Spectral index to improve the extraction of built-up area from WorldView-2 imagery', *Journal of Applied Remote Sensing*, 15(02). doi: 10.1117/1.jrs.15.024510.

Adeyemi, A. *et al.* (2021b) 'Spectral index to improve the extraction of built-up area from WorldView-2 imagery', *Journal of Applied Remote Sensing*, 15(02). doi: 10.1117/1.jrs.15.024510.

Aguilar, M. A. *et al.* (2014) 'Object-based greenhouse classification from GeoEye-1 and WorldView-2 stereo imagery', *Remote Sensing*, 6(5), pp. 3554–3582. doi: 10.3390/rs6053554.

Ahmed, B. *et al.* (2013) 'Simulating land cover changes and their impacts on land surface temperature in dhaka, bangladesh', *Remote Sensing*, 5(11), pp. 5969–5998. doi: 10.3390/rs5115969.

Aiazzi, B. *et al.* (2002) 'Advantages of hexagonal sampling grids and hexagonal shape detector elements in remote sensing imagers', *European Signal Processing Conference*, 2002-March.

Al-Kindi, K. M. *et al.* (2017) 'Modelling spatiotemporal patterns of dubas bug infestations on date palms in northern Oman: A geographical information system case study', *Crop Protection*, 93, pp. 113–121. doi: 10.1016/j.cropro.2016.11.033.

Aldred, D. and Wang, J. (2007) 'Object-oriented image classification for urban building boundary extraction from ikonos imagery', *American Society for Photogrammetry and Remote Sensing - 28th Canadian Symposium on Remote Sensing and ASPRS Fall Specialty Conference 2007*, pp. 1–10.

Alipour, T., Sarajian, M. . and Esmaeily, A. (2011) 'Land Surface Temprature Estimation From Thermal Band of Landsat Sensor , Case Study : Alashtar City', *The International Archives of the Photogrammetry, Remote Sensing and Spatial Information Sciences*, XXXVIII(2003), pp. 1–6.

Amiri, R. *et al.* (2009) 'Spatial-temporal dynamics of land surface temperature in relation to fractional vegetation cover and land use/cover in the Tabriz urban area, Iran', *Remote Sensing of Environment*, 113(12), pp. 2606–2617. doi: 10.1016/j.rse.2009.07.021.

Anusha, K. and Sathiyamoorthy, E. (2016) 'Comparative study for feature selection algorithms in intrusion detection system', *Automatic Control and Computer Sciences*, 50(1), pp. 1–9. doi: 10.3103/S0146411616010028.

Arnold Jr CL and Gibbons CJ (1996) 'Impervious surface coverage: The emergence of a key environmental indicator', *Journal of the American Planning Association*, 62(2), p. 243−258.

Artmann, M. (2014) 'Assessment of soil sealing management responses, strategies, and targets toward ecologically sustainable Urban land use management', *Ambio*, 43(4), pp. 530–541. doi: 10.1007/s13280-014-0511-1.

As-syakur, A. R. *et al.* (2012) 'Enhanced built-UP and bareness index (EBBI) for mapping built-UP and bare land in an urban area', *Remote Sensing*, 4(10), pp. 2957–2970. doi: 10.3390/rs4102957.

Asner, G. P. and Levick, S. R. (2012) 'Landscape-scale effects of herbivores on treefall in

African savannas', *Ecology Letters*, 15(11), pp. 1211–1217. doi: 10.1111/j.1461-0248.2012.01842.x.

Awrangjeb, M., Zhang, C. and Fraser, C. S. (2013) 'Automatic extraction of building roofs using LIDAR data and multispectral imagery', *ISPRS Journal of Photogrammetry and Remote Sensing*, 83, pp. 1–18. doi: 10.1016/j.isprsjprs.2013.05.006.

Belgiu, M. and Drăgu, L. (2016) 'Random forest in remote sensing: A review of applications and future directions', *ISPRS Journal of Photogrammetry and Remote Sensing*, 114, pp. 24–31. doi: 10.1016/j.isprsjprs.2016.01.011.

Belgiu, M., Drăguţ, L. and Strobl, J. (2014) 'Quantitative evaluation of variations in rule-based classifications of land cover in urban neighbourhoods using WorldView-2 imagery', *ISPRS Journal of Photogrammetry and Remote Sensing*, 87, pp. 205–215. doi: 10.1016/j.isprsjprs.2013.11.007.

Berhane, T. M. *et al.* (2018) 'Decision-tree, rule-based, and random forest classification of high-resolution multispectral imagery for wetland mapping and inventory', *Remote Sensing*, 10(4), p. 580. doi: 10.3390/rs10040580.

Bhaskaran, S., Paramananda, S. and Ramnarayan, M. (2010) 'Per-pixel and object-oriented classification methods for mapping urban features using Ikonos satellite data', *Applied Geography*, 30(4), pp. 650–665. doi: 10.1016/j.apgeog.2010.01.009.

Birch, C. P. D., Oom, S. P. and Beecham, J. A. (2007) 'Rectangular and hexagonal grids used for observation, experiment and simulation in ecology', *Ecological Modelling*, 206(3–4), pp. 347–359. doi: 10.1016/j.ecolmodel.2007.03.041.

Blaschke, T. (2004) *New contextual approaches using image segmentation for object-based classification.*

Blaschke, T. (2005) *A framework for change detection based on image objects*, *Göttinger Geographische Abhandlungen*.

Blaschke, T. (2008) *Object-based image analysis*, *International Safeguards and Satellite Imagery: Key Features of the Nuclear Fuel Cycle and Computer-Based Analysis*. doi: 10.1007/978-3-540-79132-4_8.

Bouzekri, S., Lasbet, A. A. and Lachehab, A. (2015) 'A New Spectral Index for Extraction of Built-Up Area Using Landsat-8 Data', *Journal of the Indian Society of Remote Sensing*, 43(4), pp. 867–873. doi: 10.1007/s12524-015-0460-6.

Bouziani, M., Goïta, K. and He, D. C. (2007) 'Change detection of buildings in urban environment from high spatial resolution satellite images using existing cartographic data and prior knowledge', *International Geoscience and Remote Sensing Symposium (IGARSS)*, pp. 2581–2584. doi: 10.1109/IGARSS.2007.4423372.

Breiman, L. (2001) 'Random Forests', *Machine Learning*, 45, pp. 5–32. doi: 10.1023/A:1010950718922.

C, D. and C, W. (2012) 'A biophysical composition index for remote sensing of urban environments', *Remote Sensing of Environment*, 127, pp. 247–259.

Cai, C., Li, P. and Jin, H. (2016) 'Extraction of urban impervious surface using two-season worldview-2 images: A comparison', *Photogrammetric Engineering and Remote Sensing*, 82(5), pp. 335–349. doi: 10.14358/PERS.82.5.335.

Caloz, R., & Collet, C. (2001) *Précis de télédétection - Volume 3: Traitements numériques d'images de télédétection. 10.2307/j.ctv5j018b.* Presses Universitaires du Québec-Agence Universitaire de la Francophonie, 386 p. doi: 10.2307/j.ctv5j018b.

Carlson, T. N. and Ripley, D. A. (1997) 'On the relation between NDVI, fractional vegetation cover, and leaf area index', *Remote Sensing of Environment*, 62(3), pp. 241–252. doi: 10.1016/S0034-4257(97)00104-1.

Carlson, T. N. and Traci Arthur, S. (2000) 'The impact of land use - Land cover changes due to urbanization on surface microclimate and hydrology: A satellite perspective', *Global and Planetary Change*, 25(1–2), pp. 49–65. doi: 10.1016/S0921-8181(00)00021-7.

Chen, D., Stow, D. A. and Gong, P. (2004) 'Examining the effect of spatial resolution and texture window size on classification accuracy: An urban environment case', *International Journal of Remote Sensing*, 25(11), pp. 2177–2192. doi: 10.1080/01431160310001618464.

Chen, J. *et al.* (2010) 'Extract residential areas automatically by new built-up index', in *2010 18th International Conference on Geoinformatics, Geoinformatics 2010*. doi: 10.1109/GEOINFORMATICS.2010.5567823.

Chen, J. *et al.* (2019) 'Enhanced normalized difference index for impervious surface area estimation at the plateau basin scale', *Journal of Applied Remote Sensing*, 13(01), p. 1. doi: 10.1117/1.jrs.13.016502.

Chen, L.-C. *et al.* (2016) 'DeepLab: Semantic Image Segmentation with Deep Convolutional Nets, Atrous Convolution, and Fully Connected CRFs', *IEEE Transactions on Pattern*

Analysis and Machine Intelligence, PP. doi: 10.1109/TPAMI.2017.2699184.

Chen, M. Z., Wei, W. and Wu, S. P. (2009) 'On cold materials of pavement and high-temperature performance of asphalt concrete', *Materials Science Forum*, 620 622, pp. 379–382. doi: 10.4028/www.scientific.net/MSF.620-622.379.

Chen, X. L. *et al.* (2006) 'Remote sensing image-based analysis of the relationship between urban heat island and land use/cover changes', *Remote Sensing of Environment*, 104(2), pp. 133–146. doi: 10.1016/j.rse.2005.11.016.

Cho, M. A. *et al.* (2012) 'Mapping tree species composition in South African savannas using an integrated airborne spectral and LiDAR system', *Remote Sensing of Environment*, 125, pp. 214–226. doi: 10.1016/j.rse.2012.07.010.

Chormanski, J. *et al.* (2008) 'Improving distributed runoff prediction in urbanized catchments with remote sensing based estimates of impervious surface cover', *Sensors*, 8(2), pp. 910–932. doi: 10.3390/s8020910.

Chudnovsky, A., Ben-Dor, E. and Saaroni, H. (2004) 'Diurnal thermal behavior of selected urban objects using remote sensing measurements', *Energy and Buildings*, 36(11), pp. 1063–1074. doi: 10.1016/j.enbuild.2004.01.052.

Chunyang, H. *et al.* (2010) 'Improving the normalized difference built-up index to map urban built-up areas using a semiautomatic segmentation approach', *Remote Sensing Letters*, 1, pp. 213–221.

Civco, D. *et al.* (2002) 'Characterization of suburban sprawl and forest fragmentation through remote sensing applications', in *Annual Conference of the American Society for Photogrametry and Remote Sensing (ASPRS)*. Washington, DC: ASPRS.

Colditz, R. R. (2015) 'An evaluation of different training sample allocation schemes for discrete and continuous land cover classification using decision tree-based algorithms', *Remote Sensing*, 7(8), pp. 9655–9681. doi: 10.3390/rs70809655.

Congalton, R. G. (1991) 'A review of assessing the accuracy of classifications of remotely sensed data', *Remote Sensing of Environment*, 37(1), pp. 35–46. doi: 10.1016/0034-4257(91)90048-B.

Congalton, R. G. and Green, K. (2009) *Assessing the Accuracy of Remote Sensed Data: Principle and Pratices*. London and New York,: CRC Press.

Cortez, P. (2015) *A tutorial on using the rminer R package for data mining tasks.Teaching Report*. Guimaraes, Portugal. Available at: https://repositorium.sdum.uminho.pt/handle/1822/36210.

Cracknell, M. J. and Reading, A. M. (2014) 'Geological mapping using remote sensing data: A comparison of five machine learning algorithms, their response to variations in the spatial distribution of training data and the use of explicit spatial information', *Computers and Geosciences*, 63, pp. 22–33. doi: 10.1016/j.cageo.2013.10.008.

Danjuma, K. J. (2015) 'Performance Evaluation of Machine Learning Algorithms in Post-operative Life Expectancy in the Lung Cancer Patients', *arXiv*, 12(2). Available at: http://arxiv.org/abs/1504.04646.

Demographia (2017) *Demographia world urban areas*. 13th annua, *Demographia*. 13th annua. doi: http://www.demographia.com/db-dhi-index.htm.

Deng, C. and Wu, C. (2012) 'BCI: A biophysical composition index for remote sensing of urban environments', *Remote Sensing of Environment*, 127, pp. 247–259. doi: 10.1016/j.rse.2012.09.009.

Deng, C. and Wu, C. (2013) 'Examining the impacts of urban biophysical compositions on surface urban heat island: A spectral unmixing and thermal mixing approach', *Remote Sensing of Environment*, 131, pp. 262–274. doi: 10.1016/j.rse.2012.12.020.

Deng, Y. *et al.* (2015) 'RNDSI: A ratio normalized difference soil index for remote sensing of urban/suburban environments', *International Journal of Applied Earth Observation and Geoinformation*, 39, pp. 40–48. doi: 10.1016/j.jag.2015.02.010.

Doick, K. J., Peace, A. and Hutchings, T. R. (2014) 'The role of one large greenspace in mitigating London's nocturnal urban heat island', *Science of the Total Environment*, 493, pp. 662–671. doi: 10.1016/j.scitotenv.2014.06.048.

Durgabai, R. P. L. and Ravi Bhushan, Y. (2014) 'Feature Selection using ReliefF Algorithm', *Ijarcce*, 3(10), pp. 8215–8218. doi: 10.17148/ijarcce.2014.31031.

Elvidge, C. D. *et al.* (2007) 'Global distribution and density of constructed impervious surfaces', *Sensors*, 7(9), pp. 1962–1979. doi: 10.3390/s7091962.

Environment for Visualizing Images (2016) 'How Hot Spot Analysis (Getis-Ord Gi*i*⁄) works'. Available at: http://proarcgis.com/en/ pro-app/tool-reference/spatial-statistics/h-how-hot-spot-analysis-getis-ord-gispatial- stati.htm.

Environment for Visualizing Images ENVI, 2015 (2014) ‘Environment for visualizing images: Release 5.2; Exelis Visual Information Solutions: Boulder, CO, USA: ITT Industries’.

Fan, F., Weng, Q. and Wang, Y. (2007) ‘Land use and land cover change in Guangzhou, China, from 1998 to 2003, based on Landsat TM /ETM+ imagery’, *Sensors*, 7(7), pp. 1323–1342. doi: 10.3390/s7071323.

Fang, H., Wei, Y. and Dai, Q. (2019) ‘A Novel Remote Sensing Index for Extracting Impervious Surface Distribution from Landsat 8 OLI Imagery’, *Applied Sciences*, 9, p. 2631. doi: 10.3390/app9132631.

Felde, G. W. *et al.* (2003) ‘Analysis of Hyperion Data with the FLAASH Atmospheric Correction Algorithm’, *International Geoscience and Remote Sensing Symposium (IGARSS)*, 1, pp. 90–92. doi: 10.1109/igarss.2003.1293688.

Feng, Q. *et al.* (2015) ‘Flood mapping based on multiple endmember spectral mixture analysis and random forest classifier-the case of yuyao, China’, *Remote Sensing*, 7(9), pp. 12539–12562. doi: 10.3390/rs70912539.

Feng, Y. *et al.* (2017) ‘Examining Spatial Distribution and Dynamic Change of Urban Land Covers in the Brazilian Amazon Using Multitemporal Multisensor High Spatial Resolution Satellite Imagery’, *Remote Sensing*, 9(4), p. 381. doi: 10.3390/rs9040381.

Flasse, S. T. S. (2001) ‘An evaluation of different bi-spectral spaces for discriminating burned shrub-savannah’, *International Journal of Remote Sensing*, 22(13), pp. 2641–2647. doi: 10.1080/01431160119380.

Fu, G. *et al.* (2017) ‘Classification for High Resolution Remote Sensing Imagery Using a Fully Convolutional Network’, *Remote Sensing*, 9, p. 498. doi: 10.3390/rs9050498.

Gairola, S. *et al.* (2016) ‘Remote sensing object-oriented approaches coupled with ecological informatics to map invasive plant species’, *South African Journal of Geomatics*, 5(3), p. 285. doi: 10.4314/sajg.v5i3.2.

Gao, Y. *et al.* (2014) ‘Cool roofs in China: Policy review, building simulations, and proof-of-concept experiments’, *Energy Policy*, 74(C), pp. 190–214. doi: 10.1016/j.enpol.2014.05.036.

Gao, Y. and Mas, J. (2008) ‘A comparison of the performance of pixel based and object based classifications over images with various spatial resolutions’, *Online journal of earth sciences*, 2(8701), pp. 27–35. Available at:

http://docsdrive.com/pdfs/medwelljournals/ojesci/2008/27-35.pdf.

Getis, A. and Ord, J. K. (1992) 'The Analysis of Spatial Association by Use of Distance Statistics', *Geographical Analysis*, 24(3), pp. 189–206. doi: 10.1111/j.1538-4632.1992.tb00261.x.

Ghaffarian, Saman and Ghaffarian, Salar (2014) 'Automatic building detection based on Purposive FastICA (PFICA) algorithm using monocular high resolution Google Earth images', *ISPRS Journal of Photogrammetry and Remote Sensing*, 97, pp. 152–159. doi: 10.1016/j.isprsjprs.2014.08.017.

Gong, J., Liu, C. and Huang, X. (2019) 'Advances in urban information extraction from high-resolution remote sensing imagery', *Science China Earth Sciences*, 63. doi: 10.1007/s11430-019-9547-x.

Güneralp, B. *et al.* (2018) 'Urbanization in Africa: Challenges and opportunities for conservation', *Environmental Research Letters*, 13(1). doi: 10.1088/1748-9326/aa94fe.

Guo, H. *et al.* (2014) 'Synergistic use of optical and PolSAR imagery for urban impervious surface estimation', *Photogrammetric Engineering and Remote Sensing*, 80(1), pp. 91–102. doi: 10.14358/PERS.80.1.91.

Guo, W., Lu, D. and Kuang, W. (2017) 'Improving fractional impervious surface mapping performance through combination of DMSP-OLS and MODIS NDVI data', *Remote Sensing*, 9. doi: 10.3390/rs9040375.

Guo, X. *et al.* (2020) 'Urban Impervious Surface Extraction Based on Multi-features and Random Forest', *IEEE Access*, PP, p. 1. doi: 10.1109/ACCESS.2020.3046261.

Guo, Z. *et al.* (2018) 'A new index for mapping the "blue steel tile" roof dominated industrial zone from Landsat imagery', *Remote Sensing Letters*, 9(6), pp. 578–586. doi: 10.1080/2150704X.2018.1452057.

Gutman, G. and Ignatov, A. (1998) 'The derivation of the green vegetation fraction from NOAA/AVHRR data for use in numerical weather prediction models', *International Journal of Remote Sensing*, 19(8), pp. 1533–1543. doi: 10.1080/014311698215333.

Han, M. (2010) 'Change detection of land use and land cover in an urban region with SPOT-5 images and partial Lanczos extreme learning machine', *Journal of Applied Remote Sensing*, 4(1), p. 043551. doi: 10.1117/1.3518096.

Haralick, R. M., Dinstein, I. and Shanmugam, K. (1973) 'Textural Features for Image Classification', *IEEE Transactions on Systems, Man and Cybernetics*, SMC-3(6), pp. 610–621. doi: 10.1109/TSMC.1973.4309314.

Harris, N. L. *et al.* (2017) 'Using spatial statistics to identify emerging hot spots of forest loss', *Environmental Research Letters*, 12(2). doi: 10.1088/1748-9326/aa5a2f.

He, H. *et al.* (2018) 'Matching of Remote Sensing Images with Complex Background Variations via Siamese Convolutional Neural Network', *Remote Sensing*, 10, p. 355. doi: 10.3390/rs10020355.

He, X. and Jia, W. (2005) 'Hexagonal structure for intelligent vision', in *Proceedings of 1st International Conference on Information and Communication Technology, ICICT 2005*, pp. 52–64. doi: 10.1109/ICICT.2005.1598543.

He Yang; Ben Ma; Qian Du;Chenghai Yang (2010) 'Improving urban land use and land cover classification from high-spatial-resolution hyperspectral imagery using contextual information', *Journal of Applied Remote Sensing*, 4(1), p. 041890. doi: 10.1117/1.3491192.

Heiden, U. *et al.* (2007) 'Determination of robust spectral features for identification of urban surface materials in hyperspectral remote sensing data', *Remote Sensing of Environment*, 111(4), pp. 537–552. doi: 10.1016/j.rse.2007.04.008.

Henits, L., Mucsi, L. and Liska, C. M. (2017) 'Monitoring the changes in impervious surface ratio and urban heat island intensity between 1987 and 2011 in Szeged, Hungary', *Environmental Monitoring and Assessment*, 189(2). doi: 10.1007/s10661-017-5779-8.

Hereher, M. E. (2016) 'Time series trends of land surface temperatures in Egypt: a signal for global warming', *Environmental Earth Sciences*, 75(17), p. 1218. doi: 10.1007/s12665-016-6024-4.

Herold, M. *et al.* (2002) 'The spectral dimension in urban land cover mapping from high-resolution optical remote sensing data', in *Symposium A Quarterly Journal In Modern Foreign Literatures*, p. 8 pp. Available at: http://www.geogr.uni-jena.de/~c5hema/pub/istanb_herold_gardn_hadl_roberts.pdf.

Hu, X. (2009) 'Estimating impervious surfaces from medium spatial resolution imagery using the self-organizing map and multi-layer perceptron neural networks', *Remote Sensing of Environment*, 113, pp. 2089–2102. doi: 10.1016/j.rse.2009.05.014.

Hu, Y. and Jia, G. (2010) 'Influence of land use change on urban heat island derivedfrom multi-sensor data', *International Journal of Climatology*, 30(9), pp. 1382–1395. doi: 10.1002/joc.1984.

Hua, L. *et al.* (2020) 'The impacts of the expansion of urban impervious surfaces on urban heat islands in a coastal city in China', *Sustainability (Switzerland)*, 12(2). doi: 10.3390/su12020475.

Huang, F., Yu, Y. and Feng, T. (2019) 'Automatic Extraction of Urban Impervious Surfaces Based on Deep Learning and Multi-Source Remote Sensing Data', *Journal of Visual Communication and Image Representation*, 60. doi: 10.1016/j.jvcir.2018.12.051.

Huang, G., Zhou, W. and Cadenasso, M. L. (2011) 'Is everyone hot in the city? Spatial pattern of land surface temperatures, land cover and neighborhood socioeconomic characteristics in Baltimore, MD', *Journal of Environmental Management*, 92(7), pp. 1753–1759. doi: 10.1016/j.jenvman.2011.02.006.

Iabchoon, S., Wongsai, S. and Chankon, K. (2017) 'Mapping urban impervious surface using object-based image analysis with WorldView-3 satellite imagery', *Journal of Applied Remote Sensing*, 11(04), p. 1. doi: 10.1117/1.jrs.11.046015.

Ibrahim, G. R. F. (2017) 'Urban land use land cover changes and their effect on land surface temperature: Case study using Dohuk City in the Kurdistan Region of Iraq', *Climate*, 5(1). doi: 10.3390/cli5010013.

Im, J. *et al.* (2012) 'Impervious surface quantification using a synthesis of artificial immune networks and decision/regression trees from multi-sensor data', *Remote Sensing of Environment*, 117, pp. 102–113. doi: 10.1016/j.rse.2011.06.024.

Ishimwe, R., Abutaleb, K., Ahmed, F. and Ngie, A. (2014) 'Comparison of pixeld-based and object-based classification approaches using Landsat 8 OLI and TIR spectral bands.', in *Proceedings of the 10th International Conference of AARSE*, pp. 276–284.

Ishola, K. A., Okogbue, E. C. and Adeyeri, O. E. (2016) 'Dynamics of surface urban biophysical compositions and its impact on land surface thermal field', *Modeling Earth Systems and Environment*, 2(4). doi: 10.1007/s40808-016-0265-9.

Jana, M. and Sar, N. (2016) 'Modeling of hotspot detection using cluster outlier analysis and Getis-Ord Gi* statistic of educational development in upper-primary level, India', *Modeling Earth Systems and Environment*, 2. doi: 10.1007/s40808-016-0122-x.

Janssen, L. L. F., Jaarsma, M. N. and Van Der Linden, E. T. M. (1990) 'Integrating topographic data with remote sensing for land-cover classification', *Photogrammetric Engineering & Remote Sensing*, 56(11), pp. 1503–1506.

Javed Mallick, Y. K. and B.D.Bharath (2008) 'Estimation of land surface temperature over Delhi using Landsat-7 ETM+', *J. Ind. Geophys. Union*, 12(3), pp. 131–140. Available at: http://www.igu.in/12-3/5javed.pdf.

Jayamanna, S., Kawamura, M. and Tsujiko, Y. (1996) 'Relation between social and environmental conditions in colombo, sri lanka and the urban index estimated by satellite remote sensing data', *Theme Paper for the International Archives of the Photogrammetry, Remote Sensing and Spatial Information Sciences.(Part B7)*, 31, pp. 321-326.

Jennings, D. & Jarnagin, S. T. (2000) 'Impervious surfaces and stream flow discharge: a historical remote sensing perspective in a northern Virginia sub watershed.', in *ASPRS Annual Conference*. Washington, D.C. USA.

Jia, X. and Richards, J. (1999) 'Segmented principal components transformation for efficient hyperspectral remote-sensing image display and classification', *IEEE Transactions on Geoscience and Remote Sensing*, 37(1 II), pp. 538–542. doi: 10.1109/36.739109.

Jian, P. *et al.* (2016) 'Using impervious surfaces to detect urban expansion in Beijing of China in 2000s', *Chinese Geographical Science*, 26(2), pp. 229–243. doi: 10.1007/s11769-016-0802-5.

Jiménez-Munoz, J. C. and Sobrino, J. A. (2003) 'A generalized single-channel method for retrieving land surface temperature from remote sensing data', *Journal of Geophysical Research: Atmospheres*, 108(22). doi: 10.1029/2003jd003480.

Jiménez-Muñoz, J. C. and Sobrino, J. A. (2010) 'A single-channel algorithm for land-surface temperature retrieval from ASTER data', *IEEE Geoscience and Remote Sensing Letters*, 7(1), pp. 176–179. doi: 10.1109/LGRS.2009.2029534.

Jin, H., Stehman, S. V. and Mountrakis, G. (2014) 'Assessing the impact of training sample selection on accuracy of an urban classification: A case study in Denver, Colorado', *International Journal of Remote Sensing*, 35(6), pp. 2067–2081. doi: 10.1080/01431161.2014.885152.

Juniati, E. and Arrofiqoh, E. N. (2017) 'Comparison of pixel-based and object-based classification using parameters and non-parameters approach for the pattern consistency of multi scale landcover', *International Archives of the Photogrammetry, Remote Sensing and*

Spatial Information Sciences - ISPRS Archives, 42(2W7), pp. 765–771. doi: 10.5194/isprs-archives-XLII-2-W7-765-2017.

Kaimaris, D. and Patias, P. (2016) 'Identification and Area Measurement of the Built-up Area with the Built-up Index (BUI)', *International Journal of Advanced Remote Sensing and GIS*, 5(1), pp. 1844–1858. doi: 10.23953/cloud.ijarsg.64.

Kamdoum, J. N., Adepoju, K. A. and Akinyede, J. O. (2014) 'Assessment of impervious surface area and surface urban heat island: A case study', *International Journal of Ecological Economics and Statistics*, 35(4), pp. 48–64.

Kang, Y., Cho, N. and Son, S. (2018) 'Spatiotemporal characteristics of elderly population's traffic accidents in Seoul using space-time cube and space-time kernel density estimation', *PLoS ONE*, 13(5), p. e0196845. doi: 10.1371/journal.pone.0196845.

Kaszta, Z. *et al.* (2016) 'Seasonal separation of African savanna components using WorldView-2 imagery: A comparison of pixeland object-based approaches and selected classification algorithms', *Remote Sensing*, 8(9). doi: 10.3390/rs8090763.

Kavzoglu, T. and Colkesen, I. (2009) 'A kernel functions analysis for support vector machines for land cover classification', *International Journal of Applied Earth Observation and Geoinformation*, 11(5), pp. 352–359. doi: 10.1016/j.jag.2009.06.002.

Kawakubo, F. *et al.* (2019) 'Quantification and analysis of impervious surface area in the Metropolitan Region of São Paulo, Brazil', *Remote Sensing*, 11(8). doi: 10.3390/rs11080939.

Kawamura, M., Jayamanna, S. and Tsujiko, Y. (1997) 'Quantitative evaluation of urbanization in developing countries using satellite data.', *Doboku Gakkai Ronbunshu*, pp. 45–54. doi: 10.2208/jscej.1997.580_45.

Kelsey, K. C. and Neff, J. C. (2014) 'Estimates of aboveground biomass from texture analysis of landsat imagery', *Remote Sensing*, 6(7), pp. 6407–6422. doi: 10.3390/rs6076407.

Khandelwal, S. *et al.* (2018) 'Assessment of land surface temperature variation due to change in elevation of area surrounding Jaipur, India', *Egyptian Journal of Remote Sensing and Space Science*, 21(1), pp. 87–94. doi: 10.1016/j.ejrs.2017.01.005.

Kim, H. H. (1992) 'Urban heat island', *International Journal of Remote Sensing*, 13(12), pp. 2319–2336. doi: 10.1080/01431169208904271.

Kim, S. M. and Choi, Y. (2017) 'Assessing statistically significant heavy-metal concentrations in abandoned mine areas via hot spot analysis of portable XRF data', *International Journal of Environmental Research and Public Health*, 14(6). doi: 10.3390/ijerph14060654.

Krause, K. (2005) *Radiometric Use of QuickBird Imagery, World*. Colorado. Available at: http://www.mendeley.com/research/radiometric-quickbird-imagery/.

Kussul, N. *et al.* (2017) 'Deep Learning Classification of Land Cover and Crop Types Using Remote Sensing Data', *IEEE Geoscience and Remote Sensing Letters*, PP, pp. 1–5. doi: 10.1109/LGRS.2017.2681128.

Laben, C. . and Brower, B. . (2000) 'Process for enhancing the spatial resolution of multispectral imagery using pan-sharpening', *United States Patent 6*.

LeCun, Y., Bengio, Y. and Hinton, G. (2015) 'Deep Learning', *Nature*, 521, pp. 436–444. doi: 10.1038/nature14539.

Lefever, D. W. (1926) 'Measuring Geographic Concentration by Means of the Standard Deviational Ellipse', *American Journal of Sociology*, 32(1), pp. 88–94. doi: 10.1086/214027.

Leprieur, C. *et al.* (2000) 'Monitoring vegetation cover across semi-arid regions: Comparison of remote observations from various scales', *International Journal of Remote Sensing*, 21(2), pp. 281–300. doi: 10.1080/014311600210830.

Li, J. *et al.* (2011) 'Impacts of landscape structure on surface urban heat islands: A case study of Shanghai, China', *Remote Sensing of Environment*, 115(12), pp. 3249–3263. doi: 10.1016/j.rse.2011.07.008.

Li, Y. *et al.* (2017) 'Measuring spatiotemporal features of land subsidence, groundwater drawdown, and compressible layer thickness in Beijing Plain, China', *Water (Switzerland)*, 9(1), p. 64. doi: 10.3390/w9010064.

Li, Z. L. *et al.* (2013) 'Satellite-derived land surface temperature: Current status and perspectives', *Remote Sensing of Environment*, 131, pp. 14–37. doi: 10.1016/j.rse.2012.12.008.

Li, Z., Zhang, Z. and Davey, K. (2015) 'Estimating Geographical PV Potential Using LiDAR Data for Buildings in Downtown San Francisco', *Transactions in GIS*, 19(6), pp. 930–963. doi: 10.1111/tgis.12140.

Lilian, Z. *et al.* (2018) 'An improved temporal mixture analysis unmixing method for estimating impervious surface area based on MODIS and DMSP-OLS data', *ISPRS Journal of Photogrammetry and Remote Sensing*, 142, pp. 64–77. doi: 10.1016/j.isprsjprs.2018.05.016.

Van der Linden, S. (2007) 'Classifying segmented hyperspectral data from a heterogeneous urban environment using support vector machines', *Journal of Applied Remote Sensing*, 1(1), p. 013543. doi: 10.1117/1.2813466.

Liu, C. *et al.* (2013) 'MNDISI: A multi-source composition index for impervious surface area estimation at the individual city scale', *Remote Sensing Letters*, 4(8), pp. 803–812. doi: 10.1080/2150704X.2013.798710.

Liu, H. and Weng, Q. (2009) 'Scaling effect on the relationship between landscape pattern and land surface temperature: A case study of Indianapolis, United States', *Photogrammetric Engineering and Remote Sensing*, 75(3), pp. 291–304. doi: 10.14358/PERS.75.3.291.

Liu, L. and Zhang, Y. (2011) 'Urban heat island analysis using the landsat TM data and ASTER Data: A case study in Hong Kong', *Remote Sensing*, 3(7), pp. 1535–1552. doi: 10.3390/rs3071535.

Liu, Z. J., Wang, J. and Liu, W. P. (2005) 'Building extraction from high resolution imagery based on multi-scale object oriented classification and probabilistic hough transform', *International Geoscience and Remote Sensing Symposium (IGARSS)*, 4, pp. 2250–2253. doi: 10.1109/IGARSS.2005.1525421.

Loosvelt, L. *et al.* (2012) 'Random Forests as a tool for estimating uncertainty at pixel-level in SAR image classification', *International Journal of Applied Earth Observation and Geoinformation*, 19(1), pp. 173–184. doi: 10.1016/j.jag.2012.05.011.

Lu, D. (2009) 'Extraction of Urban Impervious Surface from an IKONOS Image', *International Journal of Remote Sensing*, 30, pp. 1297–1311. doi: 10.1080/01431160802508985.

Lu, D. *et al.* (2014) 'Methods to extract impervious surface areas from satellite images', *International Journal of Digital Earth*, 7(2), pp. 93–112. doi: 10.1080/17538947.2013.866173.

Lu, D., Moran, E. and Hetrick, S. (2011) 'Detection of impervious surface change with multitemporal Landsat images in an urban-rural frontier', *ISPRS Journal of Photogrammetry and Remote Sensing*, 66(3), pp. 298–306. doi: 10.1016/j.isprsjprs.2010.10.010.

Lu, D. and Weng, Q. (2007) ‘A survey of image classification methods and techniques for improving classification performance’, *International Journal of Remote Sensing*, 28(5), pp. 823–870. doi: 10.1080/01431160600746456.

Ma, L. *et al.* (2019) ‘Deep learning in remote sensing applications: A meta-analysis and review’, *ISPRS Journal of Photogrammetry and Remote Sensing*, 152, pp. 166–177. doi: 10.1016/j.isprsjprs.2019.04.015.

Ma, W. and Li, P. (2018) ‘An Object Similarity-Based Thresholding Method for Urban Area Mapping from Visible Infrared Imaging Radiometer Suite Day/Night Band (VIIRS DNB) Data’, *Remote Sensing*, 10, p. 263. doi: 10.3390/rs10020263.

Ma, Y., Kuang, Y. and Huang, N. (2010) ‘Coupling urbanization analyses for studying urban thermal environment and its interplay with biophysical parameters based on TM/ETM+ imagery’, *International Journal of Applied Earth Observation and Geoinformation*, 12(2), pp. 110–118. doi: 10.1016/j.jag.2009.12.002.

Madonsela, S. *et al.* (2017) ‘Multi-phenology WorldView-2 imagery improves remote sensing of savannah tree species’, *International Journal of Applied Earth Observation and Geoinformation*, 58, pp. 65–73. doi: 10.1016/j.jag.2017.01.018.

Maggiori, E. *et al.* (2016) ‘Convolutional Neural Networks for Large-Scale Remote Sensing Image Classification’, *IEEE Transactions on Geoscience and Remote Sensing*, 55. doi: 10.1109/TGRS.2016.2612821.

Makinde, E. O. *et al.* (2016) ‘Object Based and Pixel Based Classification Using Rapideye Satellite Imager of ETI-OSA, Lagos, Nigeria’, *Geoinformatics FCE CTU*, 15(2), pp. 59–70. doi: 10.14311/gi.15.2.5.

Mallick, J., Rahman, A. and Singh, C. (2013) ‘Modeling urban heat islands in heterogeneous land surface and its correlation with impervious surface area by using night-time ASTER satellite data in highly urbanizing city, Delhi-India’, *Advances in Space Research*, 52, pp. 639–655. doi: 10.1016/j.asr.2013.04.025.

Man, W. *et al.* (2019) ‘Spatio-temporal variations in impervious surface patterns during urban expansion in a coastal city: Xiamen, China’, *Sustainability (Switzerland)*, 11(8). doi: 10.3390/su11082404.

Markham, B. L. and Barker, J. L. (1985) ‘Spectral characterization of the landsat thematic mapper sensors’, *International Journal of Remote Sensing*, 6(5), pp. 697–716. doi:

10.1080/01431168508948492.

Marmanis, D. *et al.* (2016) ‘SEMANTIC SEGMENTATION OF AERIAL IMAGES WITH AN ENSEMBLE OF CNNS’, *ISPRS Annals of Photogrammetry, Remote Sensing and Spatial Information Sciences*, III–3, pp. 473–480. doi: 10.5194/isprsannals-III-3-473-2016.

Masek, J. G., Lindsay, F. E. and Goward, S. N. (2000) ‘Dynamics of urban growth in the Washington DC metropolitan area, 1973-1996, from Landsat observations’, *International Journal of Remote Sensing*, 21(18), pp. 3473–3486. doi: 10.1080/014311600750037507.

Mathew, A., Khandelwal, S. and Kaul, N. (2016) ‘Spatial and temporal variations of urban heat island effect and the effect of percentage impervious surface area and elevation on land surface temperature: Study of Chandigarh city, India’, *Sustainable Cities and Society*, 26, pp. 264–277. doi: 10.1016/j.scs.2016.06.018.

Maxwell, A. E., Warner, T. A. and Fang, F. (2018) ‘Implementation of machine-learning classification in remote sensing: An applied review’, *International Journal of Remote Sensing*, 39(9), pp. 2784–2817. doi: 10.1080/01431161.2018.1433343.

McGregor, G. R. M. *et al.* (2015) *Heatwaves and Health: Guidance on Warning-System Development | World Meteorological Organization*. Geneva, Switzerland. Available at: https://public.wmo.int/en/resources/library/heatwaves-and-health-guidance-warning-system-development.

McMillin, L. M. (1975) ‘Estimation of sea surface temperatures from two infrared window measurements with different absorption’, *Journal of Geophysical Research*, 80(36), pp. 5113–5117. doi: 10.1029/jc080i036p05113.

Mellor, A. *et al.* (2015) ‘Exploring issues of training data imbalance and mislabelling on random forest performance for large area land cover classification using the ensemble margin’, *ISPRS Journal of Photogrammetry and Remote Sensing*, 105, pp. 155–168. doi: 10.1016/j.isprsjprs.2015.03.014.

Mhangara, P. *et al.* (2011) ‘Road extraction using object oriented classification’, *Visualisation technical*, Nov/Dec 20(34), pp. 45–50. Available at: http://eepublishers.co.za/article/africageo-213-11.html.

Mitchell, A. (1999) *The ESRI Guide to GIS Analysis*. 2nd editio, *Geographic Patterns & Relationships*. 2nd editio. Redlands,California: ESRI Press.

Montgomery, D.C., Peck, E.A. Vining, G. G. (2012) *Introduction to Linear Regression*

Analysis, *Technometrics*. Hoboken, NJ, USA: John Wiley & Sons. doi: 10.2307/1269673.

Montgomery, M. R. and Hewett, P. C. (2005) ‘Urban poverty and health in developing countries: Household and neighborhood effects’, *Demography*, 42(3), pp. 397–425. doi: 10.1353/dem.2005.0020.

Morabito, M. *et al.* (2015) ‘Urban-hazard risk analysis: Mapping of heat-related risks in the elderly in major Italian cities’, *PLoS ONE*, 10(5). doi: 10.1371/journal.pone.0127277.

Morabito, M. *et al.* (2016) ‘The impact of built-up surfaces on land surface temperatures in Italian urban areas’, *Science of the Total Environment*, 551–552, pp. 317–326. doi: 10.1016/j.scitotenv.2016.02.029.

Morabito, M. *et al.* (2018) ‘Urban imperviousness effects on summer surface temperatures nearby residential buildings in different urban zones of Parma’, *Remote Sensing*, 10(1). doi: 10.3390/rs10010026.

Mutanga, O. *et al.* (2015) ‘Evaluating the robustness of models developed from field spectral data in predicting African grass foliar nitrogen concentration using WorldView-2 image as an independent test dataset’, *International Journal of Applied Earth Observation and Geoinformation*, 34(1), pp. 178–187. doi: 10.1016/j.jag.2014.08.008.

Myint, S. *et al.* (2010) ‘Combined effects of impervious surface and vegetation cover on air temperature variations in a rapidly expanding desert city’, *GIScience and Remote Sensing*, 47(3), pp. 301–320. doi: 10.2747/1548-1603.47.3.301.

Myint, S. *et al.* (2013) ‘The impact of distinct anthropogenic and vegetation features on urban warming’, *Landscape Ecology*, 28. doi: 10.1007/s10980-013-9868-y.

Myint, S. W. *et al.* (2011) ‘Per-pixel vs. object-based classification of urban land cover extraction using high spatial resolution imagery’, *Remote Sensing of Environment*, 115(5), pp. 1145–1161. doi: 10.1016/j.rse.2010.12.017.

Naidoo, L. *et al.* (2015) ‘Savannah woody structure modelling and mapping using multi-frequency (X-, C- and L-band) Synthetic Aperture Radar data’, *ISPRS Journal of Photogrammetry and Remote Sensing*, 105, pp. 234–250. doi: 10.1016/j.isprsjprs.2015.04.007.

Nasarudin, N. E. M. and Shafri, H. Z. M. (2011) ‘Development and utilization of urban spectral library for remote sensing of urban environment’, *Journal of Urban and Environmental Engineering*, 5(1), pp. 44–56. doi: 10.4090/juee.2011.v5n1.044056.

Ng, E. *et al.* (2012) 'A study on the cooling effects of greening in a high-density city: An experience from Hong Kong', *Building and Environment*, 47(1), pp. 256–271. doi: 10.1016/j.buildenv.2011.07.014.

Nie, Q. *et al.* (2016) 'Spatiotemporal Impact of Urban Impervious Surface on Land Surface Temperature in Shanghai, China', *Canadian Journal of Remote Sensing*, 42(6), pp. 680–689. doi: 10.1080/07038992.2016.1217484.

Nie, Q. and Xu, J. (2015) 'Understanding the effects of the impervious surfaces pattern on land surface temperature in an urban area', *Frontiers of Earth Science*, 9(2), pp. 276–285. doi: 10.1007/s11707-014-0459-2.

Ning, J. *et al.* (2018) 'Analysis of relationships between land surface temperature and land use changes in the Yellow River Delta', *Frontiers of Earth Science*, 12(2), pp. 444–456. doi: 10.1007/s11707-017-0657-9.

Odindi, J., Mhangara, P. and Kakembo, V. (2012) 'Remote sensing land-cover change in Port Elizabeth during South Africa's democratic transition', *South African Journal of Science*, 108(5–6). doi: 10.4102/sajs.v108i5/6.886.

Ok, A. O. (2013) 'Automated Extraction of Buildings and Roads in a Graph Partitioning Framework', *ISPRS Annals of the Photogrammetry, Remote Sensing and Spatial Information Sciences*, 2(3W3), pp. 79–84. doi: 10.5194/isprsannals-II-3-W3-79-2013.

Oke, T. R. (1973) 'City size and the urban heat island', *Atmospheric Environment (1967)*, 7(8), pp. 769–779. doi: 10.1016/0004-6981(73)90140-6.

Oke, T. R. (1982) 'The energetic basis of the urban heat island', *Quarterly Journal of the Royal Meteorological Society*, 108(455), pp. 1–24. doi: 10.1002/qj.49710845502.

Okujeni, A. *et al.* (2018) 'Generalizing machine learning regression models using multi-site spectral libraries for mapping vegetation-impervious-soil fractions across multiple cities', *Remote Sensing of Environment*, 216, pp. 482–496. doi: 10.1016/j.rse.2018.07.011.

Okujeni, A., van der Linden, S. and Hostert, P. (2015) 'Extending the vegetation-impervious-soil model using simulated EnMAP data and machine learning', *Remote Sensing of Environment*, 158, pp. 69–80. doi: 10.1016/j.rse.2014.11.009.

Olarewaju Oluseyi, I., Fanan, U. and Magaji, J. (2009) 'An evaluation of the effect of land use/cover change on the surface temperature of Lokoja town, Nigeria', *African Journal of Environmental Science and Technology*, 3(3), pp. 86–90. Available at:

http://www.academicjournals.org/AJEST.

Omer, G. *et al.* (2015) ‘Performance of Support Vector Machines and Artificial Neural Network for Mapping Endangered Tree Species Using WorldView-2 Data in Dukuduku Forest, South Africa’, *IEEE Journal of Selected Topics in Applied Earth Observations and Remote Sensing*, 8(10), pp. 4825–4840. doi: 10.1109/JSTARS.2015.2461136.

Ord, J. K. and Getis, A. (1995) ‘Local Spatial Autocorrelation Statistics: Distributional Issues and an Application’, *Geographical Analysis*, 27(4), pp. 286–306. doi: 10.1111/j.1538-4632.1995.tb00912.x.

Ouyang, Z. T. *et al.* (2011) ‘A comparison of pixel-based and object-oriented approaches to VHR imagery for mapping saltmarsh plants’, *Ecological Informatics*, 6(2), pp. 136–146. doi: 10.1016/j.ecoinf.2011.01.002.

Owen, T. W., Carlson, T. N. and Gillies, R. R. (1998) ‘An assessment of satellite remotely-sensed land cover parameters in quantitatively describing the climatic effect of urbanization’, *International Journal of Remote Sensing*, 19(9), pp. 1663–1681. doi: 10.1080/014311698215171.

Özçift, A. (2011) ‘Random forests ensemble classifier trained with data resampling strategy to improve cardiac arrhythmia diagnosis’, *Computers in Biology and Medicine*, 41(5), pp. 265–271. doi: 10.1016/j.compbiomed.2011.03.001.

Pacifici, F., Chini, M. and Emery, W. (2009) ‘A neural network approach using multi-scale textural metrics from very high-resolution panchromatic imagery for urban land-use classification’, *Remote Sensing of Environment*, 113, pp. 1276–1292. doi: 10.1016/j.rse.2009.02.014.

Pappas, E. A. *et al.* (2008) ‘Impervious surface impacts to runoff and sediment discharge under laboratory rainfall simulation’, *Catena*, 72(1), pp. 146–152. doi: 10.1016/j.catena.2007.05.001.

Parece, T. E. and Campbell, J. B. (2013) ‘Comparing urban impervious surface identification using landsat and high resolution aerial photography’, *Remote Sensing*, 5(10), pp. 4942–4960. doi: 10.3390/rs5104942.

Pok, S., Matsushita, B. and Fukushima, T. (2017) ‘An easily implemented method to estimate impervious surface area on a large scale from MODIS time-series and improved DMSP-OLS nighttime light data’, *ISPRS Journal of Photogrammetry and Remote Sensing*, 133, pp. 104–

115. doi: 10.1016/j.isprsjprs.2017.10.005.

Prabhakaran, S. (2016) ‘Performance Analysis and Companion FunctionsforBinaryClassificationModels.’ Available at: https://www.rdocumentation.org/packages/InformationValue/versions/1.2.3.

Prokop, G., Jobstmann, H. and Schönbauer, A. (2011) *Report on best practices for limiting soil sealing and mitigating its effects*. Brussels, Belgium. Available at: https://www.sciencedirect.com/science/article/pii/S0013935117305297.

Pu, R. and Landry, S. (2012) ‘A comparative analysis of high spatial resolution IKONOS and WorldView-2 imagery for mapping urban tree species’, *Remote Sensing of Environment*, 124, pp. 516–533. doi: 10.1016/j.rse.2012.06.011.

Qaid, A. *et al.* (2016) ‘Urban heat island and thermal comfort conditions at micro-climate scale in a tropical planned city’, *Energy and Buildings*, 133, pp. 577–595. doi: 10.1016/j.enbuild.2016.10.006.

Qian, J., Zhou, Q. and Hou, Q. (2007a) ‘Comparison of pixel-based and object-oriented classification methods for extracting built-up areas in aridzone’, in *ISPRS Workshop on Updating Geo-spatial Databases with Imagery & The 5th ISPRS Workshop on DMGISs*, pp. 163–171.

Qian, J., Zhou, Q. and Hou, Q. (2007b) ‘COMPARISON OF PIXEL-BASED AND OBJECT-ORIENTED CLASSIFICATION METHODS FOR EXTRACTING BUILT-UP AREAS IN ARIDZONE’, *ISPRS Workshop on Updating Geo-spatial Databases with Imagery & The 5th ISPRS Workshop on DMGISs*.

Qian, Y. and Wu, Z. (2019) ‘Study on urban expansion using the spatial and temporal dynamic changes in the impervious surface in Nanjing’, *Sustainability (Switzerland)*, 11(3), p. 933. doi: 10.3390/su11030933.

Qiao, K. *et al.* (2018) ‘Examining the distribution and dynamics of impervious surface in different function zones in Beijing’, *Journal of Geographical Sciences*, 28(5), pp. 669–684. doi: 10.1007/s11442-018-1498-5.

Qin, Z., Karnieli, A. and Berliner, P. (2001) ‘A mono-window algorithm for retrieving land surface temperature from Landsat TM data and its application to the Israel-Egypt border region’, *International Journal of Remote Sensing*, 22(18), pp. 3719–3746. doi: 10.1080/01431160010006971.

Rajasekar, U. and Weng, Q. (2009) ‘Application of association rule mining for exploring the relationship between urban land surface temperature and biophysical/social parameters’, *Photogrammetric Engineering and Remote Sensing*, 75(4), pp. 385–396. doi: 10.14358/PERS.75.4.385.

Ramezan, C. A., Warner, T. A. and Maxwell, A. E. (2019) ‘Evaluation of sampling and cross-validation tuning strategies for regional-scale machine learning classification’, *Remote Sensing*, 11(2), p. 185. doi: 10.3390/rs11020185.

Raper, P. E. (1987) ‘Dictionary of Southern African Place Names’.

Richards, J. A. and Jia, X. (2006) *Remote sensing digital image analysis: An introduction*. 3rd edn, *Remote Sensing Digital Image Analysis: An Introduction*. 3rd edn. Berlin.: Springer. doi: 10.1007/3-540-29711-1.

Rinner, C. and Hussain, M. (2011) ‘Toronto’s urban heat island-exploring the relationship between land use and surface temperature’, *Remote Sensing*, 3(6), pp. 1251–1265. doi: 10.3390/rs3061251.

Robinson, D. J., Redding, N. J. and Crisp, D. J. (2002) *Implementation of a Fast Algorithm for Segmenting SAR Imagery*. Australia.

Robnik, M. and Konenko, I. (2003) ‘Theoretical and empirical analysis of ReliefF and RReliefF’, *Machine Learning*, 53(1--2), pp. 23–69.

Rodriguez-Galiano, V. F. *et al.* (2012) ‘An assessment of the effectiveness of a random forest classifier for land-cover classification’, *ISPRS Journal of Photogrammetry and Remote Sensing*, 67(1), pp. 93–104. doi: 10.1016/j.isprsjprs.2011.11.002.

Rosario, S.F. & Thangadurai, K. (2015) ‘RELIEfF: Feature Selection Approach’, *International Journal of Innovative Research and Development,* 4(11), pp. 218–224.

Rouse, J. W. *et al.* (1973) ‘Monitoring vegetation systems in the great plains with ERTS’, in *Third Earth Resources Technology Satellite (ERTS) symposium*, pp. 309–317. Available at: https://ntrs.nasa.gov/archive/nasa/casi.ntrs.nasa.gov/19740022614.pdf.

Roxburgh, C. *et al.* (2010) *Lions on the move: The progress and potential of African economies*. New York, NY, USA: McKinsey Global Institute. Available at: http://www.mckinsey.com/mgi/publications/progress_and_potential_of_african_economies.

Rozenstein, O. *et al.* (2014) ‘Derivation of land surface temperature for landsat-8 TIRS using a split window algorithm', *Sensors (Switzerland)*, 14(4), pp. 5768–5780. doi: 10.3390/s140405768.

RStudio, I. (no date) 'RStudio'. Boston, MA, USA: RStudioInc. Available at: http://www.rstudio.org/.

Sahana, M., Hong, H. and Sajjad, H. (2018) 'Analyzing urban spatial patterns and trend of urban growth using urban sprawl matrix: A study on Kolkata urban agglomeration, India', *Science of the Total Environment*, 628–629, pp. 1557–1566. doi: 10.1016/j.scitotenv.2018.02.170.

Salah, M. (2014) 'Combining Pixel-Based and Object-Oriented Support Vector Machines using Bayesian Probability Theory', *ISPRS Annals of Photogrammetry, Remote Sensing and Spatial Information Sciences*, II–7, pp. 67–74. doi: 10.5194/isprsannals-ii-7-67-2014.

Salas, E. A. L., Boykin, K. G. and Valdez, R. (2016) 'Multispectral and texture feature application in image-object analysis of summer vegetation in eastern Tajikistan Pamirs', *Remote Sensing*, 8(1). doi: 10.3390/rs8010078.

Sameen, M. I. and Pradhan, B. (2016) 'A novel built-up spectral index developed by using multiobjective particle-swarm-optimization technique', *IOP Conference Series: Earth and Environmental Science*, 37(1). doi: 10.1088/1755-1315/37/1/012006.

Samsudin, S. H., Shafri, H. Z. M. and Hamedianfar, A. (2016) 'Development of spectral indices for roofing material condition status detection using field spectroscopy and WorldView-3 data', *Journal of Applied Remote Sensing*, 10(2), p. 025021. doi: 10.1117/1.jrs.10.025021.

Schoeman, F., Newsby, T.S., Thompson, M.W. & Van den Berg, E. C. (2013) 'South African National Land-Cover Change Map', *South African Journal of Geomatics*, 2(2), pp. 94-105–105. doi: 10.4314/sajg.v2i2.

Schwarz, N., Lautenbach, S. and Seppelt, R. (2011) 'Exploring indicators for quantifying surface urban heat islands of European cities with MODIS land surface temperatures', *Remote Sensing of Environment*, 115(12), pp. 3175–3186. doi: 10.1016/j.rse.2011.07.003.

Scott, G. *et al.* (2017) 'Training Deep Convolutional Neural Networks for Land-Cover Classification of High-Resolution Imagery', *IEEE Geoscience and Remote Sensing Letters*, PP, pp. 1–5. doi: 10.1109/LGRS.2017.2657778.

Shahi, K. *et al.* (2014) 'A Novel Spectral Index for Automatic Shadow Detection in Urban

Mapping Based On WorldView-2 Satellite Imagery', *International Journal of Computer, Electrical, Automation, Control and Information Engineering*, 8(10), pp. 1482–1485. Available at: https://waset.org/publications/9999443/a-novel-spectral-index-for-automatic-shadow-detection-in-urban-mapping-based-on-worldview-2-satellite-imagery.

Shahi, K. *et al.* (2015) 'A novel spectral index to automatically extract road networks from WorldView-2 satellite imagery', *Egyptian Journal of Remote Sensing and Space Science*, 18(1), pp. 27–33. doi: 10.1016/j.ejrs.2014.12.003.

Shahtahmassebi, A. R. *et al.* (2016) 'Remote sensing of impervious surface growth: A framework for quantifying urban expansion and re-densification mechanisms', *International Journal of Applied Earth Observation and Geoinformation*, 46, pp. 94–112. doi: 10.1016/j.jag.2015.11.007.

Shariati, M. *et al.* (2020) 'Spatiotemporal analysis and hotspots detection of COVID-19 using geographic information system (March and April, 2020)', *Journal of Environmental Health Science and Engineering*, 18(2), pp. 1499–1507. doi: 10.1007/s40201-020-00565-x.

Shi, L. *et al.* (2017) 'Impervious surface change mapping with an uncertainty-based spatial-temporal consistency model: A case study in Wuhan City using landsat time-series datasets from 1987 to 2016', *Remote Sensing*, 9(11). doi: 10.3390/rs9111148.

Shi, Y., Li, Q. and Zhu, X. (2020) 'Building segmentation through a gated graph convolutional neural network with deep structured feature embedding', *ISPRS Journal of Photogrammetry and Remote Sensing*, 159, pp. 184–197. doi: 10.1016/j.isprsjprs.2019.11.004.

Shrestha, B., Ahmad, S. and Stephen, H. (2021) 'Fusion of Sentinel-1 and Sentinel-2 data in mapping the impervious surfaces at city scale', *Environmental Monitoring and Assessment*, 193(9). doi: 10.1007/s10661-021-09321-6.

Shrestha, B., Stephen, H. and Ahmad, S. (2021) 'Impervious surfaces mapping at city scale by fusion of radar and optical data through a random forest classifier', *Remote Sensing*, 13(15), p. 3040. doi: 10.3390/rs13153040.

Simwanda, M. *et al.* (2019) 'Spatial analysis of surface urban heat Islands in four rapidly growing african cities', *Remote Sensing*, 11(14). doi: 10.3390/rs11141645.

Sinha, P., Verma, N. K. and Ayele, E. (2016) 'Urban Built-up Area Extraction and Change Detection of Adama Municipal Area using Time-Series Landsat Images', *International*

Journal of Advanced Remote Sensing and GIS, 5(1), pp. 1886–1895. doi: 10.23953/cloud.ijarsg.67.

Slonecker, E., Jennings, D. and Garofalo, D. (2001) 'Remote sensing of impervious surfaces: A review', *Remote Sensing Reviews*, 20. doi: 10.1080/02757250109532436.

Smith, C. *et al.* (2014) 'Flying-Fox Species Density - A Spatial Risk Factor for Hendra Virus Infection in Horses in Eastern Australia', *PloS one*, 9, p. e99965. doi: 10.1371/journal.pone.0099965.

Sobrino, J. A. *et al.* (2008) 'Land surface emissivity retrieval from different VNIR and TIR sensors', *IEEE Transactions on Geoscience and Remote Sensing*, 46(2), pp. 316–327. doi: 10.1109/TGRS.2007.904834.

Sobrino, J. A., Jiménez-Muñoz, J. C. and Paolini, L. (2004) 'Land surface temperature retrieval from LANDSAT TM 5', *Remote Sensing of Environment*, 90(4), pp. 434–440. doi: 10.1016/j.rse.2004.02.003.

Sobrino, J. A., Raissouni, N. and Li, Z. L. (2001) 'A comparative study of land surface emissivity retrieval from NOAA data', *Remote Sensing of Environment*, 75(2), pp. 256–266. doi: 10.1016/S0034-4257(00)00171-1.

Somers, B. *et al.* (2011) 'Endmember variability in Spectral Mixture Analysis: A review', *Remote Sensing of Environment*, 115(7), pp. 1603–1616. doi: 10.1016/j.rse.2011.03.003.

Song, Y. and Wu, C. (2016) 'Examining the impact of urban biophysical composition and neighboring environment on surface urban heat island effect', *Advances in Space Research*, 57(1), pp. 96–109. doi: 10.1016/j.asr.2015.10.036.

South African Weather Service (2011) *Climate data for Pretoria*. Pretoria. Available at: http://www.weathersa.co.za/Climat/Climstats/BloemfonteinStats.jsp.

South African Weather Services (2013) *Climate data for Pretoria.* Pretoria.

Strahler, A. H., Logan, T. L. and Bryant, N. A. (1978) 'Improving forest cover classification accuracy from LANDSAT by incorporating topographic information', in *Proceedings of the Twelfth International Symposium on Remote Sensing of Environment*, pp. 927–942.

Sun, G. *et al.* (2016) 'Combinational Build-Up Index (CBI) for Effective Impervious Surface Mapping in Urban Areas', *IEEE Journal of Selected Topics in Applied Earth Observations and Remote Sensing*, 9(5), pp. 2081–2092. doi: 10.1109/JSTARS.2015.2478914.

Sun, Z. (2011) ‘Estimating urban impervious surfaces from Landsat-5 TM imagery using multilayer perceptron neural network and support vector machine’, *Journal of Applied Remote Sensing*, 5(1), p. 053501. doi: 10.1117/1.3539767.

Sun, Z. *et al.* (2017) ‘A modified normalized difference impervious surface index (MNDISI) for automatic urban mapping from landsat imagery’, *Remote Sensing*, 9(9). doi: 10.3390/rs9090942.

Sun, Z. *et al.* (2018) ‘Extracting Urban Impervious Surface from WorldView-2 and Airborne LiDAR Data Using 3D Convolutional Neural Networks’, *Journal of the Indian Society of Remote Sensing*, 47. doi: 10.1007/s12524-018-0917-5.

Sun, Z. *et al.* (2019) ‘Extracting Urban Impervious Surface from WorldView-2 and Airborne LiDAR Data Using 3D Convolutional Neural Networks’, *Journal of the Indian Society of Remote Sensing*, 47(3), pp. 401–412. doi: 10.1007/s12524-018-0917-5.

Survey, U. S. G. (2013) *Landsat 8 Landsat Data Continuity Mission. Fact Sheet 2013–3060.* Reston, Virginia, USA. Available at: https://glovis.usgs.gov/.

Susca, T., Gaffin, S. R. and Dell’Osso, G. R. (2011) ‘Positive effects of vegetation: Urban heat island and green roofs’, *Environmental Pollution*, 159(8–9), pp. 2119–2126. doi: 10.1016/j.envpol.2011.03.007.

Swan, A. R. H. and Sandilands, M. (1995) *Introduction to geological data analysis*, *Introduction to geological data analysis*. oxford: Blackwell Science. doi: 10.1016/s0191-8141(96)80002-2.

Szykier, A. (2008) *Extraction of Roof Surface for Solar Analysis.* Maps Capital Management.

Taherzadeh, E. and Shafri, H. Z. M. (2011) ‘Using hyperspectral remote sensing data in urban mapping over Kuala Lumpur’, in *2011 Joint Urban Remote Sensing Event, JURSE 2011 - Proceedings*, pp. 405–408. doi: 10.1109/JURSE.2011.5764805.

Taherzadeh, E. and Shafri, H. Z. M. (2013) ‘Development of a Generic Model for the Detection of Roof Materials Based on an Object-Based Approach Using WorldView-2 Satellite Imagery’, *Advances in Remote Sensing*, 02(04), pp. 312–321. doi: 10.4236/ars.2013.24034.

Tan, K. *et al.* (2014) ‘Modified multiple endmember spectral mixture analysis for mapping impervious surfaces in urban environments’, *Journal of Applied Remote Sensing*, 8, p. 85096. doi: 10.1117/1.JRS.8.085096.

Tang, F. and Xu, H. (2010) 'The influence of urban reconstruction in urban heat island effect: Cangxia area of Fuzhou City, China', *Remote Sensing of the Environment: The 17th China Conference on Remote Sensing*, 8203, pp. 525–528. doi: 10.1117/12.910413.

Tang, F. and Xu, H. (2017) 'Impervious Surface Information Extraction Based on Hyperspectral Remote Sensing Imagery', *Remote Sensing*, 9, p. 550. doi: 10.3390/rs9060550.

Thanh Noi, P. and Kappas, M. (2017) 'Comparison of Random Forest, k-Nearest Neighbor, and Support Vector Machine Classifiers for Land Cover Classification Using Sentinel-2 Imagery', *Sensors (Basel, Switzerland)*, 18(1), p. 18. doi: 10.3390/s18010018.

Tian, Y. *et al.* (2018) 'A novel index for impervious surface area mapping: Development and validation', *Remote Sensing*, 10(10). doi: 10.3390/rs10101521.

Tomlinson, C. J. *et al.* (2011) 'Including the urban heat island in spatial heat health risk assessment strategies: A case study for Birmingham, UK', *International Journal of Health Geographics*, 10. doi: 10.1186/1476-072X-10-42.

Tran, D. X. *et al.* (2017) 'Characterizing the relationship between land use land cover change and land surface temperature', *ISPRS Journal of Photogrammetry and Remote Sensing*, 124, pp. 119–132. doi: 10.1016/j.isprsjprs.2017.01.001.

Tsai, Y. H., Stow, D. and Weeks, J. (2011) 'Comparison of object-based image analysis approaches to mapping new buildings in Accra, Ghana using multi-temporal quickbird satellite imagery', *Remote Sensing*, 3(12), pp. 2707–2726. doi: 10.3390/rs3122707.

UN-DESA (2018) *World Urbanization Prospects: The 2018 Revision, Highlights:*

UN (2014) *Department of Economic and Social Affairs, Population Division. World Urbanization Prospects: The 2014 Revision,Highlights ST/ESA/SER.A/352.* Available at: https://esa.un.org/unpd/wup/publications/files/wup2014-highlights.

UNDP (2012) *World urbanization prospects: the 2011 revision*, *Presentation at the Center for Strategic and ….* New York. Available at: http://esa.un.org/unpd/wpp/ppt/CSIS/WUP_2011_CSIS_4.pdf.

United Nations Population Division (2009) *World Urbanization Prospects: 2009 Revision, World Urbanization Prospects*. New York, NY, USA.

United States Geological Survey (2013) *Landsat 8 Landsat Data Continuity Mission. Fact Sheet 2013–3060.* Reston, Virginia, U.S. Available at: https://www.usgs.gov/.

Vanhulsel, M. *et al.* (2011) 'Measuring dissimilarity of geographically dispersed space-time paths', *Transportation*, 38(1), pp. 65–79. doi: 10.1007/s11116-010-9286-9.

Varshney, A. and Rajesh, E. (2014) 'A Comparative Study of Built-up Index Approaches for Automated Extraction of Built-up Regions From Remote Sensing Data', *Journal of the Indian Society of Remote Sensing*, 42(3), pp. 659–663. doi: 10.1007/s12524-013-0333-9.

Voogt, J. A. and Oke, T. R. (2003) 'Thermal remote sensing of urban climates', *Remote Sensing of Environment*, 86(3), pp. 370–384. doi: 10.1016/S0034-4257(03)00079-8.

van de Voorde, T., de Roeck, T. and Canters, F. (2009) 'A comparison of two spectral mixture modelling approaches for impervious surface mapping in urban areas', *International Journal of Remote Sensing*, 30(18), pp. 4785–4806. doi: 10.1080/01431160802665918.

Wang, J. *et al.* (2018) 'Improving impervious surface estimation: an integrated method of classification and regression trees (CART) and linear spectral mixture analysis (LSMA) based on error analysis', *GIScience and Remote Sensing*, 55(4), pp. 583–603. doi: 10.1080/15481603.2017.1417690.

Wang, P. *et al.* (2007) 'Comparison of object-oriented with pixel-based classification techniques on urban classification using TM and IKONOS imagery', *Geoinformatics 2007: Remotely Sensed Data and Information*, 6752, p. 67522J. doi: 10.1117/12.760759.

Wang, Z. *et al.* (2015) 'Application of a normalized difference impervious index (NDII) to extract urban impervious surface features based on Landsat TM images', *International Journal of Remote Sensing*, 36(4), pp. 1055–1069. doi: 10.1080/01431161.2015.1007250.

Waqar, M. M. *et al.* (2012) 'Development of New Indices for Extraction of Built-Up Area & Bare Soil', *Open Access Scientific Reports*, 1(1), pp. 1–4.

Ward, K. *et al.* (2016) 'Heat waves and urban heat islands in Europe: A review of relevant drivers', *Science of the Total Environment*, 569–570, pp. 527–539. doi: 10.1016/j.scitotenv.2016.06.119.

Waser, L. T. *et al.* (2014) 'Evaluating the potential of worldview-2 data to classify tree species and different levels of ash mortality', *Remote Sensing*, 6(5), pp. 4515–4545. doi: 10.3390/rs6054515.

Waske, B. and Braun, M. (2009) 'Classifier ensembles for land cover mapping using multitemporal SAR imagery', *ISPRS Journal of Photogrammetry and Remote Sensing*, 64(5), pp. 450–457. doi: 10.1016/j.isprsjprs.2009.01.003.

Watts, J. D. *et al.* (2009) ‘Monitoring of cropland practices for carbon sequestration purposes in north central Montana by Landsat remote sensing’, *Remote Sensing of Environment*, 113(9), pp. 1843–1852. doi: 10.1016/j.rse.2009.04.015.

Watts, J. D. and Lawrence, L. R. (2008) ‘Merging Random Forest Classification With an Object-Oriented Approach for Analysis of Agricultural Lands’, *The International Archives of the Photogrammetry, Remote Sensing and Spatial Information Sciences*, 37, p. 2018.

Weber, C. (2001) *Remote sensing data used for urban agglomeration delimitation*, *Remote sensing and urban analysis*. London: Taylor & Francis.

Weber, C. *et al.* (2018) ‘Hyperspectral Imagery for Environmental Urban Planning’, in. doi: 10.1109/IGARSS.2018.8519085.

Wei, C. and Blaschke, T. (2018) ‘Pixel-Wise vs. Object-Based Impervious Surface Analysis from Remote Sensing: Correlations with Land Surface Temperature and Population Density’, *Urban Science*, 2(1), p. 2. doi: 10.3390/urbansci2010002.

Weng, Q. (2009) ‘Thermal infrared remote sensing for urban climate and environmental studies: Methods, applications, and trends’, *ISPRS Journal of Photogrammetry and Remote Sensing*, 64(4), pp. 335–344. doi: 10.1016/j.isprsjprs.2009.03.007.

Weng, Q. (2012) ‘Remote sensing of impervious surfaces in the urban areas: Requirements, methods, and trends’, *Remote Sensing of Environment*, 117, pp. 34–49. doi: 10.1016/j.rse.2011.02.030.

Weng, Q., Dengsheng, L. and Jacquelyn, S. (2004) ‘Estimation of land surface temperature–vegetation abundance relationship for urban heat island studies.’, *Remote Sensing of Environment*, 89, pp. 467–483.

Weng, Q. and Lu, D. (2008) ‘A sub-pixel analysis of urbanization effect on land surface temperature and its interplay with impervious surface and vegetation coverage in Indianapolis, United States’, *International Journal of Applied Earth Observation and Geoinformation*, 10(1), pp. 68–83. doi: 10.1016/j.jag.2007.05.002.

Wieland, M. and Pittore, M. (2014) ‘Performance evaluation of machine learning algorithms for urban pattern recognition from multi-spectral satellite images’, *Remote Sensing*, 6(4), pp. 2912–2939. doi: 10.3390/rs6042912.

Wolf, A. (2010) *Using WorldView 2 Vis-NIR MSI imagery to support land mapping and feature extraction using normalized difference index ratios.* Longmont, CO.

World Bank. (2015) *World Bank Database.*

Wu, C. (2004) 'Normalized spectral mixture analysis for monitoring urban composition using ETM+ imagery', *Remote Sensing of Environment*, 93, pp. 480–492. doi: 10.1016/j.rse.2004.08.003.

Xia, J.-S. *et al.* (2011) 'Urban impervious surface area extraction and analysis based on hyperspectral remote sensing image', *Zhongguo Kuangye Daxue Xuebao/Journal of China University of Mining and Technology*, 40, pp. 660–666.

Xian, G. *et al.* (2019) 'Performances of WorldView 3, Sentinel 2, and Landsat 8 data in mapping impervious surface', *Remote Sensing Applications: Society and Environment*, 15. doi: 10.1016/j.rsase.2019.100246.

Xian, G. and Crane, M. (2006) 'An analysis of urban thermal characteristics and associated land cover in Tampa Bay and Las Vegas using Landsat satellite data', *Remote Sensing of Environment*, 104(2), pp. 147–156. doi: 10.1016/j.rse.2005.09.023.

Xiao, H. *et al.* (2018) 'Responses of urban land surface temperature on land cover: A comparative study of Vienna and Madrid', *Sustainability (Switzerland)*, 10(2). doi: 10.3390/su10020260.

Xie, Q. and Zhou, Z. (2015) 'Impact of urbanization on urban heat island effect based on tm imagery in Wuhan, China', *Environmental Engineering and Management Journal*, 14(3), pp. 647–655. doi: 10.30638/eemj.2015.072.

Xu, H. (2007) 'Extraction of urban built-up land features from landsat imagery using a thematic-oriented index combination technique', *Photogrammetric Engineering and Remote Sensing*, 73(12), pp. 1381–1391. doi: 10.14358/PERS.73.12.1381.

Xu, H. (2008) 'A new index for delineating built-up land features in satellite imagery', *International Journal of Remote Sensing*, 29(14), pp. 4269–4276. doi: 10.1080/01431160802039957.

Xu, H. (2010) 'Analysis of impervious surface and its impact on Urban heat environment using the normalized difference impervious surface index (NDISI).', *Photogrammetric Engineering and Remote Sensing*, 76(5), pp. 557–565. doi: 10.14358/PERS.76.5.557.

Xu, H. (2013) 'Rule-based impervious surface mapping using high spatial resolution imagery', *International Journal of Remote Sensing*, 34(1), pp. 27–44. doi: 10.1080/01431161.2012.703343.

Xu, H. and Du, L. (2010) ‘Fast Extraction of Built-up Land Information from Remote Sensing Imagery’, *Geo-information Science*, 12(4), pp. 574–579. doi: 10.3724/sp.j.1047.2010.00574.

Xu, H. and Wang, M. (2016) ‘Remote sensing-based retrieval of ground impervious surfaces’, *Yaogan Xuebao/Journal of Remote Sensing*, 20(5), pp. 1270–1289. doi: 10.11834/jrs.20166210.

Xu, J. *et al.* (2018) ‘Measuring spatio-temporal dynamics of impervious surface in Guangzhou, China, from 1988 to 2015, using time-series Landsat imagery’, *Science of the Total Environment*, 627, pp. 264–281. doi: 10.1016/j.scitotenv.2018.01.155.

Xu, R., Liu, J. and Xu, J. (2018) ‘Extraction of High-Precision Urban Impervious Surfaces from Sentinel-2 Multispectral Imagery via Modified Linear Spectral Mixture Analysis’, *Sensors*, 18, p. 2873. doi: 10.3390/s18092873.

Xu, Z. *et al.* (2018) ‘Multisource Earth Observation Data for Land-Cover Classification Using Random Forest’, *IEEE Geoscience and Remote Sensing Letters*, 15(5), pp. 789–793. doi: 10.1109/LGRS.2018.2806223.

Xu, Z., Mountrakis, G. and Quackenbush, L. J. (2017) ‘Impervious surface extraction in imbalanced datasets: integrating partial results and multi-temporal information in an iterative one-class classifier’, *International Journal of Remote Sensing*, 38(1), pp. 43–63. doi: 10.1080/01431161.2016.1259677.

Yan, G. *et al.* (2006) ‘Comparison of pixel-based and object-oriented image classification approaches - A case study in a coal fire area, Wuda, Inner Mongolia, China’, *International Journal of Remote Sensing*, 27(18), pp. 4039–4055. doi: 10.1080/01431160600702632.

Yang, F. *et al.* (2012) ‘Temporal mixture analysis for estimating impervious surface area from multi-temporal MODIS NDVI data in Japan’, *ISPRS Journal of Photogrammetry and Remote Sensing*, 72, pp. 90–98. doi: 10.1016/j.isprsjprs.2012.05.016.

Yang, F., Matsushita, B. and Fukushima, T. (2010) ‘A pre-screened and normalized multiple endmember spectral mixture analysis for mapping impervious surface area in Lake Kasumigaura Basin, Japan’, *ISPRS Journal of Photogrammetry and Remote Sensing*, 65(5), pp. 479–490. doi: 10.1016/j.isprsjprs.2010.06.004.

Yang, L. *et al.* (2003) ‘An approach for mapping large-area impervious surfaces: Synergistic use of Landsat-7 ETM+ and high spatial resolution imagery’, *Canadian Journal of Remote*

Sensing, 29(2), pp. 230–240. doi: 10.5589/m02-098.

Yang, Y. *et al.* (2017) 'M-FCN: Effective Fully Convolutional Network-Based Airplane Detection Framework', *IEEE Geoscience and Remote Sensing Letters*, PP, pp. 1–5. doi: 10.1109/LGRS.2017.2708722.

Yao, Y. *et al.* (2017) 'Extracting urban impervious surface from GF-1 imagery using one-class classifiers'.

Yeom, J., Han, Y. and Kim, Y. (2013) 'Separability Analysis and Classification of Rice Fields using KOMPSAT-2 High Resolution Satellite Imagery', *Research Journal of Chemistry and Environment*, 17(12), pp. 136–144.

Yin, B.-C., Wang, W. and Wang, L. (2015) 'Review of deep learning', *Beijing Gongye Daxue Xuebao/Journal of Beijing University of Technology*, 41, pp. 48–59. doi: 10.11936/bjutxb2014100026.

Yu, S. *et al.* (2017) 'Monitoring and analyzing the spatial dynamics and patterns of megacities along the Maritime Silk Road', *Yaogan Xuebao/Journal of Remote Sensing*, 21(2), pp. 169–181. doi: 10.11834/jrs.20176031.

Yu, X. and Lu, C. (2014) 'Urban percent impervious surface and its relationship with land surface temperature in Yantai City, China', *IOP Conference Series: Earth and Environmental Science*, 17(1). doi: 10.1088/1755-1315/17/1/012163.

Yu, Y. *et al.* (2018) 'Urban impervious surface estimation from remote sensing and social data', *Photogrammetric Engineering and Remote Sensing*, 84(12), pp. 771–780. doi: 10.14358/PERS.84.12.771.

Yuan, F. and Bauer, M. E. (2007) 'Comparison of impervious surface area and normalized difference vegetation index as indicators of surface urban heat island effects in Landsat imagery', *Remote Sensing of Environment*, 106(3), pp. 375–386. doi: 10.1016/j.rse.2006.09.003.

Zha, Y., Gao, J. and Ni, S. (2003) 'Use of normalized difference built-up index in automatically mapping urban areas from TM imagery', *International Journal of Remote Sensing*, 24(3), pp. 583–594. doi: 10.1080/01431160304987.

Zha, Y., Ni, S. and Yang, S. (2003) 'An effective approach to automatically extract urban land-use from TM imagery', *Journal of Remote Sensing-Beijing-*, 7(1), pp. 37–40.

Zhang, H. (2016) ‘Mapping urban impervious surface with dual-polarimetric SAR data: An improved method’, *Landscape and Urban Planning*, 151, pp. 55–63. doi: 10.1016/j.landurbplan.2016.03.009.

Zhang, H., Lin, H. and Wang, Y. (2018) ‘A new scheme for urban impervious surface classification from SAR images’, *ISPRS Journal of Photogrammetry and Remote Sensing*, 139. doi: 10.1016/j.isprsjprs.2018.03.007.

Zhang, H., Zhang, Y. and Lin, H. (2012) ‘Evaluation of the potential of ASAR data to estimate impervious surface area’, *Annals of GIS*, 18. doi: 10.1080/19475683.2012.730059.

Zhang, L. and Shao, Z. (2017) ‘An evaluation of monthly impervious surface dynamics by fusing Landsat and MODIS time series in the Pearl River Delta, China, from 2000 to 2015’, *Remote Sensing of Environment*, 201, pp. 99–114. doi: 10.1016/j.rse.2017.08.036.

Zhang, Liangpei, Zhang, Lefei and Du, B. (2016) ‘Deep Learning for Remote Sensing Data: A Technical Tutorial on the State of the Art’, *IEEE Geoscience and Remote Sensing Magazine*, 4, pp. 22–40. doi: 10.1109/MGRS.2016.2540798.

Zhang, T. and Huang, X. (2018) ‘Monitoring of Urban Impervious Surfaces Using Time Series of High-Resolution Remote Sensing Images in Rapidly Urbanized Areas: A Case Study of Shenzhen’, *IEEE Journal of Selected Topics in Applied Earth Observations and Remote Sensing*, 11(8), pp. 2692–2708. doi: 10.1109/JSTARS.2018.2804440.

Zhang, X. *et al.* (2017) ‘Effects of land use/cover changes and urban forest configuration on urban heat islands in a loess hilly region: Case study based on yan’an city, China’, *International Journal of Environmental Research and Public Health*, 14(8). doi: 10.3390/ijerph14080840.

Zhang, X. and Du, S. (2015) ‘A Linear Dirichlet Mixture Model for decomposing scenes: Application to analyzing urban functional zonings’, *Remote Sensing of Environment*, 169, pp. 37–49. doi: 10.1016/j.rse.2015.07.017.

Zhang, Y., Odeh, I. O. A. and Han, C. (2009) ‘Bi-temporal characterization of land surface temperature in relation to impervious surface area, NDVI and NDBI, using a sub-pixel image analysis’, *International Journal of Applied Earth Observation and Geoinformation*, 11(4), pp. 256–264. doi: 10.1016/j.jag.2009.03.001.

Zhang, Y., Zhang, H. and Lin, H. (2014) ‘Improving the impervious surface estimation with combined use of optical and SAR remote sensing images’, *Remote Sensing of Environment*, 141, pp. 155–167. doi: 10.1016/j.rse.2013.10.028.

Zhao, Q. *et al.* (2015) 'Rooftop surface temperature analysis in an Urban residential environment', *Remote Sensing*, 7(9), pp. 12135–12159. doi: 10.3390/rs70912135.

Zhao, Q. and Wentz, E. (2016) 'A MODIS/ASTER Airborne Simulator (MASTER) Imagery for Urban Heat Island Research', *Data*, 1. doi: 10.3390/data1010007.

Zheng, B., Myint, S. and Fan, C. (2014) 'Spatial configuration of anthropogenic land cover impacts on urban warming', *Landscape and Urban Planning*, 130, pp. 104–111. doi: 10.1016/j.landurbplan.2014.07.001.

Zhou, J. *et al.* (2016) 'Quantification of the scale effect in downscaling remotely sensed land surface temperature', *Remote Sensing*, 8(12). doi: 10.3390/rs8120975.

Zhou, Q. and Robson, M. (2001) 'Automated rangeland vegetation cover and density estimation using ground digital images and a spectral-contextual classifier', *International Journal of Remote Sensing*, 22(17), pp. 3457–3470. doi: 10.1080/01431160010004504.

Zhou, W. and Troy, A. (2008) 'An object-oriented approach for analysing and characterizing urban landscape at the parcel level', *International Journal of Remote Sensing*, 29(11), pp. 3119–3135. doi: 10.1080/01431160701469065.

Zhou, W., Wang, J. and Cadenasso, M. L. (2017) 'Effects of the spatial configuration of trees on urban heat mitigation: A comparative study', *Remote Sensing of Environment*, 195, pp. 1–12. doi: 10.1016/j.rse.2017.03.043.

Zhou, Y. *et al.* (2014) 'A new index for mapping built-up and bare land areas from Landsat-8 OLI data', *Remote Sensing Letters*, 5(10), pp. 862–871. doi: 10.1080/2150704X.2014.973996.

Zhu, X. *et al.* (2017) 'Deep Learning in Remote Sensing: A Comprehensive Review and List of Resources', *IEEE Geoscience and Remote Sensing Magazine*, 5, pp. 8–36. doi: 10.1109/MGRS.2017.2762307.

Zhu, Y. *et al.* (2017) 'Exploring the potential of world view-2 red-edge band-based vegetation indices for estimation of mangrove leaf area index with machine learning algorithms', *Remote Sensing*, 9(10). doi: 10.3390/rs9101060.

Publications

Adeniyi Adeyemi, Abel Ramoelo, Moses Cho, Cecilia R. Masemola (2021) - Spectral index to improve the extraction of built-up area from WorldView-2 imagery, Journal of Applied Remote Sensing 15(2) 024510 (26 April 2021), https://doi.org/10.1117/1.JRS.15.024510.

Adeniyi Adeyemi, Abel Ramoelo, Moses Cho, Jacobus Strydom (2021) - Spatio-temporal analysis of built-up impervious surface area and interplay with land surface temperature in Pretoria, South Africa., Geocarto International (13 September 2021), https://doi.org/10.1080/10106049.2021.1980617

Adeniyi Adeyemi, Abel Ramoelo, Moses Cho, Jacobus Strydom - Assessment of spatio-temporal direction of impervious surface area surface temperature in Pretoria, South Africa, Geocarto International, (29 December 2021),https://doi.org/10.1080/10106049.2021.2022018

Short Certificate Courses Attended

GEOBIA training course on object-oriented classification by Centre for Geographic Analysis (CGA) from the Stellenbosch University in collaboration with Natural Resources and the Environment (NRE), Council for Scientific and Industrial Research (CSIR), Pretoria South Africa – 2017.

PRAIRIE A.I summer school (PAISS) by INRIA, Naverlabs and Universite Grenoble Alpes, Lyon, France – 2018.

Biography

Adeniyi Adedayo Adeyemi was born in Abeokuta the capital city of Ogun State, Nigeria on the 25th of March 1984. He completed his primary education in 1995 at St. Bernadette's Nursery and Primary School, Panseke, Abeokuta. In 2001 he completed West African School Certificate (WAEC) from ta Iyalode, Ita Eko, Abeokuta. After WAEC, he pursued a Bachelor of Science Honours degree in environmental sciences (Environmental Management & Toxicology) from the College of Environmental Resources Management (COLERM), Department of Environmental Management and Toxicology, University of Agriculture, Abeokuta (which is now called Federal University of Agriculture, Abeokuta (FUNAAB)) and graduated outstandingly with a second class upper division (2:1). During his honours degree, he worked on a mini dissertation for the first time in the school history on land use changes that have occurred within the university's entire land cover of about ten thousand hectares using geographical information system (GIS), remote sensing data and other in-situ measurements. After his honours, he developed a passion for applied remote sensing and GIS and worked as a junior researcher both at the Department of Ecology, Ministry of Environment and Mineral Resources, Ondo state and Department of Environmental Planning and Statistics, Ministry of Environment, Ogun state for three years.

He arrived in South Africa in 2012 and since education has always been an important aspect of his life, he decided to advance in my academic career at the University of Pretoria where he completed Master of Science in Geoinformatics (applied remote sensing and GIS – urban heat island study) at the Department of Geography, Geoinformatics & Meteorology, with research focus titled: Analysis of Impervious Surfaces and Surface Temperature over Tshwane Metropolitan using in-situ and remote sensing data. This research was supervised by Dr. Joel Botai (Department of Geoinformatics) and Dr. Abel Ramoelo (Council for Scientific and Industrial Research, CSIR). After acquiring his Master's degree in 2015, he started his PhD Environmental science in 2017, at the University of South Africa (UNISA) under the supervision of Professor Abel Ramoelo (Director: Centre for Environmental Studies (CFES), Department of Geography, Geoinformatics and Meteorology, University of Pretoria) and Professor Moses Azong Cho (Precision Agriculture Research Group, Council for Scientific and Industrial Research, CSIR) which resulted in this thesis.